

**A SIMULATION STUDY OF COLLECTIVE BEHAVIOUR
OF HADRONIC MATTER AT FAIR ENERGIES**

**A thesis submitted to the University of North Bengal
in partial fulfilment of the requirements for the degree of
DOCTOR OF PHILOSOPHY
in Physics**

BY

Soumya Sarkar

SUPERVISOR

Amitabha Mukhopadhyay

Professor of Physics

UNIVERSITY OF NORTH BENGAL

December 2021

DECLARATION

I declare that the thesis entitled, A SIMULATION STUDY OF COLLECTIVE BEHAVIOUR OF HADRONIC MATTER AT FAIR ENERGIES, has been prepared by me under the guidance of Prof. Amitabha Mukhopadhyay, Department of Physics, University of North Bengal. No part of this thesis has been formed on the basis of any previously awarded degree or fellowship.

Date: 27/12/2021

Soumya Sarkar

Soumya Sarkar

Department of Physics
University of North Bengal
Siliguri 734 013, Darjeeling, India

CERTIFICATE

This is to certify that the work contained in the thesis titled “ A SIMULATION STUDY OF COLLECTIVE BEHAVIOUR OF HADRONIC MATTER AT FAIR ENERGIES” submitted by Mr. Soumya Sarkar, has been carried out in the Department of Physics, University of North Bengal under my supervision. This work has not been submitted elsewhere for any degree/diploma.

Date: 27/12/2021

Amitabha Mukhopadhyay

Prof. Amitabha Mukhopadhyay
Supervisor

Department of Physics
University of North Bengal
Siliguri 734013, West Bengal, India

Document Information

Analyzed document	Soumya Sarkar_Physics.pdf (D123562954)
Submitted	2021-12-23T08:58:00.0000000
Submitted by	University of North Bengal
Submitter email	nbuplg@nbu.ac.in
Similarity	1%
Analysis address	nbuplg.nbu@analysis.arkund.com

Sources included in the report

W	URL: https://drupal.star.bnl.gov/STAR/files/thesis_Rihan_Haque.pdf Fetched: 2021-11-03T15:04:36.5730000	 9
J	URL: e55b8639-610b-40af-970e-44e4d725c2ae Fetched: 2019-02-19T01:28:30.1470000	 2
W	URL: https://arxiv.org/pdf/2111.05248 Fetched: 2021-11-23T20:02:59.8530000	 1
W	URL: https://www.math.ucdavis.edu/~linear/linear-guest.pdf Fetched: 2020-03-21T17:02:05.8870000	 1
W	URL: https://www.science.gov/topicpages/u/ultrarelativistic+heavy-ion+collisions Fetched: 2021-11-08T08:20:36.0970000	 1
W	URL: https://d-nb.info/1043978305/34 Fetched: 2021-07-14T12:31:20.0970000	 1
W	URL: https://en.wikipedia.org/wiki/Pseudorapidity Fetched: 2020-01-17T23:52:25.3400000	 1

A SIMULATION STUDY OF COLLECTIVE BEHAVIOUR OF HADRONIC MATTER AT FAIR ENERGIES

ABSTRACT

We investigate collective behaviour of hadronic matter produced in high-energy heavy-ion collisions in the framework of microscopic transport models and in the context of upcoming Compressed Baryonic Matter (CBM) experiment to be held at the Facility for Antiproton and Ion Research (FAIR). One of the major objectives to study nucleus-nucleus (AB) collisions at high-energies is to produce a color deconfined state like the Quark-gluon Plasma (QGP), composed of strongly interacting quarks and gluons, under extreme conditions of temperature and/or pressure. The properties of QGP are guided by the rules of quantum chromodynamics (QCD), the non-abelian color gauge theory of strong interaction. It is quite intriguing to see how macroscopic and collective properties develop in the QGP from interactions among quarks and gluons, taking place within a system of a few hundred (or thousand) fm^3 in volume and an average lifetime of about 10^{-22} sec. These simulated results are going to give us an opportunity to examine the collective behaviour of hadronic matter at high baryon density and moderate temperature.

In **Chapter One** we qualitatively review various aspects of high-energy AB collisions. At the very beginning we underline the salient features of QCD. The cosmological and astrophysical relevance of AB collisions are briefly mentioned. The heavy-ion accelerator facilities that existed in the past, operating at present and are going to come up in near future, are summarily reviewed. Some general physical characteristics of the QGP state created in the LHC experiments are listed. The space-time evolution of an AB collision is sequentially described with and without taking the QGP formation into account. Apart from the QGP, several other states of strongly interacting objects are allowed in nature. The QCD phase-diagram that gives us a summary of all such states and the demarcation lines separating one phase from the others, is qualitatively described. The thermodynamics and hydrodynamics of AB collisions have been discussed in the framework of Fermi's model, MIT bag model, Landau's hydrodynamic model and Bjorken's hydrodynamic model. In order to identify QGP formation, one must set appropriate signals that survive the vigor of AB collisions. The experimental status of several such signatures are summarily described. As the present investigation deals mainly with the simulation study of collective flow, we have discussed its experimental status with a little more details. A brief outline of the CBM-FAIR experiment has been discussed thereafter. To conclude this introductory chapter, we highlight the major objectives of the present investigation.

In **Chapter Two** we qualitatively describe the event generators used in this simulation based investigation. Salient features of the Ultra-relativistic Quantum Molecular Dynamics (UrQMD), A Multi Phase Transport (AMPT) model, both in its default and string melting (SM) configuration, and the Monte-Carlo Glauber (MCG) model are discussed. MCG code is used to determine the initial state geometry and centrality of AB collisions. Some global aspects of multiparticle emission are discussed by using Au+Au event samples simulated at different incident beam energies (E_{lab}) expected at the FAIR. We observe that the charge hadron yield in the central particle producing region follows a power law dependence on the number of participating nucleons. Longitudinal scaling is observed in the pseudorapidity (η) distributions of charged hadrons and their average transverse momentum (p_T). The transverse mass spectra of different hadron species are used to determine the kinetic freeze out temperature and velocity of radial expansion. First indication of collective radial expansion is found from this analysis.

In **Chapter Three** we present our simulation results on elliptic (v_2) and triangular (v_3) flow parameters derived from the azimuthal distributions of charged hadrons in Au+Au events generated by the UrQMD and AMPT model(s) at $E_{\text{lab}} = (10 - 40)A$ GeV. Event-by-event fluctuations of the collision geometry has been taken into account while determining the initial space asymmetries associated with the overlapping parts of the collision systems. The centrality dependence of eccentricity (ε_2), triangularity (ε_3), v_2 and v_3 are studied. The v_2 -measures are found to be relatively small in the peripheral and extreme central collisions, but they peak around mid-central collisions. As ε_2 is scaled out from v_2 , these maxima shift towards higher centrality. Our AMPT (SM) results on v_2 at $E_{\text{lab}} = 30A$ GeV match with those of the STAR experiment on Au+Au collision at $\sqrt{s_{NN}} = 7.7$ GeV. Our v_2 results are also consistent with a universal scaling with respect to the transverse particle density. v_3 originates only from event-by-event fluctuations, and it is weaker than v_2 by more than an order of magnitude. UrQMD does not produce any v_3 at all. When ε_3 is scaled out of v_3 , a linear rise with centrality is observed. This indicates an entropy driven multiplicity scaling, a characteristic feature of soft-hadron production. Both the flow parameters rise approximately linearly with p_T , a behaviour that is not quite influenced by the spatial asymmetries. It appears that at higher p_T particles are producing a higher amount of flow. Mass ordering of the flow parameters at low- p_T and a scaling with the number of constituent quarks are also observed. AMPT (SM) turns out to be the best option to describe the collective flow effects at FAIR energies. The cumulant technique has also been employed to estimate v_2 and its fluctuations, which reveals that significant contribution to the fluctuations is coming from the initial state distributions of the participant nucleons.

In **Chapter Four** we have studied the dependence of v_2 and v_3 on parton scattering cross-section (σ) in Au+Au events at $E_{\text{lab}} = 30A$ GeV generated by the AMPT (SM). The

σ -dependences of charged hadron yield and average- p_T are examined too. Both the flow parameters and average- p_T are found to increase with increasing σ . The particle yield decreases marginally with increasing σ . The changes in observables however are not proportional to the changes in σ , and can at the best be called moderate. The STAR results seem to be better matching with our AMPT (SM) prediction for $\sigma = 1.5(3.0)$ mb. A longitudinal scaling with respect to the σ -variation has been observed in the η -distribution of v_2 , which is not found in v_3 .

A system-size dependence of the directed flow (v_1), v_2 and v_3 of charged hadrons produced in AB collisions is investigated in **Chapter Five**. AMPT (SM) has been used to generate $^{28}\text{Si}+^{28}\text{Si}$, $^{59}\text{Ni}+^{59}\text{Ni}$, $^{115}\text{In}+^{115}\text{In}$ and $^{197}\text{Au}+^{197}\text{Au}$ events at $E_{\text{lab}} = 30A$ GeV. The distributions of flow parameters, their centrality and p_T -dependence are examined. η -distribution of v_1 is also presented. The centrality dependence of ε_2 and ε_3 are shown. All three flow parameters are found to be normally distributed. In comparison with v_2 and v_3 , the distributions of v_1 are much more sharply peaked. The distributions of ε_2 and ε_3 are however slightly right skewed. They do not exactly coincide with the corresponding v_2 and v_3 -distributions, indicating deviation from a one to one linear dependence. The η -dependence of v_1 wiggles around the zero line, a feature typically observed also in experiments. In cascade models this wiggle is explained in terms of a space-momentum correlation and different amount of rapidity loss in different regions. All other distributions behave more or less similarly as described in Chapter Three. In general a moderate amount of system-size dependence has been observed in the behaviour of all three flow parameters. Most of our simulation based results however can be interpreted in terms of geometrical effects and/or multiplicity scaling.

In order to explore the collective radial flow of charged hadrons, in **Chapter Six** the azimuthal distributions of their multiplicity values, total radial velocity (V_T) and mean transverse velocity (v_T) are compared with each other using Au+Au events generated by the AMPT (SM) model at $E_{\text{lab}} = 10A$ and $40A$ GeV. v_T seems to be a good choice for studying the radial expansion. While the anisotropic part of each distribution indicates a collective radial expansion, its isotropic part characterizes a thermal motion. We have studied the centrality and p_T -dependence of both the anisotropic and isotropic parts. Our results on centrality dependence suggest that v_2 associated with V_T is strongest, which predominantly is due to the contribution coming from azimuthal anisotropy in the charged hadron multiplicity distributions. v_2 associated with v_T has been found to be rather weak. The isotropic component on the other hand is found to be strongest for the multiplicity distribution, a characteristic feature of soft-hadron production. In contrast, the p_T -dependence of v_2 shows that variations are more or less similar (linearly dependent) for all three observables, a feature that again is not quite unexpected. Higher p_T corresponds to a higher v_T . As a

result, the linear dependence between v_2 and p_T is directly mapped into a similar $v_2 - v_T$ dependence. Our study on p_T -dependence also suggests that at FAIR energies the isotropic component dominates the radial expansion. However, perhaps an analysis for different hadron species is required to better understand these observations.

In **Chapter Seven** we have used transverse sphericity (S_T), a unique event shape variable, to classify AB events into isotropic and jetty categories. A systematic study is presented on the p_T -spectra, particle yield and collective flow parameters of different charged hadrons for these two categories of Au+Au events generated once again at $E_{\text{lab}} = 30A$ GeV by the AMPT (SM). The p_T -spectra of charged hadrons obtained for the isotropic and jetty events themselves provide an indication of the onset of collective behaviour. v_2 for the jetty events are found to be much higher in magnitude than those obtained from both the isotropic and S_T -integrated class of events. However, no such dependence on S_T is noticed for v_3 .

The present thesis concludes with a brief and critical discussion on our results, that would help us to understand the early stage dynamics of the compressed QCD matter and set a reference baseline to the real experiments to be conducted at FAIR. However, there is an appendix at the end, where the kinematics of two-body interaction is discussed.

Acknowledgments

I would like to take this opportunity to express my sincere appreciation for all those who have supported, encouraged, and inspired me in the pursuit of my research work. My thesis work would have not been possible without the support and encouragement from my teachers, colleagues, friends and family members. First and foremost, I would like to thank my supervisor Prof. Amitabha Mukhopadhyay of the Physics Department of North Bengal University for teaching me many Physics courses in the post-graduate level, and also for guiding my Ph.D. research. My interactions with him during the past several years has been a great experience. His constructive criticism on my research work was essential for a successful completion of this thesis. I would like to express my sincere gratitude to Dr. Provash Mali of the Physics Department of North Bengal University for his constant help and support, particularly at the beginning of my research career in the area of computational work and in developing software. I also acknowledge the discussions that on several occasions I had with Prof. Subhasis Chattopadhyay and Dr. Partha Pratim Bhaduri, both from the Variable Energy Cyclotron Centre, Kolkata, during my stay there at the early stages of my research career. My heartfelt gratitude goes to Mr. Sanjib Kumar Manna, Mr. Somnath Ghosh and especially to Mr. Joydeep Thakur, research students of the Physics Department of North Bengal University, for maintaining an enjoyable working atmosphere in the laboratory and for their very warm hearted help and support. It is also a great pleasure to thank all my colleagues at the Siliguri College. Finally and most importantly, I would like to convey my deepest sense of gratitude to my family for the much and often needed moral support, which has kept me going.

Soumya Sarkar

*Dedicated to the memory of
My Father*

Contents

Declaration	i
Certificate	ii
Abstract	iv
Acknowledgments	viii
List of Tables	xiii
List of Figures	xiv
1 A general overview of high-energy heavy-ion interaction	1
1.1 Introduction	1
1.1.1 Experimental facilities	6
1.2 Relativistic heavy ion collision and QGP	8
1.2.1 Space-time evolution	10
1.2.2 Thermodynamics of the fireball	12
1.2.3 Hydrodynamics of the fireball	14
1.2.4 QCD phase diagram	18
1.3 Signatures of QGP signal : Experimental observables	21
1.3.1 Charmonium suppression	21
1.3.2 Jet quenching	22
1.3.3 Strangeness enhancement	24
1.3.4 Electromagnetic probes	25
1.3.5 Collective flow	26
1.4 CBM experiment at FAIR	35
1.5 Objective of the thesis	37
2 Simulation models and some bulk properties of charged hadron production at expected FAIR energies	43
2.1 Brief description of the models	44
2.1.1 UrQMD model	44
2.1.2 AMPT model	46
2.1.3 Glauber model	49

2.2	Bulk properties of hadron production	52
2.2.1	Pseudorapidity distribution: Longitudinal scaling	55
2.2.2	Integrated yield	57
2.2.3	Transverse momentum spectra: Radial flow	59
2.3	Conclusion	63
3	Elliptic and triangular flow parameters at expected FAIR energies	66
3.1	Methodology	67
3.2	Results and discussion	73
3.2.1	Centrality dependence of v_2 and v_3	76
3.2.2	Transverse momentum dependence of v_2 and v_3	85
3.2.3	Species dependence of v_2 and v_3	91
3.2.4	Averaging scheme of v_n	94
3.2.5	Cumulants and flow fluctuations	96
3.3	Conclusion	100
4	Dependence of elliptic and triangular flow parameters on partonic scattering cross-section	104
4.1	Results and discussion	105
4.1.1	Initial geometric dependence of v_2 and v_3	106
4.1.2	Centrality dependence of v_2 and v_3	108
4.1.3	Relative strength of v_2 and v_3	112
4.1.4	Transverse momentum dependence of v_2 and v_3	113
4.1.5	Pseudorapidity dependence of v_2 and v_3	116
4.2	Conclusion	118
5	System-size dependence of collective flow parameters	120
5.1	Results and discussions	121
5.1.1	Distributions of the flow parameters	125
5.1.2	The directed flow	127
5.1.3	Centrality dependence of v_2 and v_3	130
5.1.4	Transverse momentum dependence of v_2 and v_3	134
5.2	Conclusion	136
6	Radial flow of charged hadrons at FAIR conditions	139
6.1	Methodology	140
6.2	Results and discussion	141
6.2.1	Centrality dependence of v_2 and v_0	142
6.2.2	Transverse momentum dependence of v_2 and v_0	144
6.3	Conclusion	146
7	Sphericity based flow analysis at FAIR conditions	149
7.1	Methodology	150
7.2	Results and discussions	151

7.2.1	p_T spectra and mean p_T	152
7.2.2	Integrated yields	155
7.2.3	Collective flow	157
7.3	Conclusion	163
Concluding remarks		165
Appendix A		169
List of publications		175

List of Tables

1.1	Chronological commissioning of HIC accelerator facilities (past and present).	7
1.2	Physics issues and their corresponding observables for the CBM experiment.	36
2.1	N_{part} , N_{coll} at different centrality (in %) as obtained from MCG model in Au+Au collisions at $E_{\text{lab}} = (10 - 40)A$ GeV and central particle density estimated from AMPT(default), AMPT(string melting) and UrQMD model.	53
2.2	Centroid of the pseudorapidity distribution (η_0) in Au+Au collisions corresponding to different energies (in GeV) as obtained from the AMPT (default), AMPT(string melting) and UrQMD model.	55
2.3	Fit parameters of Equation (2.12) as obtained at different energies for AMPT (default), AMPT (string melting), and UrQMD model.	59
2.4	The values of kinetic freeze-out temperature T_{kin} (in MeV) and square of radial flow velocity $\langle\beta_T\rangle^2$ (in c^2) for the 0 – 5% most central Au+Au events corresponding to different energies for the AMPT (default), AMPT (string melting), and UrQMD models.	62
3.1	N_{coll} , N_{part} , S , $\varepsilon_2^{\text{std}}$, $\varepsilon_2^{\text{part}}$ and ε_3 at different centralities in Au+Au collision at $E_{\text{lab}} = 30A$ GeV obtained from the MCG simulation.	75
5.1	N_{part} dependence of the asymmetry parameters and midrapidity particle densities in different colliding systems at $E_{\text{lab}} = 30A$ GeV.	124
7.1	Limiting values of transverse sphericity for jetty and isotropic events	152

List of Figures

1.1	Measurements of the strong field coupling constant (α_s) against energy-momentum transfer Q . Lines refer to the perturbative QCD prediction which are in excellent agreement with the experiments. The figure is taken from [8].	2
1.2	A probable timeline of the universe since Big Bang [21].	5
1.3	A typical nucleus-nucleus interaction before and after the collision. Particles are produced in the participants' zone, while the spectators remain uninfluenced. The figure is taken from Ref. [23].	8
1.4	Schematic exemplar of different stages of a heavy-ion collision, the <i>Little Bang</i> . The figure is taken from Ref. [26]	10
1.5	Space time evolution of a high-energy collision between two nuclei in their CM frame, (a) without and (b) with QGP formation. The figure is taken from Ref. [27].	11
1.6	A schematic of the QCD phase diagram showing locations of different states of hadronic/partonic matter [51].	19
1.7	Centrality dependence of J/ψ R_{AA} . This figure is taken from Ref. [56].	22
1.8	Left: Schematic of di-jet production. Right: Distribution of azimuthal angle difference between trigger and associated particles at STAR from central Au+Au, d+Au, and p+p collisions. The figure is taken from Ref. [62].	23
1.9	R_{AA} values for jets considering two different p_T intervals at midrapidity as a function of N_{part} . The figure is taken from Ref. [63].	23
1.10	Strangeness enhancements at midrapidity as a function of N_{part} , showing LHC, RHIC and SPS data simultaneously. The figure is taken from Ref. [66].	24
1.11	Schematic of initial space anisotropy w.r.t the reaction ($x - z$) plane being converted into momentum space anisotropy due to in-medium interactions among the final state hadrons.	27
1.12	First measurement of in-plane elliptic flow by the E877 Collaboration at 11.8A Gev [74]. The solid line is a distribution with Fourier coefficients v_0, v_1, v_2 at three different pseudorapidity.	28

1.13	Elliptic flow at midrapidity in 20 – 30% centrality bin as a function of energy from FOPI, AGS, SPS, RHIC to LHC. The basic figure is taken from [76] except certain textual changes.	29
1.14	Elliptic flow as a function of centrality defined as n_{ch}/n_{max} reported by STAR Collaboration at $\sqrt{s_{NN}} = 130$ GeV [77]. The open rectangles show a range of values expected for v_2 in the hydrodynamic limit, scaled from ε , the initial space eccentricity of the overlap region.	29
1.15	Elliptic flow integrated over the p_T range $0.2 < p_T < 5.0$ GeV/c at $\sqrt{s_{NN}} = 2.76$ TeV as a function of centrality [78]. RHIC measurements at $\sqrt{s_{NN}} = 200$ GeV is integrated over the p_T range $0.15 < p_T < 5.0$ GeV/c.	30
1.16	p_T dependence of $v_2\{4\}$ at $\sqrt{s_{NN}} = 2.76$ TeV for various centralities compared to STAR measurements at $\sqrt{s_{NN}} = 200$ GeV [78].	30
1.17	Left: Differential elliptic flow at RHIC ($\sqrt{s_{NN}} = 200$ GeV) as a function of transverse momentum compared to hydrodynamical predictions [81]. Right: Hydrodynamical prediction of differential elliptic flow for 20 – 30% centrality at $\sqrt{s_{NN}} = 200$ GeV (dashed lines) and $\sqrt{s_{NN}} = 2.76$ TeV (solid lines) [80].	31
1.18	Left: v_2 against transverse kinetic energy (KE_T) for different species for minimum bias Au+Au collisions at $\sqrt{s_{NN}} = 200$ GeV. Right: Same but after scaling by NCQ. The figure is taken from [84].	32
1.19	Eccentricity scaled v_2 as a function of particle density in the transverse plane at AGS, SPS to RHIC. The figure is from Ref. [88].	33
1.20	Difference in v_2 for particles and their corresponding anti-particles measured by the STAR collaboration at RHIC for 0 – 80% central events. Dashed lines are fits to some power law function, the details of which can be found in [89].	33
1.21	Transverse momentum dependence of different order flow harmonics (v_n) estimated by the ALICE Collaboration. [93].	34
1.22	Left: Hadronic freeze out line on the temperature versus net-baryon density plane as obtained in statistical model [98]. Right: Interaction rate reached by existing and future heavy-ion experiments as a function of beam energy [99].	35
2.1	Charged hadron multiplicity distribution in Au+Au collisions at $E_{lab} = (10 - 40)A$ GeV.	52
2.2	Impact parameter dependence of N_{part} and N_{coll} in Au+Au collisions at $E_{lab} = (10 - 40)A$ GeV.	54
2.3	Azimuthal angle distribution of charged hadrons at midrapidity in Au+Au collisions at $E_{lab} = (10 - 40)A$ GeV.	54
2.4	Pseudorapidity distribution of charged hadrons in Au+Au collisions at $E_{lab} = (10 - 40)A$ GeV.	55

2.5	Variation of $dN_{\text{ch}}/d\eta$ with η for 0 – 5% central Au+Au collisions at $E_{\text{lab}} = (10 - 40)A$ GeV.	56
2.6	Variation of $\langle p_T \rangle$ of charged hadrons with η in Au+Au collisions at $E_{\text{lab}} = (10 - 40)A$ GeV.	56
2.7	Centrality dependence of the integrated yield of charged hadrons per participant pair at midrapidity in Au+Au collisions at $E_{\text{lab}} = (10 - 40)A$ GeV. The solid lines represent the fit following Equation (2.12).	58
2.8	Transverse momentum spectra of all charged hadrons at midrapidity in Au+Au collisions at $E_{\text{lab}} = (10 - 40)A$ GeV. For clarity the UrQMD and AMPT (default) results are scaled with appropriate factors.	60
2.9	Transverse mass spectra for pion, kaon and proton at midrapidity for 0 – 5% central Au+Au collisions at $E_{\text{lab}} = 30A$ GeV. The UrQMD and AMPT (default) results are scaled properly for clarity.	60
2.10	Hadronic mass dependence of effective temperature for 0 – 5% central Au+Au collisions at $E_{\text{lab}} = (10 - 40)A$ GeV. The solid lines are linear fit following Equation (2.14). The NA49 points are taken from [40]	61
2.11	Average transverse momentum of charged hadrons at midrapidity plotted against centrality in Au+Au collisions at $E_{\text{lab}} = (10 - 40)A$ GeV.	62
3.1	Left: Schematic of a non-central heavy-ion collision in the transverse plane [16]. Right: v_2 scaled by ε_{std} as a function of N_{part} [4].	68
3.2	Left: Schematic of a heavy-ion collision illustrating the reaction plane and participant plane. Right: v_2 scaled by $\varepsilon_{\text{part}}$ as a function of N_{part} [4].	69
3.3	Exemplar of elliptic and triangular anisotropies generated after a collision between two nuclei. The pink circles represent the participating nucleons. The figure is taken from [18]	70
3.4	Centrality dependence of ε_n of the overlapping region for Au+Au collision at $E_{\text{lab}} = 30A$ GeV.	74
3.5	Centrality dependence of the elliptic flow parameter of charged hadrons at midrapidity in Au+Au collision at $E_{\text{lab}} = (10 - 40)A$ GeV without considering initial fluctuations. Experimental data points are from [9].	77
3.6	$v_2/\varepsilon_2^{\text{std}}$ as a function of N_{part} for the charged hadrons at midrapidity in Au+Au collisions at $E_{\text{lab}} = (10 - 40)A$ GeV without considering initial fluctuations.	78
3.7	Centrality dependence of elliptic flow of charged hadrons at midrapidity in Au+Au collision at $E_{\text{lab}} = (10 - 40)A$ GeV after considering initial fluctuations. Experimental data points are from Ref. [9].	79

3.8	$v_2/\varepsilon_2^{\text{part}}$ as a function of N_{part} for the charged hadrons at midrapidity in Au+Au collisions at $E_{\text{lab}} = (10-40)A$ GeV after considering initial fluctuations.	80
3.9	Variation of scaled elliptic flow with scaled particle density.	81
3.10	Centrality dependence of triangular flow of charged hadrons at midrapidity in Au+Au collision at $E_{\text{lab}} = (10-40)A$ GeV	83
3.11	v_3/ε_3 as a function of N_{part} for the charged hadrons at midrapidity in Au+Au collisions at $E_{\text{lab}} = (10-40)A$ GeV.	83
3.12	v_3/v_2 -ratio computed at midrapidity plotted as a function of N_{part} in different p_T intervals in Au+Au collision at $E_{\text{lab}} = 30A$ GeV for the AMPT (string melting) model simulation (upper panel). The v_3/v_2 -ration for a p_T interval is scaled by the corresponding ratio for the entire p_T -range ($0 \leq p_T \leq 2.0$ GeV/c) (lower panel).	85
3.13	v_2 and v_2/ε_2 plotted against p_T for charged hadrons at midrapidity in Au+Au collisions at $E_{\text{lab}} = 10A$ GeV. v_2 for the last two centralities are slightly shifted for clarity.	86
3.14	Same as in Figure 3.13 but at $E_{\text{lab}} = 20A$ GeV.	86
3.15	Same as in Figure 3.13 but at $E_{\text{lab}} = 30A$ GeV. The available experimental results (STAR data) are shown by continuous curves.	87
3.16	Same as in Figure 3.13 but at $E_{\text{lab}} = 40A$ GeV.	87
3.17	v_3 and v_3/ε_3 plotted against p_T for charged hadrons at midrapidity in Au+Au collisions at $E_{\text{lab}} = 10A$ GeV.	89
3.18	Same as in Figure 3.17 but at $E_{\text{lab}} = 20A$ GeV.	89
3.19	Same as in Figure 3.17 but at $E_{\text{lab}} = 30A$ GeV.	90
3.20	Same as in Figure 3.17 but at $E_{\text{lab}} = 40A$ GeV.	90
3.21	Species dependence of v_2 as a function of p_T at midrapidity for Au+Au collision at $E_{\text{lab}} = 30A$ GeV.	91
3.22	Species dependence of v_3 as a function of p_T at midrapidity for Au+Au collision at $E_{\text{lab}} = 30A$ GeV.	92
3.23	v_2 scaled by the constituent quark numbers of hadrons as a function of K_T/n_q at midrapidity for Au+Au collision at $E_{\text{lab}} = 30A$ GeV. The solid line is fitted following Equation (3.31).	93
3.24	v_3 scaled by the constituent quark numbers of hadrons as a function of K_T/n_q at midrapidity for Au+Au collision at $E_{\text{lab}} = 30A$ GeV. The solid line is fitted following Equation (3.31).	93
3.25	Comparison between particle-wise and event-wise averaged values of v_2 plotted against η in Au+Au collisions at $E_{\text{lab}} = (10-40)A$ GeV.	95

3.26	Comparison between particle-wise and event-wise averaged values of v_3 plotted against η in Au+Au collisions at $E_{\text{lab}} = (10 - 40)A$ GeV.	95
3.27	v_2 estimated by various techniques as a function of N_{part} at midrapidity in Au+Au collision at $E_{\text{lab}} = 30A$ GeV. $v_2\{\text{est}\}$ values are slightly shifted for clarity.	97
3.28	ε_2 estimated by various techniques as a function of N_{part} in Au+Au collision at $E_{\text{lab}} = 30A$ GeV. $\varepsilon_2\{\text{est}\}$ values are slightly shifted for clarity.	97
3.29	Centrality dependence of elliptic flow fluctuation and eccentricity fluctuation in Au+Au collisions at $E_{\text{lab}} = 30A$ GeV.	98
3.30	v_2 computed by various techniques and fluctuation in v_2 plotted against p_T for charged hadrons at midrapidity in Au+Au collisions at $E_{\text{lab}} = 30A$ GeV.	98
3.31	Relative v_2 fluctuation as a function of p_T . Experimental data points at RHIC are taken from [64, 65] and those at LHC from [66].	99
4.1	Centrality dependence of integrated yield of charged hadrons in Au+Au collisions at $E_{\text{lab}} = 30A$ GeV for different parton interaction cross sections.	105
4.2	Average transverse momentum of charged hadrons at midrapidity plotted against centrality in Au+Au collisions at $E_{\text{lab}} = 30A$ GeV for different parton interaction cross sections.	106
4.3	v_2 as a function of ε_2 in different N_{part} intervals for Au+Au collision at $E_{\text{lab}} = 30A$ GeV for different parton interaction cross sections.	107
4.4	v_3 as a function of ε_3 in different N_{part} intervals for Au+Au collision at $E_{\text{lab}} = 30A$ GeV for different parton interaction cross sections.	107
4.5	Centrality dependence of elliptic flow of charged hadrons at midrapidity in Au+Au collision at $E_{\text{lab}} = 30A$ GeV for different parton interaction cross sections. STAR data is taken from [3]	108
4.6	Centrality dependence of triangular flow of charged hadrons at midrapidity in Au+Au collision at $E_{\text{lab}} = 30A$ GeV for different parton interaction cross sections.	109
4.7	Elliptical flow scaled by eccentricity against centrality for different parton interaction cross sections at midrapidity for Au+Au collision at $E_{\text{lab}} = 30A$ GeV.	110
4.8	Triangular flow scaled by triangularity against centrality for different parton interaction cross sections at midrapidity in Au+Au collision at $E_{\text{lab}} = 30A$ GeV.	110
4.9	Elliptical flow scaled by eccentricity plotted against particle density in the transverse plane for Au+Au collision at $E_{\text{lab}} = 30A$ GeV for different parton interaction cross sections. Solid lines represent best fits to the data.	111

4.10	Triangular flow scaled by triangularity against $\sqrt{N_{\text{part}}}$ for different parton interaction cross sections at midrapidity in Au+Au collision at $E_{\text{lab}} = 30A$ GeV. Solid lines represent best fits to the data.	112
4.11	Dependence of v_3/v_2 on N_{part} in different p_T bins for Au+Au collision at $E_{\text{lab}} = 30A$ GeV for different parton interaction cross sections.	113
4.12	p_T dependence of v_2 for different centrality windows at midrapidity in Au+Au collision at $E_{\text{lab}} = 30A$ GeV for different parton interaction cross sections. STAR data is derived from [3].	114
4.13	p_T dependence of v_3 for different centrality windows at midrapidity in Au+Au collision at $E_{\text{lab}} = 30A$ GeV for different parton interaction cross sections.	115
4.14	NA49 data on p_T dependence of v_2 obtained from Pb+Pb interactions at 40A GeV compared with UrQMD and AMPT simulation (both default and string melting) for pions and protons at different partonic cross sections and at different centralities. The experimental values are shown as points, while corresponding simulations are shown by continuous curves.	116
4.15	Elliptic flow as a function of pseudorapidity for different parton interaction cross sections in Au+Au collision at $E_{\text{lab}} = 30A$ GeV.	117
4.16	Triangular flow as a function of pseudorapidity for different parton interaction cross sections in Au+Au collision at $E_{\text{lab}} = 30A$ GeV.	117
5.1	Multiplicity distribution of charged hadrons for different colliding systems at $E_{\text{lab}} = 30A$ GeV.	121
5.2	Eccentricity as a function of centrality measured in terms of N_{part}	122
5.3	Triangularity as a function of N_{part}	122
5.4	Distributions of v_1 of charged hadrons in the final state.	125
5.5	(Color online) Distributions of $v_2/\langle v_2 \rangle$ and $\varepsilon_2/\langle \varepsilon_2 \rangle$ of final state charged hadrons.	126
5.6	Distributions of $v_3/\langle v_3 \rangle$ and $\varepsilon_3/\langle \varepsilon_3 \rangle$ of final state charged hadrons.	126
5.7	N_{part} dependence of v_1 of charged hadrons for different colliding systems.	128
5.8	η dependence of v_1 of charged hadrons for different colliding systems.	128
5.9	p_T dependence of v_1 of charged hadrons for different colliding systems.	129
5.10	N_{part} dependence of (a) the elliptic flow parameter v_2 , (b) v_2 scaled by the standard eccentricity ε_{std} , and (c) v_2 scaled by the participant eccentricity $\varepsilon_{\text{part}}$, for charged hadrons in various AB collisions at $E_{\text{lab}} = 30A$ GeV.	131
5.11	Variation of eccentricity scaled elliptic flow with transverse particle density.	132
5.12	(a) Triangular flow and (b) triangular flow scaled by triangularity of charged hadrons against N_{part} for various AB collisions at $E_{\text{lab}} = 30A$ GeV.	133

5.13	Ratio of v_3 to v_2 of charged hadrons as a function of N_{part} for different colliding systems at $E_{\text{lab}} = 30A$ GeV.	134
5.14	p_T dependence of v_2 (upper panel) and v_2/ε_2 (lower panel) of charged hadrons for different colliding systems at $E_{\text{lab}} = 30A$ GeV.	135
5.15	p_T dependence of v_3 (upper panel) and v_3/ε_3 (lower panel) of charged hadrons for different colliding systems at $E_{\text{lab}} = 30A$ GeV.	135
6.1	Azimuthal distribution of (a) total radial velocity, (b) multiplicity, (c) mean radial velocity and (d) all the aforesaid quantities properly normalized for charged hadrons produced in Au+Au collisions at $E_{\text{lab}} = 40A$ GeV.	141
6.2	Centrality dependence of anisotropy parameter v_2 obtained from the azimuthal distributions of total radial velocity, multiplicity, and mean radial velocity in Au+Au collision at $E_{\text{lab}} = 10A$ and $40A$ GeV.	143
6.3	Centrality dependence of isotropic flow coefficient v_0 obtained from the azimuthal distributions of total radial velocity, multiplicity and mean radial velocity in Au+Au collision at $E_{\text{lab}} = 10A$ and $40A$ GeV.	144
6.4	Transverse momentum dependence of anisotropy parameter v_2 obtained from the azimuthal distributions of total radial velocity, multiplicity and mean radial velocity in Au+Au collision at $E_{\text{lab}} = 10A$ and $40A$ GeV.	145
6.5	Transverse momentum dependence of isotropic coefficient v_0 obtained from the azimuthal distributions of total radial velocity, multiplicity and mean radial velocity in Au+Au collision at $E_{\text{lab}} = 10A$ and $40A$ GeV.	146
7.1	Sphericity distribution of charged hadrons in Au+Au collision at $E_{\text{lab}} = 30A$ GeV.	151
7.2	p_T -spectra of different charged hadrons in the midrapidity region for isotropic, jetty and S_T -integrated events in 20–30% central Au+Au collisions at $E_{\text{lab}} = 30A$ GeV. Inset: Ratio of p_T -spectra for the isotropic and jetty events to S_T -integrated events.	153
7.3	Crossing point of the ratio of the p_T spectra of isotropic and jetty events to S_T -intergrated events as a function of particle mass in Au+Au collisions at $E_{\text{lab}} = 30A$ GeV.	153
7.4	N_{part} dependence of average p_T of different charged hadrons at midrapidity in isotropic, jetty and S_T integrated events in Au+Au collisions at $E_{\text{lab}} = 30A$ GeV.	154
7.5	Integrated yields in the midrapidity region of different charged hadrons as a function of N_{part} for the isotropic, jetty and S_T -integrated events in Au+Au collisions at $E_{\text{lab}} = 30A$ GeV.	155

7.6	Integrated yields in the midrapidity region of different charged hadrons per participant nucleon pair as a function of N_{part} for the isotropic, jetty and S_T -integrated events in Au+Au collision at $E_{\text{lab}} = 30A$ GeV.	156
7.7	Elliptic flow coefficient (v_2) as a function of N_{part} at midrapidity for isotropic, jetty and S_T -integrated events in Au+Au collisions at $E_{\text{lab}} = 30A$ GeV.	157
7.8	Triangular flow coefficient (v_3) as a function of N_{part} at midrapidity for isotropic, jetty and S_T integrated events in Au+Au collisions at $E_{\text{lab}} = 30A$ GeV.	158
7.9	Eccentricity (upper panel) and triangularity (lower panel) against N_{part} for isotropic, jetty and S_T -integrated events in Au+Au collisions at $E_{\text{lab}} = 30A$ GeV.	159
7.10	Elliptic flow coefficient (v_2) scaled by the eccentricity parameter (ε_2) plotted against N_{part} at midrapidity for isotropic, jetty and S_T -integrated events in Au+Au collisions at $E_{\text{lab}} = 30A$ GeV.	160
7.11	Triangular flow coefficient (v_3) scaled by the triangularity parameter (ε_3) plotted against N_{part} at midrapidity for isotropic, jetty and S_T -integrated events in Au+Au collisions at $E_{\text{lab}} = 30A$ GeV.	160
7.12	p_T -dependence of v_2 of charged hadrons at different centrality classes for isotropic, jetty and S_T -integrated events in Au+Au collisions at $E_{\text{lab}} = 30A$ GeV.	162
7.13	p_T -dependence of v_3 of charged hadrons at different centrality classes for isotropic, jetty and S_T -integrated events in Au+Au collisions at $E_{\text{lab}} = 30A$ GeV.	162

Chapter 1

A general overview of high-energy heavy-ion interaction

1.1 Introduction

The standard model (SM) of particle physics is basically a reductionist approach, that explains the dynamics of quarks and leptons, the most fundamental building blocks of all material objects that we see in nature [1–3]. In particular the dynamics of quarks and gluons, the constituent particles (fields) of hadrons, are guided by Quantum Chromodynamics (QCD), a non-abelian quantum field theory based on the $SU_c(3)$ color gauge group that describes the physics of strong interaction [4]. Unlike the photons in quantum electrodynamics (QED), the gluons are self interacting, which gives rise to two very special features of strong interaction, namely the asymptotic freedom [5, 6] and color confinement [7]. Because the gluons themselves have color, it leads to an anti-screening of the color charge. The bare color charge of a quark seated at the origin is diluted away in space by the gluons. If one tries to see the bare charge of the quark through the surrounding gluonic field, one will actually be able to see only a small portion of it. This feature of color fields is reflected in the behavior of the dimensionless coupling constant α_s , that determines the dynamics of strong interaction. Using the renormalization technique, formal infinities in α_s arising out of momentum contributions coming from virtual particles, are traded for a finite value,

$$\alpha_s(Q^2) = \frac{12\pi}{\beta_0 \ln \left(\frac{Q^2}{\Lambda_{qcd}^2} \right)} \quad (1.1)$$

upto the second order in perturbation theory. Here Q is the 4-momentum transfer, $\Lambda_{qcd} = (0.1 - 0.5)$ GeV, is a characteristic cut off scale of strong interaction down to which the perturbation theory works, $\beta_0 = 33 - 2N_f$ is the first coefficient of the β -function – higher order coefficients are neglected due to renormalization, and N_f is the effective number of quark flavors present in the system. In Figure 1.1 values of α_s , extracted from different experiments, are plotted against Q , and as we can see the experimental values are quite nicely reproduced by the Lattice QCD calculation [8]. In the $Q^2 \gg \Lambda_{qcd}^2$ region the strength

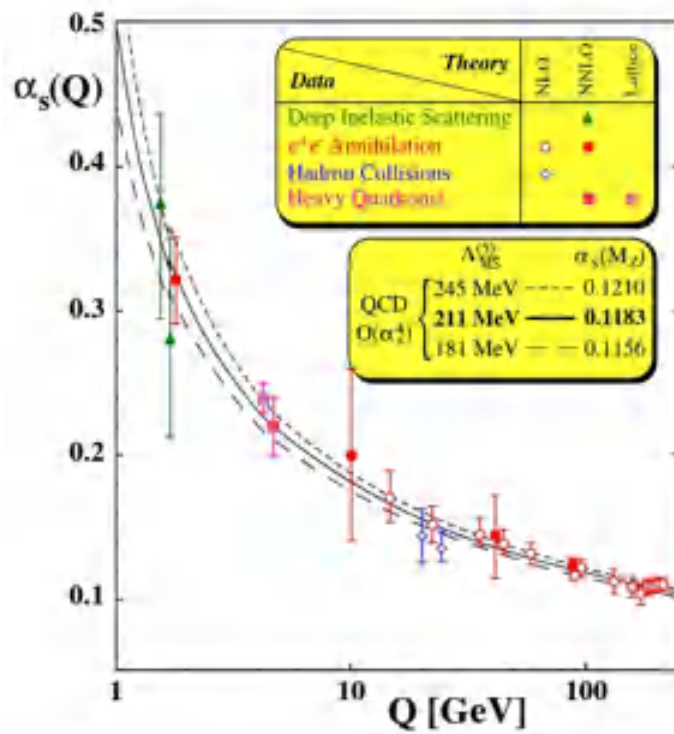


Figure 1.1: Measurements of the strong field coupling constant (α_s) against energy-momentum transfer Q . Lines refer to the perturbative QCD prediction which are in excellent agreement with the experiments. The figure is taken from [8].

of α_s decreases logarithmically with Q^2 . At large momentum transfer or equivalently at short distances the coupling between quarks (and gluons) becomes small, and they are asymptotically free. The phenomenon is known as *asymptotic freedom*. Asymptotic freedom provides a very simple description of how quarks and gluons interact over distance scales $\lesssim 1$ fm, i.e. as long as they are inside a nucleon. However, as Q^2 decreases down to Λ_{qcd}^2 , the value of α_s becomes of the order of 1, and the perturbative calculation that leads to Equation (1.1), falls through. We can try to gain some physical insight in the $Q^2 \rightarrow 0$ limit by using a simple model proposed in [9, 10]. According to this model, the color potential between a quark (q) and an antiquark (\bar{q}) at rest with respect to each other can be written

as,

$$V(r) = -\frac{4\alpha_s}{3r} + \kappa r \quad (1.2)$$

where $\alpha_s = g^2/4\pi$ and g is the strength of color charge. The first term of Equation (1.2) represents a normal Coulomb-like force which gives rise to the dipolar lines of force as in the QED. At large r the second term takes over, implying that the $q\bar{q}$ -potential rises linearly with separation, and that the field strength remains constant. A flux tube fills up the intervening space of the $q\bar{q}$ -system, and the energy required to completely separate the $q\bar{q}$ -pair becomes infinite. However, when the energy stored in the flux tube exceeds twice the rest energy of a quark, a new $q\bar{q}$ -pair is produced, with the new particles acting either as the source or the sink for the flux lines. Hadrons remain as color neutral objects and free quarks and gluons have never been observed in experiments. Although the model provides a nice intuitive picture, it is hard to quantify. Rigorously explaining the *color confinement* of massive quarks remains hitherto an unresolved problem. High energy hadronic/nuclear collisions can be studied in the framework of QCD using quarks and gluons as the primary degrees of freedom. The final observables in the laboratory are however jets of composite hadrons originating presumably from the struck quarks and radiating gluons. Hadronization, or the process by which the leading high momentum quark leaves behind a trail of $q\bar{q}$ -pairs, is modeled by fragmentation functions which are understood only up to a phenomenological level [11].

It was recognized that the QCD implies existence of a new high temperature phase of weakly interacting quarks and gluons [12–14]. However, the idea of a limiting temperature (T_c) for color neutral hadronic matter predates the discovery of QCD, and a quantitative prediction $T_c = 170$ MeV was obtained in the statistical bootstrap model proposed by R. Hagedorn [15]. The measured density of hadronic states grows exponentially as,

$$\frac{d\rho}{dm} \sim m^\alpha \exp\left(\frac{m}{m_0}\right) \quad (1.3)$$

where m represents the mass of the observed hadron and α is a parameter. Using the methods based on statistical mechanics Hagedorn showed that this exponential behavior implies a limiting temperature beyond which the states cannot be composed of color neutral hadrons. He interpreted this limiting temperature as the melting point of hadrons. Indeed, the observed number of hadronic states within an energy interval E and $E + dE$ can be written as [16],

$$dn(E) \sim dE \int_0^E p E \frac{d\rho}{dm} \exp\left(-\frac{E}{kT}\right) dm \quad (1.4)$$

We can use Equation (1.4) and relativistic energy-momentum relation $E^2 = p^2 + m^2$ to write,

$$dn(E) \sim dE \int_0^E m^\alpha \exp\left(\frac{m}{m_0}\right) \exp\left(-\frac{E}{kT}\right) E \sqrt{E^2 - m^2} dm \quad (1.5)$$

In the high-energy limit ($E/m_0 \gg 1$) we may approximate Equation (1.5) and compute the above integral,

$$dn(E) \sim E^{\alpha+3} \sqrt{\frac{\pi m_0^3}{2E^3}} \exp\left(\frac{E}{m_0} - \frac{E}{kT}\right) dE \quad (1.6)$$

We observe that the total energy $\int E dn(E)$ diverges for $kT > kT_0 = m$. One may therefore conclude that either no temperature beyond T_0 is possible, or there should be some new physics that would describe the states.

If the above does not provide enough motivation to study high-energy collisions of elementary particles and/or nuclei and explore the issues related to color deconfinement, then there are implications of confinement – deconfinement transition in cosmology and astrophysics too. It is believed that at the time of *Big Bang* all four fundamental forces of nature, namely Gravitational, Weak, Electromagnetic and Strong, had equal strengths and were unified into one fundamental interaction [17, 18]. At about 10^{-43} s. after the Big Bang, the gravitational interaction was separated out while the other three remained unified. At about 10^{-36} s. the strong interaction got decoupled from the electromagnetic and weak. Thereafter the universe expanded exponentially, a primordial cosmological phenomenon popularly known as the *cosmic inflation*. This was followed by a radiation dominated thermal era of the universe. As the universe further expanded and lost its temperature, it went through a series of symmetry breaking processes and corresponding phase transitions. Material objects started to evolve in the form of most fundamental particles, namely quarks, antiquarks, and leptons. It is during this stage when the universe was only a few micro-seconds old, the Quark-Gluon Plasma (QGP), a color deconfined, weakly coupled state of quarks and gluons was created [19]. It was a hot QGP where the number densities of quarks and antiquarks were same. For a very brief period of time the quarks and gluons could roam around freely outside the boundaries of hadrons, and the entire universe was filled up with a QGP-like state along with the leptons. However, subsequent expansion and cooling down brought the universe to such a stage that allowed the quarks to coalesce into color neutral baryonic matter like the protons and neutrons. A probable scenario of the expanding universe after the Big Bang and subsequent stages of its evolution are presented in Figure 1.2. A QGP state, similar but not quite alike to that prevailed in the early universe, can also be found inside the cores of very compact astrophysical objects like the white dwarfs and neutron stars [20]. In this case due to enormous (inward) gravitational pressure the boundaries of individual baryons melt down leading to a deconfinement. The temperature however, is

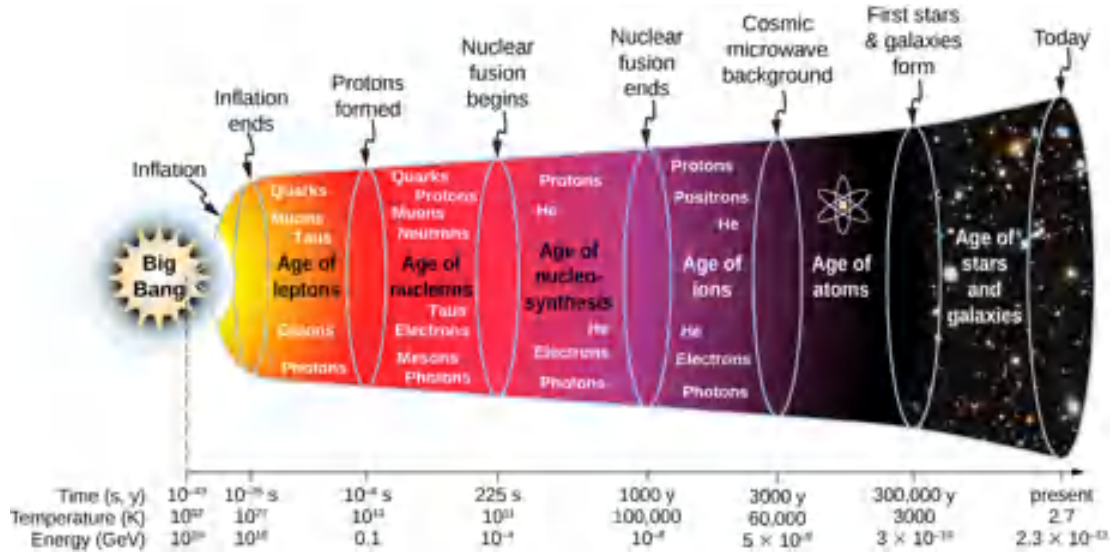


Figure 1.2: A probable timeline of the universe since Big Bang [21].

much below than that of the early universe, the density is 5 – 10 times the normal nuclear density, and the QGP system is quite rich in baryons.

It was T. D. Lee who first suggested that by distributing high energy or high nucleon-density over a relatively large volume, it might be possible to restore the broken symmetries and create an ultra-dense state of quark-gluon matter, pertaining to the early universe, a few microseconds after the Big Bang [22]. Later Collins and Pery suggested that existence of abnormally dense matter with deconfined quarks and gluons is an implicit manifestation of the asymptotic freedom [12]. We explore how under the controlled conditions of a laboratory, in high-energy nucleus-nucleus (AB) collisions these two seemingly different approaches can both lead to a deconfined state of quarks and gluons. The nucleons (radius ~ 1 fm) are composite objects, bound states of quarks and gluons. If two heavy-nuclei are allowed to collide with each other at a moderately high-energy, say at $E_{\text{lab}} = 30A - 40A$ GeV, they are going to squeeze each other very hard. With increasing pressure/density, the nucleons belonging to each colliding nuclei would thus overlap, until a state is reached in which each quark finds within its immediate vicinity a considerable number of other quarks. There is no way that it can identify which of these had been its partners in a specific nucleon at some other previous state of lower pressure/density. Beyond a certain point, the concept of a hadron thus loses its meaning, and a system of unbound quarks and gluons, quite rich in its net baryon content, is created. However, the energy density and therefore, the temperature of such a deconfined state is not going to be very high. This is called cold compression, a process that might be happening all the time inside compact stars [20].

On the other hand, as a QCD vacuum of finite volume is heated up, only mesonic degrees

of freedom are excited at low temperatures. Abundance of higher baryonic masses is reduced through the Boltzmann factor, the baryonic thermodynamic weight. The interaction between mesons is resonance dominated. All light quark mesonic states, independent of their mass, have the same characteristic size with a radius of about 1 fm. Mesons appear to allow arbitrary overlap, and by increasing the temperature one may be able to create a quite densely populated state of mesons. Once again we have a situation where the hadronic boundaries are going to melt down and a deconfined QCD state with a little or zero net baryon content is created. Such a hot plasma might have filled up our entire universe just a few micro-seconds after its birth, and perhaps have already been created on the earth in high-energy heavy-ion experiments. Nucleons, on the other hand, in addition to a short range repulsion, experience a long range attraction. Both these forces are non-resonant in nature, so that the interaction in baryonic matter at low temperature and high density is quite different from that of the mesons. A nucleon, also with a hadronic radius of about 1 fm, has an effective hard core of about half of its size. Nevertheless with increasing density, be it through heating or compression, a cluster formation eventually leads to more quarks per hadronic volume than meaningful for a partitioning into color-neutral hadrons. In other words, increasing either the temperature T or the baryochemical potential μ_B , both will eventually result in color deconfinement.

1.1.1 Experimental facilities

Before we delve further into the issues related to AB collision and QGP-state, let us have a look at the accelerator facilities that are either being built up at present or were built up in the past. The first ever heavy-ion collisions in laboratory began at the Lawrence Berkeley National Laboratory (LBNL), Berkeley, USA, and at the Joint Institute for Nuclear Research (JINR), Dubna, USSR. Heavy (light) nuclei were accelerated by employing respectively, the Bevatron and Synchrophasotron in a few (several) GeV per nucleon energy range. The experimental data obtained from these experiments were able to address some significant issues related to the collective behavior of nuclear matter and hadron production in AB collisions. The success of LBNL and JINR experiments encouraged the heavy-ion physics community to extend their investigations to higher energies. Accelerator facilities were built up for fixed target experiments at the Alternating Gradient Synchrotron (AGS) at Brookhaven National Laboratory (BNL), USA, and at Super Proton Synchrotron (SPS) at the European Centre of Research in Nuclear Physics (CERN), Switzerland. These facilities were designed to accelerate both light (^{28}Si , ^{16}O , ^{32}S) and heavy (^{197}Au , ^{208}Pb) ions, respectively at ~ 10 GeV/nucleon and $\sim 10^2$ GeV/nucleon incident energies. Some other heavy-ion programmes were also undertaken like one in the Schwer Ionen Synchrotron (SIS-18, and SIS-100) at GSI, Darmstadt, Germany. These fixed target experiments certainly improved our understanding

Table 1.1: Chronological commissioning of HIC accelerator facilities (past and present).

Year	Accelerator	Projectile	Maximum Energy
1975	Synchrophasotron	C, Mg, Ne, Si	4.5A GeV
1984	Bevatron	C, Ca, Kr, U	1 - 2A GeV
1986	AGS	Si	14.6A GeV
1986	SPS	O, S	200A GeV
1990	SIS-18	Ni, Au	2A GeV
1992	AGS	Au	11A GeV
1994	SPS	Pb	200A GeV
2000	RHIC	Au, Cu	$\sqrt{s_{NN}} = 200$ GeV
2008	LHC	Pb, Xe	$\sqrt{s_{NN}} = 5.5$ TeV
2011	SPS (NA61)	Pb, Be, Ar, Xe	158A GeV
2022	NICA	Au	$\sqrt{s_{NN}} = 11$ GeV
2025	SIS-100 (FAIR)	Au, Ca	11A GeV

of the multiparticle dynamics, but hardly provided any clear signal about QGP formation. However, these experiments have definitely provided a direction or clue, regarding exactly where among the debris of several hundreds (thousands) of particles that are produced per event in the final state, one has to look for to find out if a QGP-like state is formed or not. The AGS-SPS experiments also indicated that there is a specific need to scale up the collision energy further by at least a few orders of magnitude. This is possible only by using a collider system, where particle beams coming from two opposite directions collide with each other. The first AB collider experiments started collecting data at the Relativistic Heavy Ion Collider (RHIC) built in the year 2000 at BNL, USA, which provided first unambiguous signal of QGP formation. RHIC covered an energy domain of $\sqrt{s_{NN}} = 7.7$ to 200 GeV, and comprised of four experiments (detector systems), namely STAR, PHENIX, PHOBOS, and BRAHMS. In 2009 the largest ever particle accelerator, the Large Hadron Collider (LHC) at CERN came into operation, which was designed to study AB collisions upto $\sqrt{s_{NN}} = 5.5$ TeV and pp collisions upto $\sqrt{s_{NN}} = 13$ TeV. Like the RHIC, LHC also comprises of four different experiments, namely ALICE, ATLAS, CMS, and LHCb. The data that came out from the LHC experiments are still being analyzed. So far, the results have supplemented the RHIC observation. It has been possible to create a color deconfined extended QCD state of strongly interacting quarks and gluons. The QGP behaves almost (not exactly) like an ideal fluid, that has a very small specific viscosity. In the last decade or so, several projects have been undertaken to examine and explore the other possibility, i.e. QGP at high baryon density and low/moderate temperature. NA61/SHINE is one such facility that at present is operating at the CERN-SPS. Other such facilities are, (i) the Facility for Anti-proton and Ion Research (FAIR) that is being installed near GSI, Darmstadt, and (ii) NICA at JINR, Dubna which is already in operation. Specific information about the projectile ions and collision energies available in these facilities are listed in Table 1.1.

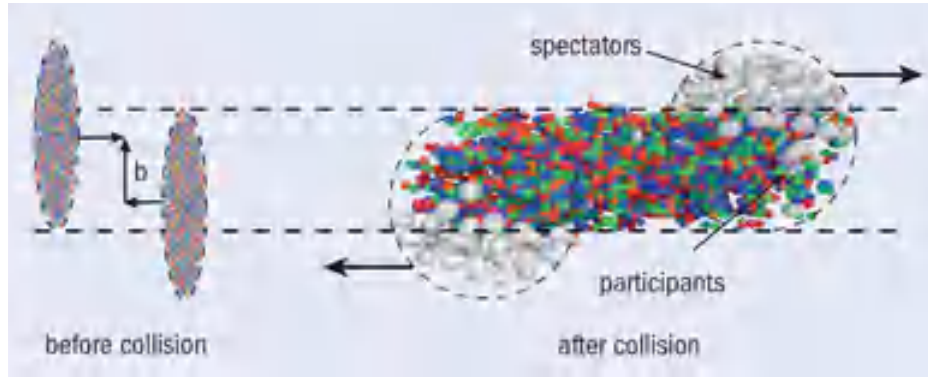


Figure 1.3: A typical nucleus-nucleus interaction before and after the collision. Particles are produced in the participants' zone, while the spectators remain uninfluenced. The figure is taken from Ref. [23].

1.2 Relativistic heavy ion collision and QGP

In its ground state a nucleus of mass number A can be considered like a sphere of radius $R = r_0 A^{1/3}$ fm and volume $V = (4\pi/3)r_0^3 A$, where $r_0 = 1.2$ fm is called the nuclear radius parameter. The nuclear matter density $\rho_N \approx 0.16$ nucleons/fm³ and the corresponding energy density $\epsilon_N \approx 0.15$ GeV/fm³. In order to produce a well equilibrated hot and dense fireball matter, for more than one reason AB collisions are always preferred over pp collisions. First, to achieve a local thermal equilibrium the system must be sufficiently randomized, which is possible only in a large collision system where multiple rescattering among the constituent particles can take place. Second, on an average an AB collision produces a larger number of particles, resulting thereby a smaller amount of relative fluctuation. It is also pertinent to examine how heavy the nucleus should be. The total cross section for $pp \rightarrow n\pi$ is ~ 30 mb at high energies, which gives an equilibration time of 6×10^{-34} s. The total time available for hadron production is of the same order as the time for which the colliding nuclei overlap, i.e. $t = 0.2 r_0 A^{1/3}/c_s$. Here, $c_s = \sqrt{1/3}c$ is the speed of sound in an ideal gas of mesons and nucleons at or near T_c , and the factor 0.2 is incorporated since half the mass of a uniformly dense nucleus is contained within $0.2R$ of its surface. This implies that the disassembly time will be long enough if $A > 50$. Figure 1.3 schematically depicts a high-energy AB event, before and after the collision. Before collision, two such nuclei approaching each other with relativistic speed will look like pancakes, Lorentz contracted along their common (but opposite) direction of motion. The impact parameter (b) of an AB collision is defined as the perpendicular distance between their lines of motion. Head on collisions, also called central events, are associated with small values of b ($b \rightarrow 0$), while grazing collisions have high b -values and they are called peripheral events. After the collision takes place, the overlap volume between the two colliding nuclei forms the intermediate fireball. The fireball created in a central and a peripheral collision would be very much different

in their properties, and hence it is essential to study the centrality dependence of different observables. The nucleons inside the overlap region are called *participant* nucleons, whereas those which do not directly participate in the collision process, are called the *spectators*. Often the centrality of a collision is measured in terms of the average number of participant nucleons (N_{part}), which varies directly with the mass number of the nuclei. Centrality is also measured in terms of the number of nucleon-nucleon binary collisions (N_{coll}) which varies as $A^{4/3}$ [24].

In statistical mechanics the state of a system in local thermal equilibrium, composed of many particles, is characterized by the average values of a few global observables like temperature, energy density, entropy, net charge etc. For different values of these observables, the system may exhibit fundamentally different average properties. Accordingly, there exist different states of matter, and as the system changes from one state to the other, phase transitions take place. Whatever may be the constituent particles, if the intermediate fireball created in an AB collision has to qualify as a state, it should have well defined values of temperature, volume, pressure etc. This is possible only when the motion of the constituent particles is sufficiently random. An order of magnitude calculation in this regard may not be totally out of context. A hadron typically has a radius of 1 fm and it fills up a volume of 5 – 6 fm³. So the hadronic matter density is about $n \sim 0.2$ per fm³. Typical cross-section of a high-energy hadronic interaction is $\sigma \sim 50$ mbarn or ~ 5 fm². Collisions between two heavy-nuclei increase the density by a few orders of magnitude. As a result the hadronic density increases to $n \sim 10$. The mean free path of the constituent particles will therefore be $\lambda \sim (n\sigma)^{-1} \approx 0.02$ fm, and one can expect that multiple ($\sim 10^3$) rescattering are going to take place within a collision volume of dimension (10 – 15) fm. This with all probability will lead to sufficient randomization of motion of the particles involved, and therefore to an equilibration of the system. The thermodynamic conditions of the intermediate fireball that can be and have been reached in high-energy heavy-ion experiments conducted at the LHC, are listed below [25].

1. Temperature: $T = (100 - 1000)$ MeV (1 MeV \equiv 10 billion degrees) [up to a million times the temperature of the core of the sun].
2. Pressure: $P = (100 - 300)$ MeV/fm³ (1 MeV/fm³ \equiv 1028 atm.) [pressure at the center of the earth = 3.6 million atm.].
3. Density: $\rho = (5 - 10)\rho_0$ [ρ_0 is the density of a gold nucleus ~ 3000 g/cm³; density of a gold atom = 19 g/cm³].
4. Volume: nearly 1500 fm³, nucleus radius $R = 1.15 \times A^{1/3}$ fm [for an Au-nucleus $A \approx 200$, $R \simeq 7$ fm and $V = 4\pi R^3/3 \simeq 1500$ fm³].

5. Duration: $(10 - 50) \text{ fm}/c \sim 10^{-22} \text{ s}$.
6. Baryochemical potential: $\mu_B = (400 - 600) \text{ GeV}$.
7. Magnetic field: $B \sim 10^{15} - 10^{16} \text{ Tesla}$ [in neutron stars $B \sim 10^{11} \text{ Tesla}$].

1.2.1 Space-time evolution

As we do not have any direct access to the intermediate fireball, so it is extremely important to understand the space-time evolution of a heavy-ion collision. Figure 1.4 shows different stages of an AB collision system as it evolves with the proper time. The schematic is quite similar to that of the evolving universe after the Big Bang. A schematic representation of

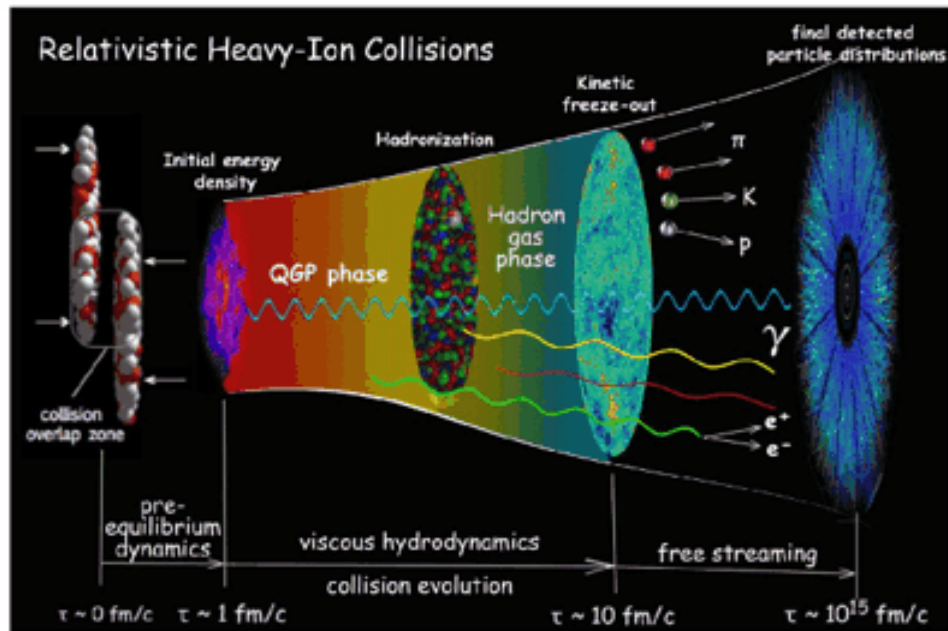


Figure 1.4: Schematic exemplar of different stages of a heavy-ion collision, the *Little Bang*. The figure is taken from Ref. [26]

the space-time evolution of an AB collision in its CM frame is also schematically represented in Figure 1.5, in a light-cone (b) with and (a) without taking QGP formation into account. The beam (longitudinal) direction is plotted along the horizontal and proper time is plotted along the vertical axis. As the system is expanding under pressure gradients and cools down with evolving time, different stages of its space-time evolution are broadly classified in the following way.

- **Initial Stage:** Two nuclei approach each other with relativistic speed. Due to Lorentz contraction along the beam direction they look like pancakes. Conventionally, these two nuclei collide at $\tau = 0 \text{ fm}/c$ and produce a nuclear matter with non-uniform

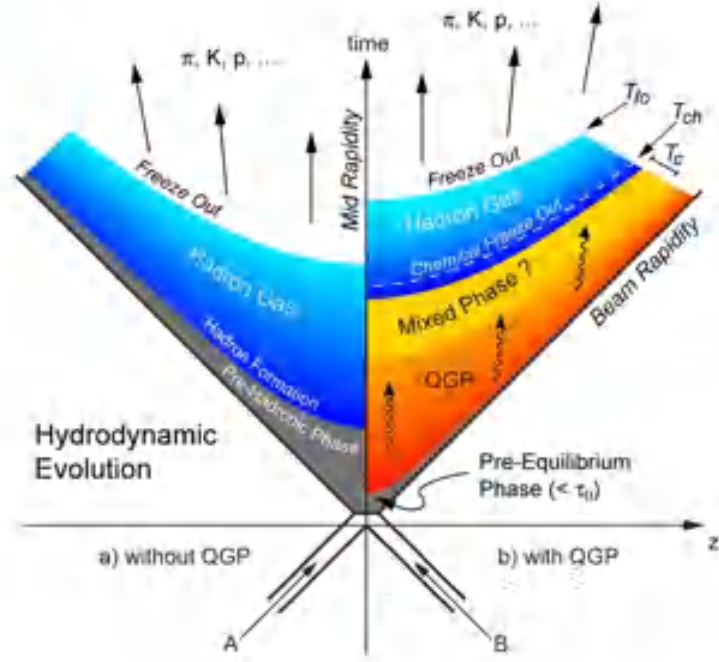


Figure 1.5: Space time evolution of a high-energy collision between two nuclei in their CM frame, (a) without and (b) with QGP formation. The figure is taken from Ref. [27].

energy density. This type of non-uniformity plays an important role in the final state flow measurements. The overlapping part of the colliding nuclei form an intermediate fireball. If sufficient amount of energy is available during the collision, the hadronic boundaries may melt down and partonic degrees of freedom are excited within the fireball. If not, then depending on the amount of stopping suffered by the colliding nuclei, the fireball is either dominated by mesons or rich in baryons. The system remains in a pre-equilibrium state for about $\lesssim 1$ fm/c, and till date very little is understood about this stage of the collision.

- **Thermalization:** Due to multiple scattering between the constituent particles local thermal equilibrium is quickly achieved in the fireball within a time period of $\tau_0 = 1$ fm/c, and remains in the equilibrated condition for a duration of $1 - 10$ fm/c. If partonic degrees of freedom are excited then after thermalization, the quarks and anti-quarks present in the thermalized matter follow Fermi-Dirac distribution, whereas the gluons follow Bose-Einstein distribution. Due to a pressure gradient that builds up during thermalization the fireball matter is then driven radially outward.
- **Hadronization:** The equilibrated fireball expands and cools down. When the temperature goes below a critical temperature (T_c) the quarks, antiquarks and gluons start to combine to form colorless bound states, a process known as hadronization. It is quite possible that for some time the fireball remains in a mixed state of QGP

and hadron gas. If on the other hand sufficient heating and/or compression is/are not achieved, the interacting nucleons will directly produce new particles, most of which are π -mesons. The process is known as multiparticle production and it takes about 20 – 50 fm/c of time. How these particles are produced, still remains an unresolved issue, one has to depend mostly on speculative measures.

- **Hadron Gas:** As hadronization stops, the fireball system forms a Hadron Gas (HG). The newly produced hadrons are weakly coupled. However, the entire system is still in equilibrium because of the inelastic interactions taking place within it, and it exhibits a collective behavior. Moreover, the hadrons in the HG state have sufficient energy to exchange quarks and antiquarks among themselves. The lifetime of this state is small and hence it has limited influence on the evolution process [28]. However, both the equilibrium and HG stages are guided by viscous hydrodynamics.
- **Chemical freeze-out:** As the HG expands further, the temperature drops down, and as a result the inelastic interactions cease to take place. At this moment the hadrons stop exchanging quarks among themselves or in other words the relative abundance (chemical composition) of every hadron species becomes fixed. This is known as *chemical freezeout*.
- **Kinetic freeze-out:** The momentum exchange among the hadrons continues until the elastic interactions cease. When that happens a *kinetic freezeout* is achieved, and the momentum spectra of the produced hadrons remain unchanged hereafter, final state particles freely stream out from the collision zone. Studies related to the momenta spectra aids to extract the freeze-out temperature and radial flow velocity.

1.2.2 Thermodynamics of the fireball

E. Fermi first applied statistical mechanics to multiple meson production in high-energy collisions [29]. He assumed that when two nucleons collide they release their energies within a very small volume $V = 2m_N V_0 / \sqrt{s_{NN}}$, where $V_0 = 4\pi R_\pi^3/3$ and $R_\pi = 1/m_\pi$ is the Lorentz contracted characteristic length associated with the pion field. A large number of particles are formed instantaneously. The mean free path of these particles is small compared to the dimension of the interaction volume, and a statistical equilibrium is set up. Subsequently the system decays into one of the many accessible multiparticle states. The decay probability is calculated in the framework of standard statistical physics. The main reason behind using statistical concepts was the large value of strong coupling constant that prohibits any application of perturbative methods. The transition probability from an initial to a given final state is proportional to the modulus square of the transition matrix element, treated as

a constant, and to the density of states. The main effect comes therefore from the available phase space, which grows with increasing collision energy. The probability of having an n -particle final state is proportional to,

$$S(n) = \left[\frac{V}{(2\pi)^3} \right]^{(n-1)} \frac{dN}{dE} \quad (1.7)$$

where dN/dE is the density of states. The power $(n-1)$ comes because only $(n-1)$ particles have independent momentum. Fermi argued that at very high energies even a detailed statistical description may not be necessary [29]. Assuming that the matter is thermalized, one can calculate the temperature of the produced hadronic system from thermodynamic considerations valid for massless particles as,

$$T^4 = \frac{3\varepsilon^2}{2\pi^2 V_0 m_N} = \frac{9\varepsilon^2 m_\pi^3}{8\pi^3 m_N}$$

The above equation may be used to calculate the abundance of produced particles from the thermodynamic relations giving the particle densities in terms of temperature.

In the framework of MIT bag model we can construct a static idealization of the fireball system created in AB collisions [30, 31]. Complexities and finer details that are needed to describe a more realistic system can be gradually added on at later stages. In the bag model a hadron is considered as a spherical enclosure of radius R . Each quark and/or antiquark, a spin- $\frac{1}{2}$ fermion, is massless inside the bag but infinitely massive outside. Gluons on the other hand are massless spin-1 bosons. Due to the presence of quarks (anti-quarks) normal QCD vacuum is destroyed within the bag and a perturbative QCD vacuum prevails inside. Energy and momentum conservation at the bag surface is ensured by introducing an external (inward) pressure at the bag surface to balance the internal (outward) pressure of the confined quarks. This bag pressure is characterized by a constant B . The quark-gluon system can be treated as an ideal relativistic gas of massless ($\epsilon = pc$) particles at an equilibrium temperature T . The energy densities of the quarks, antiquarks and gluons can be derived by using the respective distribution formulae, and that for the QGP system (ε_{qgp}) by adding these energy densities together and combining the degeneracy factors [32–34],

$$\varepsilon_{qgp} = \varepsilon_q + \varepsilon_{\bar{q}} + \varepsilon_g = \left(\frac{37\pi^2}{30} T^4 + 3\mu_q^2 T^2 + \frac{3\mu_q^4}{2\pi^2} \right) \quad (1.8)$$

Here $\mu_q = \mu_{\bar{q}}$ is the quark (anti-quark) chemical potential, ε_q ($\varepsilon_{\bar{q}}$) is the energy density of an ideal quark (ant-quark) gas and ε_g is the same for an ideal gluon gas. One expects a stable QGP when the pressure inside $P = \frac{1}{3}\varepsilon \geq B$, the equality holds at the boundary of stability. The condition may be used to arrive at the limiting critical values of the temperature T_c ,

the chemical potential μ_c and the baryon number density n_c ,

$$\begin{aligned} T_c(\mu_q = 0) &= \left(\frac{90B}{37\pi^2}\right)^{\frac{1}{4}} \approx 147 \text{ MeV} \\ \mu_c(T = 0) &= (2\pi^2 B) = 0.43 \text{ GeV} \\ n_c(T = 0) &= \frac{2}{3\pi^2} (2\pi^2 B)^{\frac{3}{4}} = 0.72 \text{ fm}^{-3} \end{aligned} \quad (1.9)$$

If the quark – quark and quark – anti-quark interactions are taken into account, then the above expression of energy density is modified as [35],

$$\varepsilon = \left(\frac{37\pi^2}{30} - \frac{11\pi}{3}\alpha_s\right) T^4 + \left(1 - \frac{2}{\pi}\alpha_s\right) 3\mu_q^2 T^2 + \left(1 - \frac{2}{\pi}\alpha_s\right) \frac{3\mu_q^4}{2\pi^2} \quad (1.10)$$

Using the stability condition and setting the corresponding chemical potential μ_c and temperature T_c we get

$$B = \left(\frac{37\pi^2}{90} - \frac{11\pi}{9}\alpha_s\right) T_c^4 + \left(1 - \frac{2}{\pi}\alpha_s\right) \mu_c^2 T_c^2 + \left(1 - \frac{2}{\pi}\alpha_s\right) \frac{\mu_c^4}{2\pi^2} \quad (1.11)$$

Under the limiting conditions

$$T_c(\mu_q = 0) = \left[\frac{B}{\left(\frac{37\pi^2}{90} - \frac{11\pi}{9}\alpha_s\right)}\right]^{\frac{1}{4}} \quad \text{and} \quad \mu_c(T = 0) = \left[\frac{2\pi^2 B}{\left(1 - \frac{2}{\pi}\alpha_s\right)}\right]^{\frac{1}{4}} \quad (1.12)$$

Depending on the values of B and α_s chosen, the critical temperature T_c would lie somewhere between 150 – 200 MeV and the chemical potential μ_c somewhere between 450 – 600 MeV.

1.2.3 Hydrodynamics of the fireball

Relativistic hydrodynamics provides a simple picture of the space-time evolution of the hot and dense fireball matter produced in the central rapidity region (see Appendix A for details on rapidity) in a relativistic AB collision. It is assumed that the expanding system stays in local thermodynamic equilibrium. Without going into the details of any microscopic aspect, hydrodynamics allows us to describe all the stages of expansion of the fireball, starting possibly from the QGP, through hadronization and ending at the freeze out. Hydrodynamics, although classical in concept and formulation, provides an important computational tool to describe the gross features of AB collisions. It uses the fundamental conservation laws of energy and momentum to build an equation of state for the evolving system.

Landau's hydrodynamic model

Landau [36, 37] argued that one should not expect the number of finally emitted particles to be determined only from the equilibrium condition at the instant of collision. Rather the system continues interacting even after the initial stages and the number of particles becomes definite only when they are far apart in phase space. Landau too assumed that a compound system is formed, and energy is deposited in a small volume V , subjected to Lorentz contraction. In comparison with the dimension of the collision volume the mean free path of the produced particles is small, and a statistical equilibrium is set up. In the second stage of the collision, under the influence of a longitudinal velocity gradient the system starts expanding. The transverse gradients are also present, but initially the longitudinal gradient is predominant and the early expansion is approximated as one-dimensional. The expanding system is regarded as an ideal fluid with zero viscosity and zero thermal conductivity. During the expansion velocities of the particles are comparable to that of the light, justifying thereby the use of relativistic hydrodynamics. Particles are formed and absorbed in the system throughout the first and second stages of the collision. As the system expands, the mean free path of the particles becomes comparable to the dimension of the colliding system, and the interaction between the particles becomes weak. The expanding system then breaks up into individual particles when its temperature $T \sim m_\pi$. For a perfect fluid only one equation of state is necessary to describe the hydrodynamic expansion. A perfect fluid does not have any viscosity and during the hydrodynamic expansion the total entropy ($S = sV$) of the system remains unchanged. The number of pions produced was derived as,

$$N_\pi \propto sV \propto E_{cm}^{3/2} V / \gamma_{cm} \propto A E_{cm}^{1/2} \propto A E_{lab}^{1/4}$$

which implies that heavy nuclei are better suited for pion production and that pion multiplicity grows slowly with collision energy. Landau solved the hydrodynamic equations in one and three-dimensions. An exact solution was obtained in one-dimension [38] which gave the same result as Landau's in the asymptotic region. A necessary condition for the applicability of Landau's picture to central relativistic AB collisions is that, the nucleons in the front part of each colliding nuclei, while traversing through the other nucleus, must lose all of their kinetic energies in the center of mass frame. This demands that the average energy loss of these nucleons per unit length should be greater than a critical value given by,

$$\left| \frac{dE}{dz} \right|_{cr} = \frac{E_{cm}/2}{(2R/\gamma_{cm})} \quad (1.13)$$

Although at low energies ($E_{cm} < 10$ GeV) Landau's theory gives satisfactory results, but at ultra-relativistic energies ($E_{cm} = 200$ GeV) the above condition becomes too stringent to be attained. Hence, Landau's picture breaks down when the required stopping power

becomes too large. Furthermore, in contrast to the requirements of Fermi's and/or Landau's approach, the thickness of the colliding nuclei cannot be infinitely small even in the ultra-relativistic region. Also, in this model the boundary condition is specified at the time of maximum compression, whereas the entire matter is distributed over a small but finite volume. However, particle production is not an instantaneous process and it shows the characteristics of space-time correlation, i.e., fast particles are produced later and further away from the collision center than the slow particles, which is not considered in Landau's model. The main criticism of Landau's model is that, the leading particle effect is neglected. In order to achieve full stopping, removal of the radiation energy due to deceleration is required, which is also not taken into account. These difficulties can be removed if one assumes that during the collision, the valence quarks should move without much interaction and the energy carried by the gluon fields is stopped within the collision volume [39–41]. Such an assumption is justified because, due to the color degeneracy gluon-gluon interaction cross-section is larger than the quark-quark cross-section. To be consistent with the initial conditions of Landau's model the gluon field should thermalize after a certain time.

Bjorken's hydrodynamical model

Based on the assumption that at sufficiently high-energy the rapidity distribution of the final state particles is uniform in the mid-rapidity region, Bjorken introduced a hydrodynamic model [42] of AB collision. It is also assumed that the strongly interacting matter present within the collision volume, reaches a state of local thermal equilibrium after the collision and then expands adiabatically. The evolution of the system is determined by the initial conditions and an equation of state (EoS) that transfers the energy and baryon density to the pressure exerted by the system. The EoS is subjected to the constraints of local conservation of energy-momentum and currents [43, 44]. The EoS for a non-dissipative ideal fluid can be mathematically formulated as,

$$\begin{aligned}\partial_\mu T^{\mu\nu}(x) &= \partial_\mu [\{\varepsilon(x) + P(x)\}u^\mu u^\nu - g^{\mu\nu}P(x)] = 0 \\ \partial_\mu j_B^\mu(x) &= \partial_\mu [n_B(x)u^\mu(x)] = 0\end{aligned}\tag{1.14}$$

where

$$T^{\mu\nu} = [\varepsilon + P] u^\mu u^\nu - g^{\mu\nu} P$$

is the relativistic stress energy tensor, ε is the energy density, P is the pressure, j_B^μ is the charge-current density, n_B is the baryon number density and $u^\mu = (\gamma, \gamma \vec{v})$ is the four-velocity, all defined in the local rest frame (x) of the fluid. In Bjorken's theory all thermodynamic quantities characterizing the central region should depend only on the longitudinal proper time $\tau = \sqrt{t^2 - z^2}$ and longitudinal velocity $u_z = z/t = \tanh y$, so that

$u^\mu = (t/\tau, 0, 0, z/\tau)$. Under the above condition Bjorken's equation can be written as,

$$\frac{\partial \varepsilon}{\partial \tau} + \frac{\varepsilon + P}{\tau} = 0 \quad (1.15)$$

Using $\varepsilon = \lambda P$ where $\lambda = dP/d\varepsilon$ measures the elastic wave velocity in the medium, and the thermodynamic relation: $\varepsilon + P = Ts + \mu_B n_B$, we get

$$\varepsilon(\tau_f) = \varepsilon(\tau_i) \left(\frac{\tau_i}{\tau_f} \right)^{1+\lambda} \quad (1.16)$$

For a zero baryon density

$$s(\tau_f) = s(\tau_i) \left(\frac{\tau_i}{\tau_f} \right) \quad \text{and} \quad T(\tau_f) = T(\tau_i) \left(\frac{\tau_i}{\tau_f} \right)^\lambda \quad (1.17)$$

A QGP to HG phase transition causes softening of the EoS. As the temperature crosses its critical value, the energy and entropy densities quickly increase while the pressure rises slowly. The derivative $dP/d\varepsilon$ has a minimum at the end of the mixed phase, known as the softest point. The diminishing driving force slows down the build-up of flow. The preliminary conditions which are the input parameters, define the initiation of the hydrodynamic evolution and the relevant macroscopic density distributions at that point of time. The hydrodynamic evolution is terminated by implementing the freeze out condition, which describes the breakdown of local equilibrium due to decreasing local thermalization rates. In non-central collisions, driven by its inner asymmetric pressure gradients, the system will expand more prominently in the direction of the reaction plane than in the direction perpendicular to the reaction plane. As the time evolves, the system becomes less and less deformed. To estimate the initial energy density of a Bjorken-type fluid element, one has to go to the fluid rest frame. All particles are originating from a cylindrical volume of cross-section A , which actually is the overlap area of the interacting nuclei, and of length $v_z t$. We concentrate on a thin slab of thickness dz centered between the two pancake-like moving nuclei. The point of impact is assumed to be the origin ($z = 0$) of our frame of reference. Therefore $dz = \tau \cosh y dy$ and we may ignore the collisions among produced hadrons. The energy density is obtained as,

$$\varepsilon_{BJ} = \frac{\Delta E}{\Delta V} = \frac{E dN}{A dz} = \frac{m_t dN}{\pi R^2 \tau dy} = \frac{1}{\pi R^2 \tau} \frac{dE_t}{dy} \quad (1.18)$$

Taking the proper time $\tau \approx 1 \text{ fm}/c$ and dN/dy to be the central rapidity density of produced particles, this relation was first derived by Bjorken [42]. However, a perfect fluid must undergo an isentropic expansion. In order to compensate the Lorentz contraction, a relation like $s_i \tau_i = s_f \tau_f$ should hold between the initial and final proper time. If we consider

massless particles, then $\varepsilon \propto T^4$ and $s \propto T^3$. Correspondingly,

$$\varepsilon_f = \varepsilon_i \left(\frac{\tau_i}{\tau_f} \right)^{4/3} \quad (1.19)$$

which contradicts Bjorken's formula, $\varepsilon_{BJ} \sim \tau^{-1}$. The energy density formula should therefore be modified as,

$$\varepsilon = \frac{1}{\pi R^2 \tau_0} \frac{dE_t}{dy} \left(\frac{\tau_f}{\tau_i} \right)^{1/3} = 2 \varepsilon_{BJ} \quad (1.20)$$

1.2.4 QCD phase diagram

The QCD phase diagram serves as a very useful summary of the properties of a many-body system of strongly interacting particles. These properties, analogous to condensed matter physics, are mostly thermodynamic in nature, and they describe the collective behavior of a system of many particles responding to a few external control parameters like the temperature (T) and baryochemical potential (μ_B). Using some general arguments arising from QCD, experimental observation and common sense, we may try to explain qualitatively some of the features depicted in the QCD phase diagram [Figure 1.6]. Quantitative details like the order of phase transition and corresponding values of control parameters, suffer from large uncertainties. Since it was first introduced [13] the phase diagram has seen quite a few changes, as new phases of QCD matter find out their places in it and new lines are being drawn to demark one phase from another. In the bottom left-hand corner of the phase diagram, where T and μ_B are both very small, the thermodynamic behavior of QCD matter can be described in terms of a hadron gas. The many-body phase at these low temperatures and densities behaves more like a vapor because the force between color-neutral hadrons is a very weak second-order effect similar to the Van der Waal's force between neutral atoms. Two regimes are of particular interest to us, (i) $T \rightarrow \infty$, $\mu_B = 0$, along the y-axis and (ii) $T = 0$, $\mu_B \rightarrow \infty$, along the x-axis of Figure 1.6. Keeping μ_B fixed at zero if we increase T , lattice calculations indicate that at a critical temperature $T_c \sim 150$ MeV the hadron gas must undergo a phase transition to a deconfined colored soup of quarks and gluons [45]. The process is similar to the ionization of atoms in a QED plasma at high temperature. An important order parameter for this phase transition is the chiral quark condensate $\langle q\bar{q} \rangle$. The nature of this transition is very sensitive to the values of quark masses. If up and down quarks are massless and the rest are infinitely massive then in QCD the transition is of second order [46]. If up, down and strange quarks are massless then the transition is of first order [47]. For realistic quark masses lattice calculations at $\mu_B = 0$ show that the HG to QGP transition is a smooth but rapid cross-over [48–50]. It should be noted that the early universe evolved from a high temperature big bang epoch, and in the process of cooling

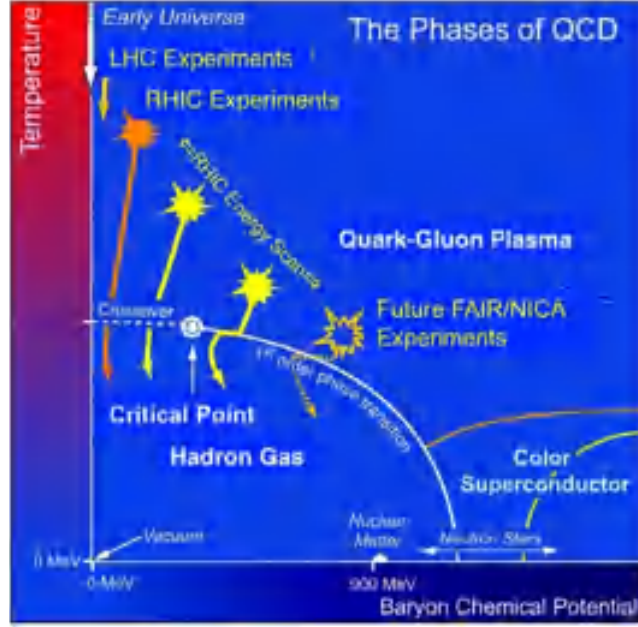


Figure 1.6: A schematic of the QCD phase diagram showing locations of different states of hadronic/partonic matter [51].

it presumably underwent the reverse phase transition from a primordial QGP into a HG. Although this regime is net baryon-free, it is still a high matter density at high temperature environment, since the energy density is sufficient to cause rapid production of $q\bar{q}$ pairs and gluons. Such an extended QCD state, strongly interacting, has perhaps already been created in the RHIC and LHC experiments on heavy-ion interactions. Along the x-axis of Figure 1.6 the dynamics however is quite different. In this region the net baryon density ρ_B , measured by its conjugate the net baryo-chemical potential μ_B , can be a good order parameter. As the chemical potential is increased, initially there is no change. Because at zero temperature the chemical potential μ_B is the energy required to add a baryon to the system, and QCD has a large mass gap for baryonic states. The first non-vacuum state one encounters along the μ_B -axis of the phase diagram is the nuclear matter, a strongly correlated superfluid composed of non-relativistic neutrons and protons. The baryon density changes discontinuously at the onset transition, from $\rho_B = 0$ to the nuclear matter density $\rho_N = 0.16 \text{ fm}^{-3}$. The discontinuity decreases as nuclear matter is heated, and the nuclear liquid-gas phase transition ends at a critical point $T \approx 18 \text{ MeV}$ [52]. For T slightly above zero, continuity ensures that the transition remains of first order, as probed in the nuclear multi-fragmentation processes [53]. As μ_B is increased further, the utility of ρ_B as an order parameter is lost, as it is only expected to increase monotonically. We have to revert back to $\langle q\bar{q} \rangle$ as the signal for chiral symmetry restoration. At $\mu_B \gtrsim 1 \text{ GeV}$, corresponding to matter densities $\sim 5 - 10$ times the nuclear matter density, in a completely Fermi-degenerate sea of quarks chiral symmetry is expected to be restored. Various theoretical studies indicate that the phase transition in this region is of first order. For slight temperature perturbations

in this Fermi-degenerate chirally symmetric phase, interesting dynamics like quark-quark pairing on the Fermi-surface is expected, leading to the remarkable Cooper pair-like color superconductive states. For our purpose, it is sufficient to note that, since on the x-axis we have a first order phase transition and along the y-axis there is a smooth crossover, by continuity it follows that the mutation from first order transition to cross-over should be marked by a critical end point (CEP). The CEP is interesting because it is the only thermodynamically stable point on the phase transition line at which the correlation length diverges. This means that the CEP may manifest itself in heavy-ion collisions in terms of enhanced fluctuations of dynamically and intrinsically conserved quantities. The CEP is indicated in Figure 1.6 and its exact location is a subject of current theoretical and experimental studies.

In the ideal version of QCD the quarks are considered as massless objects. The left and right-handed quarks are decoupled from each other, corresponding quark currents are separately conserved and QCD Lagrangian is invariant under their interchange. Hadrons on the other hand, have well defined parities and for them no parity partners are observed. This paradox is resolved by a phenomenon called the spontaneous breakdown of chiral symmetry. The quarks inside a nucleon/hadron polarize the surrounding gluonic medium. The resulting gluon cloud around each quark provides it with a dynamically generated effective mass, which results in a spontaneous breaking of the chiral symmetry of the QCD Lagrangian. One would expect that this symmetry is restored at high energies where quarks and gluons are the correct degrees of freedom. As mentioned above, in high-energy heavy-ion collisions it is possible to sufficiently heat up and/or squeeze the nucleonic matter, so that the boundaries of individual hadrons/nucleons melt down, color-neutral states are dissolved, producing a medium of color-charged constituents. The deconfinement transition thus becomes the QCD counterpart of the insulator-conductor transition of atomic physics [54]. Hadronic matter thus shows two transitions, deconfinement and chiral symmetry restoration. Some general arguments suggest that they either occur at the same point or, deconfinement precedes the chiral symmetry restoration. It is quite possible that quarks, as they become deconfined, can maintain their effective mass up to some higher temperature or density. Lattice calculations have shown that for vanishing baryon density, deconfinement and chiral symmetry restoration do in fact coincide, indicating that the deconfinement temperature is sufficient to melt the effective quark mass. For high baryon density at low temperature, this however seems unlikely. In addition to the hadronic matter and plasma of deconfined massless quarks and gluons, an additional state of massive quarks is very much possible. We note that in particular the anti-triplet quark-quark interaction provides an attractive force, making it possible that diquarks as localized bound states exist. Such colored bosonic states can condense and therefore form a color superconductor as yet another state of strongly interacting matter.

1.3 Signatures of QGP signal : Experimental observables

A QGP state created in high-energy heavy-ion collisions should be extremely hot, dense, short lived, and it would not be directly accessible to the experiments. One can detect only the final state particles, freely streaming out from the reaction zone that went through the hadronization process. However, these particles and their distributions are quite useful to trace back the properties of fireball medium in terms of such observables that are almost insensitive to the process of hadronization. Here we are going to discuss some such experimental signatures of the QGP.

1.3.1 Charmonium suppression

J/ψ is a bound state of charm quark pairs ($c\bar{c}$). QCD calculations predict that J/ψ production should be suppressed in a QGP medium [55]. J/ψ is produced mostly at the initial stages of the collision through hard and pre-thermal processes. In a QGP medium the charm and anti-charm quarks do not bind to form hadrons while passing through the deconfined matter, instead they just move apart from each other. Due to the heavy mass associated with the charm quarks the production of $c(\bar{c})$ is also limited during hadronization. It is the quarks and gluons of the deconfined matter that screen the strong potential of the c and \bar{c} quarks. This is similar to the Debye screening of QED, which prevents them from binding together and form a J/ψ . The phenomenon can be understood as following.

The inter-quark potential is given by Equation (1.2). The parton density around c and \bar{c} gets modified due to Debye screening of color charges between c and \bar{c} . This in turn modifies the inter-quark potential to,

$$V(r) = -\frac{g \exp(-r/r_D)}{4\pi r} \quad (1.21)$$

where r_D is the Debye screening length. According to perturbative QCD estimation, r_D should be inversely proportional to the temperature of the QGP phase. At high temperature r_D becomes smaller. As a consequence the range of attractive potential in Equation (1.21) becomes smaller. Therefore, at extreme temperatures it would be impossible for $c\bar{c}$ pairs to form bound states. The separated c and \bar{c} quarks in the deconfined phase would rather hadronize by combining with other light quarks present in the system. In comparison with pp collisions where formation of QGP is not expected, the J/ψ yield will be suppressed in AA collisions where QGP is expected to form. To quantify the extent of J/ψ suppression a nuclear modification factor is introduced as,

$$R_{AA}^{J/\psi} = \frac{\frac{1}{N_{ev}} \frac{d^2 N_{J/\psi}}{dp_T dy} |_{cent}}{\langle T_{AA} \rangle \frac{d^2 \sigma_{J/\psi}}{dp_T dy} |_{pp}}$$

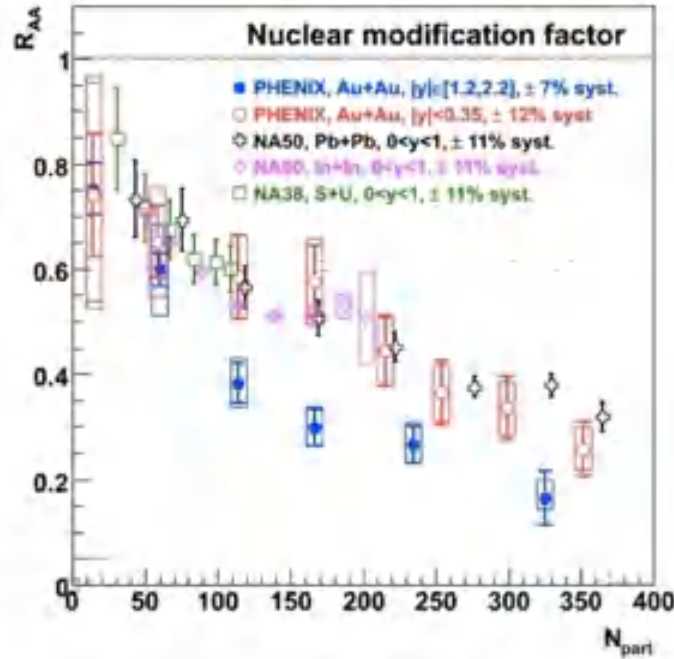


Figure 1.7: Centrality dependence of J/ψ R_{AA} . This figure is taken from Ref. [56].

Here $N_{J/\psi}$ is the J/ψ yield per centrality in AA collisions, $\langle T_{AA} \rangle$ is the average nuclear overlap function per centrality in AA collisions, and $\sigma_{J/\psi}$ is the J/ψ cross-section in pp collisions. N_{ev} is the number of AA events within a particular centrality class. $R_{AA}^{J/\psi}$ as a function of N_{part} is shown in Figure 1.7 for a wide range of energies from SPS [57, 58] to RHIC [59]. If the value of R_{AA} is less than unity, it is a manifestation of the suppression, which in turn is an evidence of a quark-gluon medium created in heavy-ion collisions.

1.3.2 Jet quenching

Jet is a group of high energy particles which are highly correlated in their direction. In AB collisions partons are produced due to hard processes. Fragmentation of these partons while escaping the collision zone results in production of jets. Figure 1.8 shows the schematic of a di-jet, a pair of jets moving in opposite directions. If a di-jet is produced near the surface of the fireball, then the near side jet will propagate normally, while the away side (opposite to the nearby fireball surface) jet will be smeared out. The smearing effect is ascribed to the fact that the away side jet passes through a longer distance in the hot and dense medium, suffering multiple interactions with the partons present therein. As a consequence its momentum will be lost and the phenomenon is known as *jet quenching* [60, 61]. The effect was first noted at RHIC [62] while investigating the two particle azimuthal correlation. It is observed from Figure 1.8 that in Au+Au collision the away side ($\Delta\varphi = \pi$) jet disappears,

whereas the same is present in d+Au and p+p collisions. Thus, jet quenching can be considered as an unambiguous signature of the QGP formation in AB collisions. Another approach to examine the jet-medium interaction is the measurement of nuclear modification factor (R_{AA}) for an inclusive jet production, which is defined as,

$$R_{AA}^{jet} = \frac{1}{N_{ev}} \frac{d^2 N_{jet}}{dp_T dy} \Big|_{cent}}{\langle T_{AA} \rangle \frac{d^2 \sigma_{jet}}{dp_T dy} \Big|_{pp}}$$

where the symbols have similar meaning as described in 1.3.1 with J/ψ being replaced by ‘jet’. Figure 1.9 shows a clear indication of jet suppression at a LHC energy relative to the pp collision. Jet quenching is maximum for the most central collisions, decreases monotonically from central to peripheral events, which again confirms the formation of a dense partonic

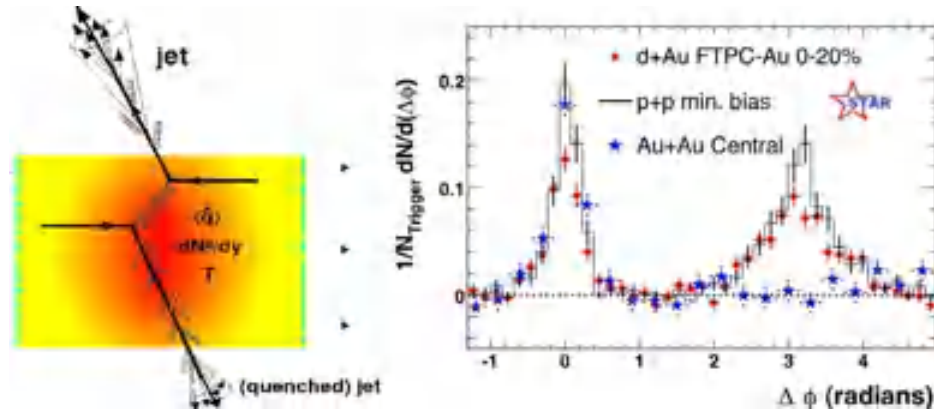


Figure 1.8: Left: Schematic of di-jet production. Right: Distribution of azimuthal angle difference between trigger and associated particles at STAR from central Au+Au, d+Au, and p+p collisions. The figure is taken from Ref. [62].

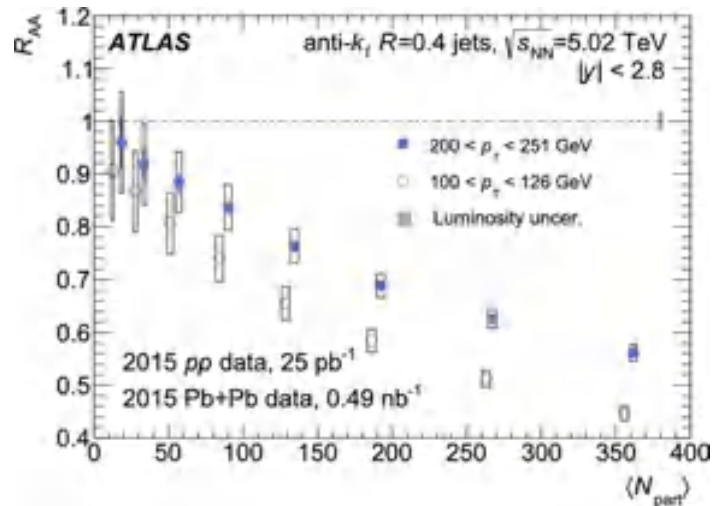


Figure 1.9: R_{AA} values for jets considering two different p_T intervals at midrapidity as a function of N_{part} . The figure is taken from Ref. [63].

medium in central collisions. Jet quenching is also observed to decrease (increase in R_{AA}) with increasing jet- p_T at almost all centrality classes for which $N_{\text{part}} \geq 50$. Below $N_{\text{part}} = 50$ the differences are not statistically significant.

1.3.3 Strangeness enhancement

Unlike the u and d quarks, the strange (s) quarks are not present in the colliding nuclei. Thus, any detection of a strange particle is attributed to a s -quark formation using the kinetic energy of the colliding system. Strangeness production is believed to be a key observable having the potential to deliver an in-depth information on the reaction dynamics of AB collisions [64, 65]. It should be noted that strangeness disappears only through weak

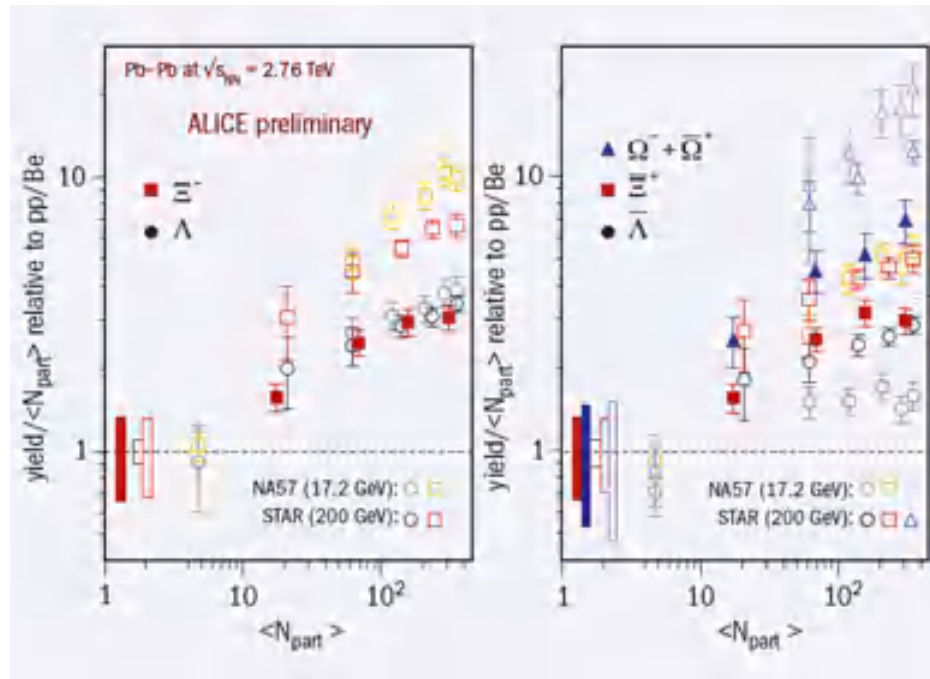


Figure 1.10: Strangeness enhancements at midrapidity as a function of N_{part} , showing LHC, RHIC and SPS data simultaneously. The figure is taken from Ref. [66].

decay. This decay mode being a longer process than hadronization, strange hadrons can survive hadronization and can bring out undistorted information about the initial stages of the fireball system. Coupling of gluons, $g+g \rightarrow \bar{s}+s$ is the dominating process of strangeness production in a QGP phase. These interactions occur very rapidly and s -quark abundance is equilibrated in plasma. Strangeness enhancement in dense baryonic matter may be a consequence of Pauli's exclusion principle. Strangeness enhancement is measured in terms of its enhancement factor defined as the yield per participating nucleons of a particular type of strange particle in AB collisions relative to the strange particle yield in a reference system like say, pp collisions. Figure 1.10 shows the strangeness enhancement as a function

of centrality observed at midrapidity for various species of particles in SPS [67], RHIC [68] and LHC [66] energies. Strangeness enhancement is noticed to increase with centrality and also with the strangeness content.

1.3.4 Electromagnetic probes

Photons associated with different amounts of momentum transfer are produced during the entire lifetime of the fireball formed in heavy-ion collisions. Photons do not interact strongly and in addition their mean free path is so large in comparison to the system size, that they suffer almost no collision in the medium before reaching the detectors. In other words, photons can bring out undistorted information from their time of production. Different processes of photon production from the instant of collision to freeze-out can be summarized as following:

1. The hard parton-parton scattering during the first stage of the collision gives rise to prompt photons. These photons are expected to be produced isotropically. The rate of their production decreases as an inverse power of p_T and increases with energy.
2. Next is the QGP phase where the dominating process of photon production are:
 - (i) Annihilation – this is generally a quark-antiquark interaction like, $q + \bar{q} \rightarrow \gamma + g$ and $q + \bar{q} \rightarrow \gamma + \gamma$. The probability of occurrence of the second process is smaller by a factor of $\alpha_e/\alpha_s \approx 0.02$ and usually not considered.
 - (ii) Compton process – in this process a gluon interact with a quark and produce a quark and photon like, $g + q \rightarrow q + \gamma$ and $g + \bar{q} \rightarrow \bar{q} + \gamma$. These *thermal* photons help to investigate the thermodynamic properties of the fireball medium.
3. As the system expands and cools down, hadronization follows the QGP state. Photons produced during hadronization are labeled as *hadron gas* photons which are produced from resonance decays and scattering of π, ρ, ω , and others. Most common contribution to the photons in this stage are from the following schemes: $\pi^+ + \pi^- \rightarrow \gamma + \rho^0$ and $\pi^\pm + \rho^0 \rightarrow \gamma + \pi^\pm$.
4. Additional photons may also originate from hadronic decays after freeze out by $\pi^0 \rightarrow \gamma + \gamma$, $\eta \rightarrow \gamma + \gamma$, and higher resonances.

The direct photons (thermal and hadron gas) produced in phase 2 and 3 provide some idea about the degree of thermalization of the fireball. The rapidity distribution of these photons unveil the initial rapidity of the produced mesons or directly the QGP [69]. However, it should be noted that it is extremely difficult to extract these direct photons from the

huge background produced from the prompt photons and also hadronic decays of π^0 and η . The contribution from direct photons in heavy-ion collisions is estimated by obtaining the direct photon distribution in pp collisions and then scaling the yield with number of binary collisions. On the other hand, the contribution from aforementioned hadronic decays are experimentally removed using the invariant mass reconstruction technique.

1.3.5 Collective flow

The major focus of this thesis is on collective flow analysis and allied effects of charged hadrons. In this context we are going to provide a review with a little more details than the other signatures described above, on some results pertaining to the collective flow of hadronic matters available from different experimental facilities like AGS, SPS, RHIC, and LHC. With reference to heavy-ion collisions collectivity refers to some common properties exhibited by the emitted particles. There may be emission of many hadrons with a common velocity or in a common direction or even ejection of many particles of similar type. There are many underlying collective phenomena related to the common feature of the final state particles that can be broadly classified in the following manner.

- *Longitudinal flow* illustrates the collective behavior of the particles along the beam direction.
- *Radial flow* describes the motion of particles emitted from the source with a common velocity independent of the direction. This type of flow is mainly observed in central collisions where the system is azimuthally almost symmetric.
- An enhanced emission of particles along the direction of orientation of the impact parameter vector is termed as the *directed flow* or *side flow*.
- *Anisotropic flow* or particularly the *elliptic flow* refers to the non-uniform azimuthal distribution of particles where the final state have some azimuthal preference with back to back symmetry.

Ollitrault in 1992 for the first time predicted that “anisotropies in transverse-momentum distributions [will] provide an unambiguous signature of transverse collective flow in ultra-relativistic nucleus-nucleus collisions” [70]. Different equations of state and initial conditions were incorporated in his ideal hydrodynamic calculations to quantify this effect. In non-central collisions, the initial spatial anisotropy of the fireball, which is generally of almond shape, through multiple (re)scatterings among the particles is converted to a final momentum space anisotropy. A pictorial representation of the effect is depicted in Figure 1.11.

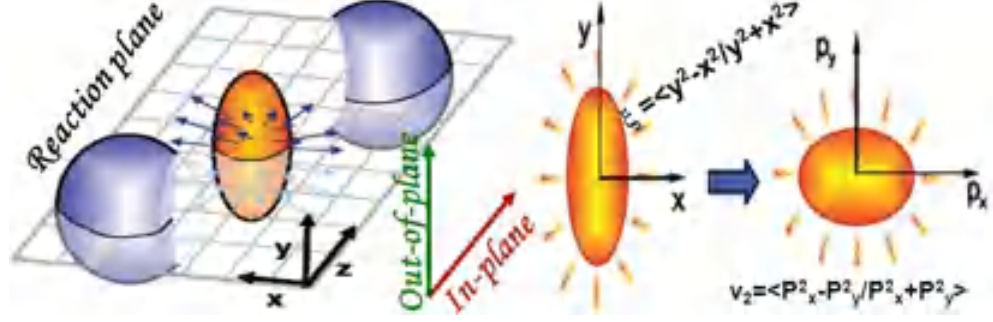


Figure 1.11: Schematic of initial space anisotropy w.r.t the reaction ($x - z$) plane being converted into momentum space anisotropy due to in-medium interactions among the final state hadrons.

As the fireball system expands and cools down this anisotropy decreases, i.e. the system becomes more spherical. As a consequence there is a self quenching of the driving force. So, a scrutiny of the anisotropic flow will be sensitive to the dynamics that determines the early stage evolution of the collision [71]. It should be understood that in absence of strongly interacting matter, the distribution of the produced particles will be uniform on the transverse plane, thus anisotropic flow is a strong signature of presence of QGP. In order to understand different transverse flow effects, Voloshin and Poskanzer suggested a Fourier analysis of the azimuthal distribution of produced hadrons w.r.t to the reaction plane, a plane spanned by the beam axis and the impact parameter vector [72, 73]. This is generally expressed as,

$$E \frac{d^3 N}{dp^3} = \frac{d^3 N}{d\mathbf{p}_T dy} = \frac{d^2 N}{2\pi p_T dp_T dy} [1 + 2v_1 \cos(\phi - \Psi_{RP}) + 2v_2 \cos 2(\phi - \Psi_{RP}) + \dots] \quad (1.22)$$

where ϕ is the azimuthal angle of a produced particle and Ψ_{RP} is the reaction plane angle defined as the angle between the reaction plane and the x -axis of the laboratory system. v_n is the Fourier coefficient associated with the n -th harmonic. The flow harmonics are usually given by,

$$v_n = \langle \langle \cos n(\phi - \Psi_{RP}) \rangle \rangle \quad (1.23)$$

where $\langle \langle \rangle \rangle$ denotes averaging over events and particles within a selected kinematic region. The first harmonic v_1 is called the *directed flow* parameter, which implies a preferential direction of particle emission either parallel ($v_1 > 0$) or anti-parallel ($v_1 < 0$) to the beam direction. Voloshin first coined the term *elliptic flow* to the 2nd harmonic (v_2). It is to be noted that the scenario of elliptic anisotropy changes from lower to higher energies for the colliding beams. At low energies the elliptic shape of the particle transverse momentum distribution is elongated along a direction perpendicular to the reaction plane. This is due to the shadowing by the spectator nucleons due to which particle production in the reaction plane is blocked. This is referred to as squeeze-out or out-of-plane flow. It corresponds to

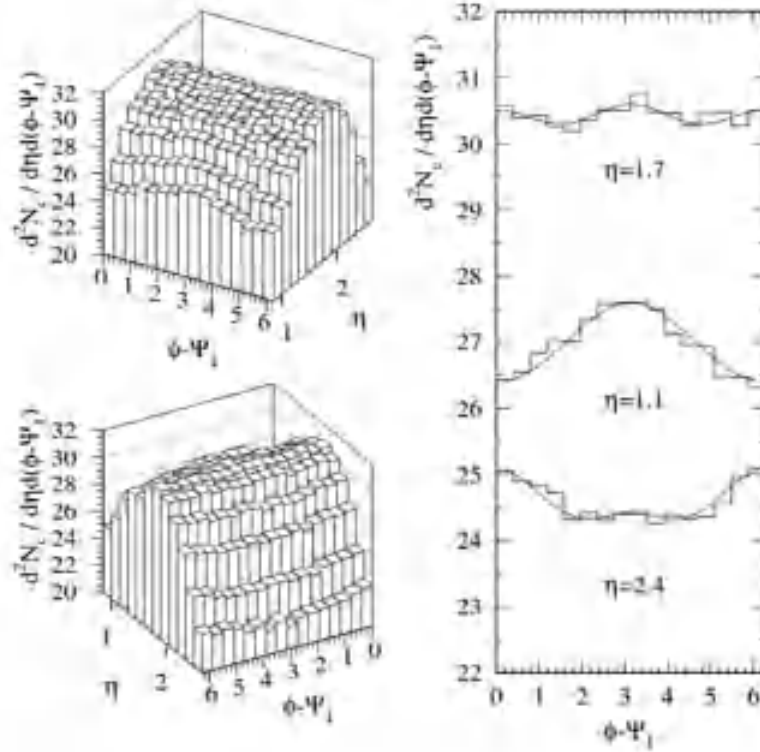


Figure 1.12: First measurement of in-plane elliptic flow by the E877 Collaboration at 11.8A GeV [74]. The solid line is a distribution with Fourier coefficients v_0 , v_1 , v_2 at three different pseudorapidity.

a negative value of v_2 and there is a preferential emission around $\Delta\phi = \frac{\pi}{2}$ and $\Delta\phi = \frac{3\pi}{2}$. The squeeze-out effect has got a special importance in AB collisions in the sense that any flow of nuclear/hadronic matter out of the reaction plane might escape the rescattering with the target and projectile spectators, thereby keeping the information of the interaction zone unaffected by the vigor of the collision. At higher energies the longitudinal size of the Lorentz contracted nuclei becomes negligible compared to its transverse size. In addition, the passing time of the nuclei becomes very small in comparison to the time required for development of elliptic flow. These factors interplay in such a manner that the shadowing is washed out and an in-plane elliptic flow develops. Now, there is a preferential emission at around $\Delta\phi = 0$ and $\Delta\phi = \pi$ which corresponds to positive v_2 values. In-plane elliptic flow was first observed at the AGS by the E877 Collaboration [74] as depicted in Figure 1.12. Later in the low energy scan at the AGS the E895 Collaboration [75] reported elliptic flow in the transition region from an out-of-plane to in-plane flow. However, at very low energies the picture is completely different, where the major effect is from the nuclei bouncing off from each other and then their fragmentation. These observations can be confirmed from Figure 1.13, where the p_T -integrated elliptic flow at midrapidity in the 20–30% centrality bin is compared from measurements at lower energies to the LHC range. Integrated v_2 increases

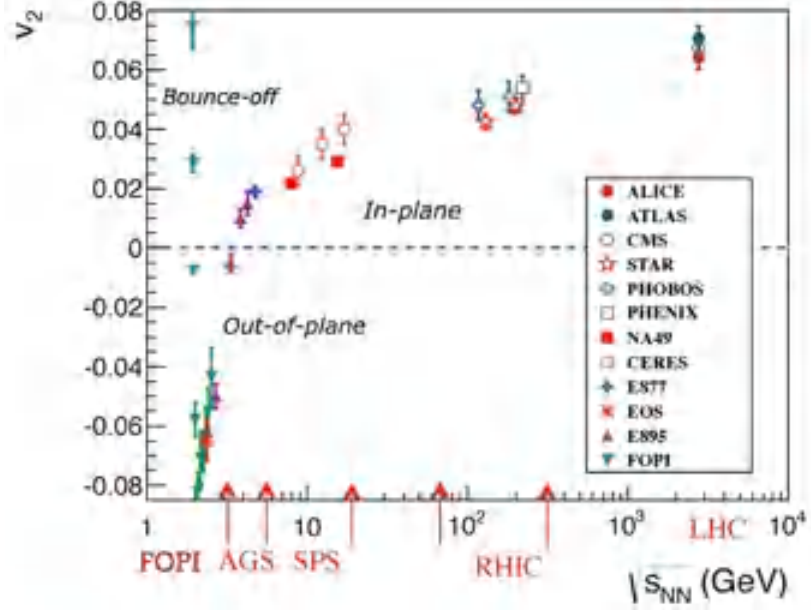


Figure 1.13: Elliptic flow at midrapidity in 20 – 30% centrality bin as a function of energy from FOPI, AGS, SPS, RHIC to LHC. The basic figure is taken from [76] except certain textual changes.

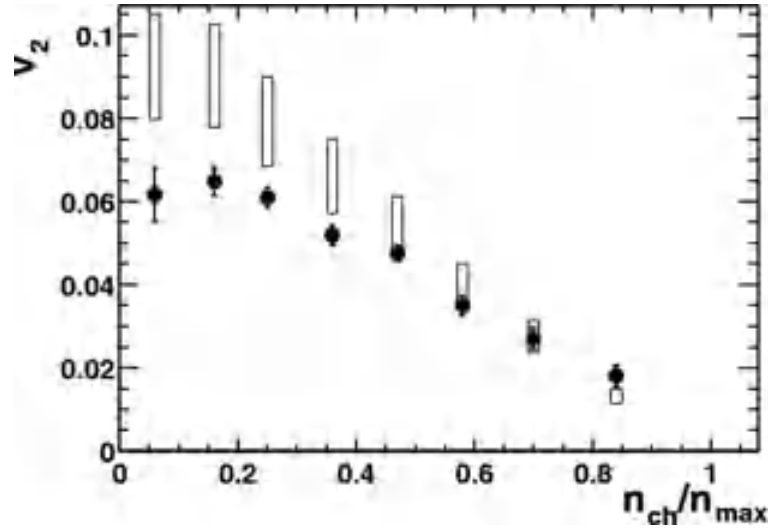


Figure 1.14: Elliptic flow as a function of centrality defined as n_{ch}/n_{max} reported by STAR Collaboration at $\sqrt{s_{NN}} = 130$ GeV [77]. The open rectangles show a range of values expected for v_2 in the hydrodynamic limit, scaled from ϵ , the initial space eccentricity of the overlap region.

by 30% from RHIC $\sqrt{s_{NN}} = 200$ GeV to LHC $\sqrt{s_{NN}} = 2.76$ TeV. The first measurement of v_2 at RHIC [77] is shown in Figure 1.14. The open rectangles are prediction of v_2 from hydrodynamic calculations. It is observed that the RHIC data agrees well with ideal hydrodynamics for $n_{ch}/n_{max} \geq 0.5$. This observation is an evidence of rapid thermalization of the system. The first results on elliptic flow at LHC energy [78] reported by the ALICE

collaboration is presented in Figure 1.15 and also compared with measurements at RHIC as obtained from STAR, shown by the solid lines. The elliptic flow at LHC follows the same trend as in RHIC but is higher in magnitude at same centrality. Elliptic flow coefficient

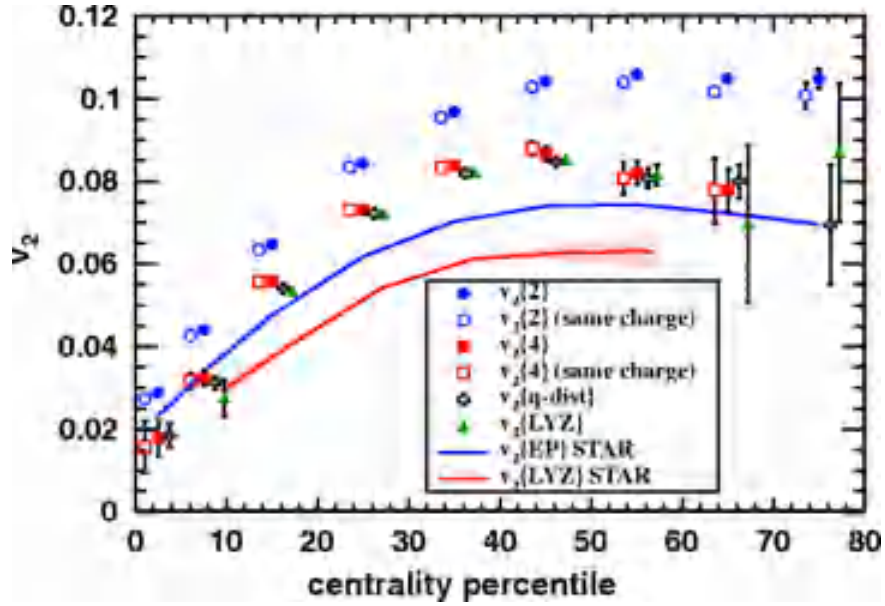


Figure 1.15: Elliptic flow integrated over the p_T range $0.2 < p_T < 5.0$ GeV/c at $\sqrt{s_{NN}} = 2.76$ TeV as a function of centrality [78]. RHIC measurements at $\sqrt{s_{NN}} = 200$ GeV is integrated over the p_T range $0.15 < p_T < 5.0$ GeV/c.

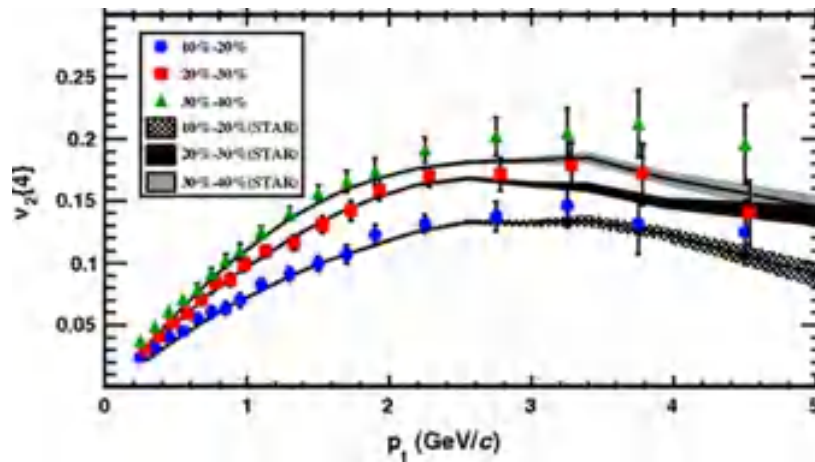


Figure 1.16: p_T dependence of $v_2\{4\}$ at $\sqrt{s_{NN}} = 2.76$ TeV for various centralities compared to STAR measurements at $\sqrt{s_{NN}} = 200$ GeV [78].

(v_2) is further examined as a function of p_T to study the evolution from RHIC to LHC. Figure 1.16 shows the p_T -dependence of elliptic flow employing the 4-particle cumulant method, $v_2\{4\}$ is measured by the ALICE group in three different centrality classes. STAR estimates are shown by dashed areas. Although a $\sim 30\%$ difference is observed between the

integrated v_2 values obtained from RHIC and LHC, the p_T differential estimates are in good agreement within uncertainties upto $p_T \approx 3.0$ GeV/c.

Thus, the increase in integrated flow at LHC can be ascribed to the increase in average transverse momentum, or in other words radial flow has a remarkable effect at high p_T and these effects can be well understood from hydrodynamic models [79, 80]. It is believed that the mutual interaction between elliptic flow and radial flow will lead to a species mass dependent p_T -differential flow. Indeed a mass ordering of v_2 at low- p_T where flow decrease with increasing hadronic mass, was observed at RHIC energy [81] as shown in the left panel of Figure 1.17. Hydrodynamic results [79] including phase transition at $T_c = 165$ MeV and kinetic freeze out at 130 MeV shown by dotted curves, are found to reproduce the mass ordering effect. Heavier particles experience a strong push towards high- p_T due to radial flow and subsequently have a smaller v_2 at a particular p_T . To put a tight constraint on radial flow and mass dependent v_2 , hydro estimates from LHC and RHIC were reported together in 20 – 30% centrality in [80]. Looking at the right panel of Figure 1.17 it may be inferred that v_2 of lighter particles increases but that of heavier particles decreases from RHIC to LHC energies. This results in a similar magnitude of $v_2(p_T)$ at the two collision energies which differs from each other by almost two orders of magnitude. This is one of the remarkable findings from hydrodynamic simulations. A complete review on collective flow and hydrodynamics can be found in [82, 83]. The mass ordering of v_2 at low- p_T at

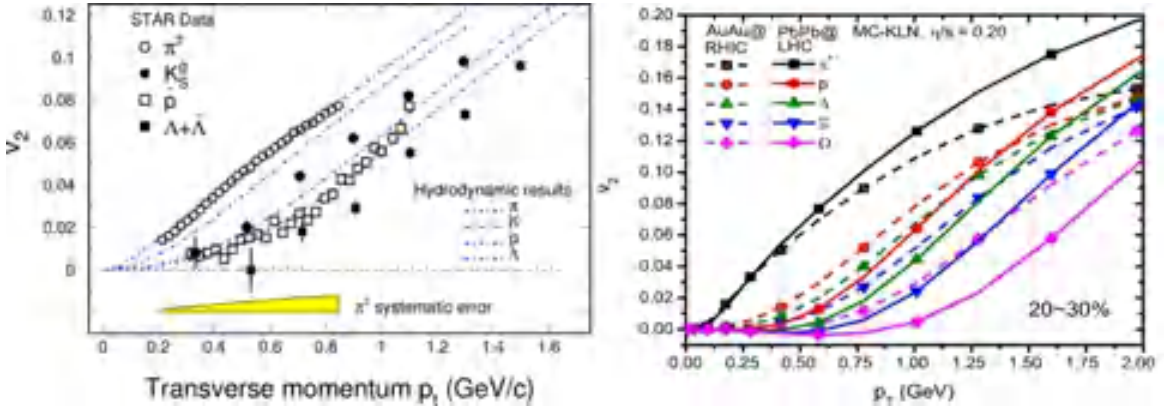


Figure 1.17: Left: Differential elliptic flow at RHIC ($\sqrt{s_{NN}} = 200$ GeV) as a function of transverse momentum compared to hydrodynamical predictions [81]. Right: Hydrodynamical prediction of differential elliptic flow for 20 – 30% centrality at $\sqrt{s_{NN}} = 200$ GeV (dashed lines) and $\sqrt{s_{NN}} = 2.76$ TeV (solid lines) [80].

RHIC energies is attributed to hydrodynamic pressure gradient which further predicts that p_T -differential v_2 should scale with transverse kinetic energy defined as $KE_T = m_T - m_0$, as the driving force of elliptic flow is directly related to the collective kinetic energy of the emitted particles. Strong influence of hydrodynamic pressure gradient is confirmed from Figure 1.18 (left panel) as species-wise v_2 scales up to $KE_T \leq 1.0$ GeV/c. But the scaling

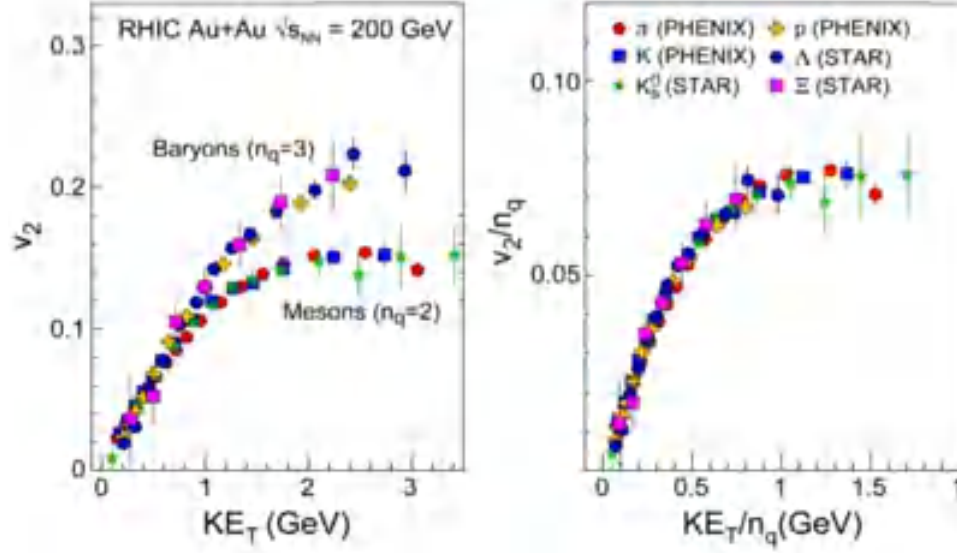


Figure 1.18: Left: v_2 against transverse kinetic energy (KE_T) for different species for minimum bias Au+Au collisions at $\sqrt{s_{NN}} = 200$ GeV. Right: Same but after scaling by NCQ. The figure is taken from [84].

is broken for $KE_T \geq 1.0$ and clear splitting into a mesonic and baryonic branch is noted. This separate scaling is believed as a signature of presence of quarkonic degrees of freedom developed at an early stage in the flowing matter. Further to confirm the same observation, both v_2 and KE_T are divided by the number of constituent quarks (NCQ), i.e. $n_q = 3$ for baryons and $n_q = 2$ for mesons. An excellent scaling of v_2/n_q over the entire range of KE_T/n_q is depicted in the right panel of Figure 1.18. The NCQ scaling is generally explained by the quark recombination or coalescence models [85, 86]. This indicates that the system has been in a deconfined state before hadronization and is a direct evidence of partonic collectivity.

Local thermalization is one of the significant characteristics of QGP. It was predicted in Ref. [87] that the centrality and system size dependence of v_2 has the potential to examine the issues related to thermalization. Upon complete thermalization, v_2 in different systems and centrality bins would depend only on the initial anisotropy quantified as eccentricity (ϵ). However, in the low density limit, the mean free path is larger or comparable to the system size and the system is well away from equilibrium. Under this condition elliptic flow depends both on eccentricity and system size or centrality bins. Voloshin and Poskanzer [87] suggested that the physics of these observations can be best studied by plotting the elliptic flow parameter scaled by eccentricity (v_2/ϵ) as a function of transverse particle density related to the probability of interactions and quantified as $\frac{1}{S} \frac{dN_{ch}}{dy}$. It is noteworthy that eccentricity (ϵ) and the overlap area (S) can be computed from the Glauber model based simulations [24]. A non-smooth nature of such a plot would indicate the presence of new physics mechanism, whereas a saturation at high density would be an indication towards

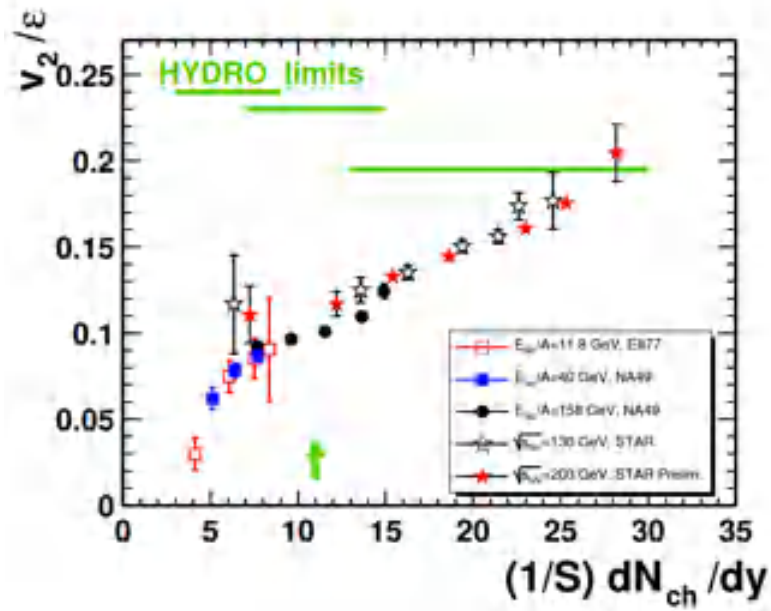


Figure 1.19: Eccentricity scaled v_2 as a function of particle density in the transverse plane at AGS, SPS to RHIC. The figure is from Ref. [88].

ideal hydrodynamic evolution. Figure 1.19 shows the eccentricity scaled v_2 plotted against $\frac{1}{S} \frac{dN_{ch}}{dy}$ over a wide range of energies from AGS, SPS, RHIC to LHC. It is observed that v_2/ϵ -values obtained from quite different collision systems fall approximately on a single curve. Beside that, for near central collisions at top RHIC energy, eccentricity scaled v_2 is close to the predicted hydrodynamic limit, which once again reflects that the system created in such collision having smaller mean free paths evolves towards thermalization. Another interesting

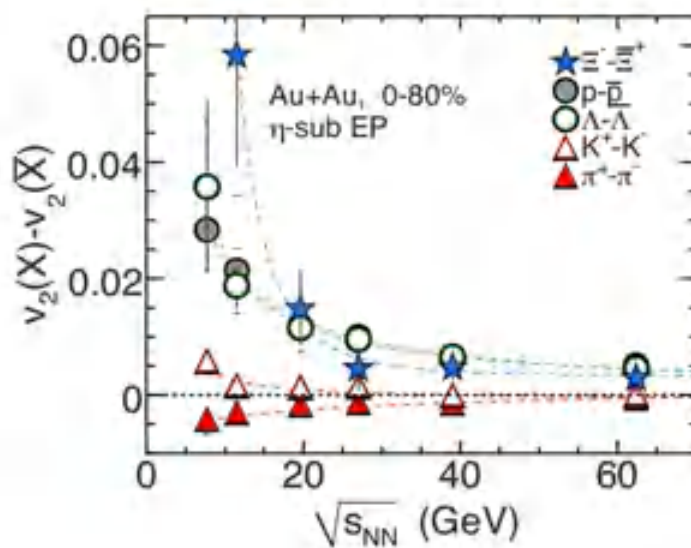


Figure 1.20: Difference in v_2 for particles and their corresponding anti-particles measured by the STAR collaboration at RHIC for 0 – 80% central events. Dashed lines are fits to some power law function, the details of which can be found in [89].

aspect is a difference in the v_2 -values for particles and antiparticles as a function of collision energy as depicted in Figure 1.20. The difference increases with increasing particle mass towards lower collision energies. The baryon chemical potential is held responsible for the observed particle dependent splitting in the elliptic flow [89]. Nevertheless, the effects of mean-field potential in both the partonic and hadronic phase are also to be considered for a meaningful explanation of the splitting [90].

In recent years the third-harmonic coefficient v_3 of the Fourier decomposition of the azimuthal distribution, also called the *triangular flow* parameter, has gained attention and has been studied extensively [91–93]. Originally it was perceived though, that due to a left-right symmetry prevailing in the transverse plane of a collision, the contribution from odd harmonics to the particle azimuthal distribution would vanish, and v_2 would be the only dominating contribution to transverse anisotropy. However, now it is widely accepted

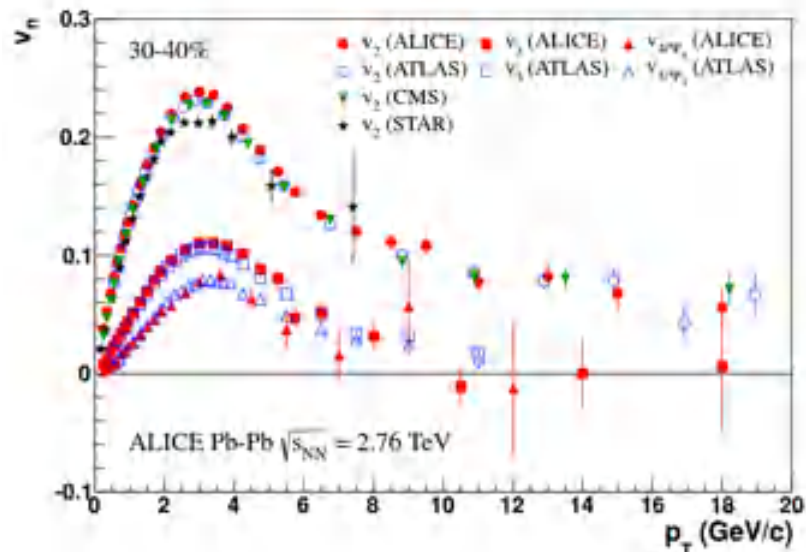


Figure 1.21: Transverse momentum dependence of different order flow harmonics (v_n) estimated by the ALICE Collaboration. [93].

that the event-by-event fluctuating position of the nucleons [94] participating in an AB collision often assumes a triangular shape, preferably called the triangularity, which with the evolution of the interacting system is converted into a momentum space anisotropy. Triangular flow is sensitive to the correlations present in the early stages of the AB collision. It has been proposed that the triangular anisotropy can explain the near side ridge and the away-side shoulder structures present in two-particle (dihadron) azimuthal correlations [91]. Furthermore, triangular flow is also believed to be sensitive to the viscous effects of the fireball medium as suggested by some simulation studies on relativistic viscous hydrodynamics [95, 96]. Transverse momentum dependence of the flow harmonics v_n for $n = 2, 3, 4$ is depicted in Figure 1.21. It is quite well understood that the signal strength of higher

harmonics decreases. A combined investigation of different orders of flow harmonics will impose significant constraints on the initial state fluctuations [96]. Further, it would be also challenging to measure the higher harmonics due to their weaker strengths, particularly in the future low-energy experiments.

1.4 CBM experiment at FAIR

In the entire landscape of heavy-ion experiments the Compressed Baryonic Matter (CBM) experiment will be of significant importance at the future Facility for Antiproton and Ion Research (FAIR), which is under construction in Darmstadt, Germany adjacent to the GSI. CBM at FAIR will facilitate the study of hot and dense matter produced in heavy-ion collisions in laboratory, but in a scenario somewhat different from its predecessors at BNL and CERN, which were devoted to investigate the properties of the strongly interacting matter at high temperature and almost zero net baryon density. The present day interest of the heavy-ion physics community is to explore the highest net baryon density region of the QCD phase diagram, which is possible only through heavy-ion collisions at moderate energies, available upto some extent at the low energy CERN-SPS experiments and will be accessible in the future FAIR facility. CBM is a dedicated fixed target experiment to collide heavy-ions in the beam kinetic energy range $2 \leq E_{\text{lab}} \leq 11$ GeV/nucleon at the SIS-100 accelerator to be extended to $40A$ GeV in an upgrade to SIS-300 [97]. It has been shown

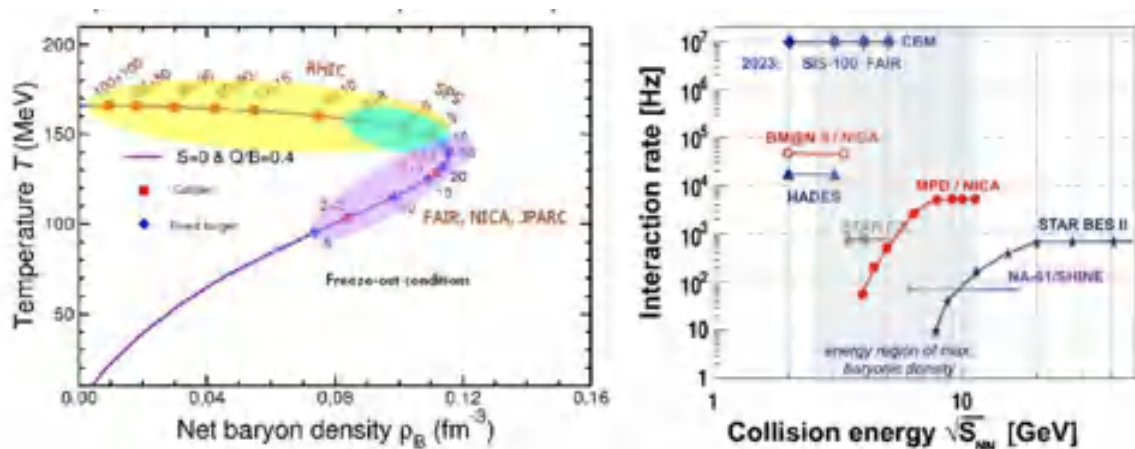


Figure 1.22: Left: Hadronic freeze out line on the temperature versus net-baryon density plane as obtained in statistical model [98]. Right: Interaction rate reached by existing and future heavy-ion experiments as a function of beam energy [99].

in [98] that the maximum net-baryon density is achievable at low SPS or FAIR energies. The observation is graphically represented in the left panel of Figure 1.22 while plotting the chemical freeze out line as a function of net-baryon density and temperature. The points represent the beam energies either in collider or fixed target experiments on Au+Au collisions. It is revealed that beam energies between 25 and $40A$ GeV are ideal to create

Table 1.2: Physics issues and their corresponding observables for the CBM experiment.

Physics Topic	Observable
Equation of state prevailing in high density matter	(i) Collective flow of identified particles. (ii) Production of multi-strange hadrons due to back-to-back collisions.
Restoration of chiral symmetry	Modification of the invariant mass spectra of dileptons via electron and muon channel.
Hadronic to partonic phase transition	(i) Excitation function of yield of multi-strange hyperons. (ii) Excitation function of invariant mass spectra of lepton pairs which provides an idea of the fireball temperature
Existence of critical point	Excitation function of higher order EbyE fluctuations of conserved quantities such as charge, strangeness, baryon number.
Hyperon puzzle in neutron stars [100]	Discovery of (double Λ) hypernuclei and measurement of their lifetime.

maximum net-baryon density matter. Transport calculations estimate an energy density upto 2.5 fm^{-3} and a baryon density 2–7 times that of the normal nuclear matter at the centre of the reaction zone at this energy range. CBM comprises of an extensive examination of the observables like low mass dilepton pairs, charmonia and open charm, collective flow of both rare (multi-strange hyperons, ϕ) and bulk particles (π, p, K), correlations and fluctuations. The basic goal is to measure the rare probes inspite of their low multiplicity and small branching ratios. In order to perform measurements of the rare probes with exceptional interaction rate of upto 10 MHz the CBM detectors are designed to consist of extremely fast, ultra-radiation hard detectors and electronics [101]. For the sake of completeness apart from the CBM we list some other ongoing and future heavy-ion experiments focused to investigate the high density hadronic matter.

1. HADES at SIS18, GSI, Germany [102].
2. Nuclotron-based Ion Collider Facility (NICA) at JINR in Dubna, Russia [103].
3. STAR Fixed Target (FXT) Programme at BNL, United States [104].
4. NA61/SHINE at SPS-CERN, Switzerland [105].
5. Heavy-ion program at J-PARC in Japan (in a nascent stage) [106].

Beside CBM the reaction rates of these experimental facilities have been presented as a function of collision energy in the right panel of Figure 1.22. One should readily understand that the uniqueness of CBM experiment lies in its unparallel reaction rate in comparison to others. Moreover, the CBM detector will also be equipped with free streaming data readout and acquisition system [99]. The fundamental physics issues and their corresponding experimental observables believed to be addressed by the FAIR-CBM [99, 101] set up, is summarized in Table 1.2.

1.5 Objective of the thesis

The study of azimuthal anisotropy and collective flow of final state hadrons is believed to be one of the most important tools that can extract significant information regarding particle interactions in a hot and dense nuclear and/or partonic medium produced in high energy heavy-ion collisions. Properties of this kind of matter is supposed to be guided by the rules of QCD. Our present understanding of collective flow at FAIR energy region is constrained by the unavailability of experimental data. Though the Alternating Gradient Synchrotron (AGS) [74], Super Proton Synchrotron (SPS) [88] and some low energy RHIC measurements [107, 108] provide us with some sort of a database, it is nevertheless necessary to scan a much wider range of collision energies involving different colliding systems that may be used to study baryon rich hadronic matter where high degree of nuclear stopping is expected. In absence of substantive experimental data, simulations that are successful in describing certain phenomenon like the collective flow, can provide us with such useful information as to what can be expected in future experiments. Such an exercise will not only help us understand the dynamics of the system but will also provide us with important clues that might constrain the models/theories to be used to characterize a baryon rich fireball. Keeping this in mind, in this thesis we have studied different aspects of collective flow of charged particles produced in Au+Au collisions at the FAIR energies using the Ultra-relativistic Quantum Molecular Dynamics (UrQMD) [109], and A Multiphase Transport (AMPT) [110] model. The Monte Carlo Glauber (MCG) model [24] is employed to characterize the collision geometry at an early stage of the evolution of an AB collision. The latest available version of these models are used to simulate symmetric fixed target nuclear collisions at incident energies $E_{\text{Lab}} = 10A, 20A, 30A, \text{ and } 40A$ GeV. The main motivation behind this kind of simulation based analysis is to examine how different flow parameters are expected to behave in a moderate temperature, baryon-rich environment, and in what respect are they similar/different from a high temperature and almost baryon free fireball created in RHIC and/or LHC experiments. The results at high energy density and high temperature in an almost baryon free condition obtained from the RHIC and LHC experiments are available in literature. We believe that it is worthwhile to compare and supplement the RHIC and LHC results with those obtained from the present analysis of simulated data.

Bibliography

- [1] S. L. Glashow, Nucl. Phys. **22**, 579 (1961).
- [2] A. Salam and J. C. Ward, Phys. Lett. **13**, 168 (1964).
- [3] S. Weinberg, Phys. Rev. Lett. **19**, 1264 (1967).

- [4] H. Fritzsche, M. Gell-Mann, and H. Leutwyler, Phys. Lett. B **47**, 365 (1973).
- [5] D. J. Gross and F. Wilczek, Phys. Rev. Lett. **30**, 1343 (1973).
- [6] H. D. Politzer, Phys. Rev. Lett. **30**, 1346 (1973).
- [7] K. G. Wilson, Phys. Rev. D **10**, 2445 (1974).
- [8] S. Bethke, Nucl. Phys. Proc. Suppl. **121**, 74 (2003).
- [9] J. Schwinger, Phys. Rev. **128**, 1, 2425 (1962).
- [10] A. Casher, J. Kogut, and L. Susskind. Phys. Rev. D **10**, 1 732 (1974).
- [11] A. H. Mueller, Nucl. Phys. B **213**, 85 (1983); *ibid* **241**, 141 (1983); Dokshitzer *et al.*, Z. Phys. C **27**, 65 (1985).
- [12] J. C. Collins and M. J. Pery, Phys. Rev. Lett. **34**, 1353 (1975).
- [13] N. Cabibbo and G. Parisi, Phys. Lett. B **59**, 67 (1975).
- [14] E. V. Shuryak, Sov. Phys. JETP **47**, 212 (1978) [Zh. Eksp. Teor. Fiz.74,408(1978)].
- [15] R. Hagedorn, Suppl. Nuovo Cim. **3** 147 (1965).
- [16] W. Greiner, S. Schramm, and E. Stein, Quantum Chromodynamics, 2nd edition, Springer-Verlag, Germany, (2002).
- [17] E. W. Kolb and M. S. Turner, The Early Universe, Addison-Wesley, USA, (1990).
- [18] J. Allday, Quarks, Leptons, and the Big Bang, Taylor and Francis, UK (2002).
- [19] E. V. Shuryak, Phys. Lett. B **78**, 150 (1978).
- [20] G. Baym *et al.*, Rep. on Prog. in Phys. **81**, 056902 (2018).
- [21] <https://www.civilsdaily.com/news/evolution-of-universe-after-the-big-bang/>
- [22] T.D. Lee and G. C. Wick, Phys. Rev. D **9**, 2291 (1974).
- [23] A. Toia, Cern Courier, **April**, 31 (2013).
- [24] M. L. Miller *et al.*, Ann. Rev. Nucl. Part. Sci. **57**, 205 (2007).
- [25] J. P. Lansberg, Physics of Ultrarelativistic Heavy-ion Collisions, Talk given in the Energy Atlas Workshop, Benasque, Spain (2015).
- [26] C. Shen and U. Heinz, Nucl. Phys. News **25**, 6 (2015).
- [27] [https://www.Evolution of collisions and QGP/Particles and friends \(wordpress.com\)](https://www.Evolution of collisions and QGP/Particles and friends (wordpress.com)).

- [28] S. Afanasiev *et al.*, Phys. Rev. Lett. **99**, 052301 (2007).
- [29] E. Fermi, Prog. Theo. Phys. **5**, 570 (1950).
- [30] A. Chodos *et al.*, Phys. Rev. D **9**, 3471 (1974).
- [31] A. Chodos, B. L. Jaffe, K. Johnson and C. B. Thorn, Phys. Rev. D **10**, 2599 (1974).
- [32] C. -Y. Wong, Introduction to High-Energy Heavy-Ion Collisions, World Scientific, Singapore, (1994).
- [33] R. Vogt, Ultrarelativistic Heavy-Ion Collisions, Elsevier, The Netherlands, (2007).
- [34] A. K. Chaudhuri, A Short Course on Relativistic Heavy-Ion Collisions, IOP Publishing, UK, (2014).
- [35] D. Evans, QCD and the Quark-Gluon Plasma, Talk given in the Summer School, Queen's University, Belfast, UK (2017).
- [36] L. D. Landau, Izv. Akad. Nauk. Ser. Fiz. **17**, 51 (1953).
- [37] S. Z. Belensky and L. D. Landau, Usp. Fiz. Nauk. **56**, 309 (1955).
- [38] I. M. Khalatnikov, J. Exp. Theor. Phys. **26**, 529 (1954).
- [39] P. Carruthers and M. Duong-Van, Phys. Rev. D **28**, 130 (1983).
- [40] S. Pokorski and L. Van Hove, Acta. Phys. Pol. B **5**, 229 (1974).
- [41] L. Van Hove and S. Pokoroski, Nucl. Phys. B **86**, 243 (1975).
- [42] J. D. Bjorken, Phys. Rev. D **27**, 140 (1983).
- [43] K. Yagi, T. Hatsuda and Y. Miake, Quark-Gluon Plasma, From Big Bang to Little Bang, Cambridge University Press, UK (2005).
- [44] P. Kolb and U. Heinz, Quark-Gluon Plasma 3, (Eds.) R. C. Hwa and X. N. Wang, World Scientific, Singapore (2003).
- [45] A. Bazavov *et al.*, Phys. Rev. D **85**, 054503 (2012).
- [46] R. D. Pisarski, F. Wilczek, Phys. Rev. D **29**, 338 (1984).
- [47] M. A. Stephanov, Prog. Theor. Phys. Suppl., **153** 139 (2004).
- [48] F. Karsch, E. Laermann and B. Peikert, Nucl. Phys. B **605**, 579 (2001).
- [49] Z. Fodor and S. D. Katz, J. High Ener. Phys. **03**, 014 (2002).

- [50] Z. Fodor and S. D. Katz, *J. High Ener. Phys.* **04**, 050 (2004).
- [51] The Frontiers of Nuclear Science, A Long Range Plan, The DOE/NSF Nuclear Science Advisory Committee, arXiv:0809.3139v1[nucl-ex].
- [52] J. Pochodzalla *et al.*, *Phys. Rev. Lett.* **75** 1040 (1995).
- [53] J. B. Elliott *et al.*, *Phys. Rev. C* **87**, 054622 (2013).
- [54] H. Satz, The Quark-Gluon Plasma, A short introduction, Talk given in 6th International Conference on Physics and Astrophysics of Quark Gluon Plasma, Dec. 5 - 10, Goa/India, 2010.
- [55] T. Matsui and H. Satz, *Phys. Lett. B* **178**, 416 (1986).
- [56] P. Steinberg (for the ATLAS Collaboration), Quarkonia and Vector Bosons measured with the ATLAS detector at the LHC, Talk given in the BNL Quarkonia Workshop, BNL, USA (2011).
- [57] M. Gonin *et al.* (NA50 Collaboration), *Nucl. Phys. A* **610**, 404c (1996).
- [58] M. C. Abreu *et al.* (NA50 Collaboration), *Nucl. Phys. A* **661**, 93 (1999).
- [59] A. Adare *et al.* [PHENIX Collaboration], *Phys. Rev. Lett.* **98**, 232301 (2007).
- [60] J. D. Bjorken, Fermilan-Pub-82-059-THY, Batavia (1982).
- [61] G. -Y. Qin and X. -N. Wang, *Int. J. Mod. Phys. E* **24**, 1530014 (2015).
- [62] J. Adams *et al.* (STAR Collaboration), *Phys. Rev. Lett.* **91**, 072304 (2003).
- [63] M. Aaboud *et al.* (ATLAS Collaboration), *Phys. Lett. B* **790**, 108 (2019).
- [64] J. Rafelski and B. Müller, *Phys. Rev. Lett.* **48**, 1066 (1982).
- [65] P. Koch, B. Müller, and J. Rafelski, *Phys. Rept.* **142**, 162 (1986).
- [66] K. Aamodt *et al.* (ALICE Collaboration), *Phys. Lett. B* **728**, 216 (2014).
- [67] F. Antonori *et al.* (NA57 Collaboration), *J. Phys. G* **32**, 427 (2006).
- [68] B. I. Abelav *et al.* (STAR Collaboration), *Phys. Rev. C* **77**, 044908 (2008).
- [69] A. Dumitru *et al.*, *Z. Phys. A* **353**, 187 (1995).
- [70] J. Y. Ollitrault, *Phys. Rev. D* **46**, 229 (1992).
- [71] H. Sorge, *Phys. Lett. B* **402**, 251 (1997).

- [72] S. A. Voloshin and Y. Zhang, *Z. Phys. C* **70**, 665 (1996).
- [73] A. M. Poskanzer and S. A. Voloshin, *Phys. Rev. C* **58**, 1671 (1998).
- [74] J. Barette *et al.* (E877 Collaboration), *Phys. Rev. C* **55**, 1420 (1997).
- [75] C. Pinkenburg *et al.* (E895 Collaboration), *Phys. Rev. Lett.* **83**, 1295 (1999).
- [76] M. J. Tannenbaum, *Universe* **5(6)**, 140 (2019).
- [77] K. H. Ackermann *et al.* (STAR Collaboration), *Phys. Rev. Lett.* **86**, 402 (2001).
- [78] K. Aamodt *et al.* (ALICE Collaboration), *Phys. Rev. Lett.* **105**, 252302 (2010).
- [79] P. Huovinen, P. Kolb, P. Ruskanen, and S. Voloshin, *Phys. Lett. B* **503**, 58 (2001).
- [80] U. Heinz, C. Shen, and H. Song, *AIP Conf. Proc.* **1441**, 766 (2012).
- [81] J. Adams *et al.* (STAR Collaboration), *Phys. Rev. C* **72**, 014904 (2005).
- [82] U. Heinz and R. Snellings, *Ann. Rev. Nucl. Part. Sci.* **63**, 123 (2011).
- [83] S. Jeon and U. Heinz. *Int. J. Mod. Phys. E* **24**, 1530010 (2015).
- [84] A. Adare *et al.* (PHENIX Collaboration), *Phys. Rev. Lett.* **98**, 162301 (2007).
- [85] D. Molnar and S. A. Voloshin, *Phys. Rev. Lett.* **91** 092301 (2003).
- [86] R. J. Fries *et al.*, *Phys. Rev. Lett.* **90** 202303 (2003).
- [87] S. A. Voloshin and A. M. Poskanzer, *Phys. Lett. B* **474**, 22 (2000).
- [88] C. Alt *et al.* (NA49 Collaboration), *Phys. Rev. C* **68**, 034903 (2003).
- [89] L. Adamczyk *et al.* (STAR Collaboration), *Phys. Rev. Lett.* **110**, 142301 (2013).
- [90] J. Xu, T. Song, C. M. Ko, and F. Li, *Phys. Rev. Lett.* **112**, 012301 (2014).
- [91] B. Alver and G. Roland, *Phys. Rev. C* **81**, 054905 (2010).
- [92] L. Adamczyk *et al.* (STAR Collaboration), *Phys. Rev. C* **88**, 014904 (2013).
- [93] K. Aamodt *et al.* (ALICE Collaboration), *Phys. Lett. B* **719**, 18 (2013).
- [94] B. Alver *et al.* (STAR Collaboration), *Phys. Lett. B* **98**, 242302 (2007).
- [95] B. Alver *et al.*, *Phys. Rev. C* **82**, 034913 (2010).
- [96] B. Schenke, S. Jeon, and C. Gale, *Phys. Rev. C* **82**, 014903 (2010); **85**, 024901 (2012).
- [97] C. Simon, I. Deppner, and N. Herrmann, *PoS CPOD17*, 014 (2017).

- [98] J. Randrup and J. Cleymans, Phys. Rev. C **74**, 047901 (2006).
- [99] T. Ablyazimov *et al.* (CBM Collaboration), Eur. Phys. J. A **53**, 60 (2017).
- [100] I. Bombaci, JPS Conf. Proc. **17**, 101002 (2017).
- [101] B. Friman, C. Hohne, J. Knoll, S. Leupold, J. Randrup, R. Rapp, and P. Senger, Lect. Notes Phys. **814**, pp. 1-980 (2011).
- [102] HADES Collaboration, <https://www-hades.gsi.de/>
- [103] N. S. Geraksiev (for the MPD Collaboration), Phys. Conf. Ser. **1023**, 012030 (2018).
- [104] K. C. Meehan (for the STAR Collaboration), J. Phys. Conf. Ser. **742**, 012022 (2016).
- [105] N. Abgrall *et al.*, (NA61/SHINE Collaboration), JINST **9**, P06005 (2014).
- [106] H. Sako *et al.*, Nucl. Phys. A **931**, 1158 (2014).
- [107] L. Adamczyk *et al.* (STAR Collaboration), Phys. Rev. C **86**, 054908 (2012).
- [108] L. Adamczyk *et al.* (STAR Collaboration), Phys. Rev. C **88**, 014902 (2013).
- [109] S. A. Bass *et al.*, Prog. Part. Nucl. Phys. **41**, 255 (1998);
M. Bleicher *et al.*, J. Phys. G **25**, 1859 (1999).
- [110] B. Zhang *et al.*, Phys. Rev. C **61**, 067901 (2000);
Z. -W. Lin *et al.*, Phys. Rev. C **72**, 064901 (2005).

Chapter 2

Simulation models and some bulk properties of charged hadron production at expected FAIR energies

Our present understanding about the dynamics of partonic and/or hadronic matter produced in AB collisions at and around FAIR conditions lacks substantive experimental evidences. We are therefore somewhat compelled to rely on model calculations and Monte Carlo simulations built thereof. For all practical purposes, simulation codes that can describe the nature of global observables associated with multiparticle production with reasonable success, should be chosen for an in-depth study of more subtle and delicate issues. In the next section, without claiming any originality, we provide a cursory review of the models that are used in this investigation. Before we go into a more detailed description of the simulation results on collective behaviour, in this chapter we have presented our simulation results on some basic distributions and spectra associated with the charged hadron emission in Au+Au collisions at $E_{\text{lab}} = 10A - 40A$ GeV.

2.1 Brief description of the models

2.1.1 UrQMD model

Ultra-relativistic Quantum Molecular Dynamics (UrQMD) is a microscopic transport model that treats an AB collision as a superposition of multiple NN interactions [1, 2]. UrQMD simulates the dynamics of an AB event over its entire duration, starting from the initial pre-equilibrium stage to the final freeze-out stage. At low and intermediate energies ($\sqrt{s_{NN}} < 5$ GeV) the hadronic interactions are modelled through known hadronic processes and their resonances. While at higher energies particle production is dominated by excitation of color strings followed by their fragmentation into hadrons. The UrQMD treats the intermediate fireball both in and out of its equilibrium. In other words, the UrQMD provides a framework to bridge a very wide energy domain from AGS to RHIC. The model is first to describe the color coherence phenomenon. The UrQMD assumes a covariant propagation of all hadrons that is based upon classical principles in amalgamation with non-linear binary scatterings, resonance decays and formation of color strings. The model consists of a large number of coupled integro-differential equations related to the time evolution of different phase space densities of particles like N , Δ , Λ etc., which are usually solved by Monte Carlo methods. A nuclei in this model is treated as a Fermi gas. The Gaussian density functions pertaining to individual nucleons are represented by,

$$\varphi_j(x_j, p_j, t) = \left(\frac{2\alpha}{\pi}\right)^{3/4} \exp\left[-\alpha\{x_j - r_j(t)\}^2 + \frac{i}{\hbar}p_j(t)x_j\right] \quad (2.1)$$

and the nuclear wave-function, a direct product of many such nucleonic wave-functions would be,

$$\Phi = \prod_i \varphi_i(x_i, p_i, t) \quad (2.2)$$

In the configuration space the mean position of these Gaussian functions are distributed at random within a sphere of radius,

$$R(A) = r_0 \left(\frac{1}{2} \left[A + (A^{1/3} - 1)^3\right]\right)^{1/3} \quad (2.3)$$

If ρ_0 is the nuclear density in its ground state, then r_0 in Equation (2.3) is given by,

$$r_0 = \left(\frac{3}{4\pi\rho_0}\right)^{1/3}$$

In order to avoid any significant fluctuation in the mean nuclear density, the phase space density at any location is computed after the placement of the nucleons. The initial momenta

of the nucleons are chosen at random between zero and the local Thomas-Fermi momentum given by,

$$p_F^{\max} = \hbar c (3\pi^2 \rho)^{1/3} \quad (2.4)$$

where ρ is the local nucleon number density. But this type of initialization has some demerits. The nuclei may not be perfectly in the ground state with respect to the Hamiltonian used to model their propagation. The parameters in the Hamiltonian are set according to the properties of finite size nuclei. So, even if the energy of the nucleons are minimized in a congruent manner, the nucleus could collapse into a particular point in the momentum space as Pauli's principle has been ignored. One possible way to overcome this complication is through anti-symmetrization of the nuclear wave-function in Equation (2.2), i.e. to invoke fermionic properties of the nucleons. Although this notion has been properly structured in Fermionic Molecular Dynamics (FMD) [3], yet due to the huge computational efforts required to model the FMD equations, its implementation is restricted. Another alternative is to incorporate the Pauli potential [4] in the Hamiltonian. The potential is repulsive in nature and aids to anti-symmetrization of the nuclear wave-function. In conventional initialization and propagation, the nuclei start to evaporate nucleons after $\approx 20 - 30$ fm/c. If instead a Pauli potential is used, the nuclei remain perfectly stable. However, a pitfall of invoking Pauli potential is that the kinetic and canonical momenta of the nucleons will no more be equal, i.e. the nucleons will bear exact Fermi-momentum but their velocity will be zero. In addition this potential will result in an incorrect specific heat that would effect the string fragmentation dynamics.

The NN interactions in UrQMD are primarily described in terms of the density dependent Skyrme potential [5]. This consists of contributions from both two-body and three-body interaction dynamics. The two-body term (V^{Sk2}), linearly dependent on density, illustrates the long range attractive part of NN interaction. The three body term (V^{Sk3}) which has a quadratic dependence on density, is capable of describing the short range repulsive component. Besides the Skyrme potential, Yukawa (V^{Yuk}), Coulomb (V^{Coul}) and as mentioned above, optional Pauli potential (V^{Pauli}) are also included in the UrQMD. Taking account of all of these contributions into the effective potential, the UrQMD Hamiltonian can be formulated as,

$$H = \sum_{j=1}^N E_j^{kin} + \frac{1}{2} \sum_{j,k=1}^N \left(E_{jk}^{Sk2} + E_{jk}^{Yuk} + E_{jk}^{Coul} + E_{jk}^{Pauli} \right) + \frac{1}{6} \sum_{j,k,l=1}^N E_{jkl}^{Sk3}. \quad (2.5)$$

Impact parameter of a collision is sampled according to a quadratic measure, $dW \sim bdb$. Two particles will collide only if their relative distance (d) satisfies the criterion, $d \leq d_0 = \sqrt{\frac{\sigma_{tot}}{\pi}}$. The total cross section (σ_{tot}) depends on the centre of mass energy of the colliding particles (\sqrt{s}), their species type and quantum numbers associated with the species. At low energies

the proton-proton and proton-neutron cross sections significantly differ among themselves. So, instead of taking a simple average of nucleon-nucleon cross sections, issues related to isospin is dealt in a delicate way. Due to isospin symmetry proton-proton and neutron-neutron cross sections are treated equivalently.

The common particle production mechanism in UrQMD are meson decays, baryon resonances, excitation of strings and their fragmentation. Resonance decays dominate the particle production mechanism for incident energies upto $E_{\text{lab}} = 10A$ GeV. The production cross sections in connection with excitation of each resonance is usually estimated in the framework of One Pion Exchange (OPE) or One Boson Exchange (OBE) models [6]. Due to energy limitations in the applicability of OPE or OBE model, it is not meaningful to compute the reaction cross sections of all the resonances by employing these models. Therefore, a simple phase space based effective parameterization has been used and the free parameters in the model are calibrated from experimental measurements. Unknown cross sections are estimated within the framework of Additive Quark Model (AQM) [7], which assumes weak interactions among the valence quarks within the hadronic boundary. It is further assumed that the hadronic cross sections, particularly at higher energies, are simply the sum total of their constituent quark cross sections. AQM forms a basis in understanding the role of resonances in multiple particle production through hadronic interactions. UrQMD simulations after inclusion of the AQM, appears to be in excellent conformity with experimental data above $p_{\text{lab}} = 300$ MeV, especially in the presence of strange baryons/mesons. Principle of detailed balance is also used to compute the unknown cross sections. It is believed to be derived from the time reversal invariance of the Hamiltonian. A comprehensive discussion can be found in [1]. The resonance decays occur in compliance with their branching ratios listed by the Particle Data Group [8]. In the rest frame of a resonance, the decay products are considered to follow an isotropic distribution. The collision term in UrQMD consists of more than fifty baryons (including nucleon, delta, and hyperon resonances) and forty five meson species (including vector meson resonances like ρ , ω and K^* decay). Charge conjugation mechanism has been successfully engaged to ensure full baryon-antibaryon symmetry. It should be noted that not only in heavy-ion collisions, but UrQMD has the potential to reproduce the particle production cross section and particle spectra even in hadronic collisions. We have used the UrQMD-3.4 version in our analysis.

2.1.2 AMPT model

A Multi Phase Transport (AMPT) model has been brought forward to illustrate nuclear collisions from pA to AB systems at CM energies ranging from $\sqrt{s_{NN}} = 5$ to 5500 GeV [9, 10]. The AMPT includes both partonic and hadronic interactions and also a transition

between these two phases. AMPT is a hybrid transport model consisting of four major components, namely the initial conditions, the partonic interactions, the conversion from partonic to hadronic matter, and finally the hadronic interactions. In AMPT the initial conditions are obtained through two-body NN interactions. It uses a Glauber formalism to determine the position coordinates of the participating nucleons, and generates hard minijets (partons) and soft excited strings (hadrons) by using the heavy-ion jet interaction generator (HIJING) [11]. The AMPT model can be used in two configurations, the default version and the string melting version. The basic difference between these two versions lies in modelling the excited strings. In the string melting mechanism beyond a certain critical energy density, excited strings (hadrons) and minijets (partons) cannot coexist. Therefore, it is necessary to melt or convert the strings into partons, i.e. a meson is converted into a quark-antiquark pair, a baryon into three quarks, etc. The scattering among quarks and the original hard partons are then described by Zhang's parton cascade (ZPC) model [12], which includes two-body elastic scattering with an in-medium cross section obtained from the perturbative QCD (pQCD), where the effective gluon screening mass is used as a parameter. After the binary collisions cease to progress, the partons from minijets and partons from melted strings hadronize through a quark coalescence mechanism. However, in the AMPT default mode the energy of the excited string is not used in the partonic stage. The scattering occurs only among the minijet partons based on the ZPC model, and their hadronization is described by the Lund string fragmentation mechanism. After hadronization, either in the string melting version or in the default version, the hadron dynamics is modelled by a relativistic transport (ART) model [13], which includes both elastic and inelastic scattering of baryonic, mesonic, and baryo-mesonic nature.

HIJING provides the initial inputs to AMPT. In HIJING, the density of the colliding nuclei follows a Wood-Saxon type of functional form, and rescattering among the participating nucleons is structured within eikonal formalism. The notion of hard and soft components is engaged to describe the particle production mechanism. The energetic minijet partons originate from hard processes whereas soft processes lead to excitation of strings. The excited strings decay in accordance with the Lund JETSET mechanism. Besides, in HIJING an impact parameter dependent and flavor independent parameterization takes care of the nuclear shadowing effect, which results in a quark-gluon distribution that is different from their simple superposition. It should be noted that the formation time of individual partons is considered to have a Lorentzian distribution having a half width $t_f = E/m_T^2$, where E and m_T denote the partonic energy and mass respectively, which in turn takes the effects of Lorentz boost into consideration. Primary position of the produced minijet partons are estimated from their parent nucleons naively using straight line trajectories. In the string melting formalism, the excited strings are converted into partons in compliance with the spin and flavor content of their valence quarks. However, the resultant partons undergo

scatterings only after a certain formation time bearing a form similar to the above, but the quantities now correspond to the parent hadrons. Once again the straight line trajectory technique is employed to determine the initial positions of the partons formed by string melting from their parent hadrons.

Considering two body scattering, interaction among the partons is described by the Boltzmann equation as,

$$p^\mu \partial_\mu f(\mathbf{x}, \mathbf{p}, t) \propto \int \sigma f(\mathbf{x}_1, \mathbf{p}_1, t) f(\mathbf{x}_2, \mathbf{p}_2, t), \quad (2.6)$$

where σ and f are respectively, the parton scattering cross section and distribution function. ZPC is used to solve the Boltzmann equation, where the partons are supposed to undergo scattering when their relative distance $d \leq d_0 = \sqrt{\frac{\sigma}{\pi}}$. Only two body partonic scatterings such as $gg \rightarrow gg$ are invoked in the ZPC, the cross sections being evaluated from parton QCD calculations. In the context of hot QGP a simple relation like,

$$\sigma_{gg} \approx \frac{9\pi\alpha_s^2}{2\mu^2} \quad (2.7)$$

exists between the total elastic cross section of the partons (σ_{gg}) and Debye screening mass (μ), where α_s is the strong coupling constant. We can tune the value of μ to obtain different scattering cross sections and investigate its effect in heavy-ion collisions, a practice that has been already adopted by the heavy-ion physics community. Higher order scatterings are missing in the ZPC, and hence AMPT lacks a true estimate of the jet energy losses.

As mentioned above, AMPT consists of two different hadronization schemes corresponding to the default and string melting mode of operation. In AMPT (default), once the minijet partons stop interacting among themselves, they are combined with their parent string and excited strings are formed. In accordance with the Lund string fragmentation model these strings are then converted to hadrons. It is presumed that a string will fragment into a quark-antiquark pair, and their transverse momentum will follow Gaussian distributions. Further a symmetric fragmentation function [14] is used to form hadrons from the $q\bar{q}$ pair. The transverse momentum of the hadrons are obtained from their constituent quarks but the longitudinal momentum is computed from the symmetric fragmentation function,

$$f(z) \propto z^{-1}(1-z)^a e^{(-bm_T^2/z)}, \quad (2.8)$$

where a and b are the Lund string fragmentation parameters. In all investigations of this thesis we have used $a = 2.2$ and $b = 0.5 \text{ GeV}^{-2}$. In the AMPT (string melting) version the hadronization of partons are modelled in a quark coalescence framework, in a way similar to the ALCOR model [15]. Two nearest partons coalesce into a meson whereas three nearest quarks and/or antiquarks into a baryon or antibaryon. It should be understood that the

inverse mass spectra of the combined partons are continuous and not discrete. As a result it is not possible to conserve the four-momentum after the partons being coalesced into hadrons. Therefore, AMPT focuses to conserve the three-momentum and ascertain the hadron species type from the invariant mass and flavor of the coalescing partons.

The final state hadron cascade in AMPT is borrowed from the ART model. ART takes into account of the isospin degrees of freedom, thereby establishing it as a proper platform to scrutinize the isotopic effects in heavy-ion collisions. Mean field potential is invoked for nucleons and kaons, the importance of hadronic equation of state can also be investigated within ART/AMPT. Reaction cross sections for different resonances are obtained from the Breit-Wigner formula and the decay widths are taken according to their values in vacuum. Potentials are turned off in AMPT as their effects are almost insignificant with respect to the extent of scatterings. Strangeness-exchange reactions like: $\bar{K}(\Lambda\Sigma) \rightarrow \pi + \Xi$ and $K + \Xi \rightarrow \pi + \Omega$ are used to incorporate multistrange baryon production like Ξ, Ω . AMPT includes their interaction with mesons but excludes their annihilation by baryons. The ϕ -meson production and decay through kaon-antikaon channel is also included, the cross section being provided by the Breit-Wigner formula. Previous investigations have shown that the flow parameters obtained from the AMPT are consistent with the experiments, and the model can successfully describe several aspects of collective behaviour of AB interactions [10, 16, 17]. The string melting version of AMPT should be even more appropriate to model particle emission data where the transition from nuclear matter to a deconfined QCD state is expected. In this investigation we have used the v1.26t4/v2.26t4 version of the AMPT (default/string melting). Unless otherwise mentioned in a specific analysis, the parton scattering cross section is always set to $\sigma = 3$ mb.

2.1.3 Glauber model

The Monte Carlo Glauber (MCG) model is a useful tool to estimate the geometrical configurations of a pair of colliding nuclei [18, 19]. The model operates in two steps, (i) determination of nucleon positions in each nucleus by some stochastic approach, and (ii) evaluation of collision properties of the colliding nuclei [20, 21]. The position of each nucleon in the nucleus is described according to a smooth quantum mechanical single-particle probability density function ρ . At least for the closed and near-closed-shell nuclei such as Au, the probability distribution in polar and azimuthal angle is taken to be uniform. On the other hand, the radial distribution function is constrained by the nuclear charged density measurement [22], and is typically characterized by the Fermi distribution,

$$\rho(r) = \frac{\rho_0}{1 + \exp[(r - R)/a]} \quad (2.9)$$

Here the nuclear radius R and the skin depth a are estimated from low energy electron scattering experiment. The overall normalization parameter ρ_0 (nucleon density) is not relevant for this calculation. In order to optimize the nuclear dimension, one may require to set a minimum inter-nucleon separation (d_{\min}) between the centers of the nucleons.

The Glauber model treats an AB interaction as a superposition of multiple independent NN collisions. In this model, at relativistic energies the nucleons are assumed to travel along the beam direction throughout the reaction process (Eikonal approximation), so that their transverse degrees of freedom are negligible for the time span during which the impinging nuclei pass through each other. The impact parameter of a collision (b) is taken at random from a distribution like $dN/db \propto b$ with a large maximum limit $b_{\max} \simeq 20$ fm, say. In the $\{x, y, z\}$ space the centers of the colliding nuclei are taken at $\{+b/2, 0, 0\}$ and $\{-b/2, 0, 0\}$. Due to this convention the reaction plane is specified by the impact parameter vector and beam direction, i.e. the x and z -axis, respectively, while the $\{x, y\}$ denotes the transverse plane. An AB interaction in the MCG model is fully specified by the inelastic NN cross section (σ_{in}^{NN}) that depends only on the collision energy. The size of each colliding nuclei is large compared to the range of the NN interaction. In the MCG model an NN interaction takes place if the Euclidean transverse distance (d) between the centers of any pair of nucleons is less than $\sqrt{\sigma_{\text{in}}^{NN}/\pi}$. At any stage of a collision, σ_{in}^{NN} is assumed to be independent of the number of NN collisions that a nucleon has already suffered.

The correlation between centrality and the number of participating nucleons has also been expounded in detail by the Glauber-type calculations using different functional forms of the nuclear density [19]. As the two nuclei collide at an impact parameter \mathbf{b} , the probability of n inelastic NN interactions is given by,

$$P(n, \mathbf{b}) = \binom{AB}{n} [T(\mathbf{b}) \sigma_{\text{in}}^{NN}]^n [1 - T(\mathbf{b}) \sigma_{\text{in}}^{NN}]^{(AB-n)}$$

where $T(\mathbf{b}) = \int \rho_A(\mathbf{b}_A, z_A) d\mathbf{b}_A dz_A \rho_B(\mathbf{b}_B, z_B) d\mathbf{b}_B dz_B t(\mathbf{b} - \mathbf{b}_A - \mathbf{b}_B)$ is the normalized thickness function for the AB collision. The total probability of having an inelastic event in the collision between A and B is,

$$\frac{d^2 \sigma_{\text{in}}^{NN}}{db^2} = \sum_{n=1}^{AB} P(n, b) = 1 - [1 - T(b) \sigma_{\text{in}}^{NN}]^{AB}$$

The total inelastic cross-section is therefore,

$$\sigma_{\text{in}}^{AB} = \int 2\pi b db [1 - (1 - T(b) \sigma_{\text{in}}^{NN})^{AB}]$$

In the framework of the Glauber model the total number of nucleons that underwent at least one interaction (N_{part}), or the total number of binary NN interactions (N_{coll}) per event, can be analytically obtained as,

$$\begin{aligned} N_{\text{part}}(b) &= \int d^2\mathbf{s} \{T_A(\mathbf{s}) [1 - \exp(-\sigma_{\text{in}}^{NN} T_B(\mathbf{s}))] + T_B(\mathbf{s} - \mathbf{b}) [1 - \exp(-\sigma_{\text{in}}^{NN} T_A(\mathbf{s}))]\} \\ N_{\text{coll}}(b) &= \int d^2\mathbf{s} \sigma_{\text{in}}^{NN} T_A(\mathbf{s}) T_B(\mathbf{b} - \mathbf{s}) \equiv \sigma_{\text{in}}^{NN} T_{AB}(\mathbf{b}) \end{aligned} \quad (2.10)$$

where $T_A(\mathbf{s}) = \int dz \rho_A(z, \mathbf{s})$ is the thickness function for the nucleus A , $T_B(\mathbf{s})$ is the same for the nucleus B , and $T_{AB}(\mathbf{b})$ is the nuclear overlap function. An arbitrary number of such AB collisions can be generated by the Monte Carlo Glauber model [18] and the resulting distributions like $d\sigma/N_{\text{part}}$, $d\sigma/N_{\text{coll}}$ and $d\sigma/db$ are obtained. The systematic uncertainties in the mean values of N_{part} and N_{coll} for each centrality class, are estimated by varying the parameters of nuclear density function, by varying the value of σ_{in} , and from the uncertainty in the determination of total AB interaction cross-section. These sources of uncertainties are treated as fully correlated in the final systematic uncertainty in the above measured variables. If certain cross-sections scale with the number of participants, they are associated with soft or small momentum transfer processes. The low- p_t hadron production, which accounts for almost 95% of the bulk hadron multiplicity, are phenomenologically described by non-perturbative models. On the other hand, in the hard QCD processes like the jet formation, heavy flavor production etc., the cross-section scales with the number of primordial NN collisions N_{coll} . In a particular centrality class N_{part} grows like A , whereas N_{coll} grows like $A^{4/3}$, hence N_{coll} is always equal to or higher than N_{part} . Sometimes, the charged particle multiplicity is given in terms of the contributions coming from both soft and hard processes by using a two-component model [23, 24] like,

$$N_{ch} = f \times N_{\text{part}} + (1 - f) \times N_{\text{coll}} \quad (2.11)$$

where f , typically valued at 85 – 90%, is the fractional contribution from soft processes. We have chosen the configuration of the MCG model, which is similar to what has been used in the PHOBOS experiment [25]. For Au+Au collision the parameters are selected as following, nuclear radius $R = 6.38$ fm, skin depth $a = 0.535$ fm, $d_{\text{min}} = 0$. With these specifications we compute the number of participant nucleons N_{part} , and the total number of binary NN collisions (N_{coll}) on an event by event basis taking the impact parameter from the UrQMD/AMPT model. The MCG model records the position of each nucleon in the nucleus which are subsequently used to determine quantities like spatial asymmetry, centrality of collisions etc. A detailed description of the geometric quantities such as the nuclear overlap area, eccentricity, triangularity and their fluctuations is available in the subsequent chapters of this thesis.

2.2 Bulk properties of hadron production

We start describing our results with plots of charged hadron multiplicity (N_{ch}) distributions as shown in Figure 2.1 for the Au+Au fixed target events at incident energies $E_{lab} = (10 - 40)A$ GeV. Each simulated sample consists of 10^6 events. For all three models used in this investigation the nature of multiplicity distribution is found to be more or less similar. However, we see that the maximum multiplicity in the UrQMD generated events is less than that obtained from the AMPT. With an increase in the collision energy the difference becomes more prominent. N_{part} and N_{coll} as obtained from the Glauber model, are graphically plotted against impact parameter in Figure 2.2. Both quantities vary similarly with b , starting from a finite maximum value at $b = 0$ fm, asymptotically falling toward zero with increasing b . However, we do not observe any noticeable energy dependence of N_{part} at the present scale of energies. In the $(0 - 5)\%$ centrality class the maximum value of N_{coll} , irrespective of the E_{lab} -value concerned, is almost double of that of N_{part} . As E_{lab} changes from $10A$ to $40A$ GeV, this maximum value N_{coll} changes by $\lesssim 5\%$. For a proper clarity in Table 2.1 we have listed their values for the Au+Au system at $E_{lab} = (10 - 40)A$ GeV. In Figure 2.3 we plot the azimuthal angle distributions of all charged hadrons produced in the Au+Au collisions at four different incident energies. We observe the presence of anisotropy in each such plot and also find that the particle density, i.e. the number of charged hadrons per unit ϕ -interval ($N_{ev}^{-1}dN_{ch}/d\phi$), is consistently highest in the AMPT (default) generated

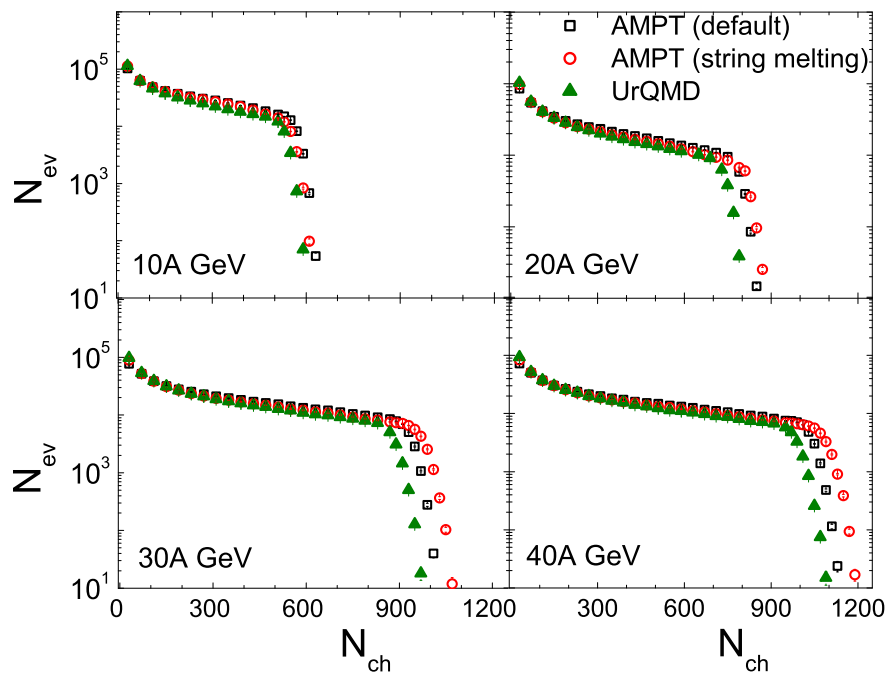


Figure 2.1: Charged hadron multiplicity distribution in Au+Au collisions at $E_{lab} = (10 - 40)A$ GeV.

Table 2.1: N_{part} , N_{coll} at different centrality (in %) as obtained from MCG model in Au+Au collisions at $E_{\text{lab}} = (10 - 40)A$ GeV and central particle density estimated from AMPT(default), AMPT(string melting) and UrQMD model.

Centrality	N_{part}	N_{coll}	$[dN_{\text{ch}}/d\eta]_{\eta_0}$		
			AMPT(def)	AMPT(SM)	UrQMD
<u>10A GeV</u>					
0-5	342.8±0.08	776.4±0.29	186.3±0.08	148.0±0.06	194.4±0.08
5-10	291.5±0.07	625.5±0.23	153.8±0.07	124.0±0.06	160.9±0.07
10-20	230.1±0.07	458.5±0.20	118.6±0.05	98.1±0.04	124.1±0.06
20-30	166.2±0.06	298.0±0.15	83.9±0.04	71.9±0.04	87.6±0.05
30-40	117.6±0.05	187.9±0.11	59.0±0.04	52.2±0.03	60.9±0.04
40-50	80.2±0.04	112.8±0.09	40.6±0.03	36.9±0.03	41.0±0.03
50-60	52.1±0.04	63.8±0.06	26.9±0.02	25.2±0.02	26.3±0.03
60-70	31.8±0.03	33.6±0.04	17.2±0.02	16.4±0.02	16.0±0.02
70-80	17.9±0.02	16.4±0.03	11.3±0.02	10.8±0.02	9.9±0.02
80-90	9.3±0.02	7.4±0.02	6.5±0.01	6.2±0.01	5.4±0.01
90-100	4.4±0.01	3.2±0.01	3.3±0.01	3.1±0.01	2.3±0.01
<u>20A GeV</u>					
0-5	343.7±0.08	793.5±0.29	245.2±0.09	214.5±0.08	244.3±0.10
5-10	292.6±0.07	639.7±0.24	204.2±0.08	180.9±0.07	201.7±0.09
10-20	231.2±0.07	468.8±0.21	159.8±0.07	143.9±0.05	155.2±0.07
20-30	167.3±0.06	304.9±0.15	115.5±0.06	106.0±0.05	109.0±0.06
30-40	118.5±0.05	192.2±0.12	82.3±0.05	77.0±0.04	75.2±0.05
40-50	80.9±0.04	115.4±0.09	57.4±0.04	54.6±0.03	50.2±0.04
50-60	52.7±0.04	65.2±0.06	38.4±0.03	37.0±0.03	32.1±0.03
60-70	32.2±0.03	34.4±0.04	24.5±0.03	23.8±0.02	19.4±0.03
70-80	18.2±0.02	16.7±0.03	15.8±0.02	15.6±0.02	12.0±0.02
80-90	9.4±0.02	7.6±0.02	9.2±0.01	9.0±0.01	6.4±0.01
90-100	4.5±0.01	3.3±0.01	4.7±0.01	4.5±0.01	2.8±0.01
<u>30A GeV</u>					
0-5	344.1±0.08	801.6±0.30	277.4±0.10	253.6±0.09	273.5±0.11
5-10	293.0±0.07	645.8±0.24	233.6±0.09	215.2±0.09	225.6±0.10
10-20	231.6±0.07	473.0±0.21	183.6±0.08	171.5±0.07	173.1±0.08
20-30	167.7±0.06	307.7±0.15	133.8±0.06	126.8±0.06	121.4±0.07
30-40	118.9±0.05	194.1±0.12	96.3±0.05	92.3±0.05	83.6±0.06
40-50	81.2±0.04	116.5±0.09	67.4±0.05	65.4±0.04	55.7±0.05
50-60	52.9±0.04	65.8±0.06	45.3±0.04	44.4±0.04	35.4±0.04
60-70	32.4±0.03	34.7±0.04	28.8±0.03	28.5±0.03	21.4±0.03
70-80	18.3±0.02	16.9±0.03	18.7±0.03	18.5±0.03	13.2±0.03
80-90	9.5±0.02	7.7±0.02	10.8±0.02	10.7±0.02	7.1±0.01
90-100	4.5±0.01	3.3±0.01	5.4±0.01	5.4±0.01	3±0.01
<u>40A GeV</u>					
0-5	344.7±0.08	812.7±0.30	293.3±0.11	275.6±0.11	293.6±0.12
5-10	293.7±0.07	654.8±0.24	248.1±0.10	234.7±0.10	242.0±0.11
10-20	232.4±0.07	480.3±0.21	196.4±0.08	187.6±0.08	185.9±0.09
20-30	168.4±0.06	312.2±0.16	143.8±0.07	139.0±0.07	129.9±0.07
30-40	119.4±0.05	196.8±0.12	103.9±0.06	101.5±0.06	89.3±0.06
40-50	81.7±0.04	118.4±0.09	73.0±0.05	71.9± 0.05	59.5±0.05
50-60	53.3±0.04	66.8±0.06	49.3±0.04	48.8±0.04	37.8±0.04
60-70	32.6±0.03	35.2±0.04	31.4±0.03	31.4±0.04	22.8±0.03
70-80	18.4±0.02	17.2±0.03	20.4±0.03	20.4±0.03	14.1±0.03
80-90	9.6±0.02	7.8±0.02	11.7±0.02	11.7±0.02	7.6±0.02
90-100	4.6±0.01	3.3±0.01	5.9±0.01	5.9±0.01	3.3±0.01

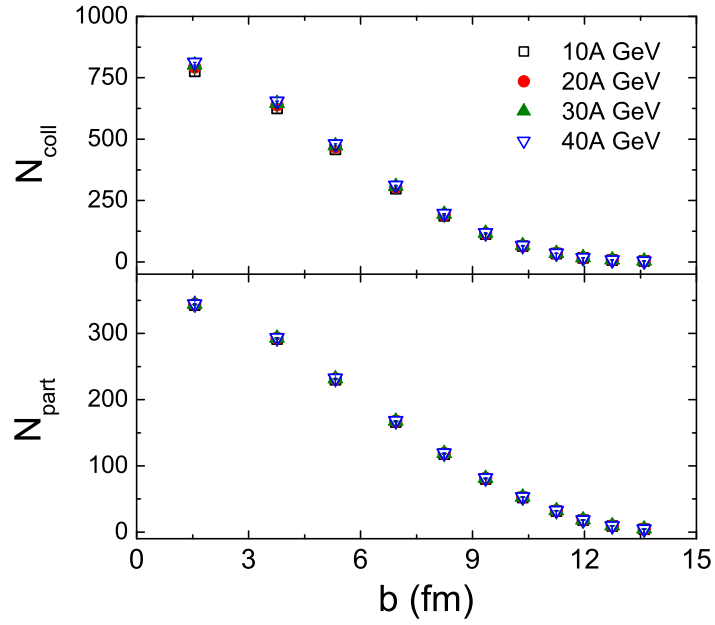


Figure 2.2: Impact parameter dependence of N_{part} and N_{coll} in Au+Au collisions at $E_{\text{lab}} = (10 - 40)A$ GeV.

event samples. It should also be noted that the anisotropy is maximum in the AMPT (SM) events, which in the subsequent chapters of this thesis, are going to be quantified in terms of the flow harmonics (v_n).

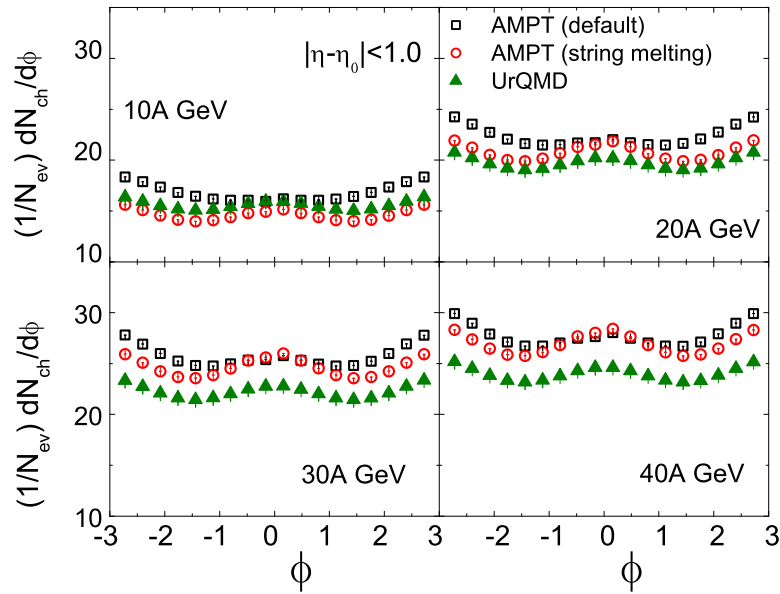


Figure 2.3: Azimuthal angle distribution of charged hadrons at midrapidity in Au+Au collisions at $E_{\text{lab}} = (10 - 40)A$ GeV.

2.2.1 Pseudorapidity distribution: Longitudinal scaling

The pseudorapidity (see Appendix A) distributions of produced charged hadrons are presented in Figure 2.4. The distributions appear to be symmetric about the respective

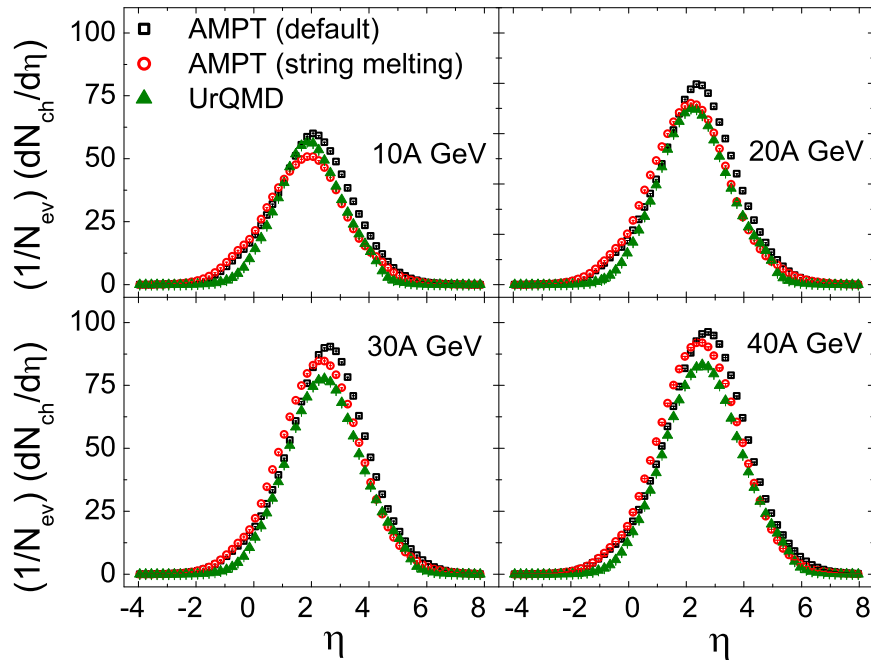


Figure 2.4: Pseudorapidity distribution of charged hadrons in Au+Au collisions at $E_{\text{lab}} = (10 - 40)A$ GeV.

Table 2.2: Centroid of the pseudorapidity distribution (η_0) in Au+Au collisions corresponding to different energies (in GeV) as obtained from the AMPT (default), AMPT(string melting) and UrQMD model.

E_{lab}	AMPT (def)	AMPT (SM)	UrQMD
10A	2.009	1.878	1.982
20A	2.306	2.098	2.283
30A	2.488	2.274	2.462
40A	2.613	2.405	2.592

centroid (η_0) of the distribution, and look very much like single Gaussian functions. For a direct comparison among different models at different energies we have listed the centroid values in Table 2.2. The importance of η -distribution lies in understanding the dynamics of longitudinal expansion of the system created in a high-energy AB interaction. The degree of stopping [26], which is an important aspect of AB collision, particularly at the FAIR and low SPS energy scales, can be estimated from such a distribution. Besides, an idea about the speed of sound and information on the (re)scattering developed in the system, can be extracted from the width of the aforesaid distributions [27]. It should be noted that the

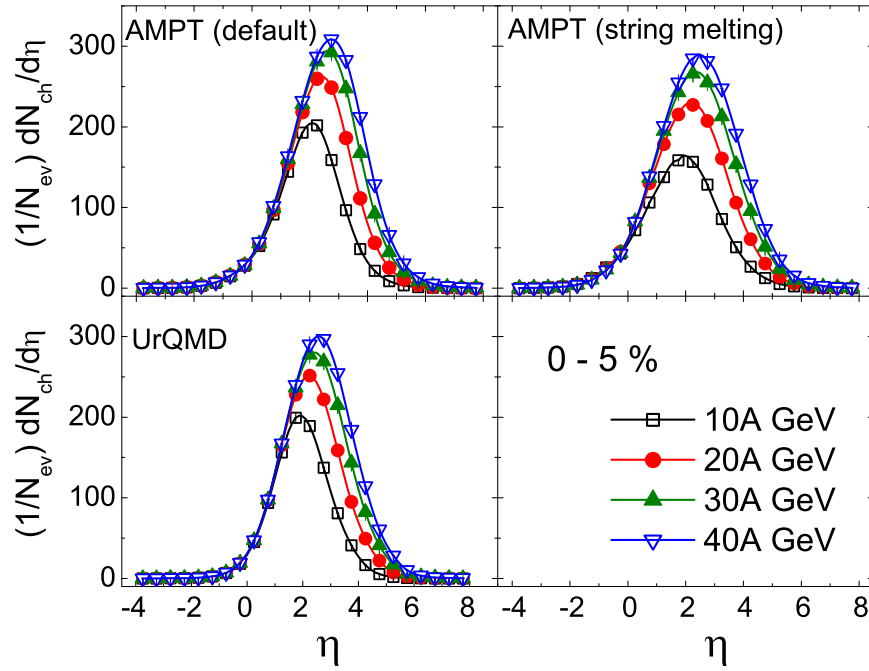


Figure 2.5: Variation of $dN_{ch}/d\eta$ with η for 0 – 5% central Au+Au collisions at $E_{lab} = (10 - 40)A$ GeV.

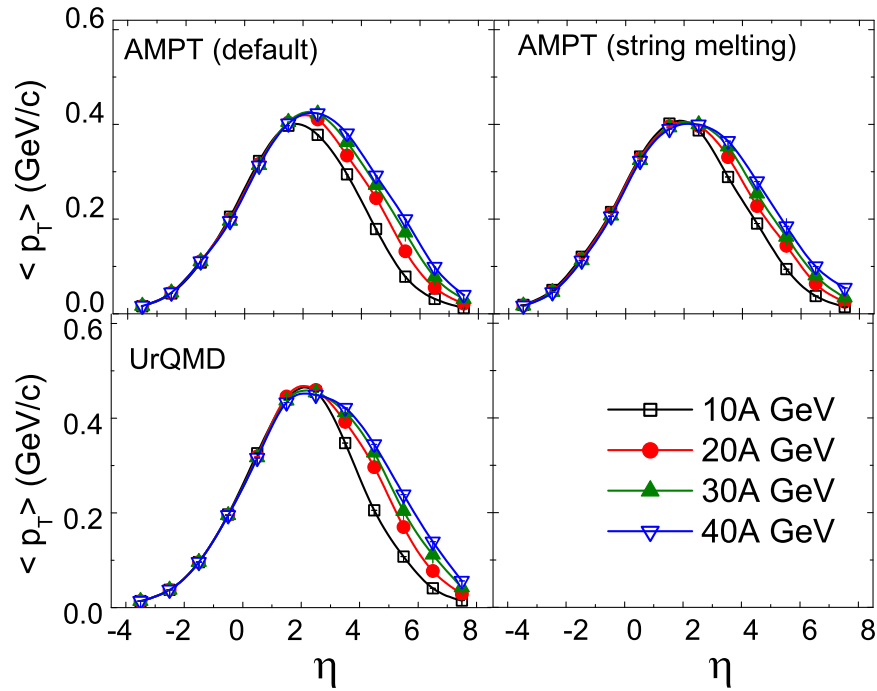


Figure 2.6: Variation of $\langle p_T \rangle$ of charged hadrons with η in Au+Au collisions at $E_{lab} = (10 - 40)A$ GeV.

central pseudorapidity density of charged hadrons ($N_{ev}^{-1}dN_{ch}/d\eta$) at $\eta = \eta_0$ consistently remains highest in the AMPT (default) model, while the central density values generated by the AMPT (string melting) exceed those of the UrQMD at $E_{lab} = 20A$ GeV and beyond. The Gaussian nature of the pseudorapidity distribution indicate a strong stopping during the collision, and it is generally explained in the framework of the Landau Hydrodynamics model [28]. In this context it should be pointed out that although the Landau model is able to describe the data over a wide range from AGS, SPS to RHIC, but it fails in the LHC region where a double Gaussian function turns out to be more appropriate [29]. In Table 2.1 we have also shown the central η -density values of charged hadrons at different centralities of Au+Au collisions at all four incident beam energies considered. As E_{lab} changes from $10A$ to $40A$ GeV, we observe that the maximum central density obtained for the (0 – 5)% centrality class increases significantly by (50 – 85)%. Neither N_{part} nor N_{coll} depends much on E_{lab} . The observation therefore shows the influence of collision energy on hadron production. In Figure 2.5 we have again plotted the η -distribution, but this time only for the most (0 – 5%) central events, and in each panel we have plotted the particle densities obtained at all energies corresponding to a particular model. Both the peak value and width of the distribution are positively correlated with energy. A longitudinal scaling is noted at extreme rapidities in all the models. It would be worthy to mention that all our computations in this investigation are by default restricted to the laboratory frame. Therefore, the usual practice of subtracting η_{beam} from η would not be necessary to observe such scaling. The scaling property is generally explained in terms of the limiting fragmentation hypothesis [30–32]. Before collisions, in the rest frame of one of the nuclei (target/projectile) the other appears to be heavily Lorentz contracted. The contraction escalates with energy but does not affect the momentum transfer process between the colliding ions. This results in an energy independent limiting distribution of the charged hadrons in the fragmentation region of one of the nuclei with respect to which the other is considered as an incoming object. Another probable reason behind such scaling is the entropy conservation, which makes $dN_{ch}/d\eta$ insensitive to certain aspects of the collision dynamics. To further justify the argument of momentum transfer we have studied the η -dependence of the average transverse momentum $\langle p_T \rangle$, a degree of freedom which is excited only after the collision takes place. The results are presented in Figure 2.6 and an almost perfect longitudinal scaling similar to that of Figure 2.5 is observed in the target fragmentation region.

2.2.2 Integrated yield

Figure 2.7 shows the particle density dN_{ch}/dy at midrapidity normalized by the number of participant pairs of nucleons ($N_{part}/2$), plotted as a function of N_{part} for the charged hadrons produced in Au+Au collisions at all four incident energies. The normalized particle yields

obtained from all three models differ among themselves which may be attributed to the different particle production mechanisms associated. For peripheral collisions the difference is maximum between the UrQMD and AMPT simulated results (except at $10A$ GeV), albeit the gross nature of both the default and SM modes of AMPT are almost consistent with each other. The origin of hadron multiplicity lies in the contribution from both soft and hard processes. While the soft processes scale with N_{part} , the hard processes are directly related to the number of binary collisions (N_{coll}) [23]. A strong energy dependence in the fraction of multiplicity originating from the hard processes has been reported at RHIC energies [23]. However, at FAIR and low SPS region particle production is believed to be dominated by the soft processes. At SPS central particle density was found to scale approximately with N_{part} [33, 34]. Deviation from a linear scaling, although not very significant ($dN_{\text{ch}}/d\eta \sim N_{\text{part}}^{1.08}$), was noted by the WA98 Collaboration [35]. In the framework of the wounded nucleon model [23] we too test the applicability of a power law dependence of the form,

$$\left(\frac{dN_{\text{ch}}}{d\eta}\right)_{\eta_0} = A \times N_{\text{part}}^\alpha \quad (2.12)$$

for our model based simulation results. Apart from a few peripheral classes in the AMPT (default), the power law appears to be a proper choice in all other cases. For a meaningful comparison we have listed the fit parameters in Table 2.3. It should be understood that

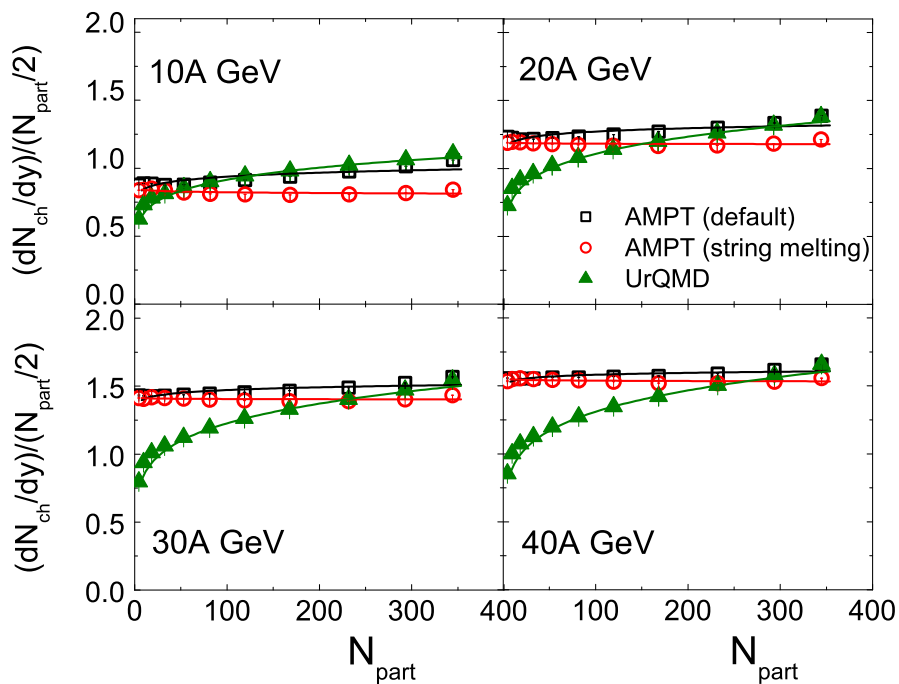


Figure 2.7: Centrality dependence of the integrated yield of charged hadrons per participant pair at midrapidity in Au+Au collisions at $E_{\text{lab}} = (10 - 40)A$ GeV. The solid lines represent the fit following Equation (2.12).

Table 2.3: Fit parameters of Equation (2.12) as obtained at different energies for AMPT (default), AMPT (string melting), and UrQMD model.

E_{lab} (GeV)	AMPT (def)		AMPT (SM)		UrQMD	
	A	α	A	α	A	α
10A	0.763±0.037	1.044±0.010	0.859±0.016	0.990±0.004	0.493±0.010	1.134±0.004
20A	1.120±0.037	1.027±0.007	1.194±0.016	0.997±0.003	0.542±0.013	1.155±0.004
30A	1.342±0.030	1.019±0.004	1.416±0.014	0.998±0.002	0.585±0.015	1.160±0.005
40A	1.492±0.024	1.012±0.003	1.557±0.014	0.997±0.002	0.618±0.017	1.162±0.005

the parameter A represents the average magnitude of the yield, while α would measure the degree of rescattering. From the α values one should note that, while the AMPT results are very close to a linear dependence, the UrQMD results indeed follow a power law type dependence on N_{part} as prescribed in Equation (2.12).

2.2.3 Transverse momentum spectra: Radial flow

In the previous chapter it has been already pointed out that the hadronic abundances are fixed after the chemical freeze-out, yet the elastic hadronic interactions continue until the kinetic freeze-out which also can result changes in the p_T -spectra in the final state. It should be kept in mind that the production of high- p_T hadrons are rare in FAIR energy domain, and owing to statistical reasons even those cases are kept out of the purview of the present analysis. In order to understand the physics of freeze-out and the phenomena following it, we have obtained the p_T -distributions or the invariant yields (see Appendix A) of charged hadrons produced in Au+Au collisions at $E_{\text{lab}} = (10 - 40)A$ GeV, and graphically plotted them in Figure 2.8. In the low p_T -region of each spectrum, we observe an approximately exponential fall in the particle numbers with increasing p_T . At the moderate p_T -region the UrQMD yield is highest and the slope associated with the corresponding exponential fall is lowest at all energies. We however note that perhaps due to the quark coalescence mechanism of hadronization embedded in the AMPT (string melting) model, the p_T -distribution is stiffest in the AMPT generated distributions. The pressure gradient developed within the intermediate fireball after an AB collision is related to the collective kinetic energy of the particles. We would like to emphasize on the radially symmetric expansion of the fireball system. In this regard the transverse kinetic energy $KE_T = m_T - m_0$ turns out to be an appropriate variable that takes care of the relativistic effects, particularly for the lighter mass particles. We consider the most central events to suppress the effect of anisotropic expansion. The m_T spectra corresponding to the (0 - 5)% centrality class at $E_{\text{lab}} = 30A$ GeV for the charged pions, kaons, and protons are graphically shown in Figure 2.9, which appears to be exponential having a thermal origin and is given by,

$$\frac{dN_{\text{ch}}}{m_T dm_T} = A \exp\left(-\frac{m_T}{T_{\text{eff}}}\right) \quad (2.13)$$

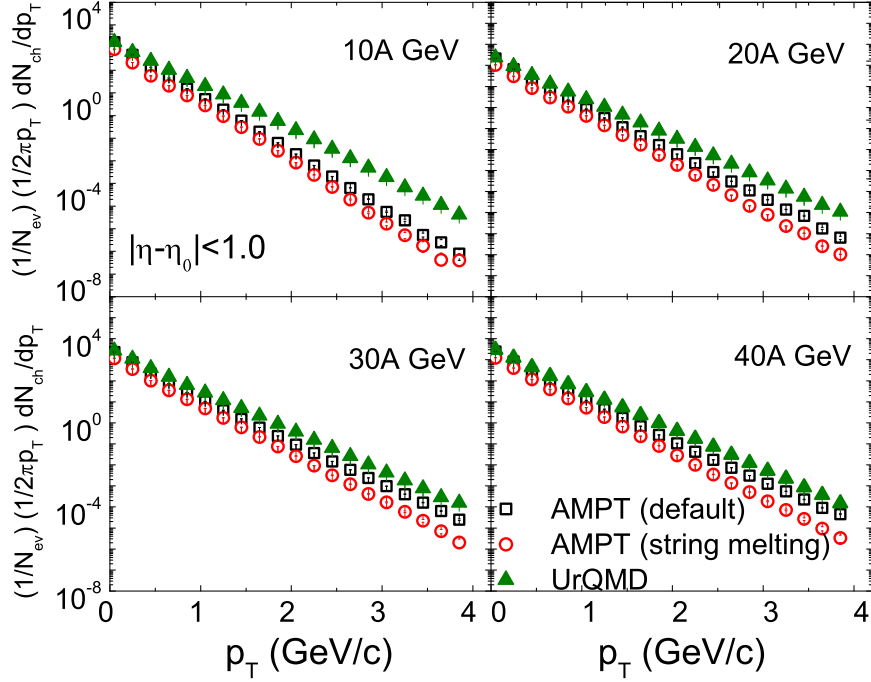


Figure 2.8: Transverse momentum spectra of all charged hadrons at midrapidity in Au+Au collisions at $E_{\text{lab}} = (10 - 40)A$ GeV. For clarity the UrQMD and AMPT (default) results are scaled with appropriate factors.

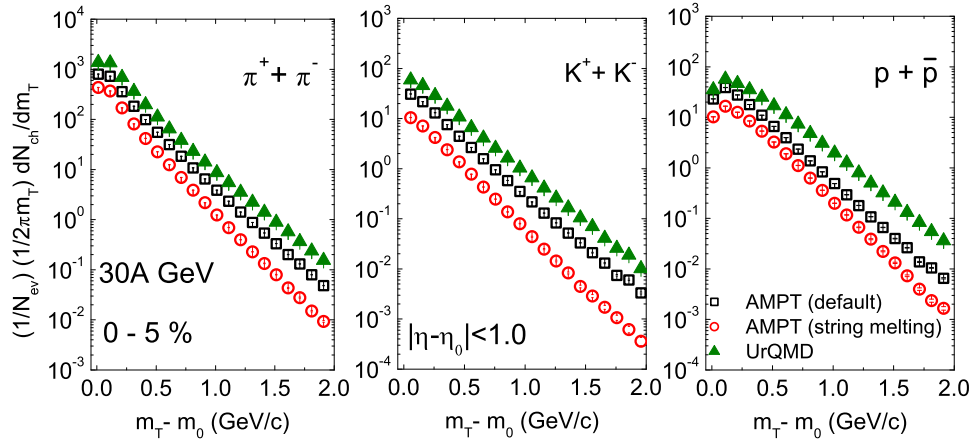


Figure 2.9: Transverse mass spectra for pion, kaon and proton at midrapidity for 0 – 5% central Au+Au collisions at $E_{\text{lab}} = 30A$ GeV. The UrQMD and AMPT (default) results are scaled properly for clarity.

We have indeed performed the same analysis at other energies as well, but have not showed them explicitly in the diagram because the gross features of the spectra at each energy is more or less similar except a slight change in their slope values. A mass dependent flattening in the spectra is noticed in all models, i.e. heavier particles gain more p_T . This simply reflects the build up of collective motion at the early stages of collision. To understand the flattening in a better way, the exponentially decaying region of individual m_T -spectra are

fitted with Equation (2.13) and the corresponding inverse slope (T_{eff}) values are extracted. It is expected that for an expanding system T_{eff} should depend on the kinetic freeze-out temperature (T_{kin}), and on the collective (independent of species) velocity ($\langle\beta_T\rangle$) of the expanding fluid like matter created in the AB collision [36, 37]. This expansion phenomenon is usually called radial flow [38]. T_{eff} is anticipated to have a form [37, 39] like,

$$T_{\text{eff}} = T_{\text{kin}} + m_0 \langle\beta_T\rangle^2 \quad (2.14)$$

In Figure 2.10 we have shown the mass (species) dependence of the inverse slope parameter T_{eff} and the same is fitted by Equation (2.14). The freeze-out temperature corresponding to a particular E_{lab} , as estimated from one of the fit parameters, is found to be model dependent and has a spread of (20 – 30) MeV when compared among different models. The fit parameters namely, the square of radial velocity and kinetic freeze-out temperature extracted at each energy corresponding to different models are listed in Table 2.4. None of the models could describe the NA49 data completely as shown for $E_{\text{lab}} = 40A$ GeV in the bottom-right panel of Figure 2.10. The values of fit parameters for the experimental data are $T_{\text{kin}} = 156 \pm 0.5$ MeV and $\langle\beta_T\rangle^2 = 0.125 \pm 0.0008$ c^2 . It would be significant to recall that T_{eff} is expected to be independent of species when extracted from the m_T spectra of pp collisions, which is expected to be devoid of any radial flow particularly in the energy range considered in this investigation.

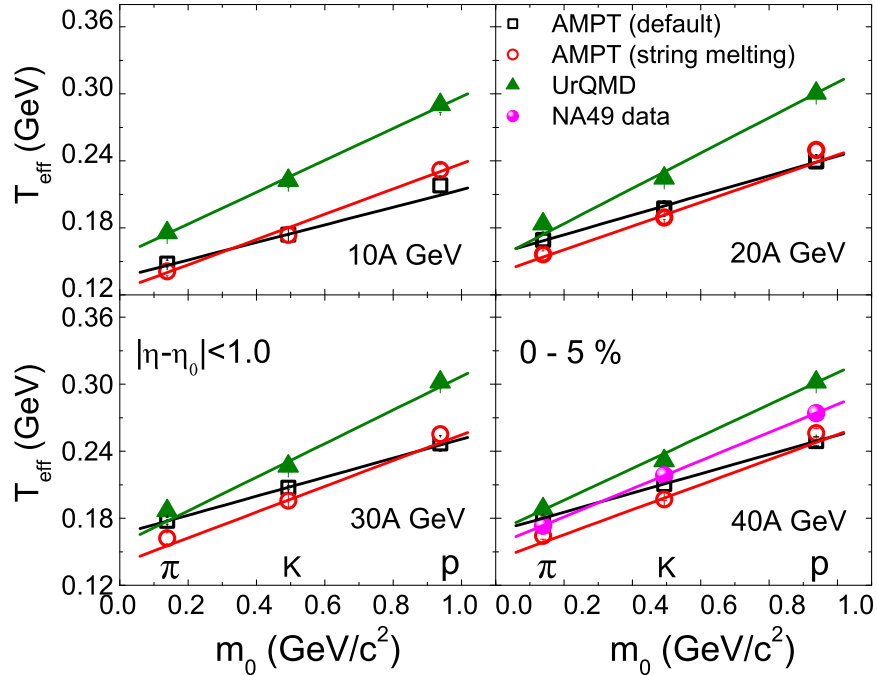


Figure 2.10: Hadronic mass dependence of effective temperature for 0–5% central Au+Au collisions at $E_{\text{lab}} = (10 - 40)A$ GeV. The solid lines are linear fit following Equation (2.14). The NA49 points are taken from [40]

Table 2.4: The values of kinetic freeze-out temperature T_{kin} (in MeV) and square of radial flow velocity $\langle\beta_T\rangle^2$ (in c^2) for the 0 – 5% most central Au+Au events corresponding to different energies for the AMPT (default), AMPT (string melting), and UrQMD models.

E_{lab} (GeV)	AMPT (def)		AMPT (SM)		UrQMD	
	T_{eff}	$\langle\beta_T\rangle^2$	T_{eff}	$\langle\beta_T\rangle^2$	T_{eff}	$\langle\beta_T\rangle^2$
10A	135±4	0.079±0.008	124±5	0.113±0.008	155±5	0.142±0.010
20A	156±6	0.088±0.010	139±4	0.106±0.008	152±6	0.158±0.007
30A	166±4	0.085±0.008	139±5	0.116±0.010	156±7	0.150±0.012
40A	168±2	0.086±0.005	142±3	0.111±0.006	168±3	0.143±0.004

Another manifestation of radial flow is the centrality dependence of average transverse momentum as shown in Figure 2.11. At low centrality $\langle p_T \rangle$ rises with N_{part} which saturates at high centrality region. In other words, the final state particles produced in central collisions experience comparatively higher radial push than those evolved from peripheral collisions. This is naively because of the fact that more energy is deposited within the fireball in central collisions, which in turn gives rise to more pressure. Further it is interesting to note that the saturation $\langle p_T \rangle$ values hardly change with the collision energy involved, which probably is due to the kinematic reasons. The transverse degrees of freedom are excited into the

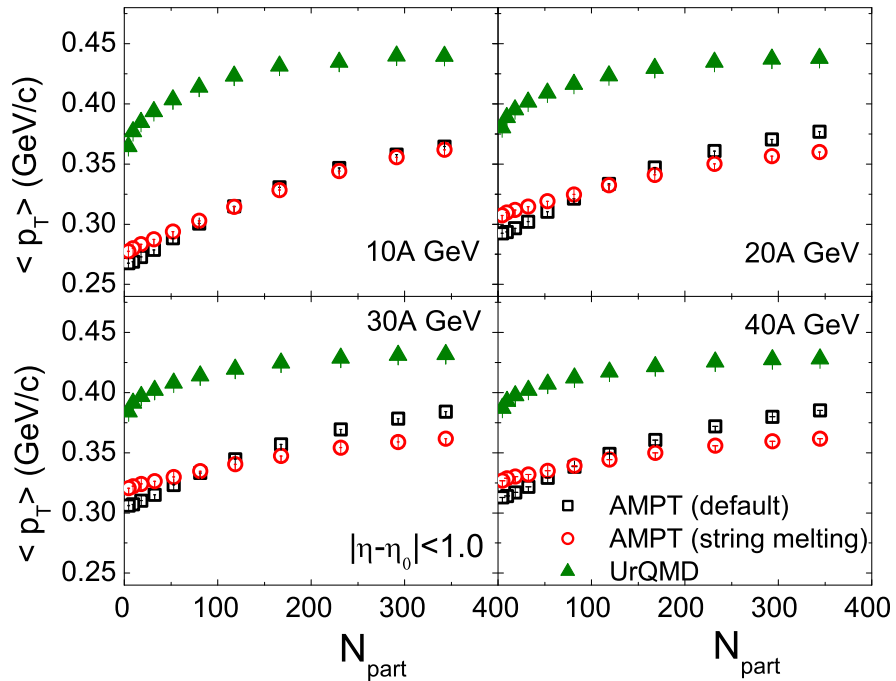


Figure 2.11: Average transverse momentum of charged hadrons at midrapidity plotted against centrality in Au+Au collisions at $E_{\text{lab}} = (10 - 40)A$ GeV.

colliding system due to multiple (re)scattering. Our results indicate that the degree of such excitations, which predominantly should depend on the number of binary collisions N_{coll} ,

appears to remain almost same for the most central Au + Au events in the FAIR energy range. However $\langle p_T \rangle$ is significantly different for the models used, highest in the UrQMD and lowest in the AMPT (string melting), except at 10A GeV where $\langle p_T \rangle$ from both AMPT (default) and AMPT (string melting) almost coincide with each other. It should be noted that the UrQMD, in spite of having the highest particle density in the most central collisions, is giving rise also to the highest $\langle p_T \rangle$ value, whereas the AMPT (string melting) has the lowest particle density as well as the lowest $\langle p_T \rangle$. The particle density in AMPT (default) is similar to that in UrQMD in magnitude, the $\langle p_T \rangle$ value on the other hand is closer to the AMPT (string melting). It looks like that in comparison with the UrQMD, not enough transversality is excited in the AMPT models. In the STAR beam energy scan program it has been reported that the difference between the central $\langle p_T \rangle$ values of protons is greater at higher beam energies in comparison with pions or kaons [41]. This actually indicates that radial flow increases with increase in energy. A strong radial flow at LHC [42] is attributed to the high energy density that gives rise to a strong pressure gradient.

2.3 Conclusion

We have investigated a few global aspects of multiparticle production at FAIR energies using our event generators. Longitudinal scaling at the FAIR energies is observed not only in the η -distributions of charged hadrons, but also when the average transverse momentum is studied as function of η . Integrated yield from UrQMD generated events tend to follow a power law type behaviour when plotted against N_{part} , while that from the AMPT linearly depends on N_{part} . The UrQMD results in this regard is consistent with the wounded nucleon model. A mass dependent flattening of the p_T -spectra confirms the presence of collectivity in the medium produced in an AB collision. Our results also provide some obvious indication of radial flow which is further investigated in one of the chapters of this thesis. We believe that these results, though a bit preliminary in nature, but would set an appropriate reference baseline before going into a comprehensive discussion on flow characteristics in the upcoming chapters.

Bibliography

- [1] S. A. Bass *et al.*, Prog. Nucl. Part. Phys. **41**, 255 (1998).
- [2] M. Bleicher *et al.*, J. Phys. G **25**, 1859 (1999).
- [3] H. Feldmeier, Nucl. Phys. A **515**, 147 (1990).

-
- [4] L. Willetes *et al.*, Nucl. Phys. A **282**, 341 (1977).
- [5] T. H. R. Skyrme, Nucl. Phys. **9**, 615 (1959).
- [6] M. Berenguer, Thesis, Goethe Universität, Frankfurt am Main, Germany (1993).
- [7] F. E. Close, Introduction to Quarks and Partons, Academic Press, London (1979).
- [8] R. M. Barnett, Phys. Rev. D **54**, 1 (1996).
- [9] B. Zhang, C. M. Ko, B.-A. Li, and Z.-W. Lin, Phys. Rev. C **61**, 067901 (2000).
- [10] Z.-W. Lin, C. M. Ko, B.-A. Li, B. Zhang, and S. Pal, Phys. Rev. C **72**, 064901 (2005).
- [11] X. N. Wang and M. Gyulassy, Phys. Rev. D **44**, 3501 (1991).
- [12] B. Zhang, Comput. Phys. Commun. **109**, 193 (1998).
- [13] B. A. Li and C. M. Ko, Phys. Rev. C **52**, 2037 (1995).
- [14] B. Anderson, G. Gustafson, and B. Soderberg, Z. Phys. C **20**, 317 (1983).
- [15] T. S. Biro, P. Levai, and J. Zimanyi, Phys. Lett. B **347**, 6 (1995).
- [16] B. Zhang, L.-W. Chen, and C. M. Ko, Nucl. Phys. A **774**, 665 (2006); L.-W. Chen and C. M. Ko, Phys. Lett. B **634**, 205 (2006); J. Xu and C. M. Ko, Phys. Rev. C **83**, 034904 (2011).
- [17] P. P. Bhaduri and S. Chattopadhyay, Phys. Rev. C **81**, 034906 (2010); M. Nasim, L. Kumar, P. K. Netrakanti, and B. Mohanty, Phys. Rev. C **82**, 054908 (2010).
- [18] M. L. Miller *et al.*, Annu. Rev. Nucl. Part. Sci. **57**, 205 (2007).
- [19] P. Shukla, arXiv:nucl-th/0112039v1.
- [20] T. W. Ludlam, A. Pfoh, and A. Shor, Brookhaven National Laboratory Report – BNL-37196 (Feb. 1986).
- [21] A. Shor and R. S. Longacre, Phys. Lett. B **218**, 100 (1989).
- [22] H. De Vries, C. W. De Jager, and C. De Vries, Atomic Data and Nuclear Data Tables **36**, 495 (1987).
- [23] D. Kharzeev and M. Nardi, Phys. Lett. B **507**, 121 (2001).
- [24] X.-N. Wang and M. Gyulassy, Phys. Rev. Lett. **86**, 3496 (2001).
- [25] B. B. Back *et al.* (PHOBOS Collaboration), Nucl. Phys. A **757**, 28 (2005).

-
- [26] W. Busza and A. S. Goldhaber, Phys. Lett. B **139**, 235 (1984).
- [27] P. K. Netrakanti and B. Mohanty, Phys. Rev. C **71**, 047901 (2005).
- [28] L. D. Landau, Izvestiya Akademii Nauk SSR, Seriya Fizicheskaya **17**, 51 (1953).
- [29] R. Sahoo *et al.*, Adv. High Energy Phys. **2015**, 612390 (2015).
- [30] J. Benecke, T. T. Chou, C. N. Yang, and E. Yen, Phys. Rev. **188**, 2159 (1969).
- [31] R. P. Feynman, Phys. Rev. Lett. **23**, 1415 (1969).
- [32] R. Hagedorn, Nucl. Phys. B **24**, 93 (1970).
- [33] P. D. Jones *et al.* (NA49 Collaboration), Nucl. Phys. A **610**, 189 (1996).
- [34] R. Albrecht *et al.* (WA80 Collaboration), Phys. Rev. C **44**, 2736 (1998).
- [35] M. M. Aggarwal *et al.* (WA98 Collaboration), Eur. Phys. J. C **18**, 651 (2001).
- [36] R. S. Bhalerao, Quark-Gluon Plasma and Hadron Physics, Narosa Publications, India (2009).
- [37] M. Kliemant, R. Sahoo, T. Schuster, and R. Stock, Lect. Notes Phys. **785**, 23 (2010).
- [38] E. Schnedermann, J. Sollfrank, and U. Heinz, Phys. Rev. C **48**, 2462 (1993).
- [39] R. Sahoo, Lecture Notes in SERC School on Experimental High Energy Physics (2013), arxiv:1604.02651 [nucl-ex].
- [40] B. Mohanty, Pramana **82**, 893 (2014).
- [41] L. Adamczyk *et al.* (STAR Collaboration), Phys. Rev. C **96**, 044904 (2017).
- [42] B. Abelev *et al.* (ALICE Collaboration), Phys. Rev. Lett **109**, 252301 (2012).

Chapter 3

Elliptic and triangular flow parameters at expected FAIR energies

It is widely accepted that studies on anisotropic azimuthal distributions of the final state particles can be used to explore the collective fluid like behaviour of hadronic matter produced under extreme thermodynamic conditions in high-energy heavy-ion collisions [1–5]. More precisely, the second harmonic coefficient of the Fourier decomposition of the azimuthal distribution of particles, also known as the elliptic flow parameter (v_2), is of special interest [6, 7]. The v_2 parameter allows us to critically examine the evolution of the early stages of a high-energy collision between two nuclei [8]. Large v_2 values obtained in nucleus-nucleus (AB) collision experiments using facilities like the Relativistic Heavy Ion Collider (RHIC) [3, 4, 9] and Large Hadron Collider (LHC) [5, 10, 11], lead us to conclude that strong anisotropies are present in the azimuthal distributions of particle multiplicities and the strongly interacting partonic/hadronic matter produced in collisions between two heavy nuclei exhibits collective effects observed only in fluid like states. The dynamics of such a state of matter can be explained by hydrodynamic calculations [12, 13] as well as by transport models. However, depending upon the collision energy involved, such models may require some fine tuning [14]. In this chapter, in the framework of the UrQMD and AMPT models, we are going to investigate some basic aspects of the flow parameters, such as their dependence on collision centrality, transverse momentum, and pseudorapidity in Au+Au collisions at some typical incident beam energies like $E_{\text{lab}} = 10A, 20A, 30A$ and $40A$ GeV that are expected at the Facility for Anti-proton and Ion Research (FAIR).

3.1 Methodology

As already discussed, anisotropic flow is quantified in terms of the Fourier coefficients of the azimuthal distribution of the produced particles given by a relation like [7, 15],

$$\frac{dN}{d\phi'} = \frac{a_0}{2} + \sum_{n=1}^{\infty} a_n \cos(n\phi') + \sum_{n=1}^{\infty} b_n \sin(n\phi') \quad (3.1)$$

where $\phi' = \phi - \Psi_{RP}$ is the azimuthal angle of the particle measured with respect to the reaction plane angle Ψ_{RP} . The reaction plane is spanned by the impact parameter vector and the incident beam direction. The Fourier coefficients are computed as following,

$$a_0 = \frac{1}{\pi} \int_{-\pi}^{\pi} \frac{dN}{d\phi'} d\phi' = \frac{N}{\pi}; \quad a_n = \frac{1}{\pi} \int_{-\pi}^{\pi} \frac{dN}{d\phi'} \cos(n\phi') d\phi'$$

We also note that

$$\langle \cos n\phi' \rangle = \frac{\int_{-\pi}^{\pi} \frac{dN}{d\phi'} \cos(n\phi') d\phi'}{\int_{-\pi}^{\pi} \frac{dN}{d\phi'} d\phi'} = \frac{a_n}{a_0}$$

Therefore, in symmetric *AA* collisions

$$a_n = a_0 \langle \cos n\phi' \rangle \quad \text{and} \quad b_n = \frac{1}{\pi} \int_{-\pi}^{\pi} \frac{dN}{d\phi'} \sin(n\phi') d\phi' = 0$$

Using these Fourier coefficients in Equation (3.1),

$$\begin{aligned} \frac{dN}{d\phi'} &= \frac{a_0}{2} + \sum_{n=1}^{\infty} a_0 \langle \cos n\phi' \rangle \cos(n\phi') + 0 \\ &= \frac{a_0}{2} \left[1 + 2 \sum_{n=1}^{\infty} \langle \cos n\phi' \rangle \cos(n\phi') \right] \\ &= \frac{N}{2\pi} \left[1 + 2 \sum_{n=1}^{\infty} v_n \cos(n\phi') \right] \end{aligned} \quad (3.2)$$

where

$$\begin{aligned} v_n &= \langle \cos n\phi' \rangle \\ &= \langle \cos [n(\phi - \Psi_{RP})] \rangle \end{aligned} \quad (3.3)$$

is quantified as the n -th order anisotropic flow coefficient. A non-central heavy ion collision on the transverse plane is schematically presented in the left panel of Figure 3.1. In transport models the impact parameter is usually taken along the x -direction and the beam axis is taken along the z -direction. The reaction plane is then nothing but the $x - z$ plane, and the reaction plane angle Ψ_{RP} becomes zero. Consequently, the n -th harmonic (v_n) of the

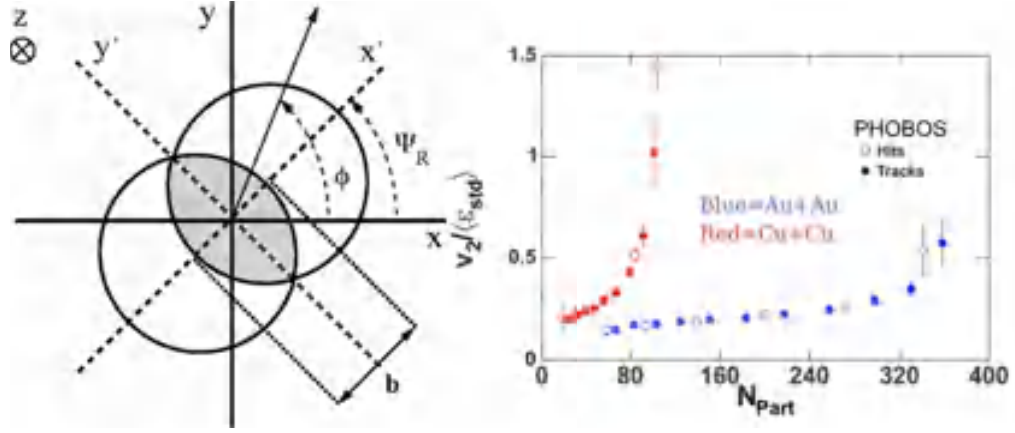


Figure 3.1: Left: Schematic of a non-central heavy-ion collision in the transverse plane [16]. Right: v_2 scaled by ϵ_{std} as a function of N_{part} [4].

underlying distribution reduces to,

$$v_n = \langle \cos n\phi \rangle \quad (3.4)$$

The anisotropy of the overlapping region of the colliding nuclei is called the standard or reaction plane eccentricity and is quantified as [17],

$$\epsilon_{\text{std}} = \frac{\sigma_x^2 - \sigma_y^2}{\sigma_x^2 + \sigma_y^2} \quad (3.5)$$

where σ_x^2 and σ_y^2 are respectively the variances of the nucleon distributions along the x and y -directions in the transverse plane of a particular event. Equation (3.5) defines the nuclear eccentricity, which is restricted only to $n = 2$, and is intrinsically biased with an asymmetry definition that drives the flow signal. In small systems and in peripheral collisions, due to large relative fluctuations in the numbers and position coordinates of the participating nucleons, the minor axis of the overlapping region may not always coincide with the impact parameter. On the other hand, in a central collision between two large nuclei the nuclear geometry and the participant geometry almost coincide with each other. ϵ_{std} was being used to measure the initial asymmetry, until in the year 2005 when the first discrepancy in this regard was reported by the PHOBOS collaboration [4]. Since elliptic flow is a consequence of the initial pressure gradient, it is expected that the elliptic flow coefficient should be small for the most central collisions and also for the smaller sized systems. The elliptic flow parameter was scaled by the corresponding eccentricity and the centrality dependence of the ratio ($v_2/\epsilon_{\text{std}}$) was studied. As shown in Figure 3.1 (right) a significantly large amount of elliptic flow, after it is scaled by the eccentricity, was observed in a comparatively smaller sized system (Cu+Cu) than that in a larger (Au+Au) system. It was predicted that the issue could possibly be addressed after considering the event-by-event (e-by-e) fluctuations in the positions of the participating nucleons, something anticipated to be more pronounced

in the smaller systems. To take care of these e-by-e fluctuations, the PHOBOS collaboration introduced the idea of $\varepsilon_{\text{part}}$ as,

$$\varepsilon_{\text{part}} = \frac{\sqrt{(\sigma_x^2 - \sigma_y^2)^2 + 4\sigma_{xy}^2}}{\sigma_x^2 + \sigma_y^2} \quad (3.6)$$

henceforth to be represented by ε_2 or $\varepsilon_2^{\text{part}}$ in most cases. Here σ_{xy} is the covariance of the distribution of the nucleons. In the centre-of-mass system of the participating nucleons Equation (3.6) takes up the following form,

$$\varepsilon_{\text{part}} = \frac{\sqrt{\langle r^2 \cos 2\varphi \rangle^2 + \langle r^2 \sin 2\varphi \rangle^2}}{\langle r^2 \rangle} \quad (3.7)$$

where (r, φ) denotes the position coordinates of participating nucleons in a plane polar system. In this framework, as illustrated in the left panel of Figure 3.2, the minor axis of

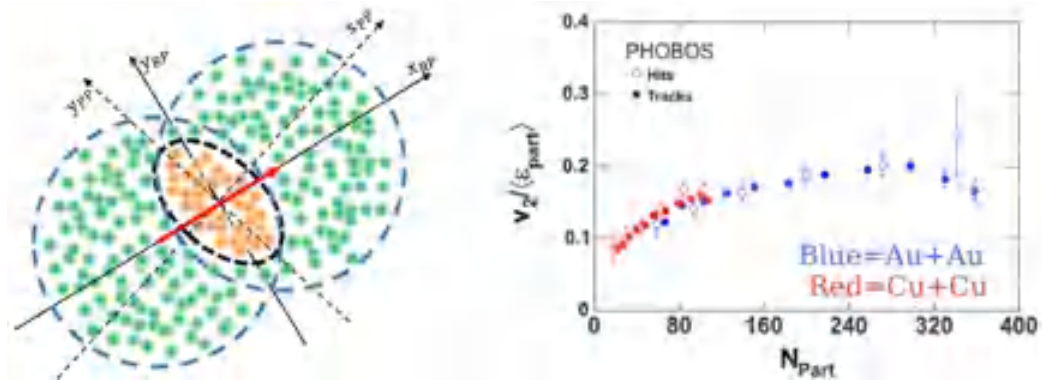


Figure 3.2: Left: Schematic of a heavy-ion collision illustrating the reaction plane and participant plane. Right: v_2 scaled by $\varepsilon_{\text{part}}$ as a function of N_{part} [4].

the ellipsoid does not necessarily point along the reaction plane vector, but in general is inclined to it at an angle ψ_2 given by,

$$\psi_2 = \frac{1}{2} \left[\arctan \frac{\langle r^2 \sin 2\varphi \rangle}{\langle r^2 \cos 2\varphi \rangle} + \pi \right] \quad (3.8)$$

The elliptic flow parameter should therefore be computed with respect to the participant plane angle ψ_2 as,

$$v_2 = \langle \cos 2[(\phi - \psi_2)] \rangle \quad (3.9)$$

rather than by using the traditional reaction plane angle. The success of this model is revealed in the right panel of Figure 3.2, where the eccentricity scaled elliptic flow for both Au+Au and Cu+Cu systems appears to agree well with each other. The consequences of initial state fluctuations in heavy-ion collisions are not only restricted to the above mentioned

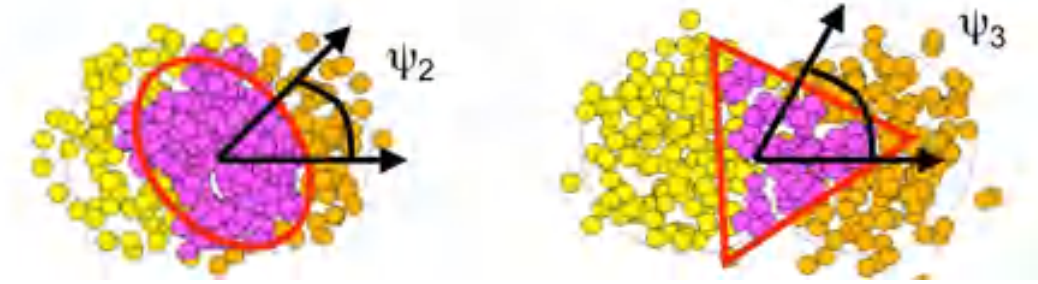


Figure 3.3: Exemplar of elliptic and triangular anisotropies generated after a collision between two nuclei. The pink circles represent the participating nucleons. The figure is taken from [18]

modification in the definition of eccentricity and introduction of the concept of participant plane. It was further suggested that these fluctuations could give rise to a triangular anisotropy in the initial state which will also be reflected in the final state particle distributions. For a better clarity of the issue, the elliptic and triangular anisotropies are simultaneously presented in Figure 3.3. In an analogy to the eccentricity, the triangularity (ε_3) is quantified as,

$$\varepsilon_3 = \frac{\sqrt{\langle r^2 \cos 3\varphi \rangle^2 + \langle r^2 \sin 3\varphi \rangle^2}}{\langle r^2 \rangle} \quad (3.10)$$

This triangularity will result in a triangular flow among the final state particles, given by

$$v_3 = \langle \cos 3[(\phi - \psi_3)] \rangle \quad (3.11)$$

where ψ_3 as shown in Figure 3.3 can be expressed as,

$$\psi_3 = \frac{1}{2} \left[\arctan \frac{\langle r^2 \sin 3\varphi \rangle}{\langle r^2 \cos 3\varphi \rangle} + \pi \right] \quad (3.12)$$

The methodology can be extended to compute higher order harmonics which is however kept beyond the purview of the present analysis.

In a real experiment neither the reaction plane nor the participant plane can be directly accessed. In order to estimate the flow coefficients, in a way that is independent of either the reaction plane or the participant plane angle, multiparticle correlation or the cumulant method [19] has therefore been widely used in the SPS [20], RHIC and LHC experiments. Moreover, higher order cumulants can also reduce the e-by-e flow fluctuations. Recently, a Q -cumulant method [16, 21] has been introduced for flow analysis, which is used to calculate the particle cumulants directly in a single pass over the data, thus significantly reducing the

computation power. The azimuthal correlation is expressed in terms of the Q -vector as,

$$Q_n = \sum_{j=1}^M e^{in\phi_j} \quad (3.13)$$

where M is the multiplicity of the selected set of particles in an event, and ϕ_j denotes their azimuthal angle. The average two-particle azimuthal correlation over all particles in the event is then calculated as,

$$\langle 2 \rangle = \frac{|Q_n|^2 - M}{M(M-1)} \quad (3.14)$$

The two-particle cumulant $c_n\{2\}$ and the anisotropic flow-parameter $v_n\{2\}$ can be obtained after averaging over all particles in all events as,

$$c_n\{2\} = \langle \langle 2 \rangle \rangle, \quad v_n\{2\} = \sqrt{c_n\{2\}} \quad (3.15)$$

However, $v_n\{2\}$ obtained in this way is susceptible to non-flow effects like resonance decays, jet fragmentation, Bose-Einstein correlation etc., which contribute to additional correlation not related to the reaction plane. These non-flow effects, in general short ranged in nature, can be suppressed by introducing a pseudorapidity gap between the particles used to construct the Q -cumulant [22]. An event is divided into two sub-events, say A and B , separated by a gap say $\Delta\eta$ (in our study $|\Delta\eta| > 1.0$). The two-particle correlation is then modified as,

$$\langle 2 \rangle_{\Delta\eta} = \frac{Q_n^A Q_n^{B*}}{M_A M_B} \quad (3.16)$$

where Q_n^A and Q_n^B are the flow vectors of the sub-events A and B respectively, M_A and M_B being the corresponding multiplicities. Finally we get $c_n\{2\}$ and $v_n\{2\}$ as,

$$c_n\{2\}_{\Delta\eta} = \langle \langle 2 \rangle \rangle_{\Delta\eta}, \quad v_n\{2\} = \sqrt{c_n\{2\}_{\Delta\eta}} \quad (3.17)$$

Non-flow effects can also be suppressed by exploiting the multiparticle cumulants, which in the 4-th order can be expressed as,

$$\begin{aligned} \langle 4 \rangle &= \left[|Q_n|^4 + |Q_{2n}|^2 - 2 \operatorname{Re}(Q_{2n} Q_n^* Q_n^*) \right. \\ &\quad \left. - 2 \{ 2(M-2) \cdot |Q_n|^2 - M(M-3) \} \right] / \\ &\quad \left[M(M-1)(M-2)(M-3) \right] \\ c_n\{4\} &= \langle \langle 4 \rangle \rangle - 2 \langle \langle 2 \rangle \rangle^2 \\ v_n\{4\} &= \sqrt[4]{-c_n\{4\}} \end{aligned} \quad (3.18)$$

The integral flow coefficients obtained from the Q -cumulant approach are often called reference flow, and the particles employed to find them out are labeled as reference particles (REPs). Once the reference flow coefficients are determined, we may proceed to estimate the differential flow, e.g. as a function of p_T of the particles of interest (POI). Similar to the Q -vector, for POI a p_n -vector is introduced as,

$$p_n = \sum_{j=1}^{m_p} e^{in\psi_j} \quad (3.19)$$

and for particles taken as both POI and REP we have,

$$q_n = \sum_{j=1}^{m_q} e^{in\psi_j} \quad (3.20)$$

where m_p and m_q are the number of selected particles in respective group. The single event average of two- and four-particle differential correlations can now be expressed as,

$$\begin{aligned} \langle 2' \rangle &= \frac{p_n Q_n^* - m_q}{m_p M - m_q}, \\ \langle 4' \rangle &= \frac{[p_n Q_n Q_n^* Q_n^* - q_{2n} Q_n^* Q_n^* - p_n Q_n Q_{2n}^* - 2M p_n Q_n^* \\ &\quad - 2m_q |Q_n|^2 + 7q_n Q_n^* - Q_n q_n^* + q_{2n} Q_{2n}^* + 2p_n Q_n^* \\ &\quad + 2m_q M - 6m_q]}{[(m_p M - 3m_q)(M - 1)(M - 2)]} \end{aligned} \quad (3.21)$$

We next quantify the 2nd and 4th-order differential cumulants as,

$$\begin{aligned} d_n\{2\} &= \langle \langle 2' \rangle \rangle \\ d_n\{4\} &= \langle \langle 4' \rangle \rangle - 2\langle \langle 2' \rangle \rangle \langle \langle 2' \rangle \rangle \end{aligned} \quad (3.22)$$

Finally, the differential flow coefficients are estimated by,

$$\begin{aligned} v_n'\{2\} &= \frac{d_n\{2\}}{\sqrt{c_n\{2\}}} \\ v_n'\{4\} &= -\frac{d_n\{4\}}{[-c_n\{4\}]^{3/4}} \end{aligned} \quad (3.23)$$

Similar to the flow parameters, cumulants of n -th order participant plane eccentricity (ε_n) may also be defined as [23],

$$\begin{aligned} c_{\varepsilon_n}\{2\} &= \langle \varepsilon_n^2\{P\} \rangle, \\ c_{\varepsilon_n}\{4\} &= \langle \varepsilon_n^4\{P\} \rangle - 2\langle \varepsilon_n^2\{P\} \rangle^2 \end{aligned} \quad (3.24)$$

where depending upon the order of the harmonic under investigation, $\varepsilon_n\{P\}$ represents the

participant plane eccentricity estimated by using either Equation (3.7) or Equation (3.10), and $\langle \rangle$ denotes an event average. The corresponding eccentricities are given by,

$$\begin{aligned}\varepsilon_n\{2\} &= \sqrt{c_{\varepsilon_n}\{2\}} \\ \varepsilon_n\{4\} &= \sqrt[4]{-c_{\varepsilon_n}\{4\}}\end{aligned}\quad (3.25)$$

Once we know how to determine the cumulant flow coefficients and eccentricities, we move on to find out the fluctuations in these quantities. The flow fluctuations in terms of the cumulants are given by [24],

$$\begin{aligned}v_n\{2\}^2 &\approx \langle v_n \rangle^2 + \sigma_{v_n}^2 \quad (\text{Neglecting nonflow}) \\ v_n\{4\}^2 &\approx \langle v_n \rangle^2 - \sigma_{v_n}^2 \quad (\text{Assuming } \sigma_{v_n} \ll \langle v_n \rangle)\end{aligned}\quad (3.26)$$

where $\langle v_n \rangle$ and σ_{v_n} are respectively, the mean and standard deviation of the v_n -distribution. From Equation (3.26) the flow fluctuation can be expressed in the form,

$$\sigma_{v_n} = \sqrt{\frac{v_n\{2\}^2 - v_n\{4\}^2}{2}}\quad (3.27)$$

and $\langle v_n \rangle$ can also be estimated from Equation (3.26) as,

$$\langle v_n \rangle\{\text{est}\} = \sqrt{\frac{v_n\{2\}^2 + v_n\{4\}^2}{2}}\quad (3.28)$$

Following the same technique [23] analogous quantities related to the eccentricity are obtained,

$$\begin{aligned}\sigma_{\varepsilon_n} &= \sqrt{\frac{\varepsilon_n\{2\}^2 - \varepsilon_n\{4\}^2}{2}} \\ \langle \varepsilon_n \rangle\{\text{est}\} &= \sqrt{\frac{\varepsilon_n\{2\}^2 + \varepsilon_n\{4\}^2}{2}}\end{aligned}\quad (3.29)$$

3.2 Results and discussion

We first examine the centrality dependence of the eccentricity and triangularity parameters associated with the overlap region of the colliding nuclei. The model parameters, collision parameters, and the number of events generated, all remain same as that used in the Chapter 2. The MCG simulated results on the asymmetry parameters obtained for the Au+Au collision at $E_{\text{lab}} = 30A$ GeV are presented in Figure 3.4. For some selected centrality classes the number of participating nucleons (N_{part}), the number of binary nucleon-nucleon collisions (N_{coll}), the transverse overlap area ($S = \pi \sqrt{\sigma_x^2 \sigma_y^2 - \sigma_{xy}^2}$) of the colliding system, and

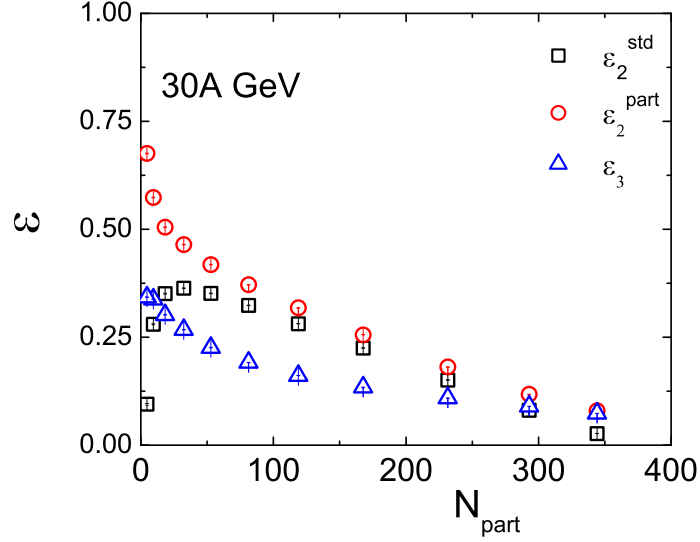


Figure 3.4: Centrality dependence of ε_n of the overlapping region for Au+Au collision at $E_{\text{lab}} = 30A$ GeV.

various measures of geometric anisotropy like $\varepsilon_2^{\text{std}}$, $\varepsilon_2^{\text{part}}$ and ε_3 are listed in Table 3.1. The numerical values as well as the figure show that in the Au+Au system participant eccentricity always exceeds the standard geometrical (nuclear) eccentricity. We see that the participant eccentricity is quite high valued ($\varepsilon_{\text{part}} \approx 60 - 70\%$) in the most peripheral collisions. As expected, with increasing centrality $\varepsilon_{\text{part}}$ monotonically drops down to rather small values, even below 10% for the most central collisions. The N_{part} dependence of the eccentricity parameter can be attributed to geometrical reasons. Peripheral (central) collisions involve smaller N_{part} . Correspondingly in a single event the periodic functions of Equation (3.7) are averaged over a small number of terms. As a result every event contributes significantly to $\varepsilon_{\text{part}}$. With increasing centrality N_{part} increases, and for every event the periodic functions are averaged over an increasing number of terms. Accordingly the contribution to $\varepsilon_{\text{part}}$ per event becomes decreasingly small. On the other hand, the nuclear eccentricities ε_{std} are quite small valued (10%) in the most peripheral Au+Au collisions. As N_{part} increases ε_{std} rises rather sharply to attain a maximum in semi-peripheral collisions, which is followed by a gradual decay to very small values at the highest centralities, as low as a few per cent in the most central collisions, which results in a right skewed distribution. In peripheral collisions the small values of $\varepsilon_2^{\text{std}}$ can be attributed to a small number of participating nucleons present within the overlapping part, which according to Equation (3.5) results in small variances in the x and y -coordinates of the participating nucleons. Sometimes the numbers are even as small as one from each colliding nuclei. Large differences in the eccentricity parameters defined in two different ways are observed in the peripheral collisions, which beyond a range ($N_{\text{part}} \gtrsim 60$) diminish with increasing centrality. Our overall observation on the N_{part} dependence of ε_2 matches with that observed in Au+Au collisions at $\sqrt{s_{\text{NN}}} = 200$

Table 3.1: N_{coll} , N_{part} , S , ϵ_2^{std} , ϵ_2^{part} and ϵ_3 at different centralities in Au+Au collision at $E_{\text{lab}} = 30A$ GeV obtained from the MCG simulation.

Centrality	N_{coll}	N_{part}	S (fm ²)	ϵ_2^{std}	ϵ_2^{part}	ϵ_3
0-5%	801.6 ± 0.30	344.1 ± 0.08	26.7 ± 0.01	0.023 ± 0.0003	0.078 ± 0.0002	0.074 ± 0.0002
5-10%	645.8 ± 0.24	293.0 ± 0.07	24.3 ± 0.01	0.074 ± 0.0003	0.114 ± 0.0003	0.089 ± 0.0002
10-20%	473.0 ± 0.21	231.6 ± 0.07	21.1 ± 0.01	0.142 ± 0.0003	0.174 ± 0.0002	0.109 ± 0.0002
20-30%	307.7 ± 0.15	167.7 ± 0.06	17.6 ± 0.01	0.215 ± 0.0003	0.247 ± 0.0003	0.134 ± 0.0002
30-40%	194.1 ± 0.12	118.9 ± 0.05	14.8 ± 0.01	0.270 ± 0.0004	0.309 ± 0.0004	0.162 ± 0.0003
40-50%	116.5 ± 0.09	81.2 ± 0.04	12.5 ± 0.01	0.311 ± 0.0005	0.362 ± 0.0004	0.192 ± 0.0003
50-60%	65.8 ± 0.06	52.9 ± 0.04	10.7 ± 0.01	0.341 ± 0.0006	0.411 ± 0.0005	0.227 ± 0.0004
60-70%	34.7 ± 0.04	32.4 ± 0.03	9.2 ± 0.01	0.352 ± 0.0007	0.457 ± 0.0005	0.267 ± 0.0004
70-80%	16.9 ± 0.03	18.3 ± 0.02	8.1 ± 0.01	0.346 ± 0.0011	0.501 ± 0.0007	0.302 ± 0.0006
80-90%	7.7 ± 0.02	9.5 ± 0.02	7.2 ± 0.01	0.278 ± 0.0011	0.568 ± 0.0006	0.337 ± 0.0005
90-100%	3.3 ± 0.01	4.5 ± 0.01	6.5 ± 0.02	0.100 ± 0.0017	0.672 ± 0.0008	0.344 ± 0.0007

GeV, a much higher collision energy [4]. It should be noted that the MCG model operates with several experimentally determined parameters. Therefore, the model-calculated values of eccentricity are not free from systematic errors incurred by the input parameters. Alver et al. [4] attempted to estimate the maximum possible systematic error in ε_2 . According to the MCG model the eccentricity values are of 90% confidence level. As the initial fluctuations are seen to play an important role, one should be careful in choosing the correct eccentricity expression. It has been argued that if the flow is independent of particle species, $\varepsilon_{\text{part}}$ and not ε_{std} , is a more appropriate parameter that can explain the elliptic flow [25]. The geometric deformation associated with the third harmonic ($n = 3$), also called the triangularity parameter (ε_3), can be obtained from Equation (3.10). We have estimated the ε_3 -values at different centralities and in Figure 3.4 plotted them against N_{part} . Starting from a moderately high value ($\varepsilon_3 \approx 35\%$) for the most peripheral class of events, the triangularity parameter decreases monotonically with increasing N_{part} . It should be noted that except for a few highest centrality classes, ε_3 is smaller than $\varepsilon_{\text{part}}$. A non-zero value of ε_3 serves as a good motivation to investigate the v_3 -parameter at FAIR energies, an energy region that lacks substantive experimental results. Our observations on ε_2 and ε_3 agree reasonably well with another simulation study made at the RHIC energies [26]. We have computed all the variables listed in Table 3.1 also at 10A, 20A and 40A GeV, but did not find significant differences in their values.

3.2.1 Centrality dependence of v_2 and v_3

The centrality dependence of the elliptic flow parameter can provide us with valuable information on the degree of thermalization achieved by the fireball created in AB collisions [27]. It has been observed that for extreme peripheral and central collisions the values of elliptic flow are smaller than what are usually observed in mid-central collisions. This is also typically found in all calculations where transport models are used [28, 29] and also in low energy collisions, especially at the AGS energies [30]. The observation could be explained in terms of the initial geometry and the pressure gradient developed thereof during the early stages of the interactions. In the most peripheral collisions the nuclear overlapping part is highly asymmetric, but not enough particles are produced to carry the corresponding flow effect to the final state. On the other hand, in highly central symmetric AA collisions the nuclear overlapping part has little asymmetry, and therefore, not enough pressure gradient is generated. The observation is also consistent with the low density limit of the hydrodynamical model (to be discussed later). In addition, the effect of shadowing by spectator nucleons plays a crucial role for suppressing the elliptic flow in peripheral collisions. At SPS [31] and RHIC [9] experiments even the most peripheral collisions produce significant amount of elliptic flow, and with increasing collision energy the flow peak moves more toward peripheral

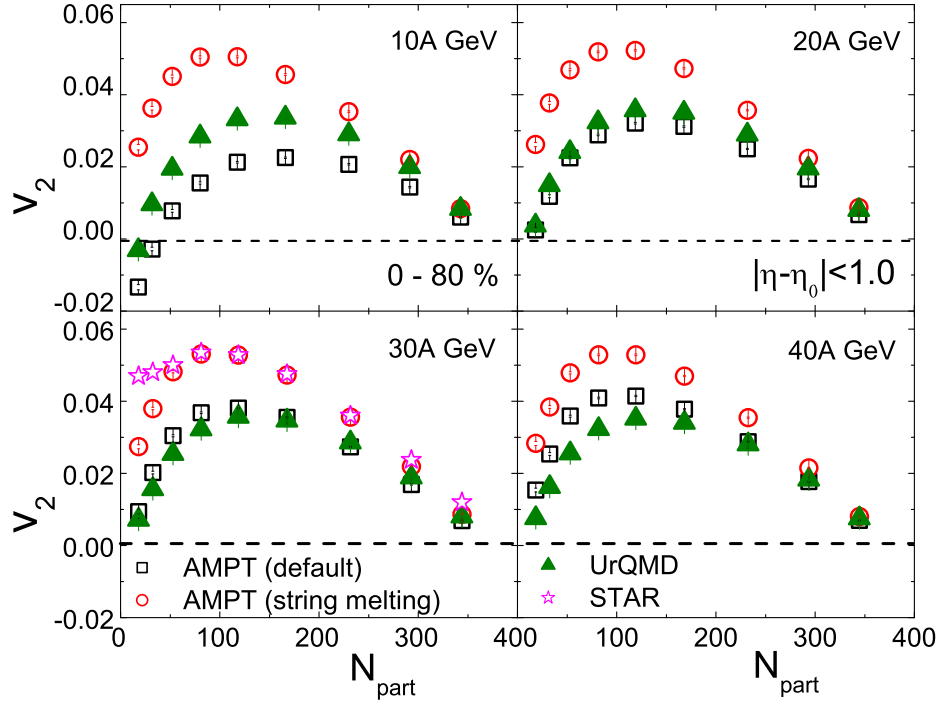


Figure 3.5: Centrality dependence of the elliptic flow parameter of charged hadrons at midrapidity in Au+Au collision at $E_{\text{lab}} = (10 - 40)A$ GeV without considering initial fluctuations. Experimental data points are from [9].

collisions. This observation itself is an indication of the onset of hydrodynamical nature of the fireball fluid created in high-energy collisions between two heavy nuclei. At SPS energies the maximum measured value of elliptic flow ($v_2 \approx 0.04$) is significantly less than the hydrodynamic prediction ($v_2 \approx 0.1$) [6, 32], and the observed centrality dependence of v_2 does not require a hydrodynamical explanation. On the other hand at the top RHIC energy, especially in the mid-central collisions the v_2 -results on soft hadron production (up to $p_T \approx 1.5$ GeV/c), can be well described by a hydrodynamic calculation [33]. Using Equation (3.4) we now compute the elliptic flow parameter (v_2) as a function of the collision centrality (N_{part}) for all event samples used in this analysis. In order to compare our simulated results with the experimental results obtained from Au+Au collision at $\sqrt{s_{NN}} = 7.7$ GeV (RHIC) [9], a kinematic cut of $p_T > 0.2$ GeV/c and $|\eta - \eta_0| < 1.0$ has been applied, which will be continued till Figure 3.8. Our results are schematically presented in Figure 3.5. It is seen that in Au+Au collisions the centrality dependence of v_2 obtained from the AMPT (string melting) and UrQMD models hardly changes as the beam energy is increased from 10 to 40 GeV per nucleon. Using the UrQMD and AMPT models a similar kind of observation was also made in Au+Au collisions at a much higher collision energy ($\sqrt{s_{NN}} = 200$ GeV) [28, 34]. However, the AMPT (default) results behave a little differently from the other two. With increasing collision energy not only the v_2 -values estimated by using the AMPT (default) model increase in magnitude, but their centrality dependence also appears to be

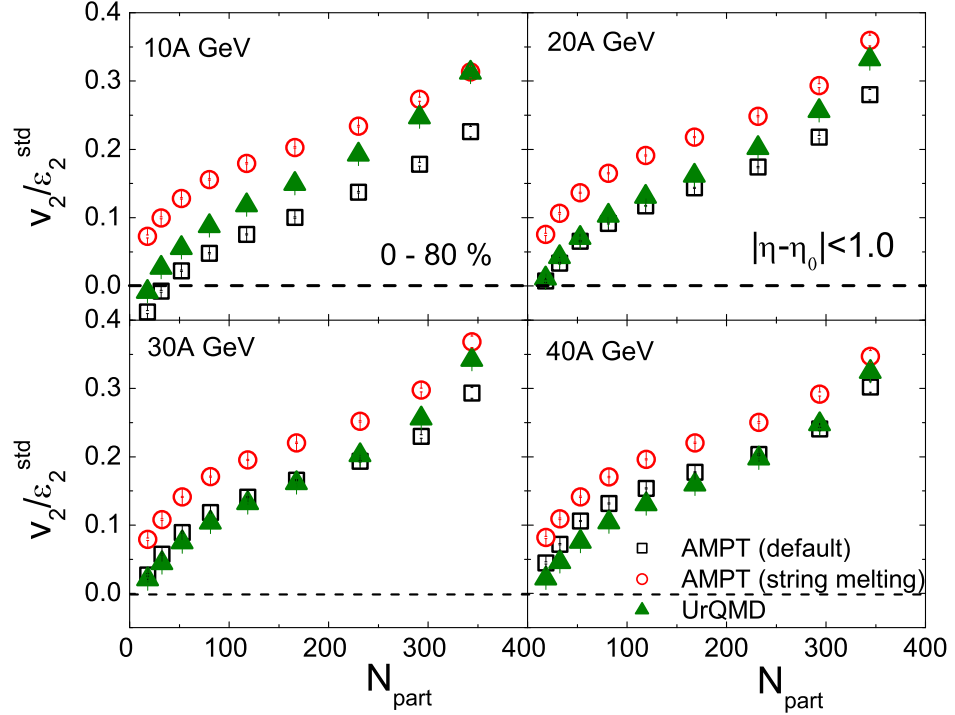


Figure 3.6: $v_2/\varepsilon_2^{\text{std}}$ as a function of N_{part} for the charged hadrons at midrapidity in Au+Au collisions at $E_{\text{lab}} = (10 - 40)A$ GeV without considering initial fluctuations.

more positively skewed. At $E_{\text{lab}} \approx 30A$ GeV AMPT (default) values surpass the UrQMD generated values. This is perhaps due to higher multiplicities produced per event by the AMPT (default) model, which more efficiently transport the initial asymmetry to the final state. The elliptic flow parameter becomes vanishingly small in the most central and most peripheral collisions. In comparison with the UrQMD and AMPT default, AMPT in its string melting configuration, produces significantly higher v_2 -values at all energies and at all centralities. This can be ascribed to the absence of partonic interactions in the UrQMD and AMPT (default) models, whereas in AMPT (string melting) the initial matter is assumed to be fully partonic in nature. As a consequence, due to a long phase of partonic interactions, the v_2 -values obtained from the AMPT (string melting) assume higher values. It is crucial to note that, except for the extreme peripheral centrality classes, the v_2 results obtained from the Au+Au collision at $\sqrt{s_{NN}} = 7.7$ GeV [9], are in well agreement with the AMPT (string melting) calculations at $E_{\text{lab}} = 30A$ GeV. Another salient feature of Figure 3.5 is that, for the same centrality class the models yield noticeably different values of v_2 in the mid-central and peripheral events ($N_{\text{part}} \leq 200$), whereas in the central region ($N_{\text{part}} > 200$) corresponding v_2 values are not much different. All these observations indicate that in central collisions the shape of the overlapping system largely dominates the flow characteristics, while in the mid-central collisions hadronic/partonic (re)scattering might have taken a leading role.

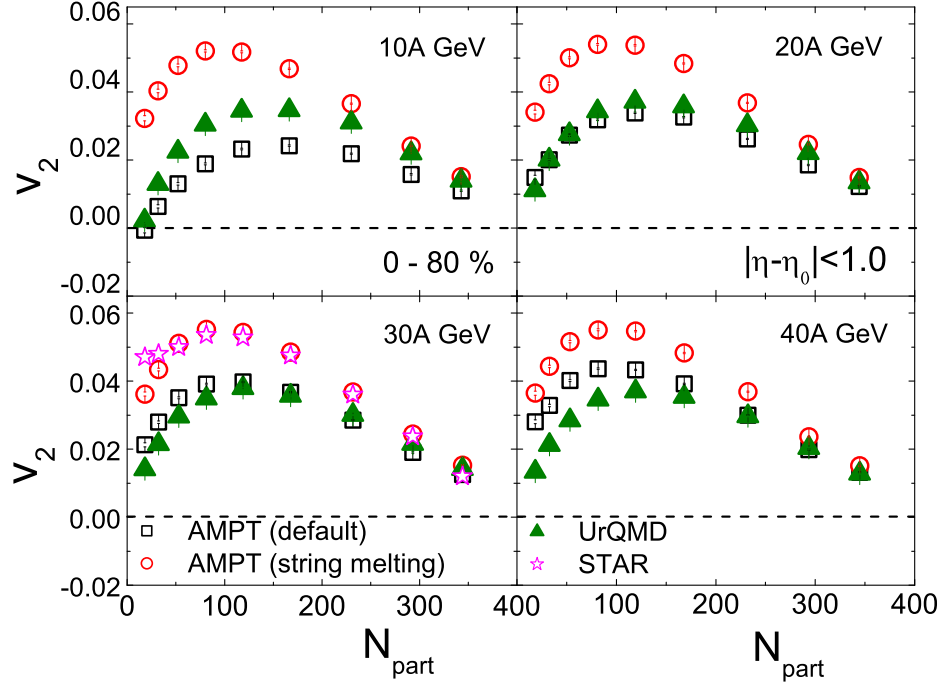


Figure 3.7: Centrality dependence of elliptic flow of charged hadrons at midrapidity in Au+Au collision at $E_{\text{lab}} = (10 - 40)A$ GeV after considering initial fluctuations. Experimental data points are from Ref. [9].

We now study the impact of shape and/or size of the fireball system created in the early stages of the collision on the elliptic flow coefficient v_2 . For a given centrality range this is done by normalizing v_2 by the corresponding eccentricity. Figure 3.6 shows the $(v_2/\varepsilon_2^{\text{std}})$ -ratio plotted against N_{part} for all the three simulations on Au+Au events at $E_{\text{lab}} = 10 - 40A$ GeV. In Figure 3.6 the $v_2/\varepsilon_2^{\text{std}}$ -values for the UrQMD and AMPT are found to increase monotonically with N_{part} over the entire centrality range irrespective of either of the model used or the collision energy involved. It is quite surprising that the bell shaped pattern of v_2 versus N_{part} plot as has been seen in Figure 3.5 is now completely washed out, and for the most central collisions we obtain the highest values of elliptic flow parameter when it is scaled by the eccentricity. We note that, starting from the initial geometry the evolution of v_2 is some kind of a quenching process. Therefore, depending on the evolution process, its value can drastically change after being normalized by the eccentricity. Our observation has a similarity with the RHIC Au+Au and Cu+Cu data [4]. From the above discussion we observe that $\varepsilon_2^{\text{std}}$ may not be an appropriate choice that can effectively represent the collision eccentricity. As already discussed, the fluctuation in the number of participating nucleons and their positions may have a formidable impact on the spatial eccentricity calculated by the MCG model. Taking account of such effects following Equation (3.9) we have computed v_2 and plotted their values against N_{part} in Figure 3.7. The gross features of v_2 obtained with respect to the participant plane is similar to that shown in Figure 3.5 except small differences

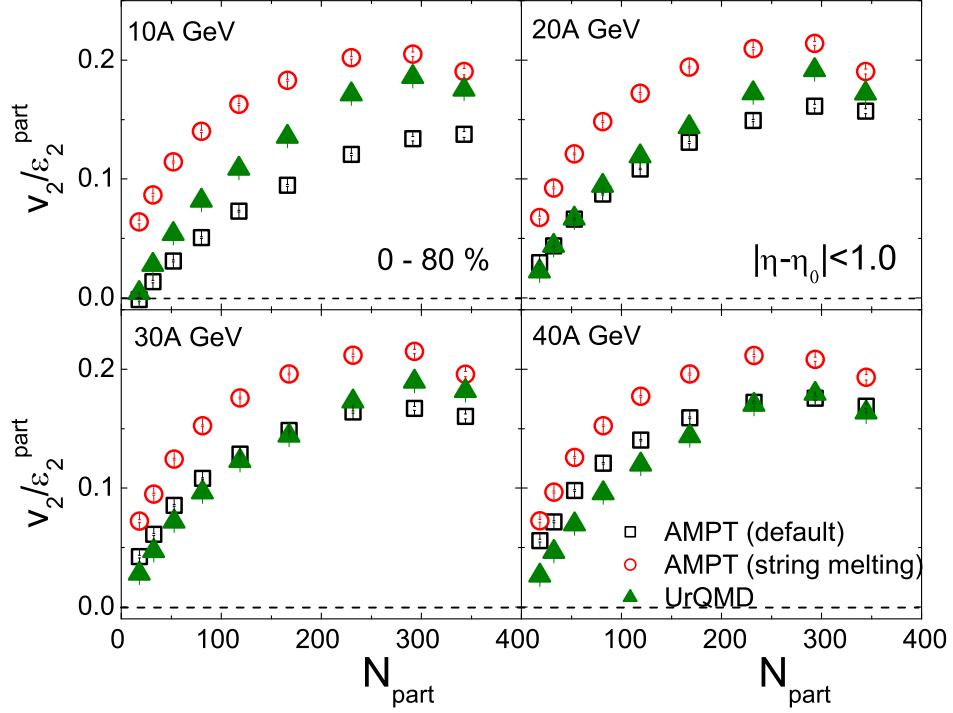


Figure 3.8: $v_2/\varepsilon_2^{\text{part}}$ as a function of N_{part} for the charged hadrons at midrapidity in Au+Au collisions at $E_{\text{lab}} = (10 - 40)A$ GeV after considering initial fluctuations.

in magnitude. The participant plane v_2 -values are 5 – 6% higher than that measured with respect to the reaction plane method. We further expect that, the significance of initial state fluctuations will be better evident, if instead of $\varepsilon_2^{\text{std}}$ we consider $\varepsilon_2^{\text{part}}$ as the eccentricity parameter. Therefore, we divide v_2 by $\varepsilon_{\text{part}}$ and in Figure 3.8 plot the ratio against N_{part} . We find that for all the models used as well as at all energies under consideration, the highest elliptic flow occurs at $N_{\text{part}} \approx 250 - 300$, i.e. in semi-central collisions. The bell shape of v_2 versus N_{part} plots is partially retrieved. However, the peak positions are now shifted toward higher N_{part} value, while the skewness of the plots gets inverted. To some extent our observations are different from the RHIC results at $\sqrt{s_{NN}} = 62.4$ and 200 GeV [4, 35], where the $v_2/\varepsilon_{\text{part}}$ -ratio was found to saturate at $N_{\text{part}} > 100$. It should be noted that ideal hydrodynamical model calculation with hadron cascade can roughly interpret the RHIC data, whereas without hadron cascade the hydrodynamic prediction is more or less similar to the behaviour observed in the present case [36]. Henceforth, until otherwise mentioned, both the eccentricity and the elliptic flow parameters will be calculated only after taking the initial state fluctuations into account. Beside, the participant eccentricity will be denoted simply by ε_2 . An important observation of hydrodynamics is that, if there is no phase transition the equation of state adopted in the model corresponds to a constant speed of sound. In that case the ratio v_2/ε_2 will be independent of the collision centrality [6]. On the other hand, in the presence of a phase transition the speed of sound is not constant, and

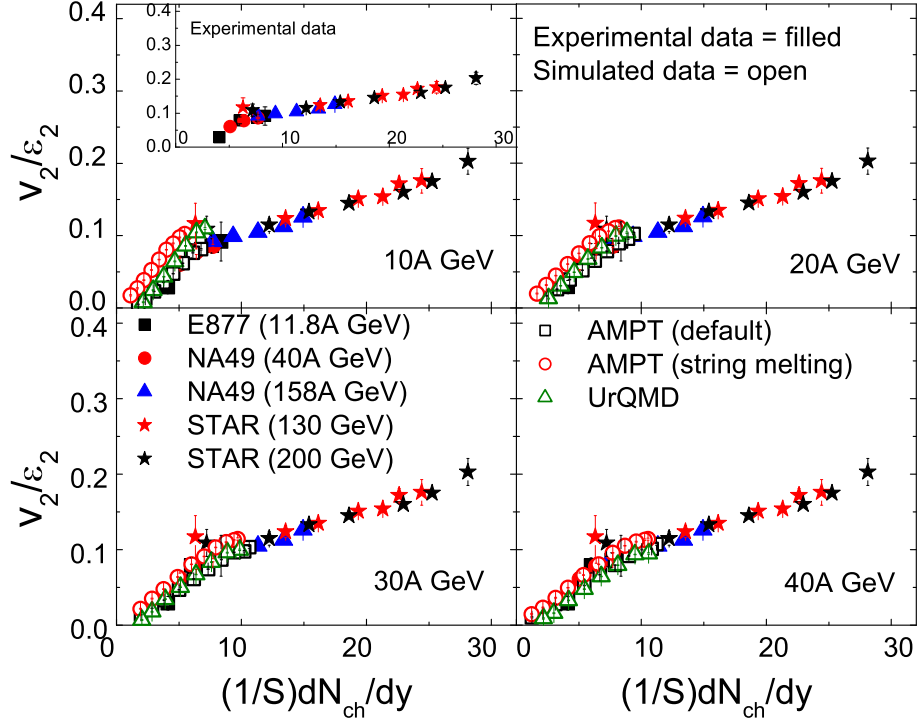


Figure 3.9: Variation of scaled elliptic flow with scaled particle density.

hydrodynamical calculation predicts a change in the v_2/ε_2 -ratio with centrality. However, such changes are not expected to exceed 10% of the values [37]. The Au+Au data obtained from E877 (AGS) [31], NA49 (SPS) [20, 38], and STAR (RHIC) [39] experiments show a smooth linear rising trend in the v_2/ε_2 -ratio with increasing centrality. The results are consistent with the so called low density limit (LDL) of hydrodynamical calculation [27, 41], where the interaction mean free path is comparable to the dimensions of the nuclear overlap region. This is to some extent similar to the interaction scheme implemented into a transport model, where the mean number of hard binary collisions per participant is typically small. For all our Au+Au event samples we calculate the ratio v_2/ε_2 as a function of charge particle rapidity density (dN_{ch}/dy) normalized by the transverse area of the overlap region S . Our simulation results are shown in Figure 3.9 along with the Au+Au collision results obtained from the AGS, SPS, RHIC and LHC experiments [20, 31, 38–40]. An approximately linear dependence like,

$$\frac{v_2}{\varepsilon_2} \propto \frac{1}{S} \frac{dN_{ch}}{dy} \quad (3.30)$$

is reproduced in all the cases studied. The observation suggests that the elliptic flow increases with particle density if the effect of nuclear geometry is taken into account. In the 5 – 70% centrality range, as we plot the elliptic flow parameter scaled by the eccentricity against the particle density scaled by transverse overlapping area of the colliding nuclei, the variation depends marginally on the collision energy and/or the colliding system involved,

indicating thereby, some kind of universal nature of the data. Ultimately, the increasing trend should saturate at the hydro limit, which corresponds to complete thermalization. If the intermediate fireball is comparatively dilute, the asymmetry in azimuthal distribution is directly proportional to the number of rescatterings, or equivalently to the particle density in the transverse plane [38, 41]. A deviation from the approximately linear scaling observed above over a widely varying collision energies, in real experiments as well as in simulations, will require an altogether different kind of physics of multiparticle production. Significantly, the transport model simulated values presented here are not very much different from the E877 and NA49 results either, which have energies comparable to the FAIR-CBM energy scale. As mentioned, a transport model prediction should in principle match with the LDL of hydrodynamical calculation. In that sense the results obtained here are not very surprising. However, we argue that the results may provide useful information to constrain the equation of state of a highly dense baryonic matter expected to be created in the FAIR-CBM experiment. One should keep in mind that there are several sources of uncertainties in the MCG model that might influence the measurement of S . Consequently, the results presented here might contain a significant amount of systematic errors. Also some of the experimental v_2 values shown in the plot are calculated under different algorithms, e.g. the 4-th order cumulant method is used in the LHC, STAR and SPS measurements. Hydrodynamic calculations have shown that the higher order flow harmonics are more sensitive towards kinematic viscosity [42].

The higher order harmonics are also supposed to be subtle to the initial geometry and the fluctuations present therein. The triangularity parameter (ε_3) and its exposure, the triangular flow (v_3), are entirely built of from the chaotic fluctuations present in the source. Therefore, triangular flow may be able to shed some light on the above mentioned issues, particularly at the FAIR energies where experimental evidences are not quite abundant. The centrality dependence of our model based estimation of v_3 in Au+Au collisions at different collision energies is presented in Figure 3.10 within $|\eta - \eta_0| \leq 1.0$. The v_3 -values obtained from the UrQMD simulation are vanishingly small at all centralities and at all collision energies considered. It looks like that in this model the particle production mechanism is not at all influenced by the initial state fluctuations. The AMPT simulations on the other hand produce small but statistically significant non-zero v_3 -values. Henceforth, in all our analysis we shall be employing only the AMPT model to investigate the issues related to v_3 . It is worthy to mention that the triangular flow was first discovered in 2010 [43] by using the string melting version of AMPT. Unlike v_2 , the triangular flow except for the 10A GeV case, and for the most peripheral events which are deficient in their particle content, is almost independent or at best weakly dependent on centrality. At $E_{\text{lab}} = 10A$ GeV with increasing N_{part} we find a slow linear growth in v_3 . Moreover, in comparison with v_2 , the v_3 -values at all energies are at least an order less in magnitude. These observations can be

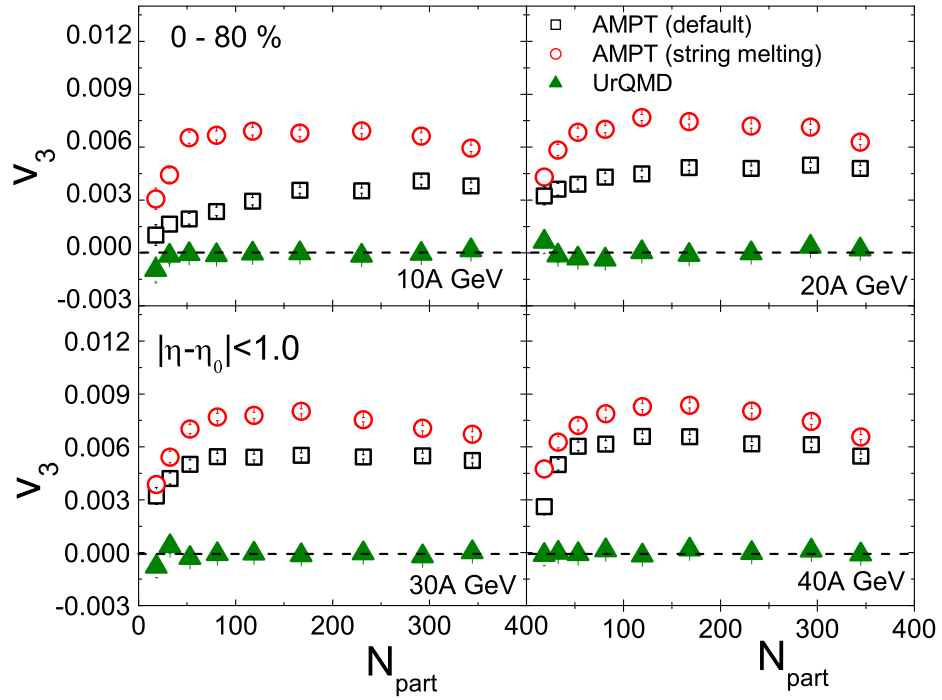


Figure 3.10: Centrality dependence of triangular flow of charged hadrons at midrapidity in Au+Au collision at $E_{\text{lab}} = (10 - 40)A$ GeV

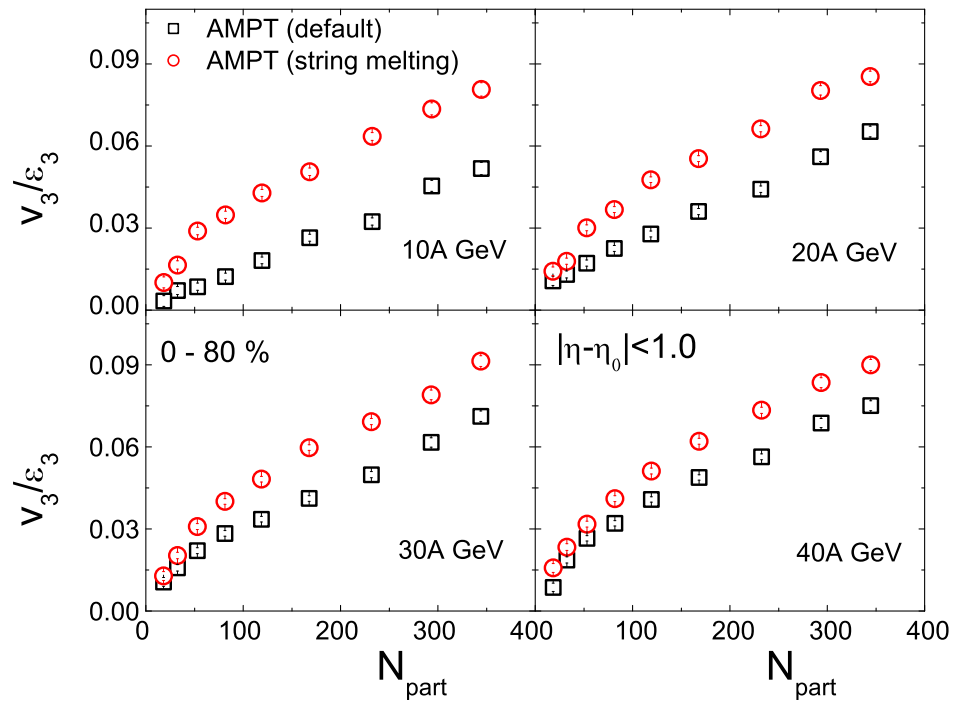


Figure 3.11: v_3/ϵ_3 as a function of N_{part} for the charged hadrons at midrapidity in Au+Au collisions at $E_{\text{lab}} = (10 - 40)A$ GeV.

generally explained in terms of the sources that the two different flow coefficients depend upon. While v_2 arises from the geometrical asymmetry of the overlapping region as well as from the initial fluctuations, v_3 results only from the initial fluctuations. Obviously, in comparison with the azimuthal asymmetry and the pressure gradient built thereof, the initial state fluctuation is a weaker phenomenon. At all energies the AMPT (string melting) generates a stronger triangular flow than the AMPT (default) simulation, which indicates a considerable influence of the initial state fluctuations on the partonic/hadronic degrees of freedom. Within the expected FAIR energy range we do not see much energy dependence in the AMPT (string melting) simulated values of v_3 . On the other hand for the default AMPT, v_3 nearly doubles in magnitude as the energy changes from 10A to 40A GeV. In this regard v_3 behaves similar to v_2 . The vigor of collision does not very much affect either the elliptical or the triangular flow in the FAIR energy range. Figure 3.11 depicts that the triangular flow parameter when scaled by the corresponding triangularity, increases monotonically (almost linear for mid-central and central collisions) with increasing centrality. We notice that the conversion of initial state fluctuations to the final state momentum asymmetry increases with centrality, and therefore with the multiplicity of charged hadrons. A decreasing trend in the v_n/ε_n -ratio with increasing n can be verified after a concurrent inspection of Figure 3.8 and Figure 3.11, that may be due to a viscous damping. Similar observation has also been made at the RHIC energies [26] for $n = 2, 3$ and 4.

Relative strength of v_2 and v_3

It is claimed that the relative magnitude of the higher order harmonics ($v_n, n \geq 3$) can be used to further constrain the magnitude of specific viscosity (η/s) of the fireball matter [43, 45]. Using the AMPT (string melting) we compute the relative magnitude of triangular flow with respect to the elliptic flow as a function of N_{part} in different p_T -intervals within the $|\eta - \eta_0| < 1.0$ -region in Au+Au interaction at different collision energies. In Figure 3.12 the v_3/v_2 -ratio is observed to increase with centrality almost like a power law. The v_3/v_2 ratio is consistently higher in a wider p_T -interval. However, when the v_3/v_2 -ratio corresponding to a particular p_T -interval is divided with that of the entire p_T -interval, which in our case is $0 \leq p_T \leq 2.0$ GeV/c, we find that within statistical uncertainties the v_3/v_2 -ratio so normalized becomes almost independent of the centrality. This result is schematically presented in the lower panels of Figure 3.12, and our observation in this regard is similar to that of the AMPT simulation of a RHIC experiment [43]. In view of the fact that the central particle density too depends in the same way: $dN_{\text{ch}}/d\eta \propto N_{\text{part}}^\alpha$, on N_{part} as the v_3/v_2 -ratio does, the observation may be attributed to an entropy driven soft-hadron production, also known as multiplicity scaling [44]. As soon as the relative measures of v_3/v_2 -ratio are considered, this multiplicity dependence disappears. Moreover we do not notice any significant energy

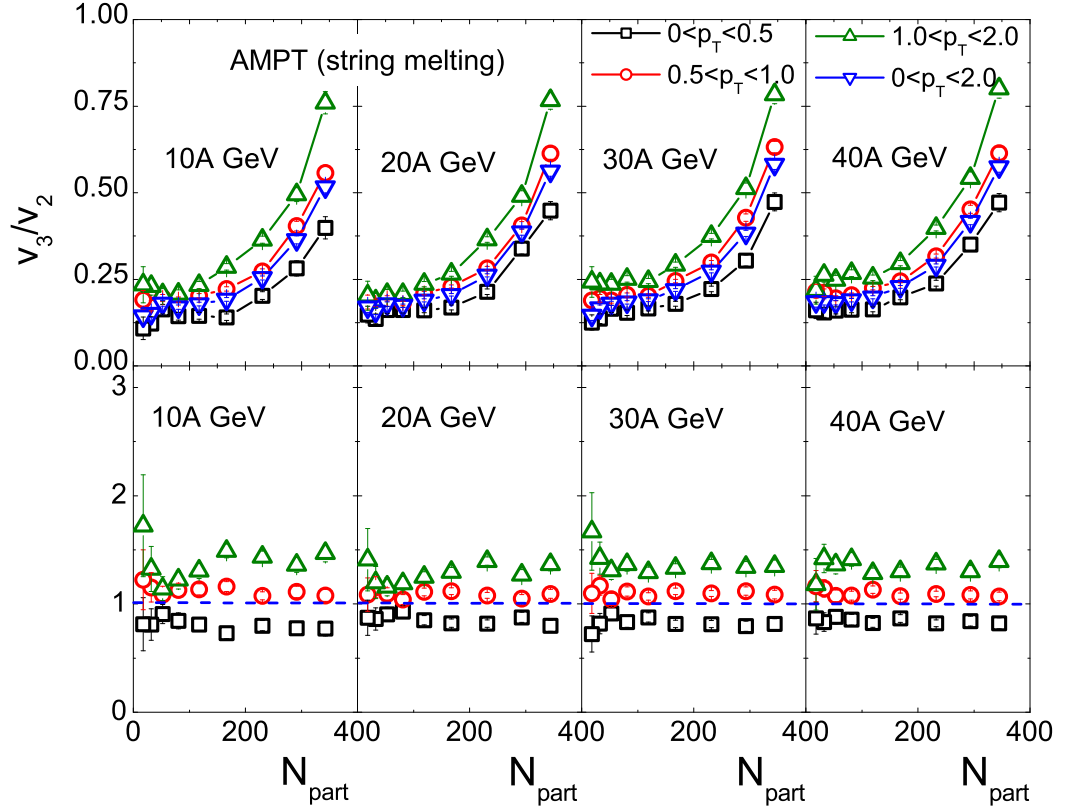


Figure 3.12: v_3/v_2 -ratio computed at midrapidity plotted as a function of N_{part} in different p_T intervals in Au+Au collision at $E_{\text{lab}} = 30A$ GeV for the AMPT (string melting) model simulation (upper panel). The v_3/v_2 -ratio for a p_T interval is scaled by the corresponding ratio for the entire p_T -range ($0 \leq p_T \leq 2.0$ GeV/c) (lower panel).

dependence in either of the results associated with the relative magnitude of v_3 and v_2 as mentioned above.

3.2.2 Transverse momentum dependence of v_2 and v_3

In the top panels of Figure 3.13 to Figure 3.16, we plot the elliptic flow parameter v_2 against p_T of charged hadrons produced in Au+Au collisions respectively at $E_{\text{lab}} = 10A$ to $40A$ GeV. We plot v_2 for some selected centrality bins, starting from $(0 - 10)\%$ and ending at $(50 - 60)\%$ with a gap of 10% between successive intervals. For few peripheral bins the v_2 -values are dominated by statistical uncertainties and are therefore kept out of our consideration. Since the high- p_T hadron production is very much collision energy dependent, and at FAIR energies high- p_T -hadrons will be rare to find out, the flow results at large p_T (> 2.0) GeV/c would not be statistically significant. They too are therefore kept outside the purview of our analysis. For an easy reference we plot the results of UrQMD, AMPT (default) and AMPT (string melting) models together in the same scale. In all the cases we see that for a given centrality, v_2 increases almost linearly with increasing p_T , the

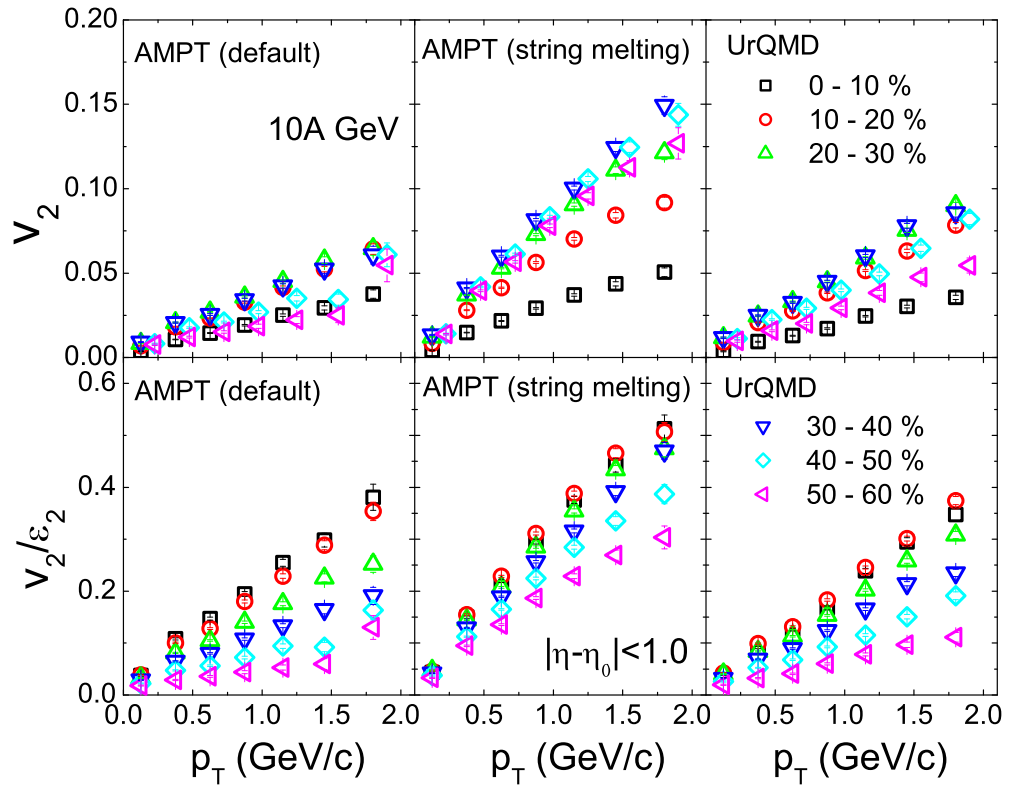


Figure 3.13: v_2 and v_2/ε_2 plotted against p_T for charged hadrons at midrapidity in Au+Au collisions at $E_{\text{lab}} = 10A$ GeV. v_2 for the last two centralities are slightly shifted for clarity.

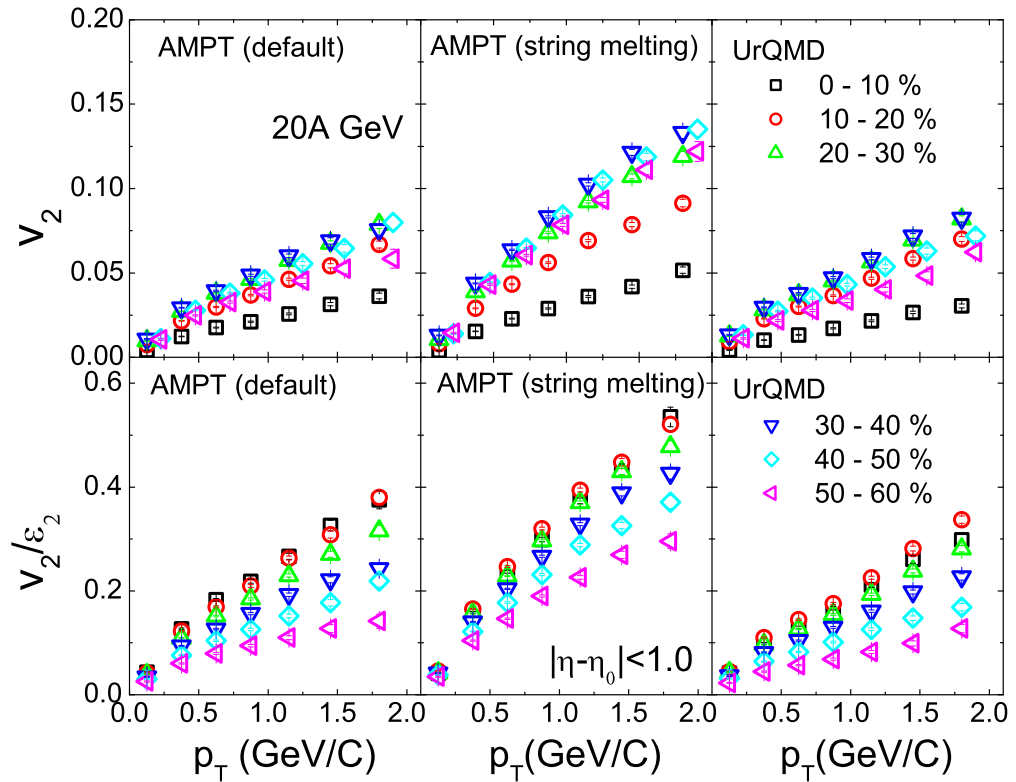


Figure 3.14: Same as in Figure 3.13 but at $E_{\text{lab}} = 20A$ GeV.

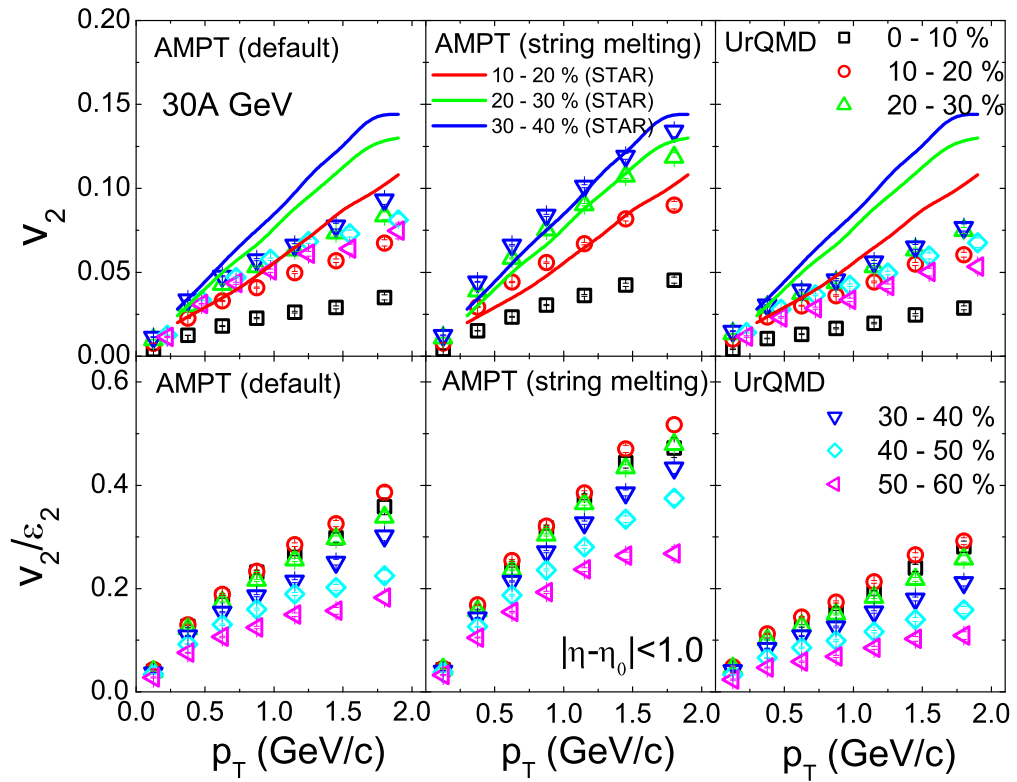


Figure 3.15: Same as in Figure 3.13 but at $E_{\text{lab}} = 30A$ GeV. The available experimental results (STAR data) are shown by continuous curves.

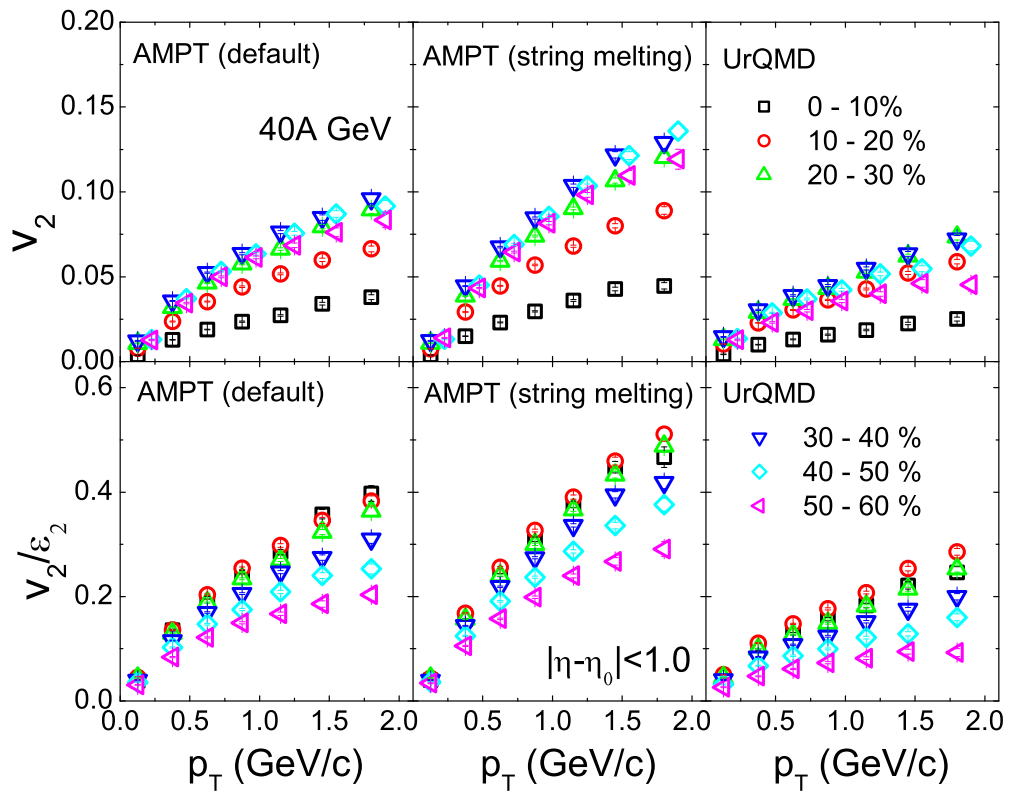


Figure 3.16: Same as in Figure 3.13 but at $E_{\text{lab}} = 40A$ GeV.

rate of increase being highest in the semi-central collisions generated by the AMPT string melting version. The increasing nature of v_2 is a consequence of higher momentum particles emerging earlier from the collision zone. The particles with higher momentum are believed to carry the signal of the earliest stage of the collision, where the spatial asymmetry is most prominent. The v_2 at highest p_T acquires quite high values, more than 10% at least for the AMPT string melting model. No significant differences in the results obtained from 10A to 40A GeV are observed. In the studied cases the v_2 -values show a centrality ordering similar to that observed in Figure 3.7. The trends of variation agree well with the same in the low p_T -region of the RHIC data [2, 46]. The results from $E_{\text{lab}} = 30A$ GeV are compared with those taken from the RHIC beam energy scan program [9], and in Figure 3.15 they are plotted along with our simulated results. The AMPT (string melting) simulation results are almost in unison with the experiment, whereas AMPT (default) and UrQMD consistently underpredict the same. The efficient generation of v_2 by the AMPT (string melting) is perhaps due to its enhanced parton density which subsequently hadronizes by the quark coalescence mechanism. The assumption of a higher Debye mass over temperature ($\mu/T \approx 2$) in the AMPT (string melting) model is responsible for more isotropic scattering within the fireball which may have amplified the v_2 to acquire large magnitudes in semi-central collisions.

The most direct evidence that v_2 is related to the spatial asymmetry that originates in the early phase of an AB interaction is that, v_2 at low- p_T approximately scales with the initial eccentricity of the overlapping part. For reasons already discussed above, we use $\varepsilon_{\text{part}}$ to scale v_2 . The model calculated v_2 -values scaled by $\varepsilon_{\text{part}}$ are plotted against p_T for the same six centrality intervals as the v_2 -plots in the bottom panels of Figure 3.13 to Figure 3.16, respectively for 10A to 40A GeV collision energies. The gross characteristics of the p_T -dependence of $v_2/\varepsilon_{\text{part}}$ and v_2 are more or less similar. At low- p_T the eccentricity scaled elliptic flow values are weakly dependent on centrality, but with increasing p_T the centrality dependence becomes more pronounced. Rather we observe a centrality re-ordering where the central collisions are found to generate higher v_2/ε_2 -ratio than the peripheral, a manifestation of collective interactions becoming stronger in presence of many participants. Our observation in this regard is consistent for all the models and for all energies under consideration. The observation on the p_T -dependence of elliptic flow also complements the results shown in Figure 3.7 and Figure 3.8. It may be noted that in the RHIC beam energy scan program a similar kind of centrality ordering of the eccentricity scaled v_2 has been observed [9]. Similar analysis pertaining to the triangular flow parameter (v_3) is schematically presented in Figure 3.17 to Figure 3.20 in Au+Au collision at 10A to 40A GeV. Arguments analogous to the v_2 vs. p_T -plot can be put forward to explain a consistently higher magnitude of v_3 obtained from the AMPT (string melting) model. Within statistical uncertainties the v_3 -values are found to be almost independent of the centrality, indicating

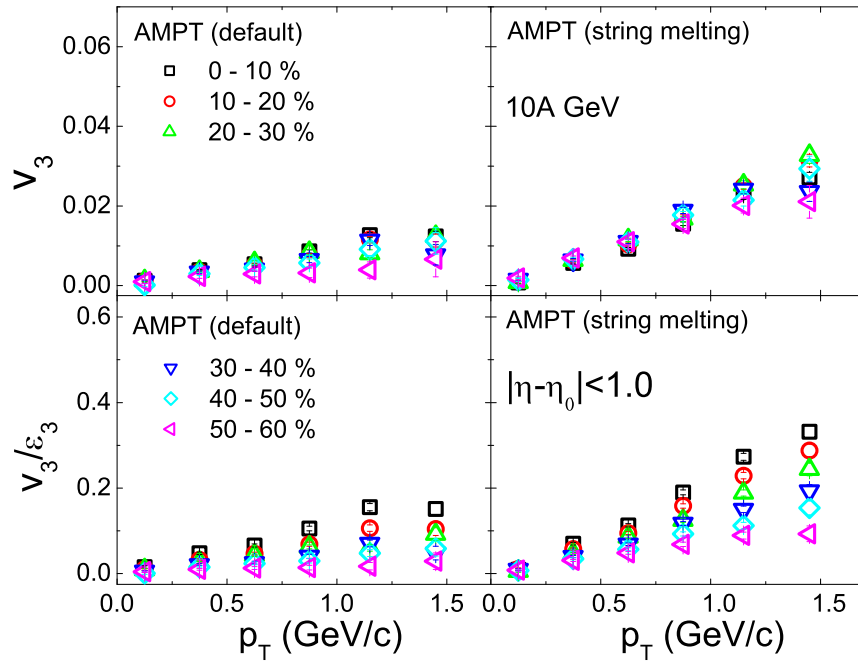


Figure 3.17: v_3 and v_3/ε_3 plotted against p_T for charged hadrons at midrapidity in Au+Au collisions at $E_{\text{lab}} = 10A$ GeV.

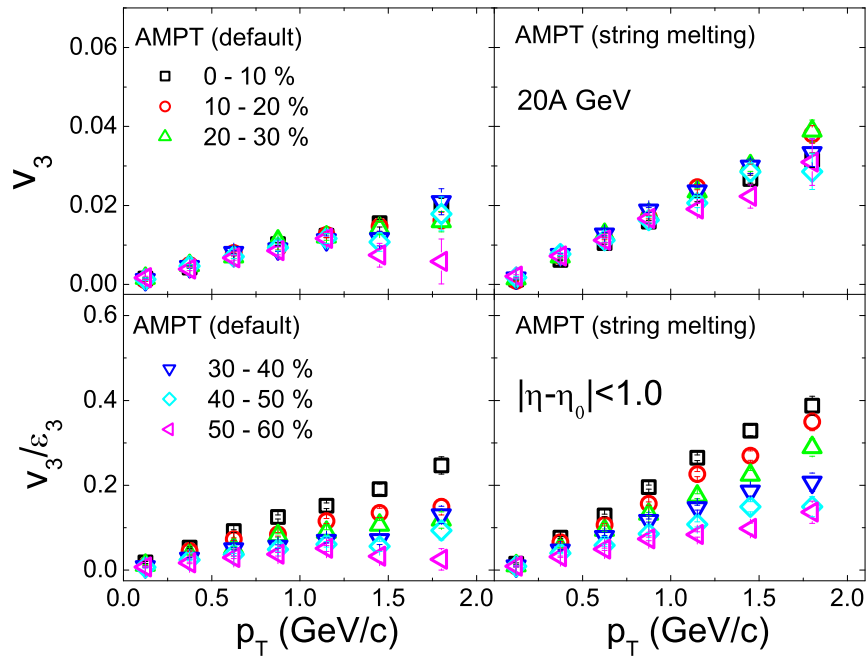


Figure 3.18: Same as in Figure 3.17 but at $E_{\text{lab}} = 20A$ GeV.

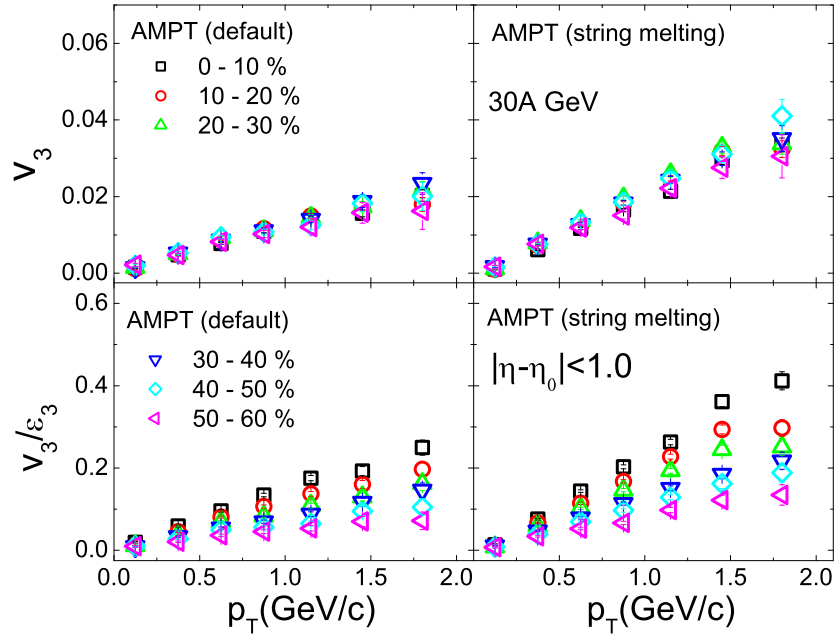


Figure 3.19: Same as in Figure 3.17 but at $E_{\text{lab}} = 30A$ GeV.

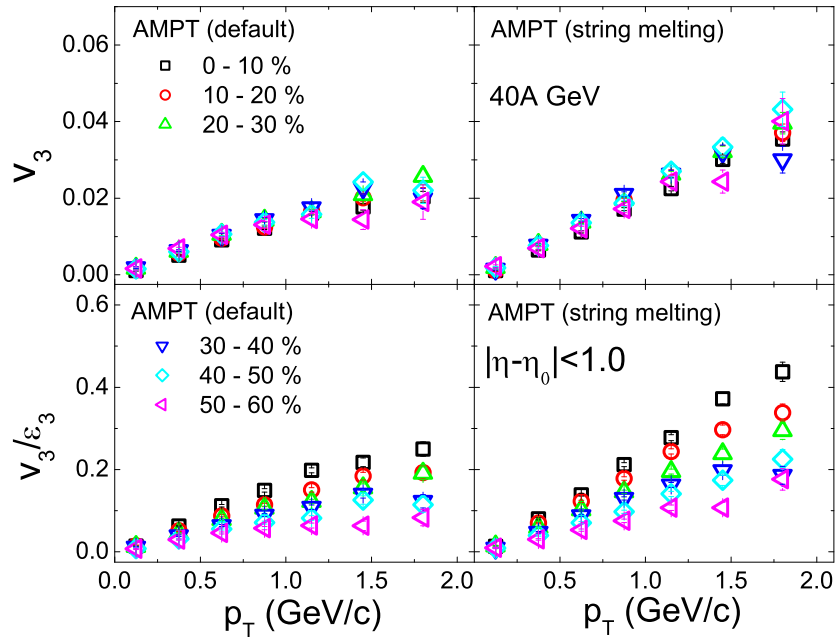


Figure 3.20: Same as in Figure 3.17 but at $E_{\text{lab}} = 40A$ GeV.

once again that it originates from the initial state fluctuations. However, the v_3/ε_3 -ratio shows a centrality ordering, e.g. higher centrality produces a higher ratio, a feature that can be easily understood from the centrality dependence of ε_3 as shown in Figure 3.4.

3.2.3 Species dependence of v_2 and v_3

Another important aspect of azimuthal anisotropy is a mass ordering in the p_T -dependence of the flow parameters for different species of identified hadrons produced in high energy AB interactions. In Figure 3.21 and Figure 3.22 we have respectively plotted the v_2 and v_3 -values against p_T at midrapidity in the 0 – 80% centrality range for different species of charged hadrons produced at $E_{\text{lab}} = 30A$ GeV. Below $p_T = 1.0$ GeV/c both the elliptic and the triangular flow parameters show an obvious mass ordering, i.e. a higher v_n for the lower mass hadrons, which is consistent with the hydrodynamic prediction [47, 48]. In order to elaborate our observation a bit more, we may consider that pions and protons tend to move with a common average velocity within the fireball medium [33]. As a consequence, particles moving with a common velocity would correspond to low- p_T pions and a comparatively higher p_T protons, and would produce a common anisotropy. In other words, at same p_T -value it will lead to a lower magnitude of flow coefficients for protons and a higher magnitude for pions. It is interesting to note that beyond $p_T = 1.0$ GeV/c the above mentioned mass ordering is no longer maintained. In particular for the AMPT (string melting) model it actually gets inverted between mesons and baryons, and at $p_T > 1.3$ GeV/c the mass ordering trends split into two separate bands, the upper one for baryons and the lower one for mesons. This feature can be ascribed to the fact that, provided an extended QCD state is formed, both v_2 and v_3 are expected to depend on the partonic constituents of the respective baryon and meson species. A redistribution of the momentum anisotropy will then build up due to a mass-dependent flattening of the p_T -spectra caused by a radial flow generated

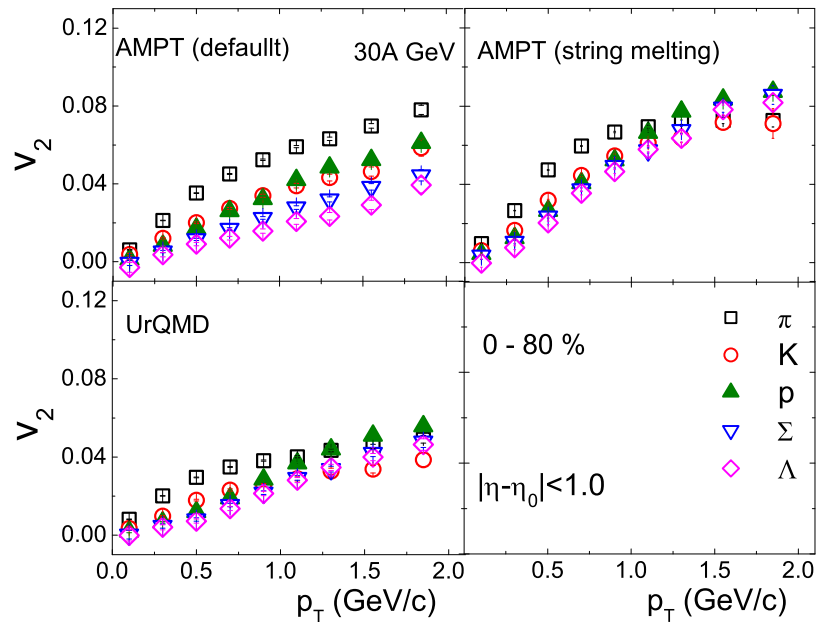


Figure 3.21: Species dependence of v_2 as a function of p_T at midrapidity for Au+Au collision at $E_{\text{lab}} = 30A$ GeV.

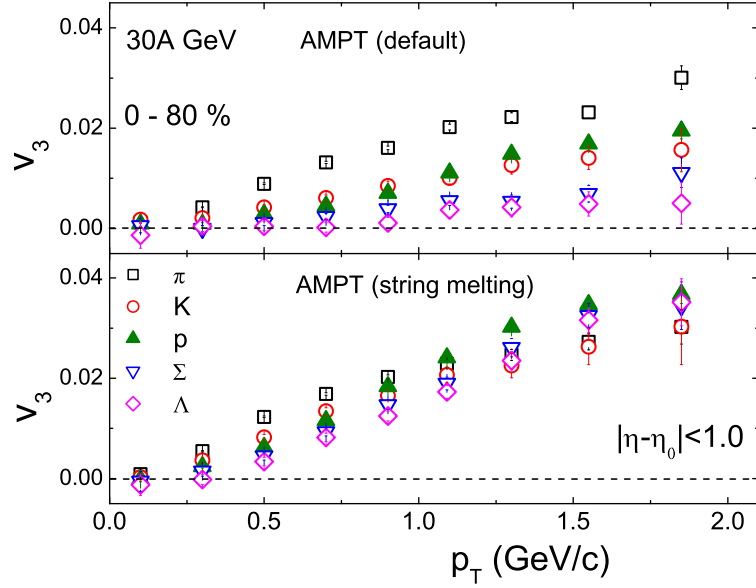


Figure 3.22: Species dependence of v_3 as a function of p_T at midrapidity for Au+Au collision at $E_{\text{lab}} = 30A$ GeV.

during the hadronization process, thus resulting in a mass splitting that we observe most prominently in our AMPT (string melting) simulated data. UrQMD and AMPT (default) results in this regard are not quite regularly behaving. The mass splitting just after the hadronization is expected to be a weak effect which would rather increase after hadronic (re)scattering. Subsequently this effect can also be considered as a probe to inspect the in-medium (re)scattering. It is said that at low- p_T the light quarks (u , d) possess higher v_2 and v_3 in comparison to their strange counterpart. With increasing p_T the flow coefficients of both light and heavy quarks approach each other and ultimately saturates. Similar mass ordering has been reported in the RHIC [50–52] and LHC experiments [10], and in AMPT simulation of AB collisions at RHIC [26, 53] and LHC [54] conditions. It is perhaps due to the quark coalescence mechanism that there is a tendency of the differential flow parameters pertaining to a particular hadron species (meson or baryon) to group together. The recombination of constituent quarks neighboring each other in phase space is also expected to lead to a uniform behaviour in the way the flow parameters should depend on the transverse degrees of freedom. In particular, when appropriately scaled by the number of constituent quarks, hadrons belonging to different species are supposed to depend identically on p_T . The phenomenon known as the number of constituent quarks (NCQ) scaling [56, 57], has been verified in RHIC [58] and LHC [10] experiments. The phenomenon is considered to be an important evidence of the partonic degrees of freedom present in the fireball, and is an integrated consequence of both partonic and hadronic interactions [54]. In Figure 3.23 and Figure 3.24 we have shown the dependence of v_2 and v_3 on the transverse kinetic energy $K_T = \sqrt{p_T^2 + m_0^2} - m_0$. Following the proposal made in Ref. [56], the K_T and v_2 values

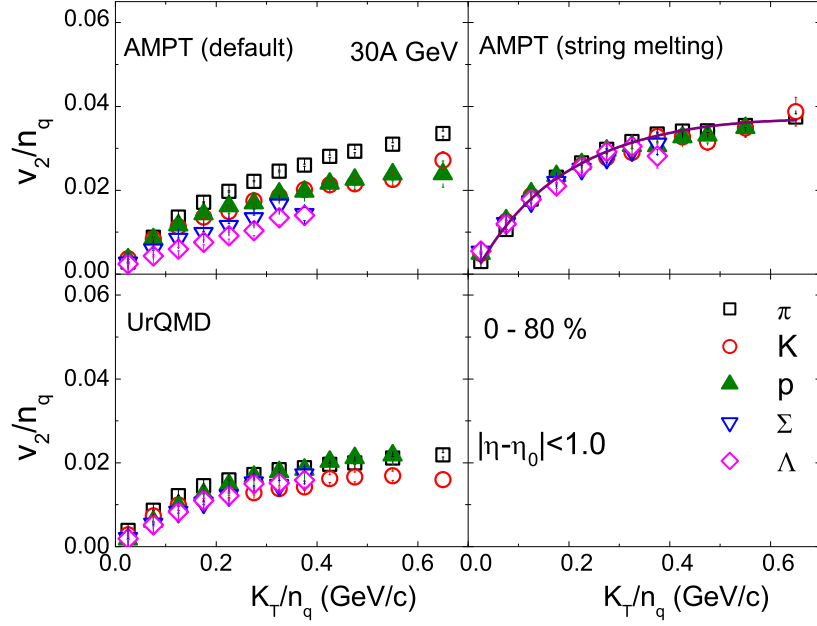


Figure 3.23: v_2 scaled by the constituent quark numbers of hadrons as a function of K_T/n_q at midrapidity for Au+Au collision at $E_{\text{lab}} = 30A$ GeV. The solid line is fitted following Equation (3.31).

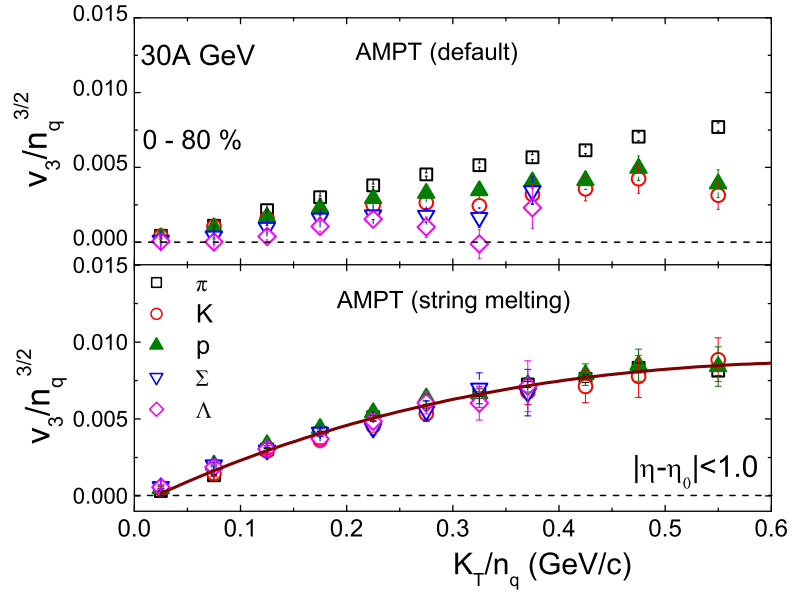


Figure 3.24: v_3 scaled by the constituent quark numbers of hadrons as a function of K_T/n_q at midrapidity for Au+Au collision at $E_{\text{lab}} = 30A$ GeV. The solid line is fitted following Equation (3.31).

are scaled by n_q , while v_3 is scaled by $n_q^{3/2}$. In general, v_n has to be scaled by $n_q^{n/2}$, which specifies how partonic interactions differently influence the flow parameters pertaining to different harmonics. Within statistical uncertainties, our results from the AMPT (string melting) model, which has an inherent partonic degrees of freedom in its hadronization process, agree reasonably well with NCQ. One may speculate that the collective behaviour has

developed quite early in the partonic stage of the fireball, and it also corroborates a quark coalescence picture of hadronization. A phenomenologically motivated fit function of the form,

$$\frac{v_n}{n_q^{3/2}} = \frac{a + bx + cx^2}{d - x} - \frac{a}{2} \quad (3.31)$$

where $x = K_T/n_q$, describes the scaling quite satisfactorily [59]. However, at this stage we do not intend to assign any physical significance to the fit. While the AMPT (default) results completely overrides the NCQ-scaling, UrQMD, although a purely hadronic cascade model, exhibits a weak NCQ-scaling for its v_2 -results. In the framework of the Additive Quark Model (AQM), the hadronic interaction cross-sections that depend on the quark content of the colliding hadrons, is a possible cause of such approximate scaling behaviour [60].

3.2.4 Averaging scheme of v_n

The averaging scheme used in Equation (3.3) and Equation (3.9) refers to the so called particle-wise averaging. As introduced in [61] there exists another kind of averaging of v_n , which is known as the event-wise averaging. Though the particle-wise average is widely accepted in data analysis and theoretical calculations [62], it does not take the influence of multiplicity fluctuations of the event sample into consideration. In connection with the elliptic flow measurement, the correlation between these two types of averaging schemes is studied in [61]. According to [61] the event-wise averaged harmonic parameter v_n^e reads as,

$$v_n^e = \left\langle \overline{\cos(n\phi)} \right\rangle_{ev} \quad (3.32)$$

where ϕ is the azimuthal angle of a charged hadron with respect to the participant plane. Here $\overline{\cos(n\phi)}$ represents the average of $\cos(n\phi)$ over all particles in an event, and $\langle \rangle_{ev}$ represents an average over all events present in a sample. Under the same notation the particle-wise average denoted by v_n^p is written as,

$$v_n^p = \left\langle \overline{\cos(n\phi)} N_{ch} \right\rangle_{ev} / \langle N_{ch} \rangle_{ev} \quad (3.33)$$

Note that if $\overline{\cos(n\phi)}$ is independent of the event multiplicity N_{ch} , then v_n^p turns into v_n^e . This is the case when the harmonic parameter is studied within a very narrow centrality (multiplicity) bin. We have measured the differences between particle-wise and event-wise averaged values of the elliptic flow parameter. Figure 3.25 displays a sample plot of such analysis, where both the particle-wise and event-wise averaged values of v_2 are plotted against η , shown within a range $0 \leq \eta \leq 4$ for the 0 – 40% most central Au+Au events. We find that at all energies, v_2 as a function of η follows more or less identical trend. For AMPT (string melting) the distributions are more or less symmetric, for AMPT (default)

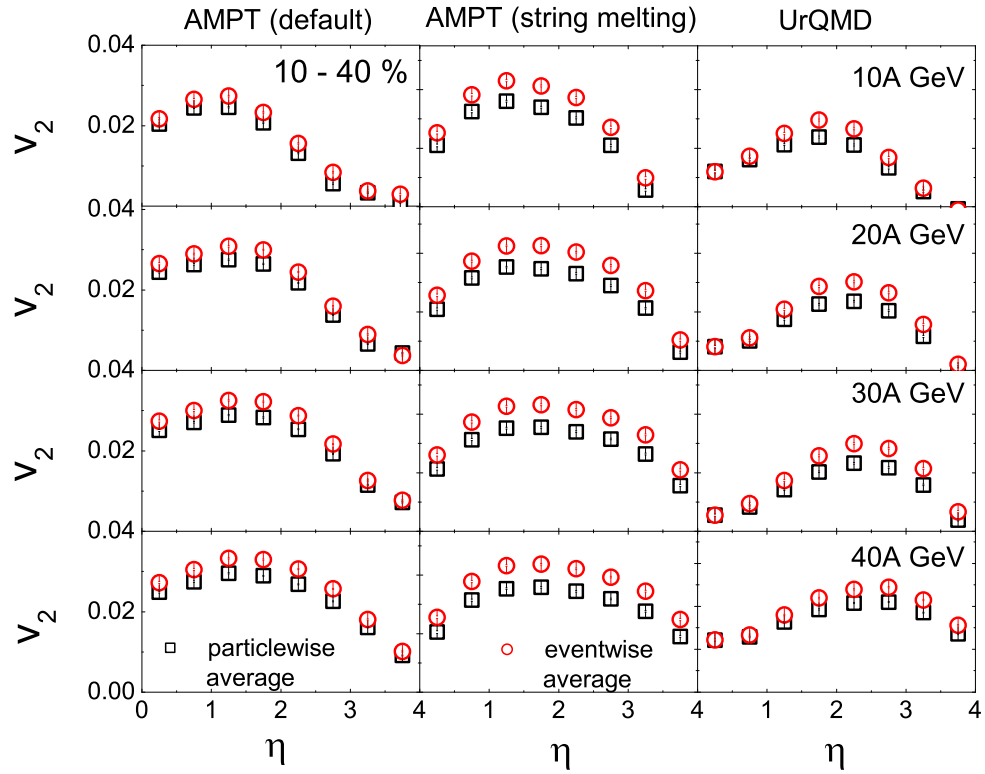


Figure 3.25: Comparison between particle-wise and event-wise averaged values of v_2 plotted against η in Au+Au collisions at $E_{\text{lab}} = (10 - 40)A$ GeV.

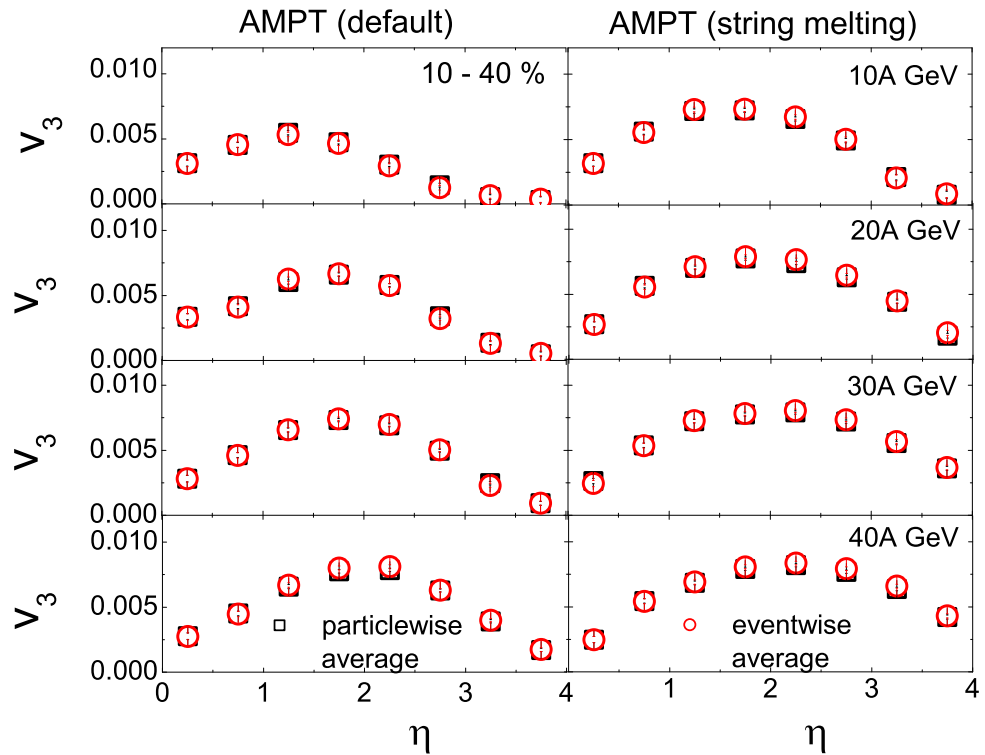


Figure 3.26: Comparison between particle-wise and event-wise averaged values of v_3 plotted against η in Au+Au collisions at $E_{\text{lab}} = (10 - 40)A$ GeV.

they are right skewed and for UrQMD they are left skewed. The event-wise averaged v_2 values consistently exceed the particle-wise averaged values by about 10 – 20%. A similar observation has been made by using the AMPT string melting model for the 0 – 40% most central Au+Au collisions at $\sqrt{s_{NN}} = 200$ GeV [34]. It appears that the systematic differences observed between the two kind of averaging methods adopted in our analysis, are independent of the collision energy involved, yet they are most prominent for the AMPT string melting model. In Figure 3.26 we have graphically shown the similar type of η -dependence of the triangular flow. The averaging schemes seem to have no impact on v_3 whatsoever. This can be easily understood in terms of a weak or almost null centrality dependence of v_3 observed before, as because the averaging scheme is an effect of the particle multiplicity which in turn is a manifestation of the collision centrality.

3.2.5 Cumulants and flow fluctuations

In Figure 3.27 we plot the v_2 -values calculated by using the participant plane method and the cumulant method against N_{part} , in the central particle producing region ($|\eta - \eta_0| \leq 1.0$) of the (0 – 70)% centrality class of Au+Au events generated by the AMPT (string melting) model at $E_{\text{lab}} = 30A$ GeV. The $v_2\{2\}$ and $v_2\{2, |\Delta\eta| > 1\}$ -values are always almost equal to each other, which signifies that non-flow effects are small in the AMPT (string melting) simulation at FAIR energies. The marginal differences that we observe between $v_2\{2\}$ and $v_2\{4\}$ may be attributed to the flow fluctuations. We also estimate $v_2\{\text{est}\}$ by using the cumulant method and include their values in the same plot, slightly shifted along the horizontal axis to maintain clarity. For a meaningful comparison once again our simulated results are compared with those obtained from the STAR experiment [9]. For $N_{\text{part}} < 200$, the $v_2\{2\}$ -values obtained from the AMPT (string melting) simulation slightly over predict the experimental data. The observation suggests that non-flow correlations, although small in amount, are present in the model. Eccentricity (ε_2) of the overlapping region of the colliding nuclei is obtained from the initial spatial distribution of the participating nucleons. Due to the fluctuating number and position of the participating nucleons ε_2 may fluctuate on an event-by-event basis even within the same centrality class.

Cumulants of ε_2 are computed by using Equation (3.25) along with the event plane method, and the results are graphically presented in Figure 3.28. Excepting the peripheral region, the average trend of the centrality dependence of ε_2 is compatible to that of v_2 , which may naively be interpreted as due to the inefficiency of the peripheral events in converting the initial state eccentricity to final state collective effects. We now examine the effect of ε_2 -fluctuation on flow fluctuation. Both the initial and final state fluctuations are estimated by employing Equation (3.27) and Equation (3.29) respectively. Figure 3.29 shows

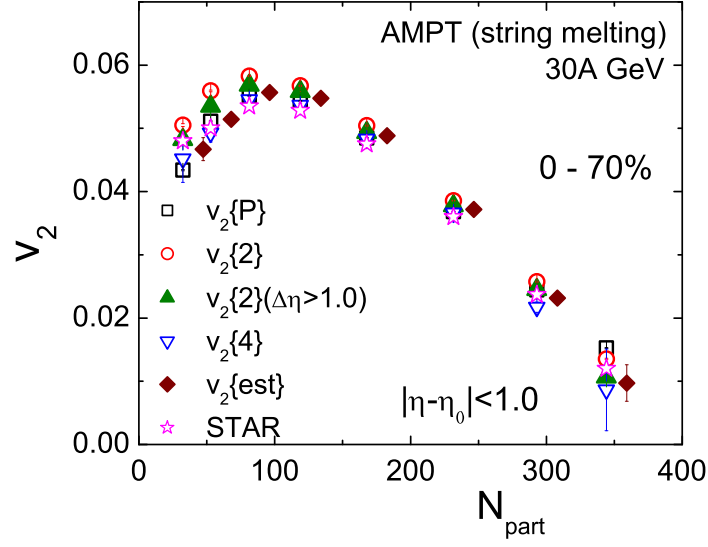


Figure 3.27: v_2 estimated by various techniques as a function of N_{part} at midrapidity in Au+Au collision at $E_{\text{lab}} = 30A$ GeV. $v_2\{\text{est}\}$ values are slightly shifted for clarity.

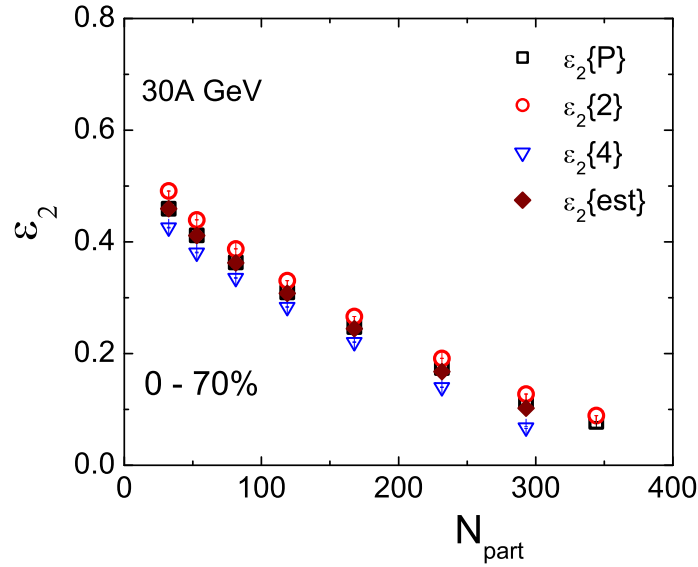


Figure 3.28: ε_2 estimated by various techniques as a function of N_{part} in Au+Au collision at $E_{\text{lab}} = 30A$ GeV. $\varepsilon_2\{\text{est}\}$ values are slightly shifted for clarity.

the correlation between σ_{ε_2} and σ_{v_2} . We notice that both σ_{ε_2} and σ_{v_2} slowly decrease with increasing N_{part} , and in the (5 – 60)% centrality class the centrality dependence of σ_{ε_2} very well captures that of σ_{v_2} . Most peripheral events are kept outside the purview of our analysis. The observation should be understood as a linear mapping of the $\sigma_{v_2} \propto \sigma_{\varepsilon_2}$ relation, which manifests that the initial eccentricity fluctuation predominantly contributes to the elliptic flow fluctuation. We also intend to compare the p_T -dependence of v_2 computed from the participant plane method and cumulant method. From Figure 3.30 we see that for all centrality classes the simulated v_2 -values computed in different ways, grow almost linearly

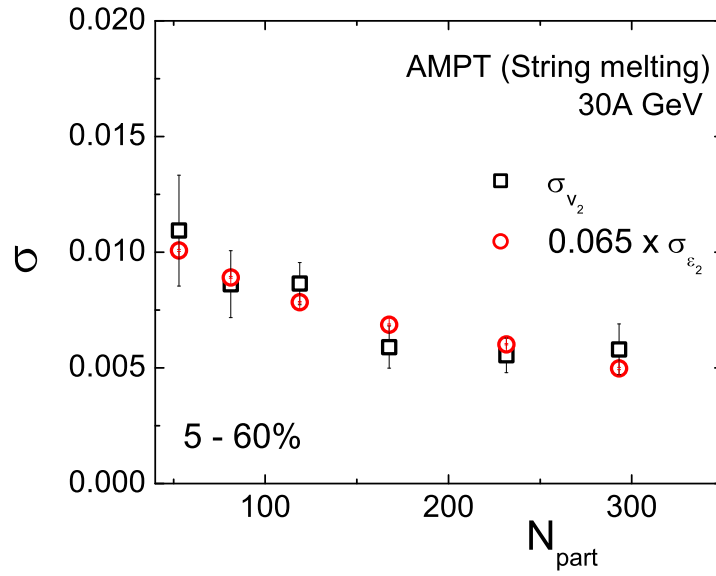


Figure 3.29: Centrality dependence of elliptic flow fluctuation and eccentricity fluctuation in Au+Au collisions at $E_{\text{lab}} = 30A$ GeV.

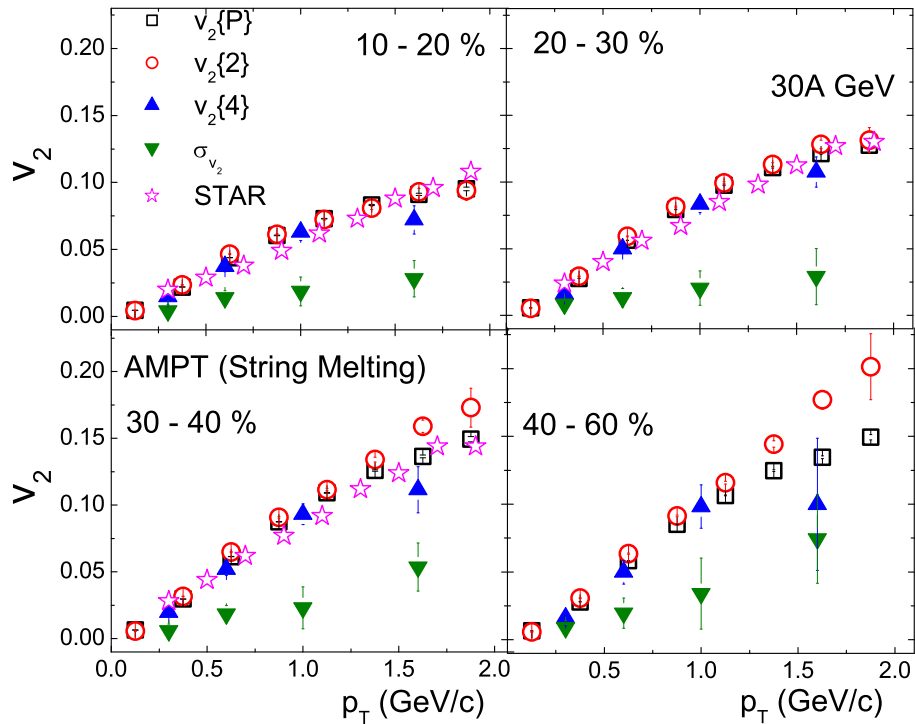


Figure 3.30: v_2 computed by various techniques and fluctuation in v_2 plotted against p_T for charged hadrons at midrapidity in Au+Au collisions at $E_{\text{lab}} = 30A$ GeV.

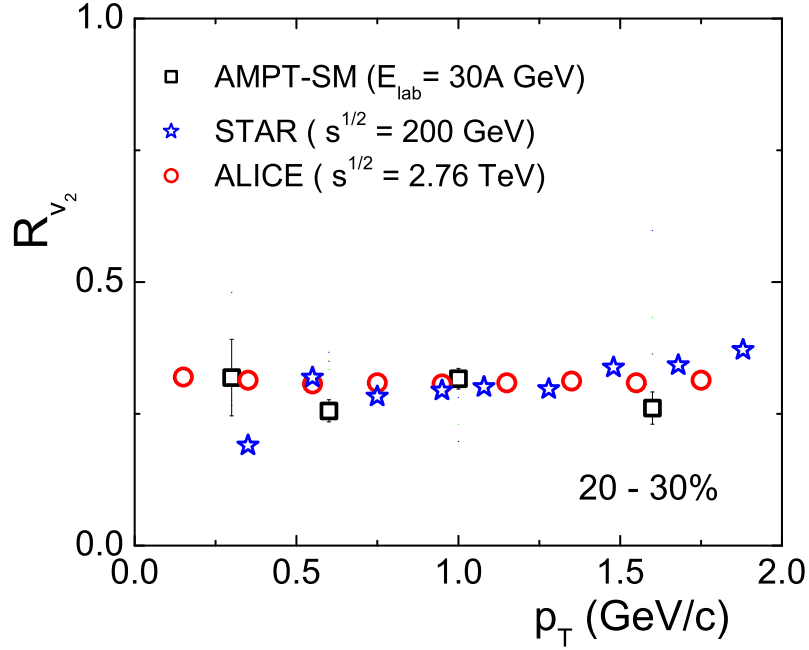


Figure 3.31: Relative v_2 fluctuation as a function of p_T . Experimental data points at RHIC are taken from [64, 65] and those at LHC from [66].

with increasing p_T , and they are in well agreement with the data on Au+Au collision at $\sqrt{s_{NN}} = 7.7$ GeV available from the RHIC experiment. Due to statistical reasons $v_2\{4\}$ is estimated for a limited number of p_T -intervals. In the high- p_T region a saturating tendency is observed in the p_T -dependence of $v_2\{4\}$. Within a particular centrality interval, fluctuations in v_2 behave almost similarly as the v_2 -values themselves. σ_{v_2} shows an approximately linear growth with p_T , which becomes more prominent in the peripheral collisions. In order to better understand the impact of collision energy on flow fluctuations, we define the relative flow fluctuation as $R_{v_2} = \sigma_{v_2}/v_2\{\text{est}\}$. In Figure 3.31 we present the p_T -dependence of R_{v_2} over a wide range of energy, starting from $E_{\text{lab}} = 30A$ GeV, through RHIC ($\sqrt{s_{NN}} = 200$ GeV) and ending at LHC ($\sqrt{s_{NN}} = 2.76$ TeV). Surprisingly, we find that within statistical uncertainties the magnitude of relative flow fluctuation remains almost same at all energies from FAIR (simulated results) to LHC, though the energy difference is about three orders in magnitude. This can be attributed to some common mechanism that gives rise to the flow fluctuation in heavy-ion systems. Moreover within errors R_{v_2} is also independent of p_T , which signifies that the most significant contribution to flow fluctuations is coming from fluctuations in the initial state distributions of participating nucleons. In a different simulation study it has been argued that R_{v_2} should be independent of hadronic scattering effects [63]. In that sense this could be a unique observable that can detect partonic effects, if there is any, particularly at the FAIR energies.

3.3 Conclusion

We have performed a simulation study on the azimuthal anisotropy, particularly on the elliptic and triangular flow of charged hadrons produced in Au+Au system at $E_{\text{lab}} = (10 - 40)A$ GeV, and presented the results obtained thereof in this chapter. We have used event generators like the UrQMD, AMPT (default) and AMPT (string melting). The collision system and collision energies are so chosen as to match with the conditions expected at the upcoming CBM experiment at FAIR. The simulated results presented in this chapter will allow us to pin point our expectations regarding the collective behaviour of particles coming out of baryon-rich fireballs produced in heavy-ion interactions at FAIR energies, and compare them with the experiments where similar as well as significantly different collision energies are involved. We observe that elliptical anisotropy is maximum in the mid-central collisions and in events generated by the AMPT string melting model. On the other hand triangular flow is almost independent of the collision centrality and the UrQMD model does not at all produce any triangular flow. We notice that $\varepsilon_{\text{part}}$, and not ε_{std} , is the proper quantification of the geometrical anisotropy present in the overlapping part of the colliding nuclei. Dependence of the flow parameters on N_{part} , p_T , and η of the emitted charged hadrons do not show any unusual behaviour. Event-to-event fluctuations not only result in a non-zero triangular flow in the AMPT models, but they also have a small but definite impact on the elliptic flow. If the effect of geometry is taken care of, both the elliptic and triangular flow parameters rises monotonically with particle density in the transverse plane, an indication of multiplicity scaling. Mass ordering of the flow parameters of charged hadrons belonging to different species are preserved in all the models involved in our analysis. But the scaling with respect to their constituent quark numbers is observed only in the AMPT string melting model. On several occasions AMPT (string melting) turns out to be most suitable candidate to explain the experimental Au+Au data at $\sqrt{s_{NN}} = 7.7$ GeV available from the STAR beam energy scan program. Elliptic flow coefficient has been estimated from two- and four-particle correlations employing the Q -cumulant method. The difference between $v_2\{4\}$ and $v_2\{2\}$, after eliminating the non-flow short range correlations, is attributed to flow fluctuations. Eccentricity fluctuation can well describe the flow fluctuation. In view of the upcoming CBM program we believe that the present investigation will be useful to serve as a precursor to the real experimental results.

Bibliography

- [1] K. Adcox *et al.* (PHENIX Collaboration), Nucl. Phys. A **757**, 184 (2005).
- [2] J. Adams *et al.* (STAR Collaboration), Nucl. Phys. A **757**, 102 (2005).

- [3] S. S. Adler *et al.* (PHENIX Collaboration), Phys. Rev. Lett. **94**, 232302 (2005).
- [4] B. Alver *et al.* (PHOBOS Collaboration), Phys. Rev. Lett. **98**, 242302 (2007).
- [5] K. Aamodt *et al.* (ALICE Collaboration), Phys. Rev. Lett. **105**, 252302 (2010).
- [6] J.-Y. Ollitrault, Phys. Rev. D **46**, 229 (1992).
- [7] S. A. Voloshin and Y. Zhang, Z. Phys. C **70**, 665 (1996).
- [8] H. Sorge, Phys. Rev. Lett. **78**, 2309 (1997).
- [9] L. Adamczyk *et al.* (STAR Collaboration), Phys. Rev. C **86**, 054908 (2012).
- [10] B. Abelev *et al.* (ALICE Collaboration), Jour. High Energy Phys. **06**, 190 (2015).
- [11] J. Adam *et al.* (ALICE Collaboration), Phys. Rev. Lett. **116**, 132202 (2016).
- [12] T. Hirano *et al.*, Phys. Lett. B **636**, 299 (2006).
- [13] M. Luzum and P. Romatschke, Phys. Rev. Lett. **103**, 262302 (2009).
- [14] N. Armesto *et al.*, J. Phys. G **35**, 054001 (2008).
- [15] A. M. Poskanzer and S. A. Voloshin, Phys. Rev. C **58**, 1671 (1998).
- [16] A. Bilandzic, Phys. Rev. C **83**, 044913 (2011).
- [17] H. Sorge, Phys. Rev. Lett. **82**, 2048 (1999).
- [18] <https://www.sdcc.bnl.gov/phobos/>
- [19] N. Borghini, P. M. Dinh, and J. -Y. Ollitrault, Phys. Rev. C **64**, 054901 (2001).
- [20] C. Alt *et al.* (NA49 Collaboration), Phys. Rev. C **68**, 034903 (2003).
- [21] A. Bilandzic *et al.*, Phys. Rev. C **89**, 064904 (2014).
- [22] Y. Zhou (for the ALICE Collaboration), Nucl. Phys. A **931**, 949 (2014).
- [23] L. Ma, G. L. Ma, and Y. G. Ma, Phys. Rev. C **94**, 044915 (2016).
- [24] S. Voloshin, A. Poskanzer, A. Tang, and G. Wang, Phys. Lett. B **659**, 537 (2008).
- [25] B. Alver *et al.* (PHOBOS Collaboration), Phys. Rev. Lett. **98**, 242302 (2007).
- [26] L. X. Han *et al.*, Phys. Rev. C **84**, 064907 (2011).
- [27] S. A. Voloshin and A. M. Poskanzer, Phys. Lett. B **474**, 27 (2000).
- [28] X. Zhu, M. Bleicher, and H. Stöcker, Phys. Rev. C **72**, 064911 (2005).

- [29] Y. Lu *et al.*, J. Phys. G **32**, 1121 (2006).
- [30] J. Barrette *et al.* (E877 Collaboration), Phys. Rev. C **55**, 1420 (1997).
- [31] J. Barrette *et al.* (E877 Collaboration), Phys. Rev. C **51**, 3309 (1995); Phys. Rev. C **55**, 1420 (1997).
- [32] P. Kolb, J. Sollfrank, and U. Heinz, Phys. Lett. B **459**, 667 (1999).
- [33] P. F. Kolb, P. Huovinen, U. Heinz, and H. Heiselberg, Phys. Lett. B **500**, 232 (2001).
- [34] D.-M. Zhou *et al.*, Euro. Phys. J. A **45**, 353 (2010).
- [35] S. Manly (for the PHOBOS Collaboration), Nucl. Phys. A **774**, 523 (2006).
- [36] J. Aichelin and K. Werner, J. Phys. G **37**, 094006 (2010).
- [37] P. F. Kolb, J. Sollfrank, and U. Heinz, Phys. Rev. C **62**, 054909 (2000).
- [38] A. M. Poskanzer and S. A. Voloshin, Nucl. Phys. A **661**, 341C (1999).
- [39] C. Adler *et al.* (STAR Collaboration), Phys. Rev. C **66**, 034904 (2002).
- [40] S. Chatrchyan *et al.* (CMS Collaboration), Phys. Rev. C **87**, 014902(2013).
- [41] H. Heiselberg and A.-M. Levy, Phys. Rev. C **59**, 2716 (1999).
- [42] B. Alver *et al.*, Phys. Rev. C **82**, 034913 (2010).
- [43] B. Alver and G. Roland, Phys. Rev. C **81**, 054905 (2010).
- [44] H. Caines, Eur. Phys. J. C **49**, 297 (2007).
- [45] R. A. Lacey, Rui Wei, N. N. Ajitanand, and A. Taranenko, Phys. Rev. C **83**, 044902 (2011).
- [46] A. Adare *et al.* (PHENIX Collaboration), Phys. Rev. Lett **105**, 062301 (2010).
- [47] P. Huovinen *et al.*, Phys. Lett. B **503**, 58, (2001).
- [48] S. A. Voloshin, Phys. Rev. C **55**, 1930 (1997).
- [49] H. Li *et al.*, Phys. Rev. C **93**, 051901(R) (2016).
- [50] C. Adler *et al.* (STAR Collaboration), Phys. Rev. Lett. **87**, 182301 (2001).
- [51] B. Abelev *et al.* (STAR Collaboration), Phys. Rev. C **81**, 044902 (2010).
- [52] C. Adler *et al.* (STAR Collaboration), Phys. Rev. Lett. **89**, 132301 (2002).

- [53] M. Nasim *et al.*, Phys. Rev. C **82**, 054908 (2010).
- [54] L. Zheng, H. Li, H. Qin, Q.-Y. Shou, and Z.-B. Yin, Eur. Phys. J. A **53**, 124 (2017).
- [55] P. P. Bhaduri and S. Chattopadhyay, Phys. Rev. C **82**, 034906 (2010).
- [56] D. Molnar and S. A. Voloshin, Phys. Rev. Lett. **91**, 092301 (2003).
- [57] X. Dong *et al.*, Phys. Lett. B **597**, 328 (2004).
- [58] S. Afanasiev *et al.* (PHENIX Collaboration), Phys. Rev. Lett. **99**, 052301 (2007); J. Adams *et al.* (STAR Collaboration), Phys. Rev. Lett. **92**, 052302 (2004); A. Adare *et al.* (PHENIX Collaboration), Phys. Rev. Lett. **98**, 162301 (2007); L. Adamczyk *et al.* (STAR Collaboration), Phys. Rev. C **93**, 014907 (2016); B. I. Abelev *et al.* (STAR Collaboration), Phys. Rev. C **77**, 054901 (2008).
- [59] P. Sorensen, Quark-Gluon Plasma 4, edited by R. C. Hwa and X.-N. Wang, World Scientific, Singapore (2010), pp.323-374.
- [60] K. Guolianos, Phys. Rep. **101**, 169 (1983).
- [61] X.-M. Li *et al.*, Mod. Phys. Lett. A **25**, 1211 (2010).
- [62] L.-W. Chen, V. Greco, C.-M. Ko, and P. F. Kolb, Phys. Lett. B **605**, 95 (2005).
- [63] L. Ma, G. L. Ma, and Y. G. Ma, Phys. Rev. C **89**, 044907 (2014).
- [64] S. Afanasiev *et al.* (PHENIX Collaboration), Phys. Rev. C **80**, 024909 (2009).
- [65] L. Kumar (for the STAR Collaboration), Nucl. Phys. A **862**, 125 (2011).
- [66] B. Abelev *et al.* (ALICE Collaboration), Phys. Lett. B **719**, 18 (2013).

Chapter 4

Dependence of elliptic and triangular flow parameters on partonic scattering cross-section

The importance of AMPT (string melting) model in describing the results related to collective flow has been established in the last chapter. Keeping this in mind we intend to study the consequences of further tuning the model with different partonic interaction cross sections. Such attempts have already been reported at RHIC and LHC energies [1–6]. The Au+Au collision system at $E_{\text{lab}} = 30A$ GeV considered in this analysis is typical to the FAIR condition. The analysis of particle emission data in heavy-ion collisions at and around $E_{\text{lab}} = 30A$ GeV has its own importances. Near this energy region the nuclear stopping power is expected to be high [7–9]. The QCD matter, if created, is expected to be rich in baryons and have a low to moderate temperature. Calculations based on a statistical model shows that in $^{210}\text{Pb}+^{210}\text{Pb}$ collision, the net baryon density of the intermediate fireball would actually be maximum around $E_{\text{lab}} = 30A$ GeV [10]. Experimental results on the strangeness enhancement suggest that the properties of hadronic/partonic matter produced near 30A GeV might be different from that produced either moderately below or above this energy [11]. Elliptic flow exhibits strong hydrodynamic behaviour which is an indication that the matter formed in an AB collision is thermalized within a very short time and collectively expands almost like a perfect fluid with low shear viscosity over entropy (η/s) [12, 13]. A combined analysis of v_2 and v_3 is recommended, particularly their relative strength has the potential to provide valuable information regarding the specific viscosity (η/s) of the medium [14]. Following the arguments of viscous hydrodynamics [15, 16], one

of the basic goals of this investigation is to shed some light on the sensitivity of the flow parameters to viscous effects. Issues related to higher harmonic viscous damping [17] can be better understood by varying the degree of partonic scattering.

4.1 Results and discussion

In this section we shall examine different issues related to the elliptic and triangular flow in Au+Au collision at $E_{\text{lab}} = 30A$ GeV using the string melting version of AMPT tuning the parton scattering cross section. In this investigation the scattering cross sections, usually denoted by σ , are chosen to be 1.5 mb, 3 mb, 6 mb, and 10 mb. While comparing our

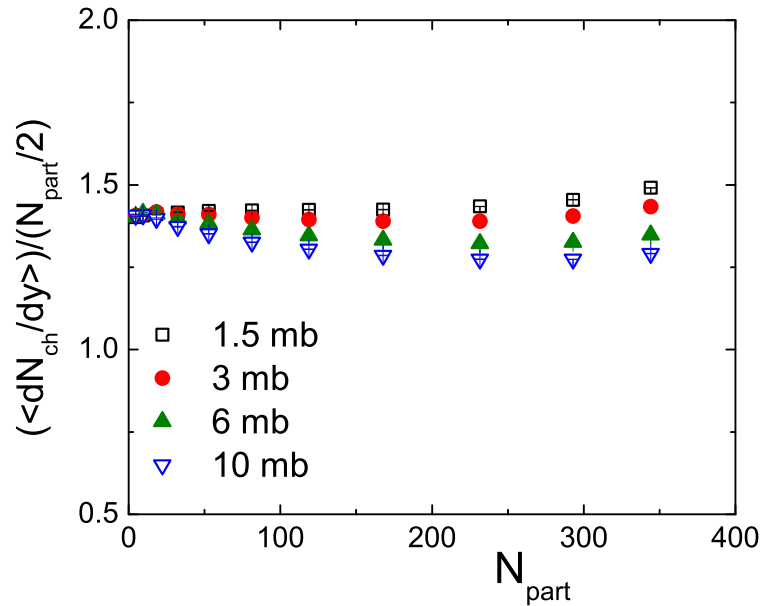


Figure 4.1: Centrality dependence of integrated yield of charged hadrons in Au+Au collisions at $E_{\text{lab}} = 30A$ GeV for different parton interaction cross sections.

simulation results with the NA49 experiment, we have used even a smaller value, $\sigma = 0.1$ mb. For each σ we have generated 10^6 minimum bias Au+Au event sample. The charged hadron multiplicity density per participant pair or the normalized yield in the central particle producing region for each σ , is graphically presented against N_{part} in Figure 4.1. For $\sigma = 1.5$ (10) mb the yield is found to be highest (lowest), and for a particular σ the yield is either independent of centrality, or decreases very slowly. We observe that a higher σ results in a marginally smaller yield, a feature that becomes a little more pronounced in central collisions. Our analysis is restricted only to the charged hadrons. Therefore, at this stage it is not quite possible to conclude whether this observation has something to do with any special feature of partonic level interactions, or is a mere artifact of energy sharing by

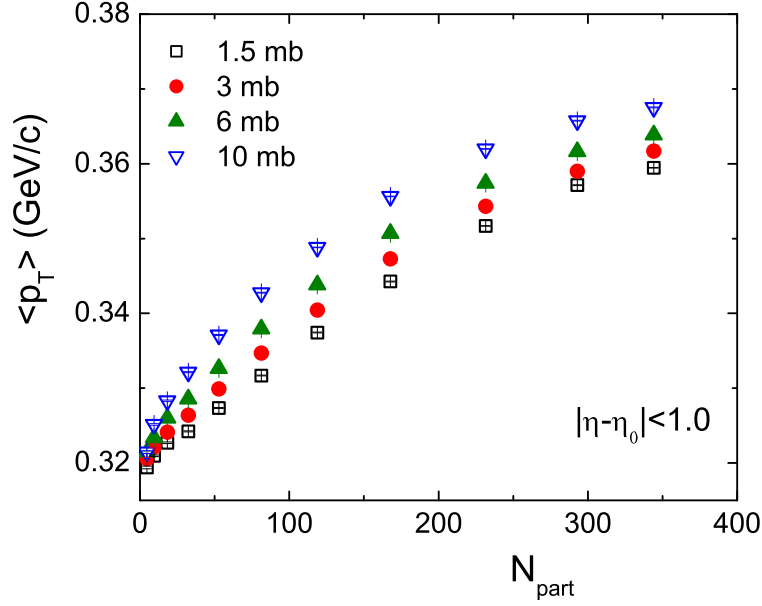


Figure 4.2: Average transverse momentum of charged hadrons at midrapidity plotted against centrality in Au+Au collisions at $E_{\text{lab}} = 30A$ GeV for different parton interaction cross sections.

some other processes like thermalization and/or collective flow. In Figure 4.2 the average transverse momentum $\langle p_T \rangle$ is plotted against the centrality measure N_{part} for different σ -values. We see that $\langle p_T \rangle$ monotonically increases with increasing N_{part} upto ≈ 300 , though at high centralities a tendency to saturate is quite visible. For the most central class of events $\langle p_T \rangle$ values for different σ lie within a narrow range between 0.32 and 0.37 GeV/c, with a mean lying somewhere around 0.34 GeV/c. At all centralities we observe that a higher σ consistently results in a higher $\langle p_T \rangle$, indicating thereby that the chance of binary interaction positively influences the extent to which transverse degrees of freedom are excited in the intermediate fireball. A higher saturation value of $\langle p_T \rangle$ is attributed to a higher isotropic radial flow of charged hadrons in the transverse plane. This also perhaps partially explains why a lower particle yield is found at a higher σ -value.

4.1.1 Initial geometric dependence of v_2 and v_3

Taking the initial fluctuations into account we have calculated the elliptic (v_2) and triangular (v_3) flow parameters as functions of respectively eccentricity and triangularity in four different intervals of centrality and for four different σ -values considered in this analysis. The results are shown in Figure 4.3 and Figure 4.4. Extreme central and peripheral collisions are kept out of the purview of this part of our analysis. It is observed that both v_2 and v_3 grow linearly with increasing geometric measure of anisotropy of the overlapping part of the colliding nuclei as well as with increasing σ . However, we also notice that with

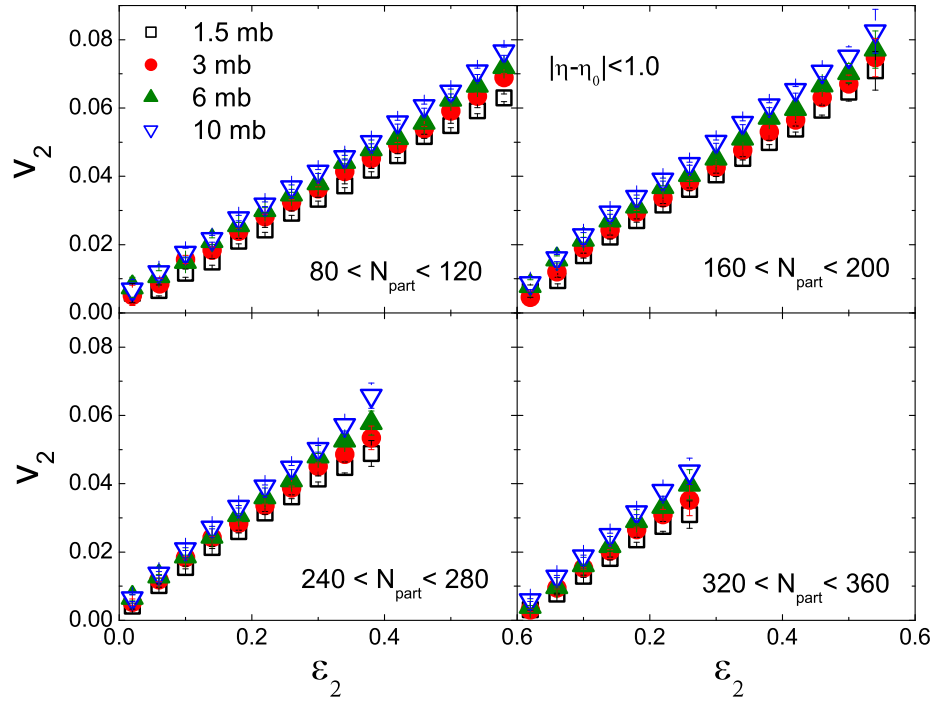


Figure 4.3: v_2 as a function of ε_2 in different N_{part} intervals for Au+Au collision at $E_{\text{lab}} = 30A$ GeV for different parton interaction cross sections.

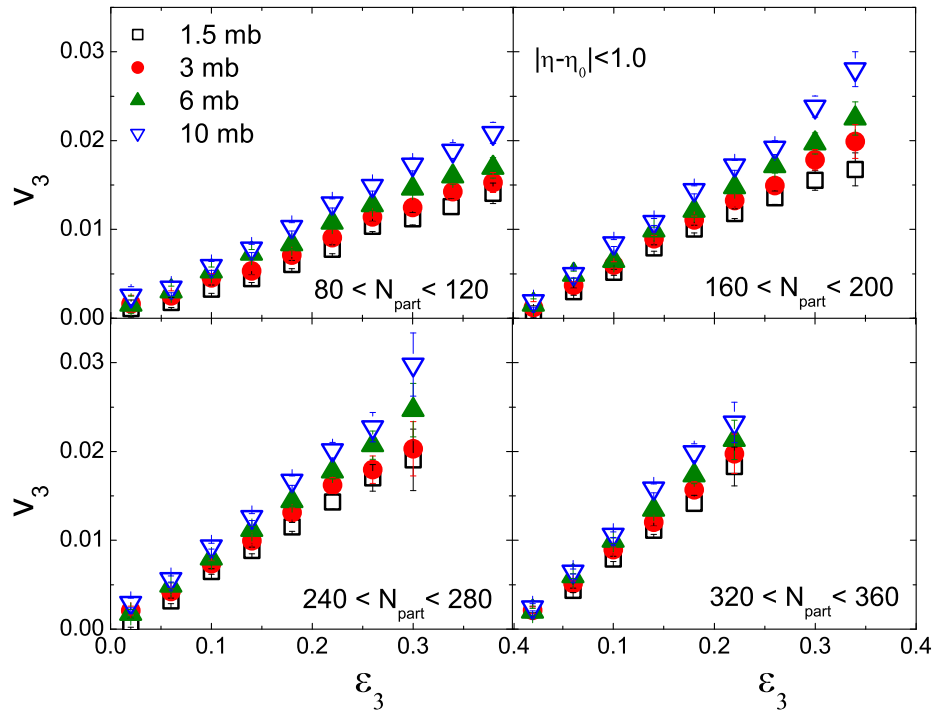


Figure 4.4: v_3 as a function of ε_3 in different N_{part} intervals for Au+Au collision at $E_{\text{lab}} = 30A$ GeV for different parton interaction cross sections.

increasing ε_2 the rise in v_2 is steeper than that of v_3 with increasing ε_3 . As expected, this is an indication that the efficiency with which the initial spatial anisotropy gets converted into the final state momentum space anisotropy, is more in elliptic flow than that in the triangular flow. One should, however, keep it in mind that the latter is not a consequence of any dynamics, but merely is an outcome of initial fluctuations in the numbers and distributions of participating nucleons in coordinate space. It is also interesting to note that for the four centrality intervals considered, the v_n versus ε_n ($n = 2, 3$) dependence becomes slightly steeper with increasing centrality, a feature that is more prominent in v_3 , and an observation which is almost similar to that of [18] at a RHIC energy.

4.1.2 Centrality dependence of v_2 and v_3

Figure 4.5 and Figure 4.6 show the centrality dependence of charged hadron elliptic flow and triangular flow parameters at midrapidity for different partonic scattering cross sections. In order to compare our v_2 -results with the available STAR data, the kinematic region $0.2 \leq p_T \leq 2.0$ GeV/c chosen for the simulation is same as that of the experiment. Both v_2 and v_3 are found to increase with N_{part} in the peripheral region, which implies that peripheral collisions are less efficient in converting the initial state spatial asymmetries into the final state momentum space anisotropy. A higher σ consistently results in a higher elliptic and triangular flow, which indicates the positive influence of partonic interactions in generating collective flow even at FAIR energies. It has been noted in the previous chapter

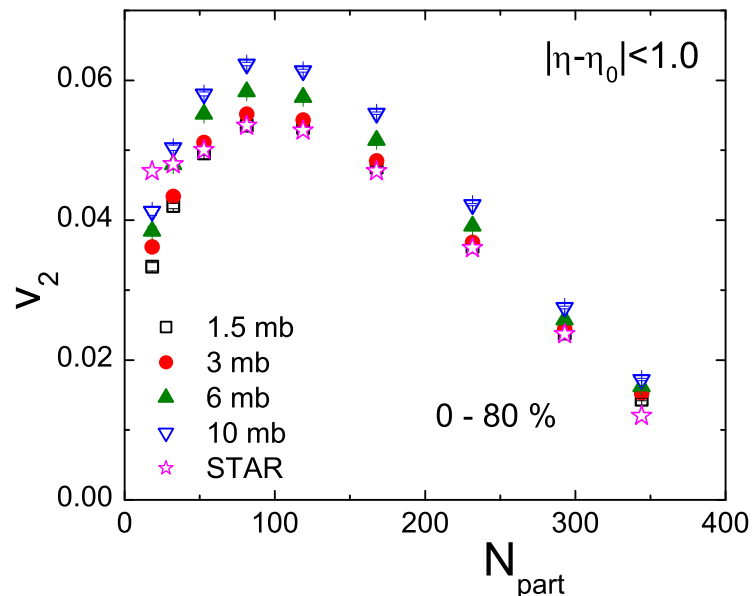


Figure 4.5: Centrality dependence of elliptic flow of charged hadrons at midrapidity in Au+Au collision at $E_{\text{lab}} = 30A$ GeV for different parton interaction cross sections. STAR data is taken from [3]

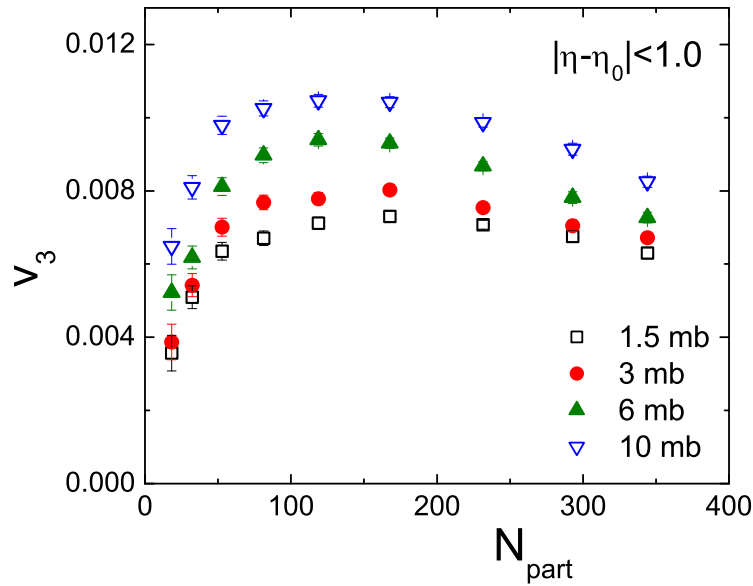


Figure 4.6: Centrality dependence of triangular flow of charged hadrons at midrapidity in Au+Au collision at $E_{\text{lab}} = 30A$ GeV for different parton interaction cross sections.

that except the most central and peripheral collisions, AMPT (string melting) with $\sigma = 3$ mb could reasonably well describe the v_2 -data without considering the initial state fluctuations. When event-by-event fluctuations present in the initial state are considered, $\sigma = 1.5$ mb seems to be a slightly better choice at $E_{\text{lab}} = 30A$ GeV. Previously it has been reported that the RHIC and LHC data are perhaps associated with a higher binary cross section [1]. However, a particular σ -value could neither describe the centrality dependence of v_2 and v_3 over the entire centrality range, nor could describe the same for v_2 and v_3 simultaneously. It is obvious that v_3 arises only from the event-by-event fluctuations of the participating nucleons present within the overlapping part of the collision system. Perhaps it is due to this reason v_3 very marginally depends on centrality in the mid-central to most central range. A comparison between Figure 4.5 and Figure 4.6 reflects that the influence of scattering cross section is more pronounced in v_3 rather than in v_2 . The maximum v_3 corresponding to the lowest and highest σ values differ almost by 43%, whereas the same for v_2 is about 16% only. It is argued in [19, 20] that within the perspective of viscous hydrodynamics higher partonic scattering cross section is analogous to lower viscosity. In that sense v_3 may be considered to be more sensitive to the in-medium viscous effects. In Figure 4.7 and Figure 4.8 we schematically represent the centrality dependence of v_n/ε_n , a ratio known to be related to the freeze-out temperature [21]. Though in Figure 4.3 we find that within large centrality intervals v_2 is proportional to ε_2 , as the minimum bias Au+Au event samples are classified into finer centrality intervals, the v_2/ε_2 -ratio actually shows a lot of variation with varying N_{part} . We see that in the low-centrality region the ratio v_2/ε_2 increases almost linearly with increasing centrality, the variation becomes nonlinear in the midcentral region reaching a

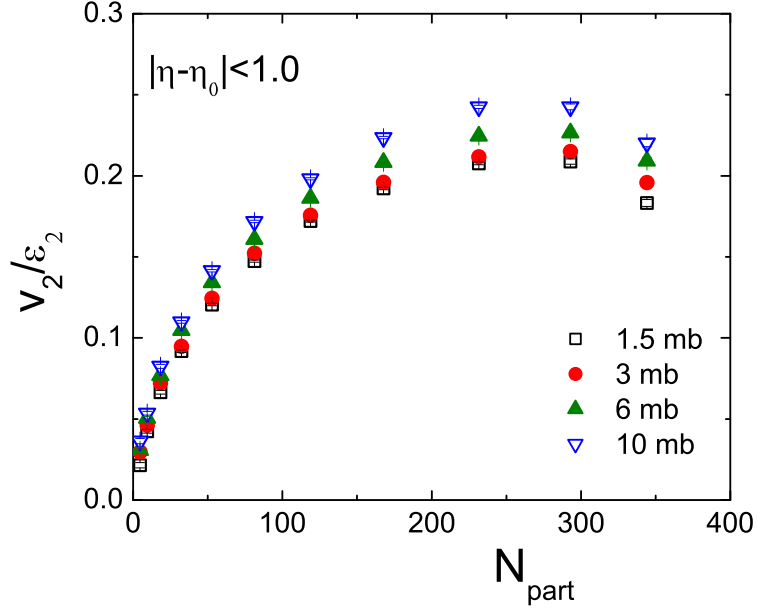


Figure 4.7: Elliptical flow scaled by eccentricity against centrality for different parton interaction cross sections at midrapidity for Au+Au collision at $E_{\text{lab}} = 30A$ GeV.

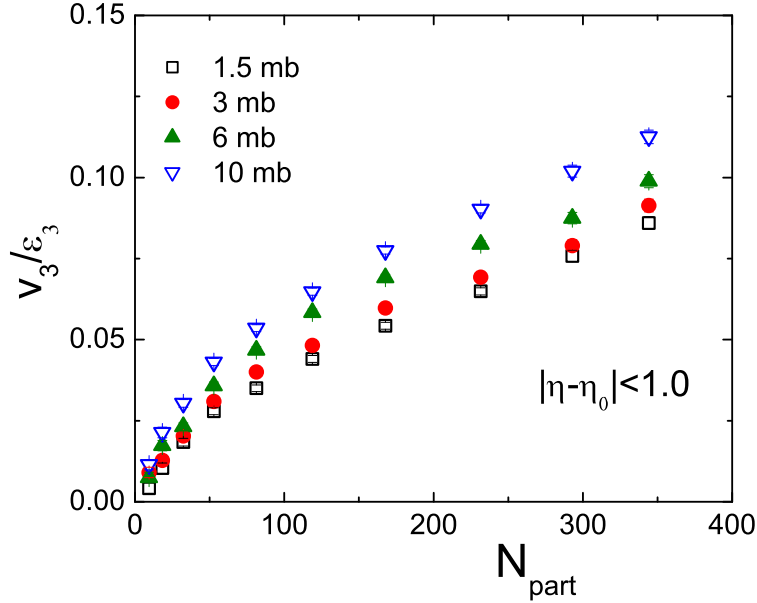


Figure 4.8: Triangular flow scaled by triangularity against centrality for different parton interaction cross sections at midrapidity in Au+Au collision at $E_{\text{lab}} = 30A$ GeV.

maximum at $N_{\text{part}} \approx 250$ for all σ -values, and finally the ratio drops down from its maximum point within a small interval of a few highest centrality classes. We note that the spatial asymmetry of the almond-shaped overlapping part of the colliding nuclei is vanishingly small in the highest centrality classes. It has been argued that in the low-density limit of the intermediate fireball created in AB collisions, the elliptic flow should be proportional to the elliptic anisotropy and the initial particle density [22], which certainly is not the case in

our analysis. As the elliptic flow parameter is scaled by the eccentricity, the ratio is higher at a higher σ -value considered in this analysis. The triangular flow parameter, when scaled by the corresponding triangularity, increases monotonically (almost linear) with increasing N_{part} . Once again a higher σ consistently results in a higher triangular flow scaled by the triangularity. It appears that an experimentally obtained v_n/ε_n -ratio can be modeled within the framework of the AMPT (string melting) model by suitably adjusting the σ -value and a few other parameters. To further verify the behaviour of scaled elliptical flow under the low-density limit, in Figure 4.9 we have plotted the v_2/ε_2 -ratio against the particle density in the transverse plane. Once again it is found that, except for a few very high centrality intervals, a proportionality like,

$$\frac{v_2}{\varepsilon_2} \propto \frac{1}{S} \frac{dN_{ch}}{dy} \quad (4.1)$$

holds good. The proportionality constant may depend on the hydro-limit of v_2/ε_2 , the binary scattering cross section, and the velocity of the elastic wave in the medium concerned [23]. Here S is the transverse area of the overlapping zone of the colliding nuclei, and dN_{ch}/dy is the rapidity density (a measure of rescattering within the fireball) of charged hadrons. A higher σ corresponds to a higher slope of the linear relationship between v_2/ε_2 and $S^{-1}(dN_{ch}/dy)$ as prescribed in Equation (4.1). At a few extreme high centralities the observed deviation from the linear rising trend of the rest, may be attributed to a large number of (re)scatterings that dilutes all kind of correlations including that related to the

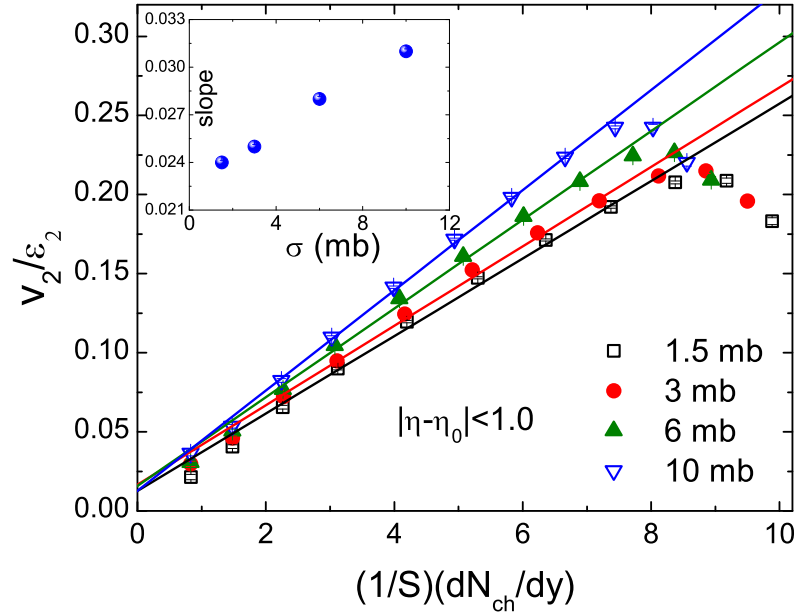


Figure 4.9: Elliptical flow scaled by eccentricity plotted against particle density in the transverse plane for Au+Au collision at $E_{\text{lab}} = 30A$ GeV for different parton interaction cross sections. Solid lines represent best fits to the data.

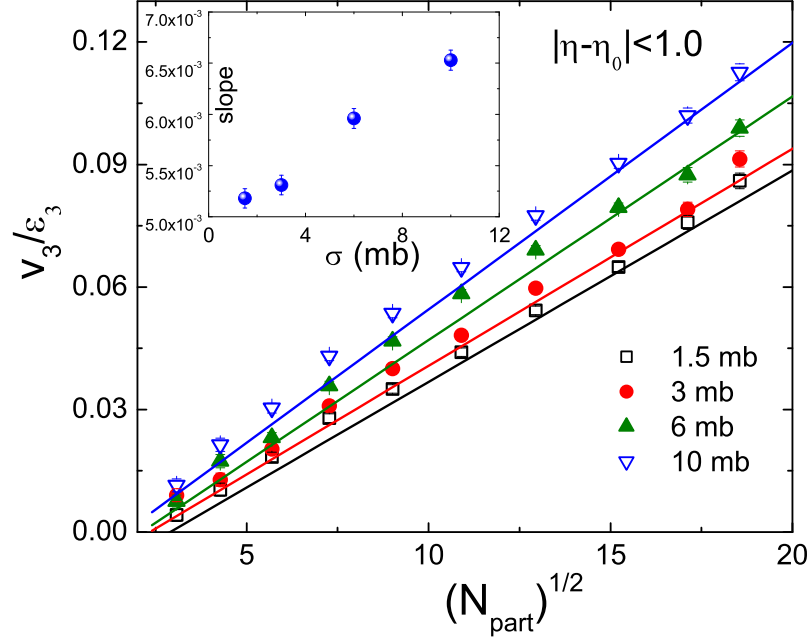


Figure 4.10: Triangular flow scaled by triangularity against $\sqrt{N_{\text{part}}}$ for different parton interaction cross sections at midrapidity in Au+Au collision at $E_{\text{lab}} = 30A$ GeV. Solid lines represent best fits to the data.

collective behaviour as well. The variation of the slope with partonic cross section is presented in the inset of Figure 4.9. We suggest that this diagram can be employed as a calibration curve to trace back the degree of partonic effect from the experimentally determined slope of the v_2/ε_2 versus transverse particle density. We follow a similar technique for v_3/ε_3 -ratio, now transverse particle density is being replaced by $N_{\text{part}}^{1/2}$. An investigation of this kind was introduced in [24] at different beam energies available at the RHIC. We have extended the idea to be applied for different partonic scattering cross sections. Unlike v_2/ε_2 -ratio where the most central events are found to deviate significantly from the linear trend of the rest, in Figure 4.10 we see that a linear relationship between v_3/ε_3 and $N_{\text{part}}^{1/2}$ is obeyed at all centralities. Once again from the inset of Figure 4.10 the slope of the linear fit is found to monotonically rises with increasing σ , and the same argument of employing it as a calibration curve to determine the extent of partonic degrees of freedom holds good in this case too.

4.1.3 Relative strength of v_2 and v_3

We now measure the relative magnitude of the triangular flow with respect to the elliptic flow as a function of N_{part} in different p_T -intervals. In Figure 4.11 we plot the v_3/v_2 -ratio against N_{part} for the 0 – 80% centrality interval and for different σ -values. It is seen that the v_3/v_2 -ratio initially remains almost unchanged and then increases non-linearly with

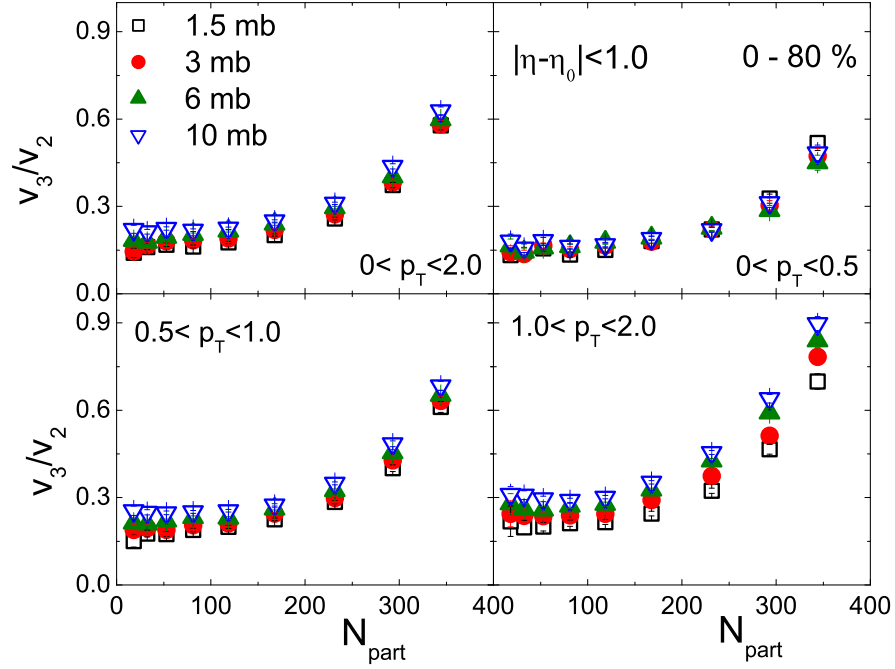


Figure 4.11: Dependence of v_3/v_2 on N_{part} in different p_T bins for Au+Au collision at $E_{\text{lab}} = 30A$ GeV for different parton interaction cross sections.

increasing centrality following almost a power-law. In the previous chapter this kind of centrality dependence was attributed to multiplicity scaling [25]. In the smallest p_T -interval ($0 \leq p_T \leq 0.5$ GeV/c), the centrality dependence of v_3/v_2 -ratio is almost independent of σ . As shown in Figure 4.11, the σ -dependence of v_3/v_2 -ratio increases in the wider p_T -ranges.

4.1.4 Transverse momentum dependence of v_2 and v_3

The role of partonic interactions in exciting the transverse degrees of freedom after a relativistic AB collision has been discussed at the beginning. Now, its time to scrutinize the concurrent influence of parton scattering cross section and transverse momentum on the harmonic flow coefficients. In Figure 4.12 we see that for the 0 – 10% most central collisions, v_2 is almost independent of σ at low- p_T . However, the σ -dependence becomes prominent as we move toward peripheral collisions. It is to be noted that v_2 -values are maximum in the mid-central collisions, where the dependence on partonic cross section at high- p_T is also found to be maximum. In mid-central collisions we see a saturation, and for $\sigma = 1.5$ mb a saturating trend in the p_T -dependence of v_2 is observed at high- p_T . These observations supplement our results presented schematically in Figure 4.5. When we compare our results on v_2 with that obtained from the STAR Au+Au collision at $\sqrt{s_{NN}} = 7.7$ GeV, no single value of σ is found to be good enough to match the experiment everywhere. While $\sigma = 1.5$ mb appears to fit well with the data up to $p_T = 1.0$ GeV/c, experimental v_2 -values at intermediate p_T ($1.0 \leq p_T \leq 1.5$ GeV/c) could be described with cross section of 3 mb, and $\sigma = 6$ mb seems

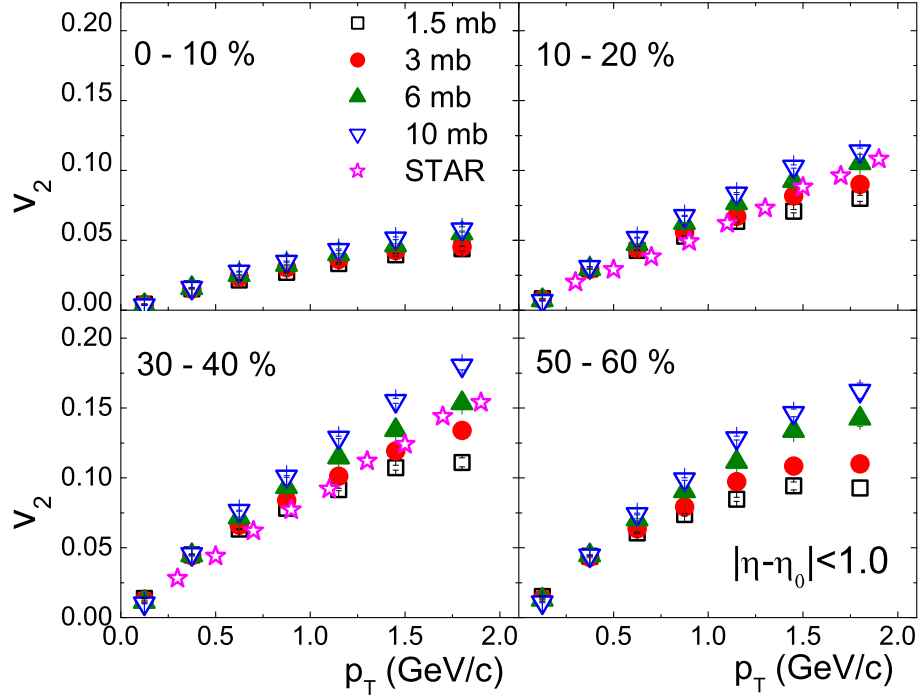


Figure 4.12: p_T dependence of v_2 for different centrality windows at midrapidity in Au+Au collision at $E_{\text{lab}} = 30A$ GeV for different parton interaction cross sections. STAR data is derived from [3].

to follow the trail for $p_T \geq 1.5$ GeV/c. In Figure 4.13 we have studied a similar p_T dependence of v_3 in four different centrality intervals. It is noticed that at each centrality interval considered, the variation of v_3 with p_T is more or less identical to that of v_2 . In other words, the triangular flow is not very sensitive to the collision centrality. This is an expected behaviour, as the elliptic flow is caused by the pressure gradient created over the almond shape of the overlapping part of a collision, while triangular flow is caused from the fluctuations of participating nucleons. Beyond the peripheral collisions, a relatively smaller eccentricity of the overlapping part results in a higher pressure gradient and therefore a larger elliptic flow. However, it is not necessary for the flow generated by initial fluctuations to be significantly influenced by collision centrality. In Figure 4.14 we have plotted v_2 against p_T for charged pions and protons separately as obtained from the NA49 experiment [26]. Corresponding UrQMD and AMPT simulated values are also shown in the graph within the same p_T and same rapidity ranges, as well as using the same centrality criteria as those used in [26]. In spite of using a reasonably wide range of σ -values, i.e. $\sigma = 0.1, 1.5, 3.0, 6.0$ mb, we observe that neither the default nor the string melting version of AMPT can match the entire set of experimental results for any single partonic cross section. In the $0 \leq p_T \leq 1.0$ GeV/c range the experimental points behave in a fairly regular manner, at least in the peripheral (more than 33.5% centrality) and midcentral (12.5–33.5% centrality) collisions. The AMPT in its string melting version however, exceeds the experiment in this region for all partonic cross

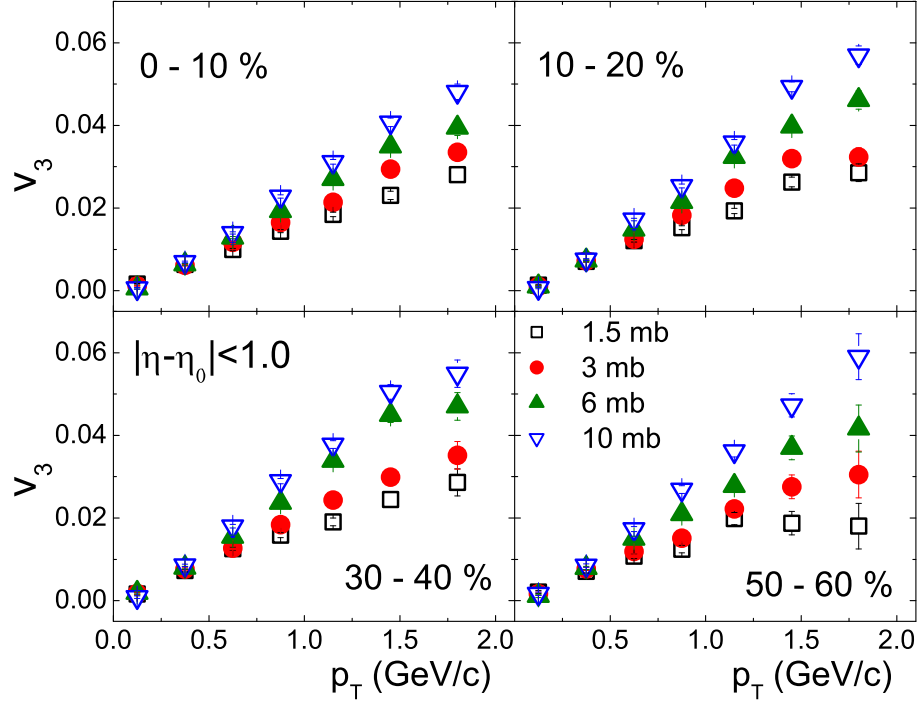


Figure 4.13: p_T dependence of v_3 for different centrality windows at midrapidity in Au+Au collision at $E_{\text{lab}} = 30A$ GeV for different parton interaction cross sections.

sections, albeit AMPT (default) and UrQMD shows fair agreement. It is to be noted that each 40A GeV Pb+Pb simulated event sample used in this context has the same statistics (i.e., 10^6 Pb+Pb min. bias events) as that of the 30A GeV Au+Au event samples used in our investigation. The disagreement between data and simulation observed at low- p_T is more prominent in mid-central collisions for pions, and in peripheral as well as mid-central collisions for protons. The percentage errors (statistical only) associated with the simulated v_2 -values for pions in the $0 \leq p_T \leq 1.0$ GeV/c range are less than 4% in peripheral and less than 3% in mid-central collisions. Corresponding errors for protons are less than 9% in peripheral and less than 5% in mid-central collisions. On the other hand, in most central collisions the experimental values at high- p_T are associated with large errors, and more than one simulation lines pass through them. In order to match the experiment with simulation, either the model perhaps requires a fine tuning and/or to reduce errors, there must be experiments with higher statistics. The CBM experiment is expected to generate much larger statistics than the NA49 experiment, and it would therefore be interesting to see to what extent the flow results of AMPT simulation can come into agreement with the CBM results.

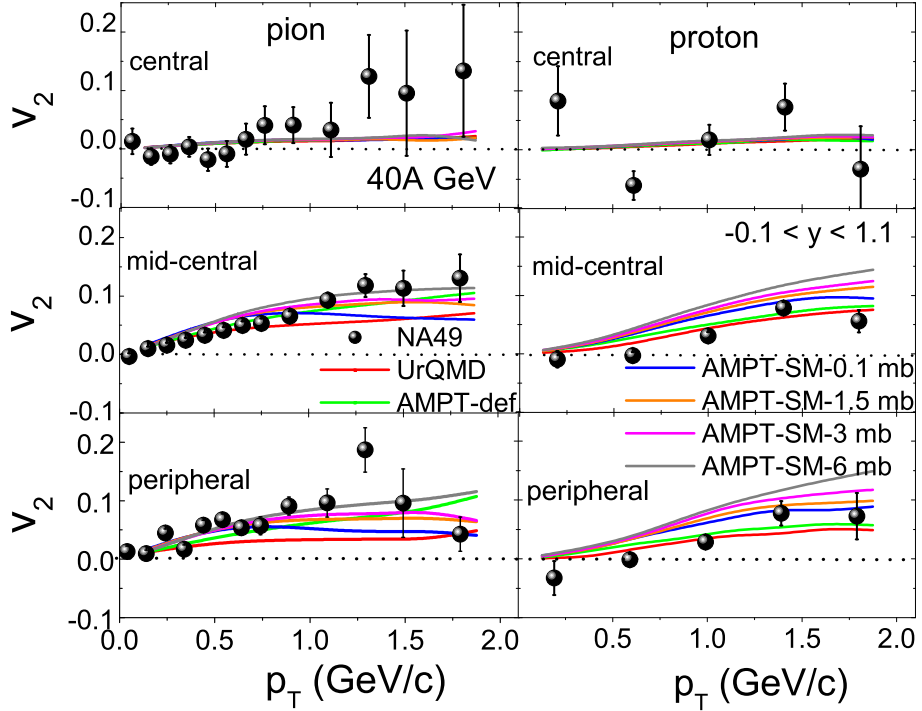


Figure 4.14: NA49 data on p_T dependence of v_2 obtained from Pb+Pb interactions at 40A GeV compared with UrQMD and AMPT simulation (both default and string melting) for pions and protons at different partonic cross sections and at different centralities. The experimental values are shown as points, while corresponding simulations are shown by continuous curves.

4.1.5 Pseudorapidity dependence of v_2 and v_3

The pseudorapidity (η) dependence of flow parameters is expected to inform us about the longitudinal expansion of the fireball system created in an AB collision. Figure 4.15 and Figure 4.16 depict that both v_2 and v_3 are highest valued at mid-rapidity ($\eta_0 \approx 2.2$) and then both fall off in the forward/backward rapidity regions. Maximum particle density in the central rapidity region results in significant (re)scattering among the hadrons, which is being reflected in the high magnitudes of v_2 and v_3 . This picture is again in conformity with the Low Density Limit (LDL) predictions. While measuring the η -dependence of v_2 we have noted that for the 6 mb data, elliptic flow drops almost by 40% in between $|\eta - \eta_0| = 0$ and $|\eta - \eta_0| = 2.0$. In this context it would be worthy to mention that the PHOBOS collaboration has reported a 25% drop in the $v_2(\eta)$ -value within the same kinematic range at $\sqrt{s_{NN}} = 200$ GeV [27], whereas at a typical LHC energy ($\sqrt{s_{NN}} = 2.76$ TeV), ATLAS collaboration noted a very weak η -dependence [28]. Thus, with decreasing collision energy a strong pseudorapidity dependence of v_2 is revealed, which can in general be ascribed to the nuclear stopping [7, 8] and allied effects at FAIR energies. Within the same η -range as discussed above, v_3 drops by approximately 65%. Both v_2 and v_3 distributions have almost Gaussian shape for all scattering cross sections under consideration. However being higher

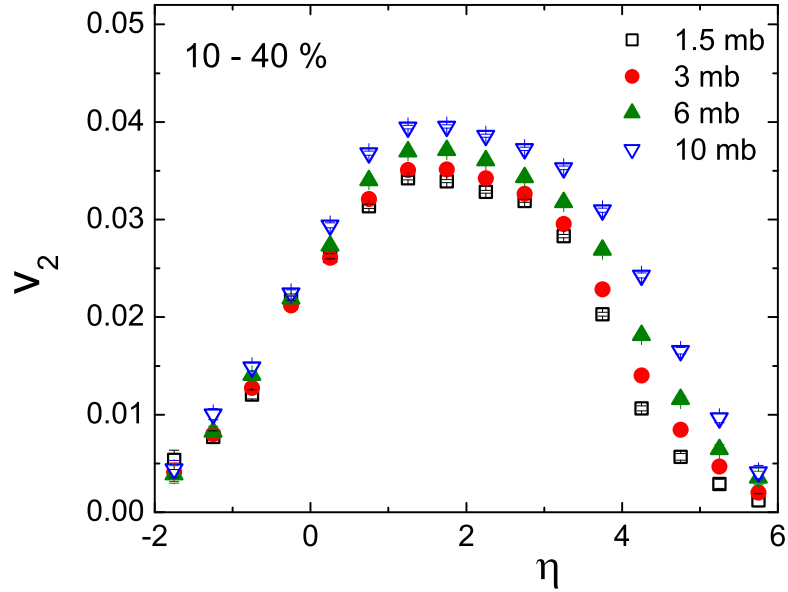


Figure 4.15: Elliptic flow as a function of pseudorapidity for different parton interaction cross sections in Au+Au collision at $E_{\text{lab}} = 30A$ GeV.

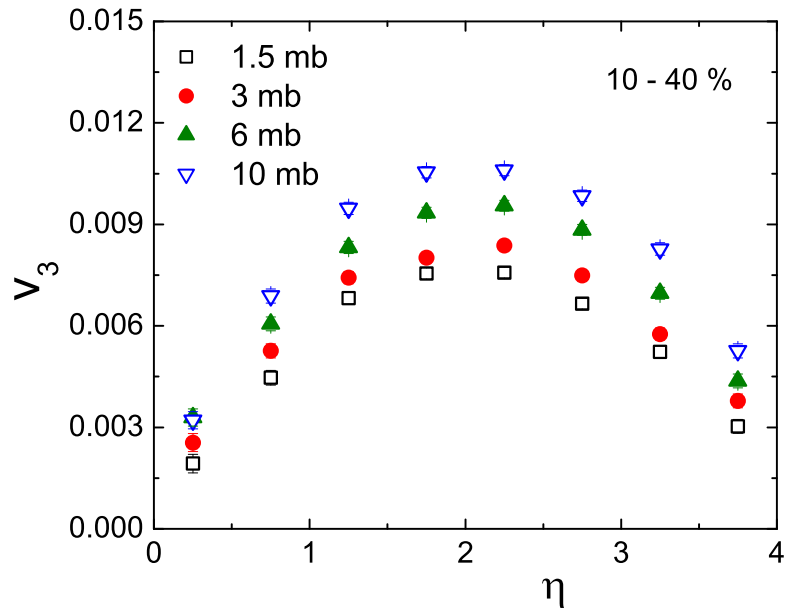


Figure 4.16: Triangular flow as a function of pseudorapidity for different parton interaction cross sections in Au+Au collision at $E_{\text{lab}} = 30A$ GeV.

valued for a higher σ , the probable cause of such a behaviour is nothing but the frequency of partonic interactions at the very early stage. Besides, one should also note a longitudinal scaling type of behaviour in v_2 in the target fragmentation region although the same is absent in v_3 .

4.2 Conclusion

In the framework of the AMPT (string melting) model we have presented some results on the elliptic and triangular flow of charged hadrons produced in Au+Au interactions at $E_{\text{lab}} = 30A$ GeV. Dependence of the flow parameters on initial conditions and partonic scattering cross section are investigated. The dependence of both elliptic and triangular flow parameters on the corresponding geometrical asymmetry, transverse momentum of charged hadrons and centrality of collision behave as expected. Most of the observations can either be interpreted in terms of geometrical effects and/or by the multiplicity scaling. A higher partonic cross section is found to be more efficient in transforming the initial anisotropy, either geometric or fluctuating in nature, to the final momentum anisotropy. The dependence of flow parameters on partonic scattering cross section is almost always qualitatively similar with but quantitatively different from each other by a small amount. Triangular flow is almost independent of the collision centrality but extremely sensitive to the scattering cross section. We also propose a technique to determine the comprehensiveness of partonic activity, if any, present in the hot and dense nuclear matter produced in an AB collision. We believe that these simulated results will help us understand several issues related to the collective behaviour of hadronic and/or partonic matter in a baryon-rich and moderate-temperature environment until real experiments are held. However, more fine tuning of the models is possible if all free parameters are appropriately adjusted.

Bibliography

- [1] L. X. Han *et al.*, Phys. Rev. C **84**, 064907 (2011).
- [2] J. Xu and C. M. Ko, Phys. Rev. C **83**, 034904 (2012).
- [3] L. Adamczyk *et al.* (STAR Collaboration), Phys. Rev. C **86**, 054908 (2012).
- [4] L. Ma, G. L. Ma, and Y. G. Ma, Phys. Rev. C **89**, 044907 (2014).
- [5] X. Sun *et al.*, Phys. G **42**, 115101 (2015).
- [6] L. Ma, G. L. Ma, and Y. G. Ma, Phys. Rev. C **94**, 044915 (2016).
- [7] W. Busza and A. S. Goldhaber, Phys. Lett. B **139**, 235 (1984).
- [8] H. Appelshauser *et al.* [NA49 Collaboration], Phys. Rev. Lett. **82**, 2471 (1999).
- [9] B. B. Back *et al.* (E917 Collaboration), Phys. Rev. C **66**, 054901 (2002).
- [10] J. Randrup and J. Cleymans, Phys. Rev. C **74**, 047901 (2006).

- [11] C. Roland (for the NA49 Collaboration), J. Phys. Conf. Ser. **27**, 019 (2005).
- [12] H. Song *et al.*, Phys. Rev. Lett. **106**, 192301 (2011).
- [13] L. P. Csernai, J. I. Kapusta, and L. D. McLerran, Phys. Rev. Lett. **97**, 152303 (2006).
- [14] E. Retinskaya, M. Luzum, and J.-Y. Ollitrault, Nucl.Phys. A **926**, 152 (2014).
- [15] B. Schenke, S. Jeon, and C. Gale, Phys. Rev. C **82**, 014903 (2010); *ibid* **85**, 024901 (2012).
- [16] E. Retinskaya, M. Luzum, and J.-Y. Ollitrault, Phys. Rev. C **89**, 014902 (2014).
- [17] C. Lang and N. Borghini, Eur. Phys. J. C **74**, 2955 (2014).
- [18] B. Alver and G. Roland, Phys. Rev. C **81**, 054905 (2010).
- [19] B. Zhang, M. Gyulassy, and C. M. Ko, Phys. Lett. B **455**, 45 (1999).
- [20] M. Gyulassy, Y. Peng, and B. Zhang, Nucl. Phys. A **626**, 999 (1997).
- [21] D. Teaney and L. Yan, Phys. Rev. C **83**, 064904 (2011).
- [22] S. A. Voloshin and A. M. Poskanzer, Phys. Lett. B **474**, 27 (2000).
- [23] H.-J. Drescher *et al.*, Phys. Rev. C **76**, 024905 (2007).
- [24] P. Sorensen (for the STAR Collaboration), J. Phys. G **38**, 124029 (2011).
- [25] H. Caines, Eur. Phys. J. C **49**, 297 (2007).
- [26] C. Alt *et al.* (NA49 Collaboration), Phys. Rev. C **68**, 034903 (2003).
- [27] B. B. Back *et al.* (PHOBOS Collaboration), Phys. Rev. C **72**, 051901 (2005).
- [28] G. Aad *et al.* (ATLAS Collaboration), Phys. Lett. B **707**, 330 (2012).

Chapter 5

System-size dependence of collective flow parameters

The PHOBOS collaboration has performed a collective flow analysis of Cu+Cu and Au+Au interactions at $\sqrt{s_{NN}} = 200$ GeV [1]. In this chapter we also intend to perform a similar study over a wider variety of colliding systems at a typical FAIR energy ($E_{\text{lab}} = 30A$ GeV) in the context of the upcoming CBM experiment. The importance of choosing this particular energy value has also been underlined in the previous chapter. We believe that it would be interesting to explore the effects of multiplicity, scattering and geometry on the collective behaviour of final state hadrons produced in small ($^{28}\text{Si}+^{28}\text{Si}$ and $^{59}\text{Ni}+^{59}\text{Ni}$), medium ($^{119}\text{In}+^{119}\text{In}$) and large ($^{197}\text{Au}+^{197}\text{Au}$) sized systems. Apart from the commonly used elliptic flow parameter, significance of non-zero odd harmonics, although not quite as large as the elliptic flow, has already been established. In order to constrain the equation of state of the fireball material, a combined analysis of the first three Fourier harmonics, namely the directed, elliptic and triangular flow is necessary [2–4]. However, in our earlier investigations we did not take the directed flow parameter (v_1) into account. It is to be noted that instead of repeating the basic ideas of second and third harmonics, we simply refer them to the previous chapters of this thesis. In the present investigation we are going to present a system-size dependence of different kinds of distributions of the first three flow harmonics, denoted respectively by v_1 , v_2 and v_3 . It would also be worthwhile to have a comparison between the simulated and experimental results available [1, 5–7]. Once again we have employed the AMPT model in its string melting version to simulate the symmetric AA collision events for the systems considered, where the parton scattering cross section is set to $\sigma = 3$ mb.

5.1 Results and discussions

The minimum bias event samples of our simulated data consist of 10^6 events for the $^{197}\text{Au} + ^{197}\text{Au}$ interaction, 2×10^6 events for the $^{115}\text{In} + ^{115}\text{In}$ interaction, 3×10^6 events for the $^{59}\text{Ni} + ^{59}\text{Ni}$ interaction and 7.5×10^6 events for the $^{28}\text{Si} + ^{28}\text{Si}$ interaction all at $E_{\text{lab}} = 30A$ GeV. If otherwise not mentioned, we shall consider only the charged hadrons falling within the central pseudorapidity region ($|\eta - \eta_0| \leq 1.0$) for our analysis, η_0 being the centroid of the corresponding η -distribution. Figure 5.1 shows the multiplicity distributions of charged hadrons falling within the kinematic cut for the minimum bias event samples mentioned above. With increasing system size an increase in the multiplicity range is an obvious observation. The influence of initial geometric deformation and e-by-e fluctuations present

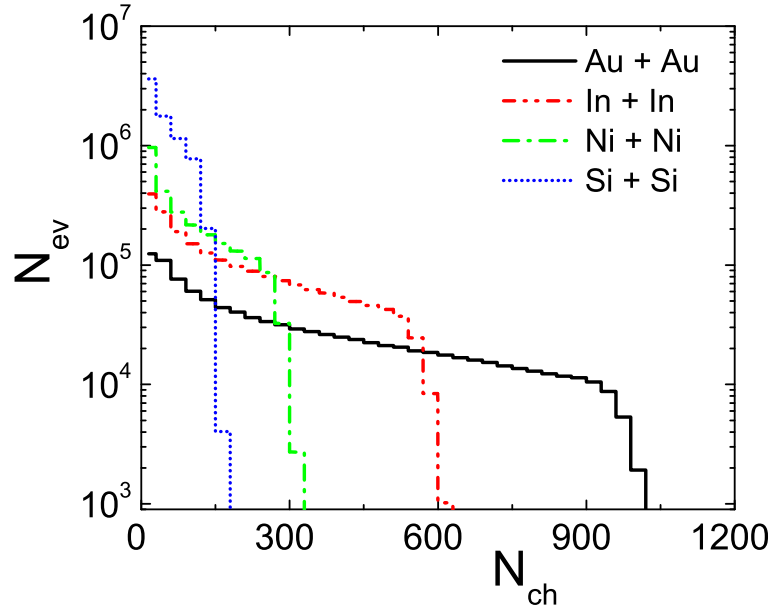


Figure 5.1: Multiplicity distribution of charged hadrons for different colliding systems at $E_{\text{lab}} = 30A$ GeV.

in the initial state has been discussed in the previous chapters, but with reference to the Au+Au system only. To maintain a continuity we briefly recall the different definitions of the initial state deformations once again. The initial geometric deformation of the overlapping region of the colliding nuclei is defined in terms of the nuclear eccentricity parameter given by,

$$\varepsilon_2 = \frac{\sigma_y^2 - \sigma_x^2}{\sigma_y^2 + \sigma_x^2} \quad (5.1)$$

where σ_x and σ_y are the variances in the respective position coordinates of the nucleons present in the overlapping part [8]. Equation (5.1) defines the nuclear eccentricity (ε_{std}), which is restricted only to $n = 2$, and intrinsically biased with an asymmetry definition that drives the flow signal. In small sized systems and peripheral collisions, due to large

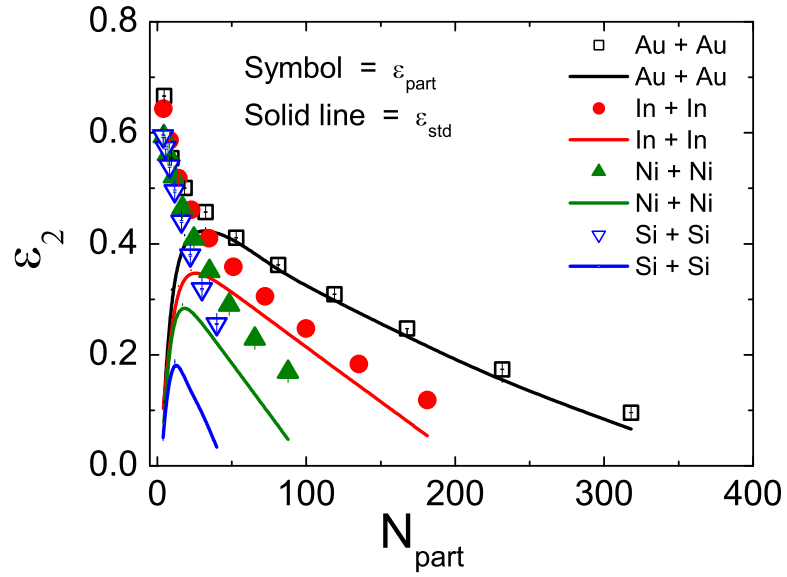


Figure 5.2: Eccentricity as a function of centrality measured in terms of N_{part} .

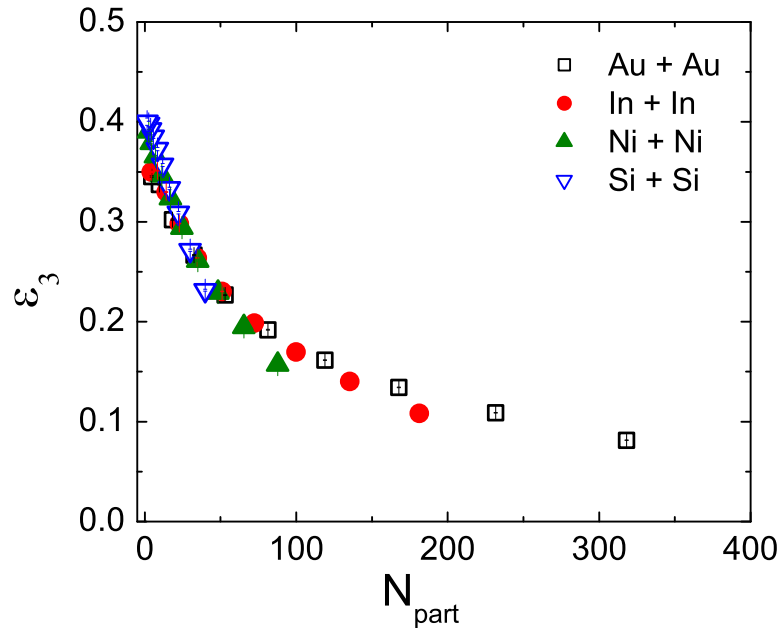


Figure 5.3: Triangularity as a function of N_{part} .

relative fluctuations in the number and position coordinates of the participating nucleons, the minor axis of the overlapping region may not always coincide with the impact parameter. On the other hand, in the central collisions between two large nuclei the nuclear geometry and the participant geometry almost coincide with each other. A more general method of measuring the asymmetry is therefore, to consider the e-by-e initial state fluctuations in the number and position coordinates of the participating nucleons. In this scheme the geometric

anisotropy associated with the n -th harmonic is expressed as [9],

$$\varepsilon_n = \frac{\sqrt{\langle r^2 \cos(n\varphi) \rangle^2 + \langle r^2 \sin(n\varphi) \rangle^2}}{\langle r^2 \rangle} \quad (5.2)$$

Corresponding ε_2 derived from Equation (5.2), is called the participant eccentricity ($\varepsilon_{\text{part}}$). In Figure 5.2 we compare the centrality dependence of both the eccentricity parameters, namely ε_{std} and $\varepsilon_{\text{part}}$. The N_{part} -dependence of the eccentricity parameters can be attributed to geometrical reasons. For all four colliding systems considered in the present analysis, we see that the participant eccentricities are quite high valued in the most peripheral collisions ($\varepsilon_{\text{part}} \approx 60 - 70\%$). As expected, with increasing N_{part} the participant eccentricities monotonically drop down to rather small values ($\varepsilon_{\text{part}} \approx 10 - 20\%$) in each case. For a smaller colliding system the rate of fall is steeper. Peripheral collisions always involve smaller N_{part} . Therefore, for a single event the periodic functions of Equation 5.2 can be averaged over a smaller number of terms. Accordingly the chance that every event will contribute significantly to $\varepsilon_{\text{part}}$, is higher. With increasing centrality N_{part} increases, and for every event the periodic functions are averaged over an increasing number of terms. As a result, the contribution to $\varepsilon_{\text{part}}$ from every event becomes smaller. On the other hand, in the most peripheral collisions nuclear eccentricities are quite small valued ($\varepsilon_{\text{std}} \lesssim 10\%$). In a small overlapping volume the transverse coordinates of the participating nucleons, irrespective of its geometrical asymmetry, are distributed within narrow regions in every direction. Corresponding variances should therefore, be very close to each other and their differences are even smaller. With increasing centrality ε_{std} rises rapidly, attains a maximum, and then falls off gradually at large N_{part} for each colliding system. The distributions are right skewed, and the skewness is higher for a larger system. We notice that only for the largest system (Au+Au), the eccentricity values defined in two different ways agree with each other, that too beyond a certain centrality measure ($N_{\text{part}} \gtrsim 60$). In all other cases ε_{std} is consistently smaller than $\varepsilon_{\text{part}}$. As the initial fluctuations are seen to play an important role, one should be careful in choosing the correct eccentricity expression. It has been argued that if the flow is independent of particle species, $\varepsilon_{\text{part}}$ and not ε_{std} , is a more appropriate parameter that can explain the behaviour of elliptic flow [1]. The geometric deformation associated with the third harmonic ($n = 3$), also called the triangularity parameter (ε_3), can be obtained from Equation (5.2). In Figure 5.3 the ε_3 values are plotted as a function of N_{part} for all the colliding systems. We observe that the variation of ε_3 with N_{part} is nearly independent of the system size. Starting from a moderately high value $\varepsilon_3 \approx (35 - 40)\%$, the triangularity parameter decreases monotonically with increasing N_{part} . Though the N_{part} dependence of ε_3 is quite similar to that of $\varepsilon_{\text{part}}$, as expected $\varepsilon_{\text{part}}$ is almost always higher in magnitude than ε_3 . Our observation on ε_2 and ε_3 agrees reasonably well with another simulation study

Table 5.1: N_{part} dependence of the asymmetry parameters and midrapidity particle densities in different colliding systems at $E_{\text{lab}} = 30A$ GeV.

Centrality	N_{part}	ε_{std}	$\varepsilon_{\text{part}}$	ε_3	$\frac{dN_{\text{ch}}}{d\eta} _{\eta_0}$
Au+Au					
0-10%	318.0±0.08	0.066±0.0003	0.096±0.0002	0.081±0.0001	238.4±0.09
10-20%	231.6±0.07	0.176±0.0003	0.174±0.0002	0.109±0.0002	171.5±0.07
20-30%	167.7±0.06	0.257±0.0004	0.247±0.0003	0.134±0.0002	126.8±0.06
30-40%	118.9±0.05	0.322±0.0005	0.309±0.0004	0.162±0.0003	92.3±0.05
40-50%	81.2±0.04	0.371±0.0006	0.362±0.0004	0.192±0.0003	65.4±0.04
50-60%	52.9±0.04	0.408±0.0007	0.411±0.0005	0.227±0.0004	44.4±0.04
60-70%	32.4±0.03	0.428±0.0009	0.457±0.0005	0.267±0.0004	28.5±0.03
70-80%	18.3±0.02	0.416±0.0013	0.501±0.0007	0.302±0.0006	18.5±0.03
80-90%	9.5±0.02	0.318±0.0014	0.554±0.0006	0.339±0.0005	10.7±0.02
90-100%	4.5±0.01	0.115±0.0021	0.666±0.0008	0.369±0.0007	5.4±0.01
In+In					
0-10%	181.2±0.04	0.054±0.0002	0.119±0.0001	0.108±0.0001	145.5±0.04
10-20%	135.3±0.04	0.144±0.0003	0.183±0.0002	0.14±0.0002	109.0±0.04
20-30%	99.8±0.03	0.214±0.0004	0.248±0.0003	0.17±0.0002	82.1±0.03
30-40%	72.3±0.03	0.269±0.0004	0.306±0.0003	0.199±0.0002	61.3±0.03
40-50%	51.0±0.03	0.311±0.0005	0.359±0.0003	0.23±0.0003	44.9±0.03
50-60%	34.7±0.02	0.341±0.0006	0.41±0.0004	0.264±0.0003	31.9±0.02
60-70%	22.7±0.02	0.353±0.0008	0.461±0.0004	0.298±0.0003	21.8±0.02
70-80%	14.1±0.02	0.324±0.001	0.518±0.0005	0.33±0.0004	14.3±0.02
80-90%	8.3±0.01	0.227±0.0012	0.587±0.0005	0.351±0.0004	9.0±0.01
90-100%	4.1±0.01	0.103±0.0013	0.634±0.0006	0.35±0.0005	5.3±0.01
Ni+Ni					
0-10%	87.7±0.04	0.048±0.0007	0.169±0.0004	0.157±0.0004	73.4±0.02
10-20%	65.5±0.04	0.129±0.0008	0.229±0.0005	0.195±0.0005	55.2±0.02
20-30%	48.3±0.04	0.191±0.001	0.29±0.0006	0.229±0.0005	41.6±0.02
30-40%	35.0±0.04	0.239±0.0012	0.351±0.0007	0.261±0.0006	31.0±0.02
40-50%	24.6±0.04	0.275±0.0014	0.409±0.0008	0.294±0.0007	22.5±0.02
50-60%	16.9±0.03	0.29±0.0018	0.465±0.0009	0.324±0.0007	16.1±0.01
60-70%	11.2±0.03	0.263±0.0021	0.521±0.001	0.347±0.0008	11.1±0.01
70-80%	7.1±0.02	0.185±0.0026	0.561±0.0011	0.366±0.0009	7.7±0.01
80-90%	4.4±0.02	0.078±0.0031	0.594±0.0013	0.379±0.0011	5.4±0.01
90-100%	2.5±0.02	0.016±0.0036	0.604±0.0016	0.391±0.0015	4.0±0.01
Si+Si					
0-10%	39.9±0.04	0.034±0.0018	0.256±0.001	0.232±0.0009	33.6±0.01
10-20%	29.9±0.05	0.097±0.0022	0.318±0.0013	0.272±0.0011	25.5±0.01
20-30%	22.2±0.05	0.135±0.0026	0.379±0.0014	0.309±0.0012	19.2±0.01
30-40%	16.3±0.05	0.173±0.0031	0.44±0.0016	0.333±0.0013	14.4±0.01
40-50%	11.7±0.04	0.188±0.0037	0.495±0.0017	0.357±0.0014	10.6±0.01
50-60%	8.3±0.04	0.157±0.0043	0.54±0.0019	0.373±0.0016	7.9±0.01
60-70%	5.7±0.03	0.104±0.005	0.573±0.0021	0.385±0.0018	5.9±0.01
70-80%	3.8±0.03	0.051±0.0059	0.594±0.0025	0.393±0.0022	4.6±0.01
80-90%	2.5±0.03	0.016±0.0069	0.604±0.0031	0.398±0.0028	3.7±0.01
90-100%	1.5±0.03	0.008±0.0081	0.613±0.0041	0.4±0.0037	3.1±0.01

made at the RHIC energies [10]. The N_{part} -dependence of the geometrical asymmetry parameters associated with the overlapping regions, obtained from the MCG model [11] are listed in Table 5.1. Corresponding percentage centralities and the charged particle densities in the central particle producing region are also incorporated in this table.

5.1.1 Distributions of the flow parameters

The directed flow parameter (v_1) measures the total amount of in-plane transverse flow. As the participating nucleons try to stop each other, due to a bounce-off effect exerted by the compressed and heated fireball, the spectator nucleons of the impinging nuclei are deflected away from the beam axis. In contrast to the bounce-off effect, v_1 is not just the averaged projection of particle momentum on the impact parameter axis, considered to be the x -axis. It is rather an averaged ratio ($v_1 = \langle p_x/p_T \rangle$) of the same projection taken with respect to the transverse momentum of the particles concerned. Apart from a difference in their magnitude, the basic features of bounce-off effect and directed flow are similar [12]. The directed flow of high- p_T particles produced at the very early stages, continues to evolve until the very late stages of an AB collision. Therefore, the directed flow can be used to look into the early time thermalization or even into the pre-equilibrium stage. In non-central collisions the directed flow is most pronounced around the target and projectile rapidities.

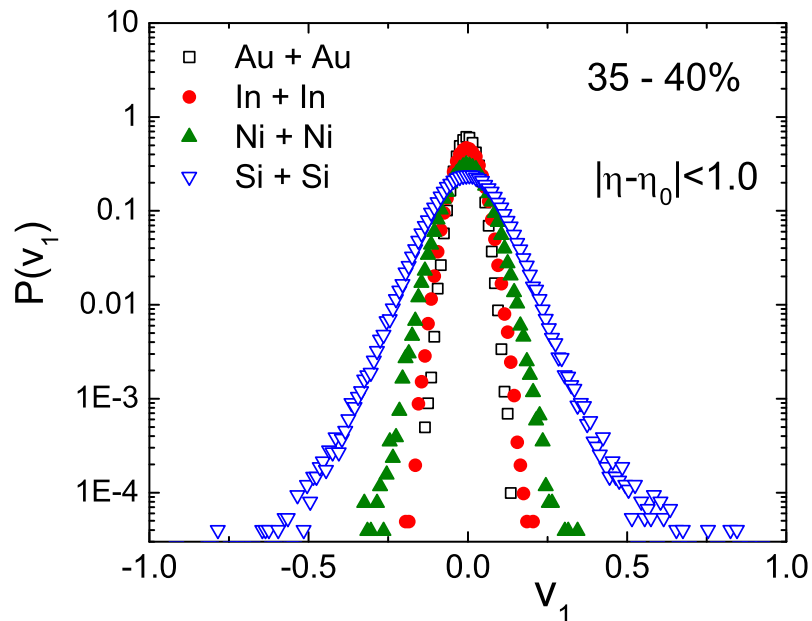


Figure 5.4: Distributions of v_1 of charged hadrons in the final state.

In Figure 5.4 we plot the probability distributions $P(v_1)$ of the directed flow parameter for the events falling within the (35 – 40)% centrality class for all the colliding systems. The

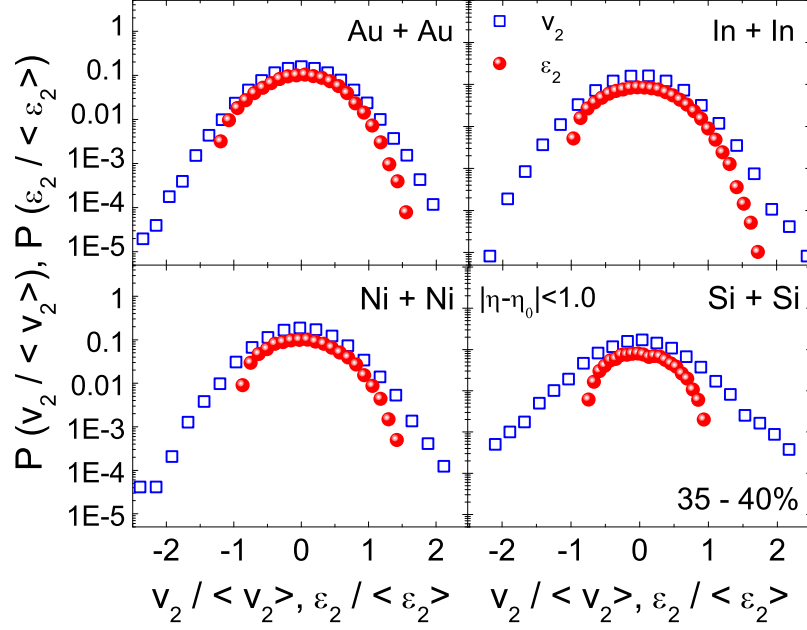


Figure 5.5: (Color online) Distributions of $v_2/\langle v_2 \rangle$ and $\varepsilon_2/\langle \varepsilon_2 \rangle$ of final state charged hadrons.

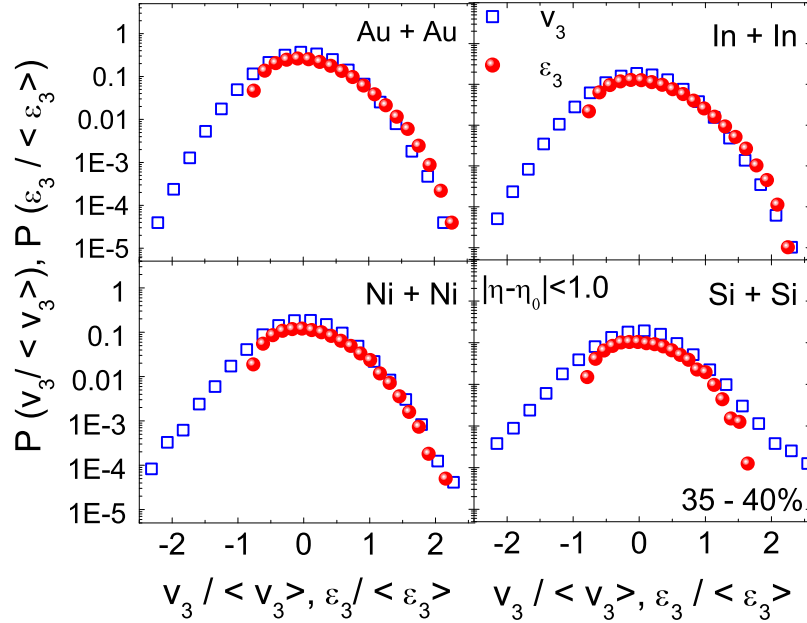


Figure 5.6: Distributions of $v_3/\langle v_3 \rangle$ and $\varepsilon_3/\langle \varepsilon_3 \rangle$ of final state charged hadrons.

distributions look like sharply peaked Gaussian functions, symmetrically centered around $v_1 = 0$. The width of the distributions however moderately increases with decreasing system size, an observation that may be attributed to statistical reasons. In a larger system, within a particular centrality class, on an average a larger number of participating nucleons will be involved, producing thereby a larger number of hadrons. As a result, in a larger system the averaging in v_1 is performed over a larger number of particles, which results in smaller

v_1 -values and correspondingly smaller fluctuations. Corresponding distributions of other flow parameters $P(v_2)$ and $P(v_3)$, are presented respectively in Figure 5.5 and Figure 5.6 in the (35 – 40)% centrality interval for all the colliding systems considered in the present investigation. We now compare these distributions with the distributions of corresponding asymmetry parameters [13]. Both v_n and ε_n for $n = 2$ and 3 are normalized by their respective mean values. The normalized flow parameters $v_2/\langle v_2 \rangle$ and $v_3/\langle v_3 \rangle$ are almost symmetrically distributed around their respective zeroes, but they are not as sharply peaked as the v_1 -distributions. The distributions of the normalized asymmetry parameters, namely $\varepsilon_2/\langle \varepsilon_2 \rangle$ and $\varepsilon_3/\langle \varepsilon_3 \rangle$, are slightly right skewed. Hydrodynamics predicts that for an ideal fluid at a given energy v_2 should scale with ε_2 [8, 14]. A strict proportionality like $v_n \propto \varepsilon_n$ should result in a complete overlapping between $P(v_n/\langle v_n \rangle)$ and $P(\varepsilon_n/\langle \varepsilon_n \rangle)$. Such an exact overlapping however is not observed in any of our colliding systems. Limited overlapping is found in all the colliding systems for both $n = 2$ and 3 , which gradually weakens as the system size becomes smaller. We may therefore conclude that, as expected the fireball material created at $E_{\text{lab}} = 30A$ GeV in the framework of AMPT, does not exactly behave like an ideal fluid.

5.1.2 The directed flow

In this section we present our simulation results on N_{part} , η and p_T -dependence of v_1 for the charged hadrons produced in all four colliding systems under consideration. We have calculated the p_T -integrated v_1 -values in the mid-pseudorapidity region ($|\eta - \eta_0| \leq 1.0$). In Figure 5.7 we plot the v_1 -values so obtained against N_{part} . We notice that except for a few highest centrality classes, however small it may be, v_1 is consistently negative valued. In medium and large systems like In+In and Au+Au, there is an initial uniformity in the v_1 against N_{part} plot, which subsequently is followed by an almost linear rise towards $v_1 \approx 0$. On the other hand, v_1 steadily approaches zero in smaller systems like Si+Si and Ni+Ni. In symmetric nuclear collisions, in the $E_{\text{lab}} = 30A$ GeV range, due to the nuclear shadowing effect an antiflow develops in the pion dominated systems as it is in the present case [15], and we get negative values of v_1 [16]. As we move from the most peripheral to the most central class of events, due to multiple rescattering the nuclear shadowing (screening) gradually disappears, and the flow effect starts to counterbalance the antiflow. As a result we see a monotonic, almost linear fall in the magnitude of v_1 . We notice that at a particular N_{part} , in a larger colliding system v_1 is larger in magnitude. Hadrons with small rapidities, produced early in the direction of normal flow, will be absorbed by the spectator nuclei. However, this process is less efficient in heavier systems. Therefore, the directed flow displays a softening in smaller sized colliding objects [12]. Our simulation results on directed flow represent a violation of the entropy-driven multiplicity scaling for different

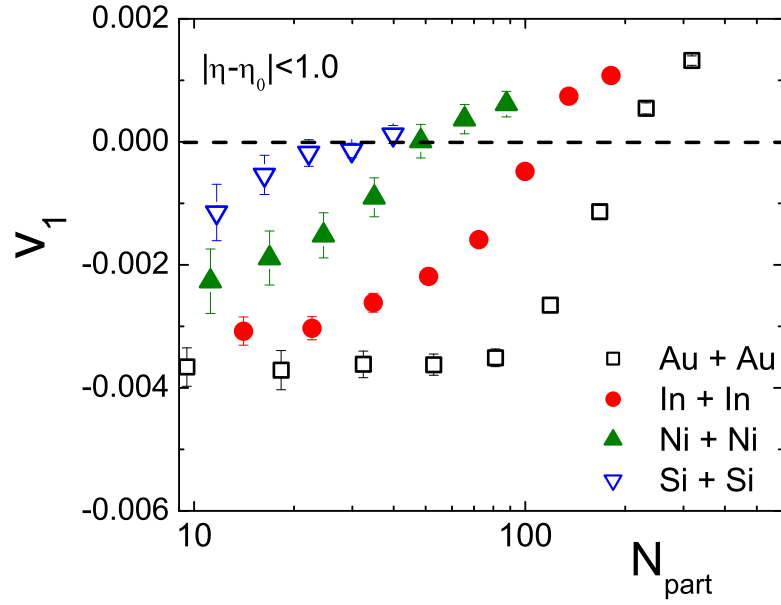


Figure 5.7: N_{part} dependence of v_1 of charged hadrons for different colliding systems.

colliding systems. The PHOBOS data showed that at all centralities, v_1 is independent of the system size [17], although a transport model simulation did not exactly substantiate such a system-size independence.

Figure 5.8 depicts the η -dependence of v_1 at different centrality intervals, i.e. in extreme

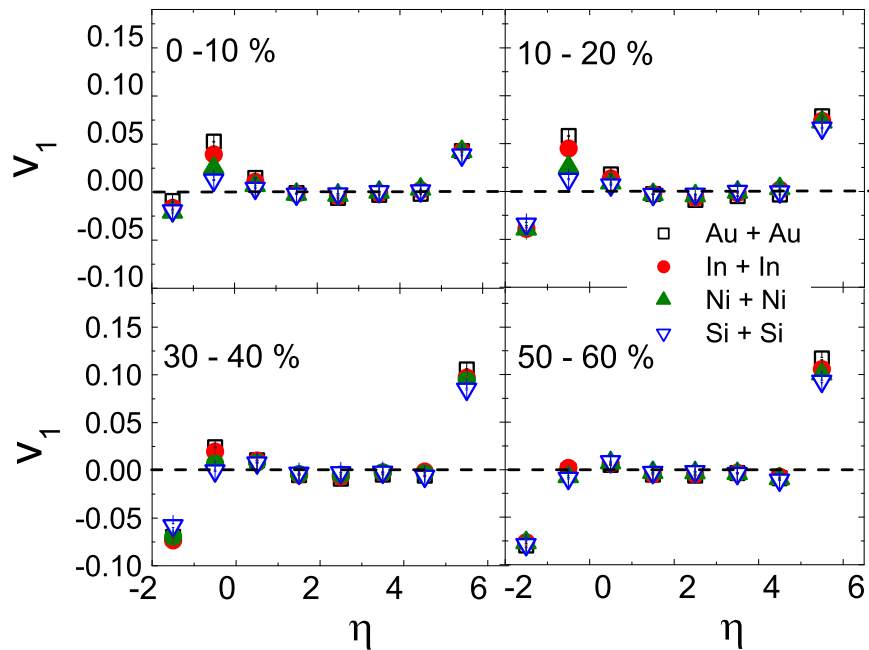


Figure 5.8: η dependence of v_1 of charged hadrons for different colliding systems.

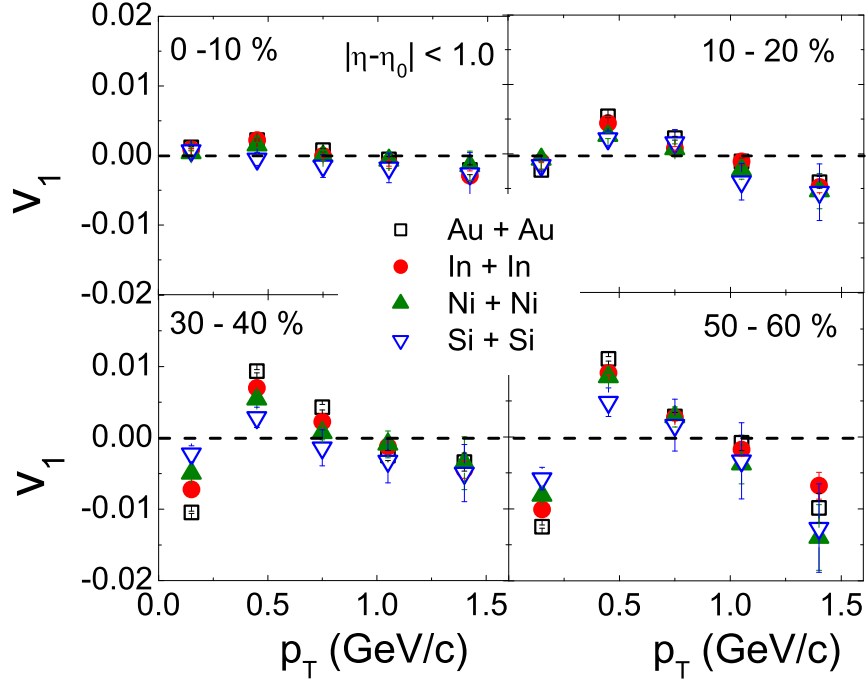


Figure 5.9: p_T dependence of v_1 of charged hadrons for different colliding systems.

central, mid-central and peripheral AA collisions. At $E_{\text{lab}} = 30A$ GeV in the mid- η region v_1 is very small valued and its variation with η appears to wiggle around the $v_1 = 0$ line. The slope of the v_1 vs. η curve is negative in the mid- η region, and positive in the fragmentation regions. However, the variation of v_1 with η is not exactly linear in the mid- η region. With increasing centrality the slope of the curve in the mid- η region increases in magnitude, and gradually a system size dependence becomes prominent. For a larger system the slope becomes larger. On the other hand in the peripheral collisions the v_1 vs. η variation becomes almost independent of the system size. In high-energy AB collisions more hadrons are produced and the spectator parts of the nuclei quickly leave the interaction zone, though in opposite directions, thus giving space to the flow to develop in both directions. Directed flow at the midrapidity drops almost to zero. In the hydrodynamical approach the wiggle is explained by using a QGP equation of state [18, 19]. On the other hand, in the cascade models the wiggle is explained in terms of a space-momentum correlation coupled with different amount of rapidity loss of the incoming nucleons in different space regions [20]. Our simulation based observations on the η -dependence of v_1 , are found to be in unison with the existing RHIC [21] and LHC [22] results. Yet the magnitude of $v_1(\eta)$ is systematically higher in our case, a characteristic feature of v_1 as reported over a wide range of energies[21–26].

In Figure 5.9, we present the p_T -dependence of v_1 within $|\eta - \eta_0| < 1.0$ at four different centralities and for all the collision systems considered in this analysis. In the extreme central (0–10%) and central (10–20%) collisions we do not see any definite p_T -dependence

of v_1 , except that its value fluctuates around the $v_1 = 0$ line. However, in mid-central (30 – 40%) and peripheral (50 – 60%) collisions, as p_T increases there is a sign change in the v_1 -values. Within $0.2 < p_T < 0.5$ GeV/c, v_1 increases with p_T from negative to positive values, and then it decreases with increasing p_T , once again crossing the $v_1 = 0$ line at $p_T \gtrsim 1.0$ GeV/c. It has been pointed out that for soft production ($0 \leq p_T \leq 1.5$ GeV/c), the probable reason of v_1 crossing the zero line a couple of times could be an artifact of combining all charged hadrons in our analysis, whereas v_1 of pions and baryons bear different signs [23, 24]. Another feature of our $v_1(p_T)$ result is that there is a definite system size dependence in the mid-central and peripheral collisions, which is not very prominent in the central collisions. A study of directed flow of identified particles for different species of particles may provide a better insight to these observations.

5.1.3 Centrality dependence of v_2 and v_3

We first compute the v_2 -parameter as a function of N_{part} in the central region ($|\eta - \eta_0| \leq 1$) for all the colliding systems considered in this analysis. The results are shown in Figure 5.10(a). Smaller v_2 -values are observed in extreme central and peripheral collisions. They are maximum in the semi-central collisions. Our observations are similar to the RHIC [17] and LHC [27] experiments. They can be explained in terms of the geometric effects and the pressure gradients developed thereof [28]. It is noticed that with increasing system-size the peak of the v_2 distribution shifts towards higher centrality. This kind of observation has been attributed to a hydro-dynamical evolution of the system [29, 30]. At a particular N_{part} , the magnitude of v_2 is found to be higher in a larger system, an observation which again is similar to that of a RHIC experiment [17]. However, in comparison with the RHIC results, the magnitude of our AMPT simulated v_2 at an expected FAIR energy, is lower by a factor of 2. Experimental results obtained from the Alternating Gradient Synchrotron (AGS) to the LHC energies, have established that the centrality dependence of v_2 provides valuable information regarding the degree of thermalization achieved in AB systems. It is understood that such equilibration is possible due to multiple rescattering among the constituent particles present in the system. Hydrodynamics predicts that v_2/ε_2 should saturate when the collision system achieves a local equilibrium. If the produced matter equilibrates, it should behave almost like an ideal fluid [8, 14]. In order to better understand how rescattering influences the results on flow parameters, it is therefore necessary to scale out the effects of geometry from our calculations [31]. In Figure 5.10(b) we plot the $v_2/\varepsilon_{\text{std}}$ -ratio against N_{part} . It is noticed that the bell shaped pattern of v_2 vs. N_{part} plot, as observed in Figure 5.10(a), disappears. Instead, the $v_2/\varepsilon_{\text{std}}$ -ratio increases monotonically with increasing N_{part} . The variation of $v_2/\varepsilon_{\text{std}}$ is non-linear, and in smaller systems the ratio rises quite rapidly with N_{part} . As the system-size increases the variation becomes flat, and for

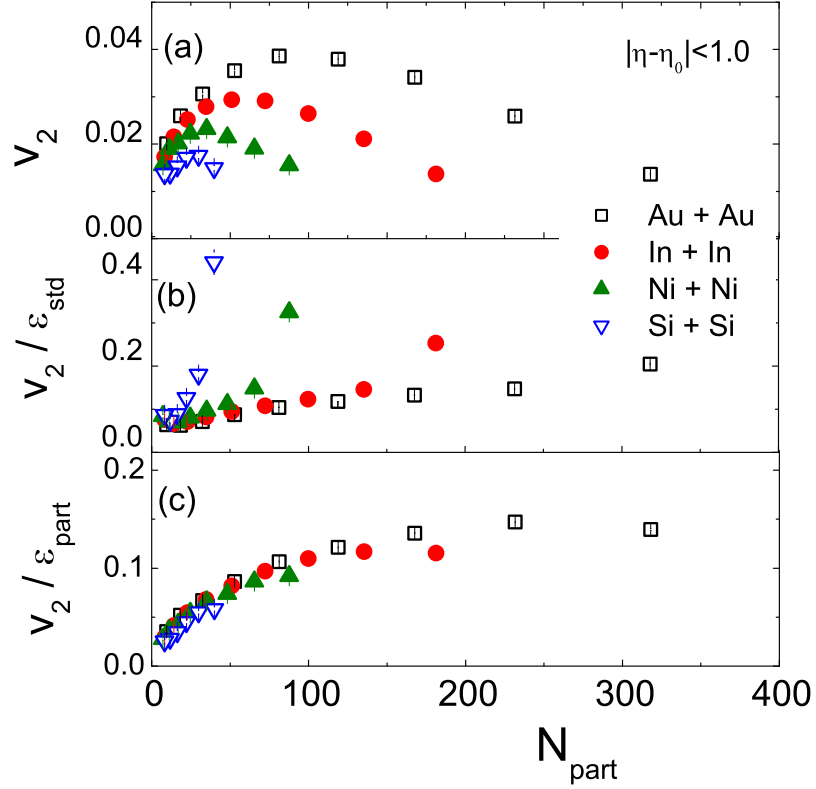


Figure 5.10: N_{part} dependence of (a) the elliptic flow parameter v_2 , (b) v_2 scaled by the standard eccentricity ε_{std} , and (c) v_2 scaled by the participant eccentricity $\varepsilon_{\text{part}}$, for charged hadrons in various AB collisions at $E_{\text{lab}} = 30.4$ GeV.

the Au+Au and In+In systems it is almost linear. However, the expected saturation is not observed, which we have previously ascribed to an eccentricity expression that does not take care of the fluctuations of the participating nucleons [1]. As soon as we replace ε_{std} by $\varepsilon_{\text{part}}$, a near scaling (system-size independence) of $v_2/\varepsilon_{\text{part}}$ is noticed in Figure 5.10(c). Once the nuclear geometry is taken care of, we are left only with the multiplicity dependence, a feature also known as the multiplicity scaling [32]. The scaling nature makes it easier for us to realise that at a particular collision energy the rescattering mechanism remains unaltered in different colliding systems. Furthermore, once again it is established that $\varepsilon_{\text{part}}$ is the appropriate eccentricity parameter to be used. Unless otherwise specified, for the rest of our discussion we shall use $\varepsilon_{\text{part}}$ as the eccentricity measure and denote the same by $\varepsilon_n : n = 2, 3$.

In Figure 5.11 we plot the v_2/ε_2 -ratio against $S^{-1} (dN_{\text{ch}}/dy)$, the produced particle density per unit transverse area of the nuclear overlapping region. The initial overlapping area of the colliding nuclei S is calculated by using the MCG model [11]. Results obtained from all the colliding systems considered in this analysis are plotted together with those obtained from other experiments [24, 33–35]. The idea is to compare data obtained from different collision

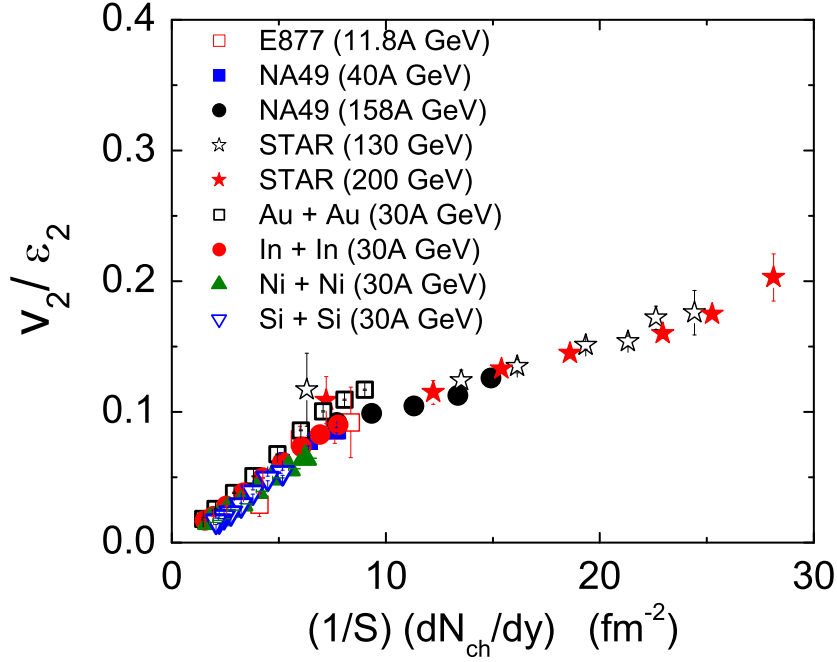


Figure 5.11: Variation of eccentricity scaled elliptic flow with transverse particle density.

systems at different energies and at different centralities. Whereas v_2 reflects the space-momentum correlation developed due to the early stage pressure gradient, $S^{-1} (dN_{ch}/dy)$ is a measure of the transverse particle density. Hence v_2/ε_2 versus $S^{-1} (dN_{ch}/dy)$ plot should be seen as an alternative to the pressure versus energy density plot. In other words it is sensitive to the sound velocity in the medium as well as the equation of state of the matter produced during the expansion stage. A non-smooth behaviour of the plot would indicate a change in the medium properties. In this connection we recall that the energy density achieved in AB collisions is determined by the Bjorken's formula [36], which looks very similar to the transverse particle density $S^{-1} (dN_{ch}/dy)$. We see that for the entire range of data a linear dependence like

$$\frac{v_2}{\varepsilon_2} \propto \frac{1}{S} \frac{dN_{ch}}{dy} \quad (5.3)$$

is only approximately obeyed and not exact. The proportionality constant should depend on the the region of fit, the hydro-limit of v_2/ε_2 ratio, the partonic scattering cross-section and the velocity of elastic wave in the medium [37]. The key feature of the plot is that, except for a few highest centrality classes in Au + Au collision, our results nearly agree with the results available from the E877 and NA49 experiments. Similar observation is made in [28], where in addition to the AMPT (string melting) version the UrQMD and the AMPT default version are used.

We now examine the centrality dependence of v_3 . In Figure 5.3 it has been shown that the initial spatial anisotropy ε_3 is higher in peripheral collisions, and almost independent

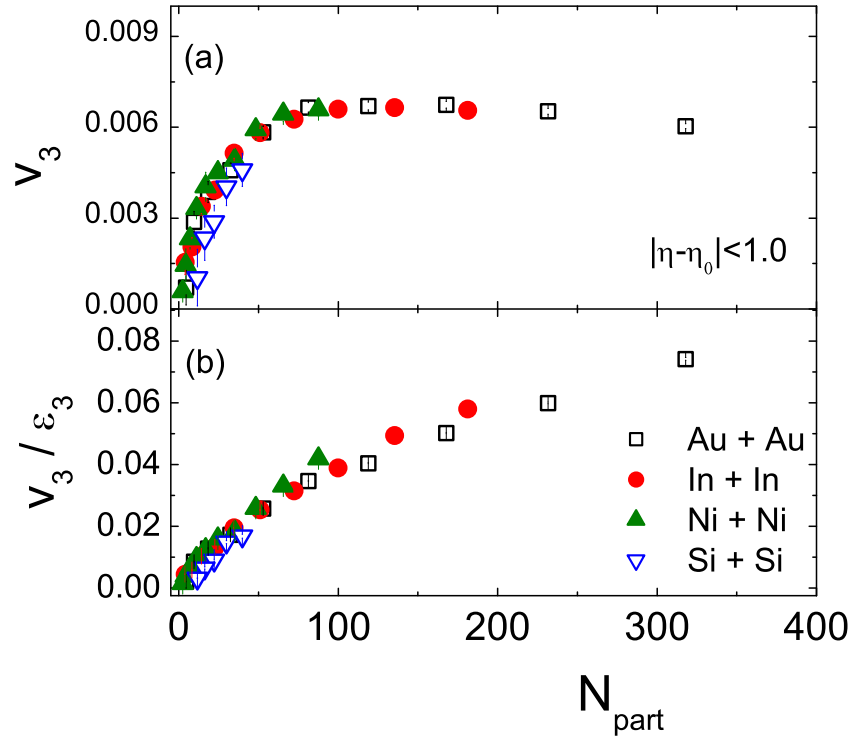


Figure 5.12: (a) Triangular flow and (b) triangular flow scaled by triangularity of charged hadrons against N_{part} for various AB collisions at $E_{\text{lab}} = 30A$ GeV.

of the system size. A similar feature can be seen in Figure 5.12(a) too, where v_3 is plotted against N_{part} . We notice that the N_{part} -dependence of v_3 is also almost independent of the system size. v_3 is small in peripheral collisions, rises with N_{part} , and saturates at higher centralities. The conversion from initial space asymmetry to final state momentum anisotropy is less efficient in peripheral collisions. However, the same appears to be equally inefficient in all the collision systems considered in our analysis. We also notice that for a particular collision system, v_2 is consistently larger in magnitude than v_3 . This is understood from the fact that v_2 arises from the geometrical asymmetry as well as from the initial state fluctuations, while v_3 originates only from the initial state fluctuations. A more detailed representation of this issue is seen in the relative magnitude of v_3 and v_2 plotted as a function of N_{part} in Figure 5.13. In all cases initially the relative strength of v_3 increases slowly with centrality, and the rate of increase suddenly rises towards more central events, almost like a power-law. Gross features of our observation in this regard are compatible to the simulation results at RHIC energies [9], and once again can be ascribed to the multiplicity scaling. In Figure 5.12(b) an nearly linear rise in the v_3/ϵ_3 -ratio with increasing N_{part} is observed, which again is almost independent of the system size. In Figure 5.12 the saturation that we see in the centrality dependence of the triangular flow parameter, can therefore be attributed to the geometrical effects, and our results in this regard also appear to be consistent with the multiplicity scaling [32].

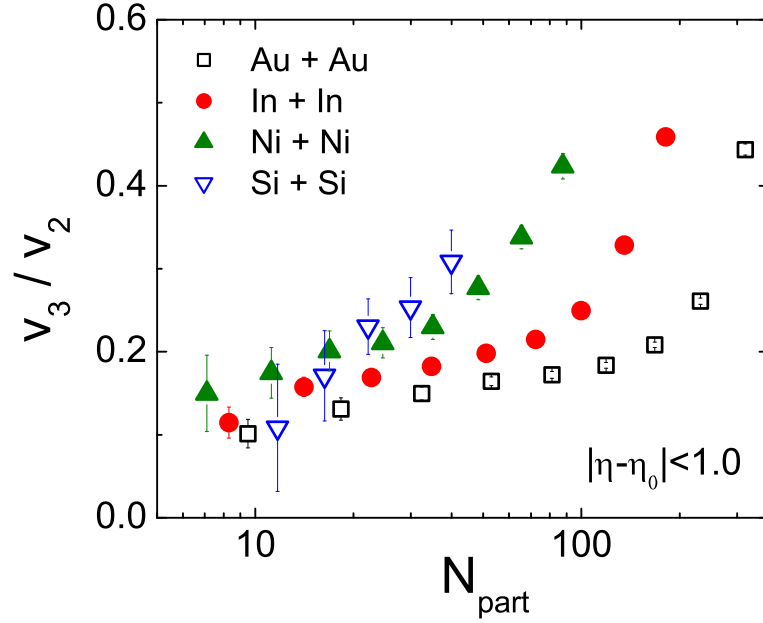


Figure 5.13: Ratio of v_3 to v_2 of charged hadrons as a function of N_{part} for different colliding systems at $E_{\text{lab}} = 30A$ GeV.

5.1.4 Transverse momentum dependence of v_2 and v_3

The p_T -dependence of flow parameters plays a vital role to understand the influence of transverse degrees of freedom on the collective motion of final state particles. Simulation based results at FAIR conditions reported so far can be found in [28, 38, 39]. Whereas resonance decays are expected to dominate the low- p_T behaviour, at high- p_T particles originate from fragmentation of jets modified in the hot and dense fireball medium [40]. Another important feature of the p_T -dependence of flow parameters, is the mass ordering of baryons in the low p_T sector, i.e. upto $p_T \gtrsim 1.0$ GeV/c at $E_{\text{lab}} = 30A$ GeV. Beyond this range, the mass ordering is found to be broken. Actually the ordering gets inverted as $p_T > 1.4$ GeV/c – the p_T dependence of baryons and mesons are found to split into two separate bands [38]. Hydrodynamical model(s) can describe the related issues at RHIC energies [41, 42] In this investigation we would like to study the effects of (re)scattering or equivalently that of the multiplicity on the p_T -dependence of v_2 and v_3 . It would have been ideal, if for each colliding system under investigation, we could fix a precise N_{part} for all the variables studied in this work. However, as the maximum N_{part} is widely distributed in our chosen collision systems, starting from 56 in Si + Si and ending up at 394 in Au + Au, for a proper justification we have categorized our data into different N_{part} -groups. To study the p_T -dependence we have chosen $\langle N_{\text{part}} \rangle = 100$ for the Au+Au and In+In, and $\langle N_{\text{part}} \rangle = 35$ for the Ni+Ni and Si+Si systems. Both choices correspond to semi-central collisions, where high values of flow parameters are expected. In the upper panels of Figure 5.14 and Figure 5.15 we schematically present the p_T -dependence of v_2 and v_3 , and in the lower panels of the same figures

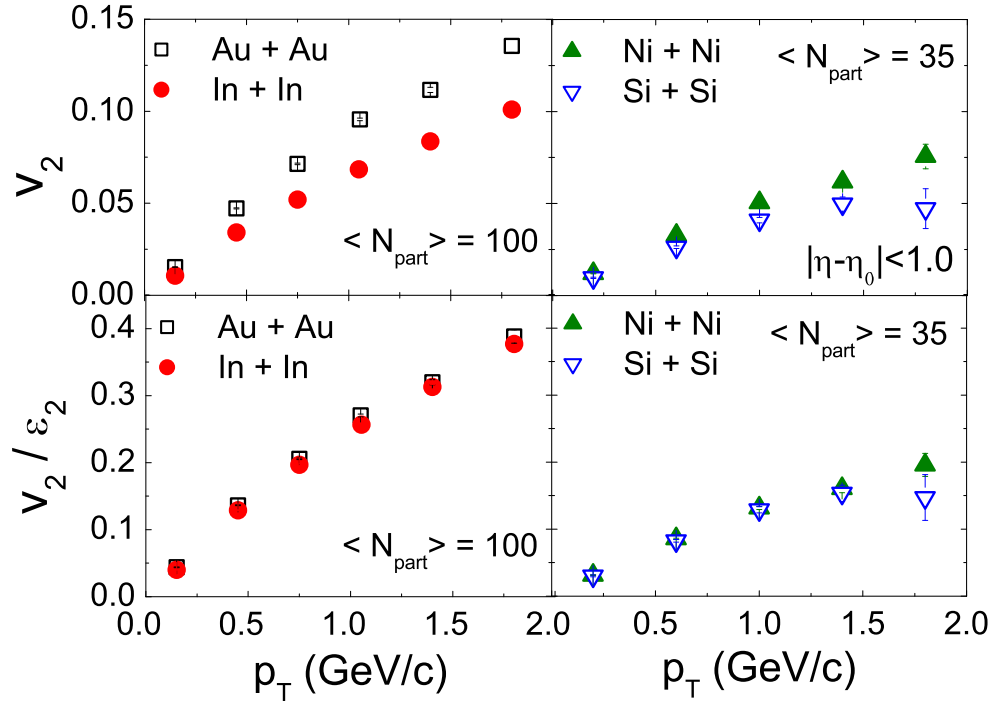


Figure 5.14: p_T dependence of v_2 (upper panel) and v_2/ϵ_2 (lower panel) of charged hadrons for different colliding systems at $E_{\text{lab}} = 30A$ GeV.

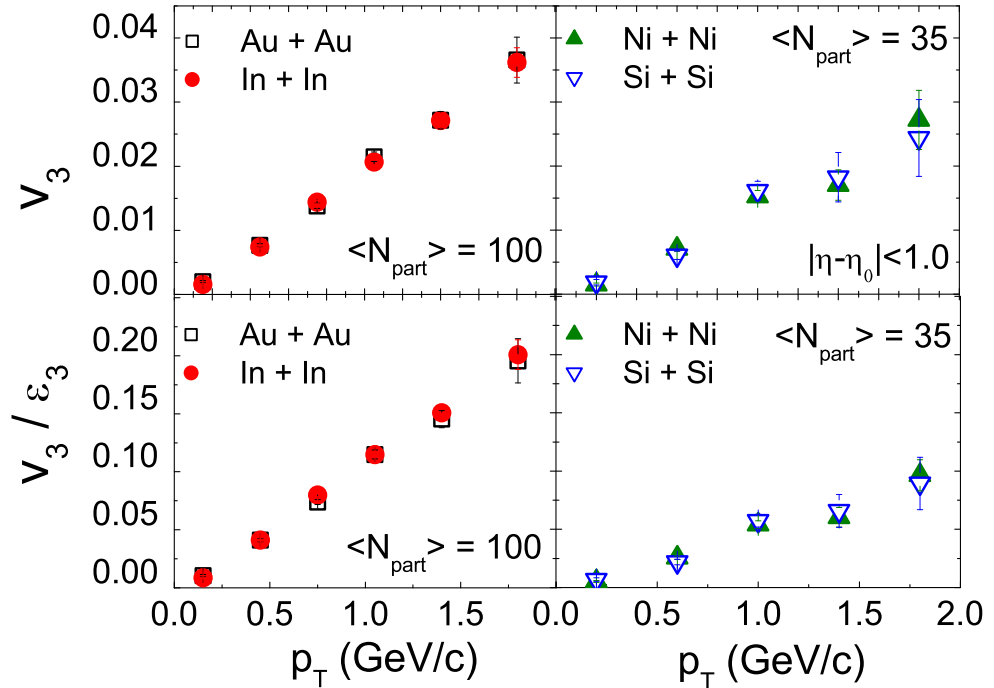


Figure 5.15: p_T dependence of v_3 (upper panel) and v_3/ϵ_3 (lower panel) of charged hadrons for different colliding systems at $E_{\text{lab}} = 30A$ GeV.

similar plots for the ratio v_n/ε_n ($n = 2, 3$) are made. The p_T -dependence of v_2 shows its usual nature, increasing almost linearly with p_T . The rate of increase is higher in a larger system. However, once again as the geometric effects are removed, the v_2/ε_2 -ratio becomes independent of the system size, an observation also reported by the PHOBOS collaboration in Au+Au and Cu+Cu systems at $\sqrt{s} = 200$ GeV [1]. This scaling nature can be attributed to a common particle production mechanism and the collective flow developed thereof. At a particular $\langle N_{\text{part}} \rangle$ the transverse particle density is expected to be approximately same. The v_2/ε_2 -ratio being linearly dependent on it, should have the identical values. It is believed that the in-medium viscous effects present in large magnitude should introduce a system-size dependence on $v_2(p_T)$ [43–45]. Furthermore, the viscosity will cause v_2 to saturate at low- p_T in small sized systems. A system-size independent scaling of $v_2(p_T)$ is therefore, a manifestation of insignificant presence (or absence) of viscous effects in the hadronic/partonic medium created in the AB interactions of our consideration after the collective flow is developed. The pattern of p_T -dependence of v_3 is almost similar to that of v_2 . However, we observe that neither v_3 nor v_3/ε_3 -ratio has any significant dependence on the system size.

5.2 Conclusion

In this investigation we have presented some simulation results on the system-size dependence of some gross aspects of the first three harmonic flow parameters in $^{28}\text{Si}+^{28}\text{Si}$, $^{59}\text{Ni}+^{59}\text{Ni}$, $^{115}\text{In}+^{115}\text{In}$ and $^{197}\text{Au}+^{197}\text{Au}$ interactions at $E_{\text{lab}} = 30A$ GeV. The AMPT model in its string melting version has been used to generate the event samples. Our results however, do not warrant any significant change in the properties of the fireball medium, even though the collision size is changed significantly. It has been pointed out that many aspects of soft-hadron production (within $0 \leq p_T \leq 2.0$ GeV/ c) depend only on the rapidity density [32]. There should be no significant dependence on the beam energy, centrality, or mass of the colliding nuclei. This type of scaling is known as entropy-driven soft physics. Except for the centrality dependence of the directed flow parameters, almost all of our flow results are found either due to the geometrical effects, or they are an outcome of the multiplicity scaling, or both. The present analysis pertains to all charged hadrons, and no segregation in terms of different particle species has been made. It is expected that the flow behaviours of hadrons with different intrinsic properties should also be different.

Bibliography

- [1] B. Alver *et al.* (PHOBOS Collaboration), Phys. Rev. Lett. **98**, 242302 (2007).
- [2] B. Schenke, S. Jeon, and C. Gale, Phys. Rev. Lett. **106**, 042301 (2011).
- [3] B. Schenke, S. Jeon, and C. Gale, Phys. Rev. C **82**, 014903 (2010); **85**, 024901 (2012).
- [4] B. Alver *et al.*, Phys. Rev. C **82**, 034913 (2010).
- [5] L.-W. Chen and C. M. Ko, Phys. Lett. B **634**, 205 (2006).
- [6] A. Adare *et al.* (PHENIX Collaboration), Phys. Rev. Lett. **98**, 162301 (2007).
- [7] A. Adare *et al.* (PHENIX Collaboration), Phys. Rev. C **94**, 054910 (2016).
- [8] H. Sorge, Phys. Rev. Lett. **82**, 2048 (1999).
- [9] B. Alver and G. Roland, Phys. Rev. C **81**, 054905 (2010).
- [10] L. X. Han *et al.*, Phys. Rev. C **84**, 064907 (2011).
- [11] A. Shor and R. Longacre, Phys. Lett. B **218**, 100 (1989); C. Loizides, Phys. Rev. C **94**, 024914 (2016) .
- [12] L. V. Bravina and E. E. Zabordin, Eur. Phys. J. A **52**(8), 245 (2016).
- [13] C. Gale *et al.*, Phys. Rev. Lett. **110**, 012302 (2013).
- [14] J.-Y. Ollitrault, Phys. Rev. D **46**, 229 (1992).
- [15] S Ghosh *et al.*, J. Phys. G: Nucl. Part. Phys. **48**, 125106 (2021).
- [16] J. Y. Ollitrault, Nucl. Phys. A **638**, 195 (1998).
- [17] B. I. Abelev *et al.* (STAR Collaboration), Phys. Rev. C **77**, 054901 (2008).
- [18] J. Brachmann *et al.*, Phys. Rev. C **61**, 024909 (2000).
- [19] L. P. Csernai and D. Rohrlich, Phys. Lett. B **458**, 454 (1999).
- [20] R. Snellings *et al.*, Phys. Rev. Lett. **84**, 2803 (2000).
- [21] B. B. Back *et al.* (PHOBOS Collaboration), Phys. Rev. Lett. **97**, 012301 (2006).
- [22] B. Abelev *et al.* (CMS Collaboration), Phys. Rev. Lett. **111**, 232302 (2013).
- [23] B. I. Abelev *et al.* (STAR Collaboration), Phys. Rev. Lett. **101**, 252301 (2008).
- [24] C. Alt *et al.* (NA49 Collaboration), Phys. C **68** 034903 (2003).

- [25] H. Liu *et al.* (E877 Collaboration), Phys. Rev. Lett. **84**, 5488 (2000).
- [26] L. Adamczyk *et al.* (STAR Collaboration), Phys. Rev. Lett. **112**, 162301 (2014).
- [27] K. Aamodt *et al.* (ALICE Collaboration), Phys. Rev. Lett. **105**, 252302 (2010).
- [28] S. Sarkar, P. Mali, and A. Mukhopadhyay, Phys. Rev. C **95**, 014908 (2017).
- [29] P. F. Kolb, P. Huovinen, U. Heinz, and H. Heiselberg, Phys. Lett. B **500**, 232 (2001).
- [30] P. F. Kolb, J. Sollfrank, and U. W. Heinz, Phys. Lett. B **459**, 667 (1999).
- [31] S. A. Voloshin and A. M. Poskanzer, Phys. Lett. B **474**, 27 (2000).
- [32] H. Caines, Eur. Phys. J. C **49**, 297 (2007).
- [33] J. Barrette *et al.* (E877 Collaboration), Phys. Rev. C **51**, 3309 (1995); Phys. Rev. C **55**, 1420 (1997).
- [34] A. M. Poskanzer and S. A. Voloshin, Nucl. Phys. A **661**, 341c (1999).
- [35] C. Adler *et al.* (STAR Collaboration), Phys. Rev. C **66**, 034904 (2002).
- [36] J. D. Bjorken, Phys. Rev. D, **27**, 140 (1983).
- [37] H.-J. Drescher *et al.*, Phys. Rev. C **76**, 024905 (2007).
- [38] S. Sarkar, P. Mali, and A. Mukhopadhyay, Phys. Rev. C **96**, 024913 (2017).
- [39] P. P. Bhaduri and S. Chattopadhyay, Phys. Rev. C **81**, 034906 (2010).
- [40] G. Aad *et al.* (ATLAS Collaboration), Phys. Lett. B **707**, 330 (2012).
- [41] P. Huovinen *et al.*, Phys. Lett. B **503**, 58 (2001).
- [42] U. Heinz, C. Shen, and H. Song, AIP Conf. Proc. **1441**, 766 (2012).
- [43] P. Romatschke and U. Romatschke, Phys. Rev. Lett. **99**, 172301 (2007).
- [44] M. Luzum and P. Romatschke, Phys. Rev. C **78**, 034915 (2008).
- [45] H. Song and U. W. Heinz, Phys. Rev. C **77**, 064901 (2008).

Chapter 6

Radial flow of charged hadrons at FAIR conditions

Before any collision the nucleons belonging to individual nucleus possess only longitudinal degrees of freedom. Transverse degrees of freedom are excited only after an interaction takes place. In mid-central collisions the overlapping area of the colliding nuclei has an almond shape in the transverse plane. This initial asymmetry in the geometrical shape gives rise to different kinds of pressure gradients along the long and short-axis of the overlapping zone, and correspondingly to a momentum space asymmetry in the final state. As a result, if the matter present in the intermediate fireball behaves like a fluid, then a collective flow in the final state particles is observed, which is reflected in the azimuthal distribution of particle number as well as in the azimuthal distribution of a few other kinematic variable like transverse momentum (p_T), transverse rapidity (y_T) and transverse or radial velocity (v_T) [1]. The radial velocity has two components, the radial flow velocity and the velocity due to random thermal motion of the particles. For an ideal fluid the radial flow velocity should be isotropic. However, for a non-ideal viscous fluid, as the case may be at FAIR conditions, the shear tension is expected to be proportional to the gradient of the radial velocity along the azimuthal direction, which again is related to the anisotropy of radial velocity [2]. An analysis of experimental data over a pretty wide energy range ($E_{\text{lab}} \approx 1 - 160$ GeV) has shown that the observed v_2 -values are lower than what is expected from a phenomenology based on the three-fluid dynamics [3]. The difference has been attributed to dissipative effects like viscosity. A successful single parameter (the Knudsen number) fit of the v_2 -values over a wide range of collision energy suggests that the ratio between the upper limit of shear viscosity and specific entropy $\eta/s \sim 1 - 2$, a value much higher than what is estimated for

an almost ideal fluid created at the RHIC or LHC energies. However, to understand the exact nature of the flow characteristics, or the nature of the fluid expected to be created at FAIR energies, we shall have to wait till the CBM results in this regard become available.

6.1 Methodology

We introduce the transverse (radial) velocity as,

$$v_T = \frac{p_T}{E} = \frac{p_T}{m_T \cosh y} \quad (6.1)$$

where $E = m_T \cosh y$ is the energy of the particle, $m_T = \sqrt{m_0^2 + p_T^2}$ is its transverse mass, m_0 is the particle rest mass, and y is its rapidity. For a large sample of events the total radial velocity $\langle V_T(\phi_m) \rangle$ of all particles falling within the m -th azimuthal bin is defined as,

$$\langle V_T(\phi_m) \rangle = \frac{1}{N_{ev}} \sum_{j=1}^{N_{ev}} \sum_{i=1}^{n_m} v_{T,i}(\phi_m) \quad (6.2)$$

where $v_{T,i}(\phi_m)$ is the radial velocity of the i -th particle, n_m is the total number of particles present in the m -th bin, N_{ev} is the number of events under consideration, and $\langle \rangle$ denotes an averaging over events. In this analysis we have chosen the transverse velocity as the basic variable in terms of which the azimuthal asymmetry has been studied, and compared our simulation results obtained thereof with those obtained from the azimuthal asymmetry associated with the charged particle multiplicity distribution. An azimuthal distribution of $\langle V_T(\phi_m) \rangle$ contains information regarding the multiplicity as well as that of the radial expansion. By taking an average over particle number the mean transverse velocity $\langle\langle v_T(\phi_m) \rangle\rangle$ is introduced as,

$$\langle\langle v_T(\phi_m) \rangle\rangle = \frac{1}{N_{ev}} \sum_{j=1}^{N_{ev}} \frac{1}{N_m} \sum_{i=1}^{N_m} v_{T,i}(\phi_m) \quad (6.3)$$

where $\langle\langle \rangle\rangle$ represents first an average over all particles present in the m -th azimuthal bin and then over all events present in the sample. This double averaging reduces the multiplicity influences significantly, and the corresponding distribution measures only the radial expansion. In this context we must mention that the mean radial velocity actually consists of contributions coming from three different sources, the average isotropic radial velocity, the average anisotropic radial velocity, and the average velocity associated with the thermal motion. It should be noted that both radial and thermal motion contribute to an isotropy in the velocity distribution. Like the azimuthal distribution of charged particle multiplicities ($dN_{ch}/d\phi$), it is also possible to expand the azimuthal distribution of total and

mean transverse velocities in Fourier series as,

$$\frac{d\langle V_T \rangle}{d\phi} \approx v_0 (\langle V_T \rangle) [1 + 2v_2 (\langle V_T \rangle) \cos(2\phi)], \quad (6.4)$$

$$\frac{d\langle\langle v_T \rangle\rangle}{d\phi} \approx v_0 (\langle\langle v_T \rangle\rangle) [1 + 2v_2 (\langle\langle v_T \rangle\rangle) \cos(2\phi)] \quad (6.5)$$

In these expansions only the leading order terms ($n = 0$ and 2) are retained. The anisotropy present in any of the distributions [Equation (6.4) and Equation (6.5)] is quantified by the second Fourier coefficient v_2 , whereas v_0 is a measure of the corresponding isotropic flow.

6.2 Results and discussion

In this section we describe our results on the radial flow of charged hadrons obtained from a sample of Au+Au minimum bias events simulated by the AMPT (string melting) model at $E_{\text{lab}} = 10A$ and $40A$ GeV. A representative value ($\sigma = 3$ mb) of the parton scattering cross section is used while simulating the events. The σ -value is chosen so as to match with a previously studied collective behaviour at an expected FAIR energy. We have indeed

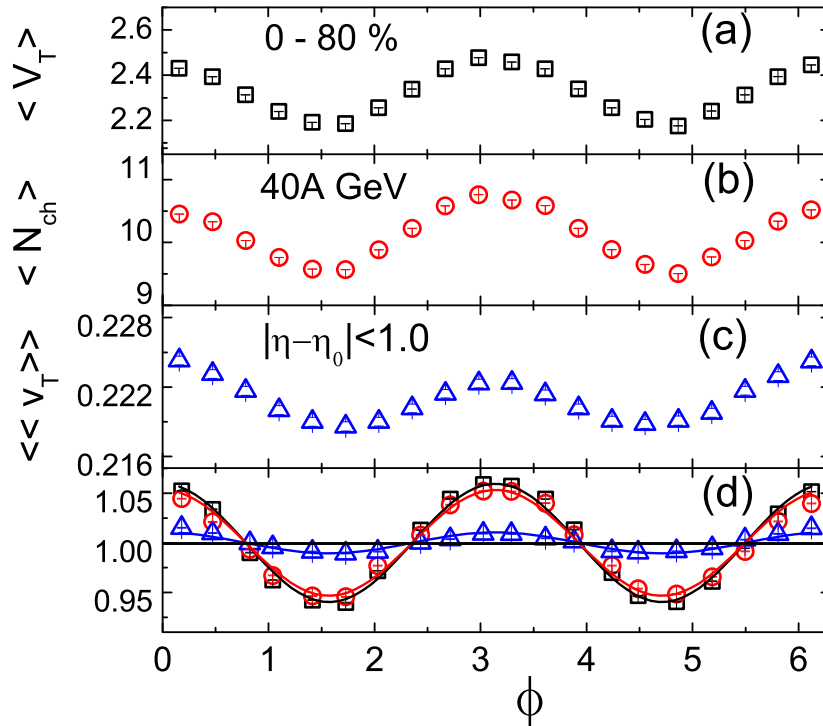


Figure 6.1: Azimuthal distribution of (a) total radial velocity, (b) multiplicity, (c) mean radial velocity and (d) all the aforesaid quantities properly normalized for charged hadrons produced in Au+Au collisions at $E_{\text{lab}} = 40A$ GeV.

compared the NA49 results [4] on the p_T -dependence of elliptic flow parameter v_2 by varying σ over a range of 0.1 to 10 mb, and in Section 4.1.4 we have seen that even though the σ -values vary almost by a couple of orders of magnitude, corresponding differences in the simulated v_2 -values at an expected FAIR energy, are not that significant. We begin with the azimuthal distributions of (a) the total radial velocity $\langle V_T \rangle$, (b) the multiplicity (N_{ch}) and (c) the mean radial velocity $\langle\langle v_T \rangle\rangle$ of charged hadrons produced at $E_{\text{lab}} = 40A$ GeV in the mid-rapidity region ($|\eta - \eta_0| \leq 1.0$) chosen symmetrically about the central value η_0 , for the 0 – 80% centrality class. Our results in this regard are graphically shown in Figure 6.1. Presence of anisotropy in all three distributions is clearly visible. It is also to be noticed that while all three distributions exhibit same periodicity, their amplitudes are different. In order to show that all three distributions can analytically be described by a single function like $N [1 + \alpha \cos(2\phi)]$, without significant contributions coming from the other harmonics, we fit the distributions with exactly the same relative vertical axis range with respect to the value of the parameter α centred around the same value of the other parameter N (here $N = 1.0$), and plot them together in Figure 6.1(d) along with the respective fitted lines. When appropriately scaled, we find that the elliptic anisotropy present in the distribution of total radial velocity is almost equal in magnitude to that coming from the anisotropy in multiplicity distribution. In comparison, the anisotropy present in the mean radial velocity is quite small. The results at $E_{\text{lab}} = 10A$ and $40A$ GeV are qualitatively similar.

6.2.1 Centrality dependence of v_2 and v_0

Elliptic flow originates from the interactions among particles comprising the intermediate fireball, and therefore it is a useful probe for the identification of local thermodynamic equilibrium. We have already observed that the v_2 -values are smaller for the extreme central and peripheral collisions, a feature that can be explained in terms of the initial geometric effects and the pressure gradient produced thereof [5]. In the hydrodynamical limit v_2 is proportional to the elliptic eccentricity (ε_2) of the overlapping region of the colliding nuclei, whereas in the low density limit v_2/ε_2 is proportional to a product of the rapidity density of charged particles dN_{ch}/dy and inverse of the overlapping area of the colliding nuclei. It is believed that the centrality dependence of elliptic flow provides valuable information regarding the degree of equilibration achieved by the intermediate fireball, and also regarding the characteristics of (re)scattering effects present therein [6]. At FAIR energies some simulation results have already been reported [7–9].

In Figure 6.2 we compare the centrality dependence of the v_2 -parameter obtained from the distributions of all three variables under consideration. The overall centrality dependence of $v_2(\langle V_T \rangle)$ is found to be similar to that of $v_2(\langle N_{\text{ch}} \rangle)$. However, the $v_2(\langle\langle v_T \rangle\rangle)$ -values, which are

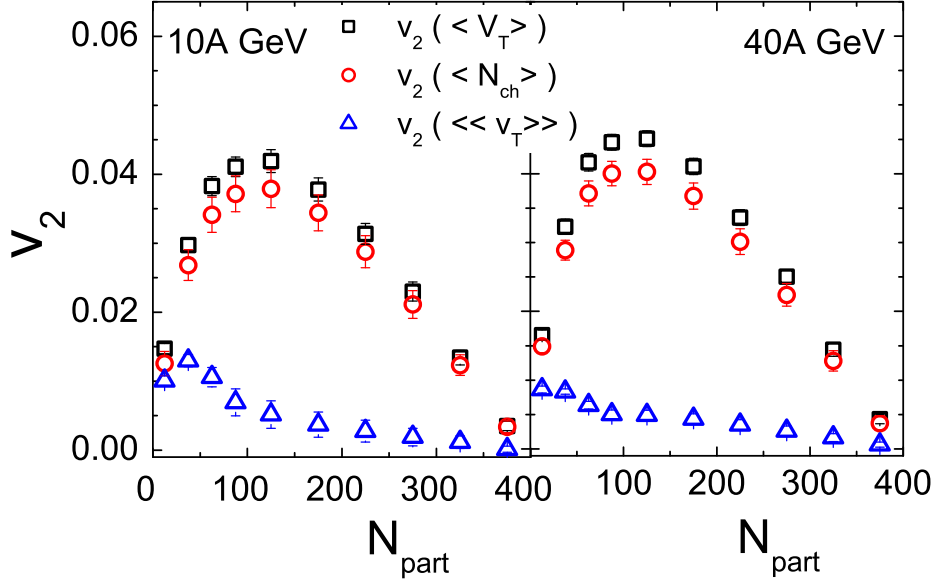


Figure 6.2: Centrality dependence of anisotropy parameter v_2 obtained from the azimuthal distributions of total radial velocity, multiplicity, and mean radial velocity in Au+Au collision at $E_{\text{lab}} = 10A$ and $40A$ GeV.

quite small in comparison with the v_2 -values obtained from the other two variables, behave quite differently. The bell shape of the distribution observed for $v_2(\langle V_T \rangle)$ and $v_2(\langle N_{\text{ch}} \rangle)$, is either absent, as it is in the $40A$ GeV case, or shifts toward extreme peripheral class of events, as it is seen in the $10A$ GeV case. In all three cases however, our observations on N_{part} -dependence of v_2 are consistent with Figure 6.1(d). It is to be noted that the anisotropy in mean radial velocity, which describes the radial expansion, is significantly smaller than that of the corresponding multiplicity distribution in mid-central region. In this regard we also intend to examine the dependence on the collision energy involved. It is observed that $v_2(\langle V_T \rangle)$ and $v_2(\langle N_{\text{ch}} \rangle)$ at $E_{\text{lab}} = 40A$ GeV are marginally higher than those at $10A$ GeV, a general feature of any measurement on v_2 that has been confirmed over a much wider energy range [10–13]. The $v_2(\langle\langle v_T \rangle\rangle)$ values are not significantly different at the two collision energies involved. We expect that the isotropy parameter (v_0) of all aforesaid distributions are also of certain importance, and in Figure 6.3 we graphically plot them against N_{part} for all three variables and both collision energies considered. The v_0 -values associated with both $\langle V_T \rangle$ and $\langle N_{\text{ch}} \rangle$ distributions show a linear dependence with increasing N_{part} , being highest in the most central events. This feature of v_0 can be ascribed to the fact that the azimuthally integrated magnitude of transverse flow increases with increasing centrality of the collisions. On the other hand, an increasing trend in the $v_0(\langle\langle v_T \rangle\rangle)$ -values with increasing N_{part} , is restricted only to the peripheral collisions, and beyond $N_{\text{part}} = 80$ the $v_0(\langle\langle v_T \rangle\rangle)$ -values achieve a saturation, being nearly independent of the centrality of the collisions. A significant energy dependence of v_0 is also observed for all the variables considered in this analysis. We do not see any significant energy dependence in the variation

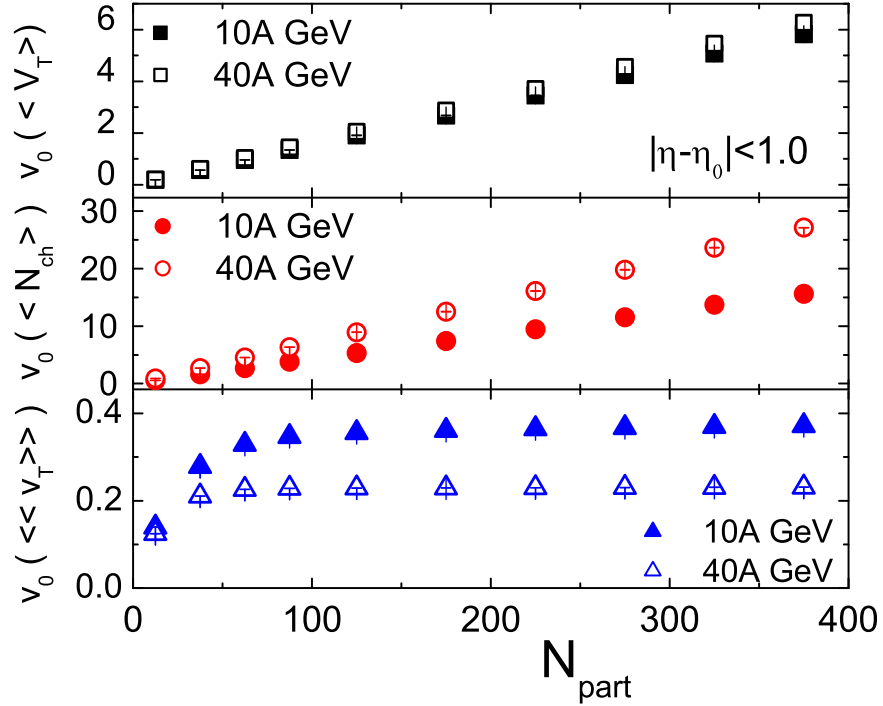


Figure 6.3: Centrality dependence of isotropic flow coefficient v_0 obtained from the azimuthal distributions of total radial velocity, multiplicity and mean radial velocity in Au+Au collision at $E_{\text{lab}} = 10A$ and $40A$ GeV.

of $v_0(\langle\langle V_T \rangle\rangle)$ with N_{part} . The $v_0(\langle N_{\text{ch}} \rangle)$ values are however consistently higher at $E_{\text{lab}} = 40A$ GeV than those at $E_{\text{lab}} = 10A$ GeV, the difference getting larger with increasing N_{part} . Once again $v_0(\langle\langle v_T \rangle\rangle)$ behaves quite differently in this regard. The values at lower energy (10A GeV) are consistently higher than those obtained at higher (40A GeV) energy. We may recall that the mean radial velocity has been defined in a way such that the multiplicity effects are removed. Therefore, we conclude that the particle multiplicity plays a dominant role to determine the total transverse flow, and a higher energy input results in a smaller amount of azimuthally integrated transverse flow. It seems that a higher energy is rather utilized to generate the pressure gradient and momentum space anisotropy.

6.2.2 Transverse momentum dependence of v_2 and v_0

It is well known that the anisotropy coefficient v_2 depends on the p_T of charged hadrons. Hydrodynamics as well as resonance decays both are expected to dominate at low- p_T behaviour, whereas at high- p_T particles are expected to stem out from the fragmentation of jets modified in the hot and dense medium of the intermediate fireball [14]. At FAIR energies the production of high- p_T hadrons would be rare, and owing to statistical reasons we restrict our analysis up to $p_T = 2.0$ GeV/c. The v_2 -values arising from multiplicity distributions of the produced hadrons has been studied widely as a function of p_T using the data available

from the experiments held at RHIC [15] and LHC [16]. Simulation results under FAIR-CBM conditions utilizing the UrQMD, AMPT (default) and AMPT (string melting) models can be found in [7, 8]. Figure 6.4 depicts that the anisotropy present either in $\langle N_{\text{ch}} \rangle$, $\langle V_T \rangle$ or

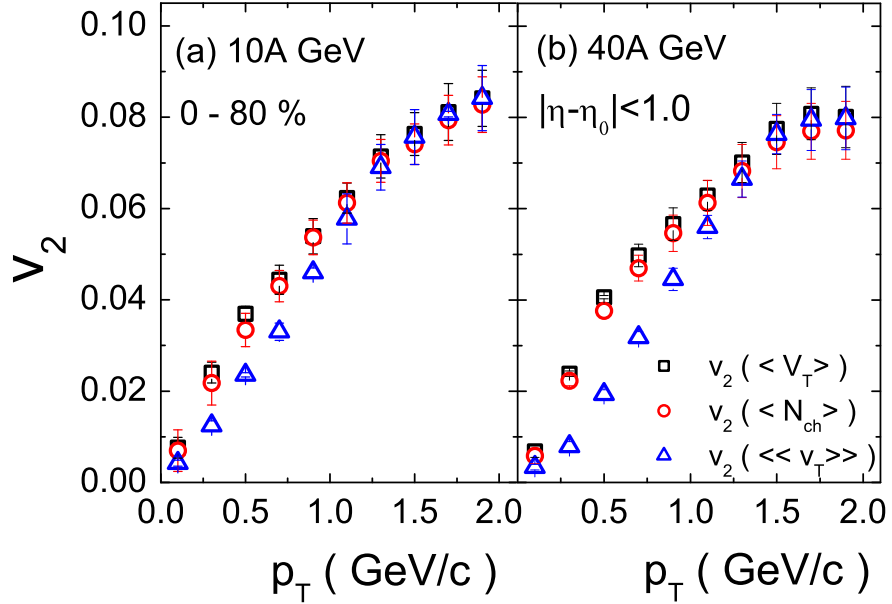


Figure 6.4: Transverse momentum dependence of anisotropy parameter v_2 obtained from the azimuthal distributions of total radial velocity, multiplicity and mean radial velocity in Au+Au collision at $E_{\text{lab}} = 10A$ and $40A$ GeV.

in $\langle\langle v_T \rangle\rangle$, rises monotonically with increasing p_T . At $E_{\text{lab}} = 40A$ GeV, beyond $p_T = 1.5$ GeV/c there is a trend of saturation in the v_2 -values extracted from all three variables. Once again we conclude that at a particular p_T bin, the multiplicity dominates over the radial velocity, and $v_2(\langle N_{\text{ch}} \rangle)$ and $v_2(\langle V_T \rangle)$ are both found to be almost equal to each other in the $0 \leq p_T \leq 2.0$ GeV/c range. Once we get rid of the multiplicity effects, the actual anisotropy present in the radial velocity comes out, which we can see in the plot of $v_2(\langle\langle v_T \rangle\rangle)$ against p_T , shown in the same diagram. As a result, within $0.25 \leq p_T \leq 1.25$ GeV/c the $v_2(\langle\langle v_T \rangle\rangle)$ -values become slightly lower at higher E_{lab} . At FAIR energies however, we do not find any noticeable deviation in the trend of this kind of p_T -dependence of v_2 from its nature observed even at the RHIC energies [1]. Comparing Figure 6.4(a) with Figure 6.4(b), we see a very weak, almost insignificant, energy dependence of v_2 in terms of all three variables concerned. We may reckon that the FAIR-CBM condition may not provide us with a very nice platform to study the energy dependence of anisotropy, rather it may be more suitable to study the issues related to the isotropy measure v_0 . The p_T -dependence of v_0 has been shown in Figure 6.5. It is observed that the v_0 -coefficients associated with $\langle N_{\text{ch}} \rangle$, $\langle V_T \rangle$ and $\langle\langle v_T \rangle\rangle$ while plotted against p_T , exhibit similar nature. In the low- p_T region, the v_0 values extracted from each variable rise with increasing p_T , attain a maximum, and beyond

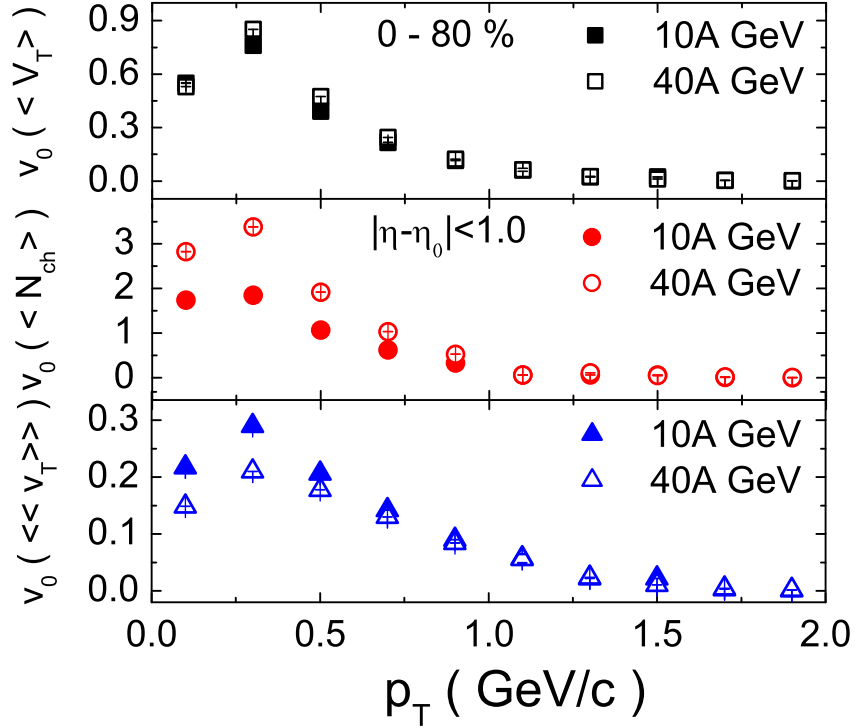


Figure 6.5: Transverse momentum dependence of isotropic coefficient v_0 obtained from the azimuthal distributions of total radial velocity, multiplicity and mean radial velocity in Au+Au collision at $E_{\text{lab}} = 10A$ and $40A$ GeV.

$p_T = 1.25$ GeV/c fall off to a very small saturation value (almost zero) at both incident energies. Once again, while $v_0(\langle V_T \rangle)$ values at $E_{\text{lab}} = 10A$ and $40A$ GeV are almost identical to each other, in the low- p_T region ($p_T \lesssim 0.7$ GeV/c) the $v_0(\langle N_{\text{ch}} \rangle)$ -values at $E_{\text{lab}} = 40A$ GeV are higher than those at $10A$ GeV. On the other hand, the $v_0(\langle\langle v_T \rangle\rangle)$ -values obtained at $E_{\text{lab}} = 40A$ GeV are lower in the low- p_T region ($p_T \lesssim 0.5$ GeV/c) than those at $10A$ GeV. It seems that at FAIR energies the random thermal motion of particles perhaps dominates over their collective behaviour, which at high- p_T leads to a very small amount of azimuthally integrated magnitude of the net flow.

6.3 Conclusion

In this investigation we present some basic simulation results on the elliptic and radial flow of charged hadrons. The study is based on the azimuthal distributions of total transverse velocity, mean transverse velocity and multiplicity of charged hadrons coming out from Au+Au events generated by the AMPT (string melting) model at $E_{\text{lab}} = 10A$ and $40A$ GeV. We observe that azimuthal asymmetries are indeed present in all three distributions. However, we also note that in our simulation results the azimuthal anisotropy of the

final state particles is predominantly due to the asymmetry of particle multiplicity distribution, and only a small fraction of this asymmetry is actually due to the kinematic reasons. The overall nature of the centrality and transverse momentum dependence of the elliptic anisotropy parameter, is similar for the three variables considered in the present analysis. The elliptic flow parameter is highest in the mid-central collisions, and within the interval $0 \leq p_T \leq 2.0$ GeV/c it is highest at the highest p_T . From our simulated results in the FAIR energy range we find a very small energy dependence of the elliptic flow parameter. On the other hand, the azimuthally integrated magnitude of the radial flow is maximum for the most central collisions and its values are high in the low- p_T region. From this analysis we see that the contribution to v_0 from the asymmetry in multiplicity distribution and that coming from the asymmetry in kinematic variable v_T , exhibit an opposite incident beam energy dependence. While the former is slightly higher at higher E_{lab} , the latter is higher at lower E_{lab} . Our simulated results are consistent with those obtained from the RHIC and LHC experiments, and do not require any new dynamics for their interpretation. However, in future there is enough scope to appropriately model these results in terms of relevant thermodynamic and hydrodynamic parameters associated with the intermediate fireballs produced in high-energy AB collisions.

Bibliography

- [1] L. Li, N. Li, and Y. Wu, *Chin. Phys. C* **36**, 423 (2012).
- [2] L. Li, N. Li, and Y. Wu, *J. Phys. G* **40**, 075104, (2013).
- [3] Y. B. Ivanov *et al.*, *Phys. Rev. C* **80**, 064904 (2002).
- [4] C. Alt *et al.* (NA49 Collaboration), *Phys. Rev. C* **68**, 034903 (2003).
- [5] B. Alver *et al.* (PHOBOS Collaboration), *Phys. Rev. Lett* **98**, 242302 (2007).
- [6] S. A. Voloshin and A. M. Poskanzer, *Phys. Lett. B* **474**, 27 (2000).
- [7] S. Sarkar, P. Mali, and A. Mukhopadhyay, *Phys. Rev. C* **95**, 014908 (2017).
- [8] P. P. Bhaduri and S. Chattopadhyay, *Phys. Rev. C* **81**, 034906 (2010).
- [9] S. Sarkar, P. Mali, and A. Mukhopadhyay, *Phys. Rev. C* **96**, 024913 (2017).
- [10] L. Adamczyk *et al.* (STAR Collaboration), *Phys. Rev. C* **88**, 014904 (2013).
- [11] K. Aamodt *et al.* (ALICE Collaboration), *Phys. Lett. B* **719**, 18 (2013).
- [12] D. Solanki *et al.*, *Phys. Lett. B* **720**, 352 (2013).

-
- [13] X. Sun (for the STAR Collaboration), Nucl. Phys. A **931**, 1194 (2014).
- [14] G. Aad *et al.* (ATLAS Collaboration), Phys. Lett. B **707**, 330 (2012).
- [15] K. Adcox *et al.* (PHENIX Collaboration), Nucl. Phys. A, **757** 184 (2005).
- [16] K. Aamodt *et al.* (ALICE Collaboration), Phys. Rev. Lett. **105**, 252302 (2010).

Chapter 7

Sphericity based flow analysis at FAIR conditions

The concept of event shape determination in high-energy physics was introduced in the late seventies as a quantitative method to understand the nature of gluon bremsstrahlung process [1–3]. Experimental data analysis in this regard was performed for the first time by the OPAL Collaboration [4] while attempting to test the asymptotic freedom in e^+e^- annihilation, and then by the ZEUS Collaboration [5] in an attempt to extract the strong force coupling constant from lepton induced deep inelastic scattering. Later, hadronic event shape [6, 7] was examined in pp collisions at the LHC energies phenomenologically by using PYTHIA8 [8, 9], and experimentally by the ALICE [10, 11], ATLAS [12, 13], and CMS [14] collaborations. An event shape variable called transverse sphericity (S_T), has successfully been employed to understand the dynamics of particle production mechanism, collective flow of hadronic matter, and in medium jet modification etc., in pp collisions at the LHC energies [10, 12]. This however is not to be confused with the transverse sphericity [15], another event shape variable that too has been used to separate out the jetty and isotropic events in some of the above mentioned experiments. In this simulation based study we are going to present an analysis on the centrality dependence of the yields of charged hadrons, their transverse momentum spectra and some characteristics of the second (v_2) and third (v_3) harmonic flow coefficients, with reference to an event shape engineering implemented by using the S_T -parameter. It has been reported that in a sphericity based event classification, the magnitude of v_2 -coefficient for the jetty events is larger, whereas the same for the isotropic events is smaller than those obtained for the entire class of events [15]. This clearly suggests that measurements made without incorporating any classification scheme do not contain

every piece of information about collectivity. For our analysis a sample of minimum bias Au+Au events at $E_{\text{lab}} = 30A$ GeV has been generated by using the AMPT (string melting) model. One of the major objectives of this investigation is to study the dynamics of particle production with different degrees of collectivity in the framework of the AMPT model in its string melting configuration.

7.1 Methodology

The event shape variables generally refer to the geometrical distribution of p_T of the outgoing particles. This restriction to the transverse plane is imposed in order to avoid any bias coming from the longitudinal boost along the beam direction [6]. To define the transverse sphericity parameter we start with a transverse momentum matrix [10, 12],

$$\mathbf{S}_{\mathbf{xy}} = \begin{pmatrix} a_{11} & a_{12} \\ a_{21} & a_{22} \end{pmatrix} \quad (7.1)$$

where

$$a_{11} = \frac{1}{\sum_i p_{T_i}} \sum_i \frac{p_{x_i}^2}{p_{T_i}}, \quad a_{22} = \frac{1}{\sum_i p_{T_i}} \sum_i \frac{p_{y_i}^2}{p_{T_i}}, \quad a_{12} = a_{21} = \frac{1}{\sum_i p_{T_i}} \sum_i \frac{p_{x_i} p_{y_i}}{p_{T_i}} \quad (7.2)$$

Here p_{T_i} is the transverse momentum of the i th particle in an event, p_{x_i} and p_{y_i} are the components of p_{T_i} . In Equation (7.2) each sum runs over the particle number within the kinematic limit(s) considered and belonging to an event. In the above expressions the $1/\sum_i p_{T_i}$ term is introduced to avoid the dependence on possible collinear splittings of particle momenta. The diagonalization of the matrix $\mathbf{S}_{\mathbf{xy}}$ will result in two eigenvalues, say λ_1 and λ_2 . If we assume $\lambda_1 > \lambda_2$, the transverse sphericity S_T is defined as [10, 12],

$$S_T = \frac{2\lambda_2}{\lambda_1 + \lambda_2} \quad (7.3)$$

By definition S_T has been made infrared and collinear safe [16]. The quantity however has a multiplicity dependence. The event-wise S_T values should lie between 0 and 1, and the extreme limits are classified as,

$$S_T = \begin{cases} 0 & \text{'jetty limit'} \\ 1 & \text{'isotropic limit'} \end{cases}$$

The jetty events originate from hard QCD-processes corresponding to high- p_T jets with a pencil-like emission structure, while the isotropic events have a large number of soft productions associated with low momentum transfer, and as the name suggests, an isotropic

emission of the final state particles (hadrons). Once the jetty events are properly identified, it would be possible to study the jet medium modification and jet chemistry in an efficient way.

7.2 Results and discussions

In this section we describe some simulation results obtained from the Au+Au collision at an incident beam energy $E_{\text{lab}} = 30A$ GeV. We have used 10 million minimum bias Au+Au events generated by the AMPT (string melting) model. The analysis is performed over all charged hadrons falling within the central pseudorapidity (η) region defined by $|\eta - \eta_0| < 1.0$, where η_0 is the centroid of the η -distribution. In Figure 7.1 we plot the sphericity

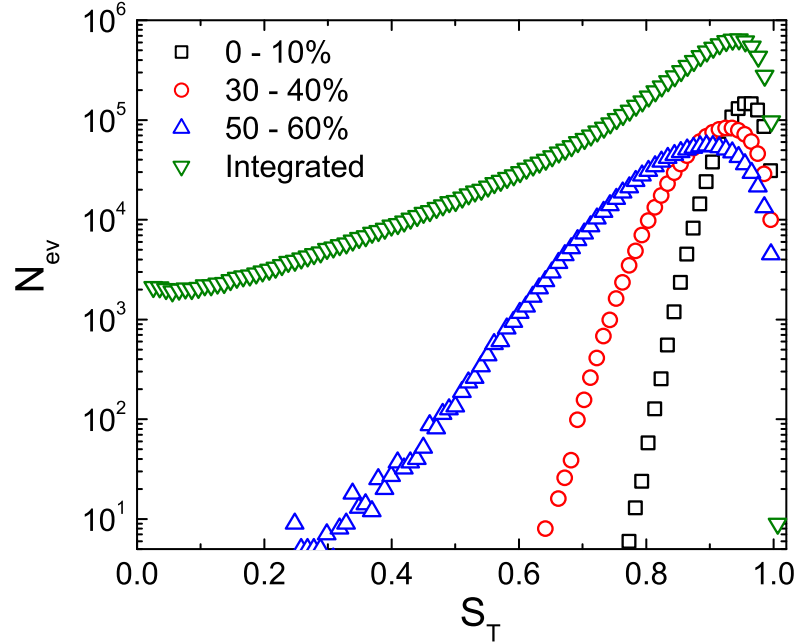


Figure 7.1: Sphericity distribution of charged hadrons in Au+Au collision at $E_{\text{lab}} = 30A$ GeV.

distributions for events belonging to different centrality classes, as well as for the entire event sample. We observe that the S_T -distributions are strongly left-skewed, and as we move from peripheral to central collisions the peak of the distribution shifts more and more towards isotropic limit ($S_T = 1.0$). In the 0 – 10% centrality class almost every event has a S_T -value more than 80%. At $E_{\text{lab}} = 30A$ GeV the jet production cross section should be small. Compared to the number of isotropic events, not too many jetty events are therefore expected in our min-bias event sample. They should predominantly belong to the peripheral collisions in which the overlapping part of the colliding nuclei is small sized. On the other hand, in central collisions the pencil-like structures of the jets are either destroyed by multiple

rescattering or absorbed in the medium as they try to penetrate through a comparatively larger sized collision region. With increasing system size a shift towards isotropy in the sphericity distribution has been reported as well [17]. These observations suggest that the event shape engineering should have a significant implication on the event characteristics, which may be useful to explore different mechanisms of multiparticle production in different classes of events. In order to disentangle the low and high sphericity events we have followed

Table 7.1: Limiting values of transverse sphericity for jetty and isotropic events

Centrality (%)	Jetty	Isotropic
0 - 10	0 - 0.8938	0.91405 - 1
10 - 20	0 - 0.8736	0.89385 - 1
20 - 30	0 - 0.8433	0.88375 - 1
30 - 40	0 - 0.8232	0.87365 - 1
40 - 50	0 - 0.8023	0.85345 - 1
50 - 60	0 - 0.7828	0.83325 - 1
60 - 70	0 - 0.7424	0.81305 - 1
70 - 80	0 - 0.6616	0.76255 - 1
80 - 100	0 - 0.4293	0.63125 - 1

the criterion set in [17], and applied a 20% cut from both of the extreme limits of the sphericity distribution. In other words, events having the lowest 20% values of S_T are classified as jetty events, while those falling within the highest 20% group are called isotropic. The sphericity range for the isotropic and jetty events corresponding to different centralities are listed in Table 7.1. We see that most of the Au+Au events of our minimum bias sample are neither jetty nor isotropic in structure, and except for a few extreme peripheral classes most of them fall within a small S_T -range.

7.2.1 p_T spectra and mean p_T

In Figure 7.2 we present the p_T -spectra of pions, kaons, protons and sigma particles in the (20 – 30)% centrality range for different sphericity classes of events. The spectra have their usual characteristics, exponentially decaying in the low- p_T region ($0.5 < p_T < 1.5$ GeV/c), and falling like a power law in the high- p_T region (~ 2.0 GeV/c). It is also noticed that in the low- p_T region the number of particles produced by the isotropic events exceed those coming out from the jetty events. However, with increasing p_T an opposite trend with respect to the particle number is observed. At higher p_T -values the number of particles produced by the jetty events exceed that coming from the isotropic events. This p_T -value where this trend reversal takes place, is referred to as the crossing point. The feature can be more clearly seen in the insets of Figure 7.2, where the ratio (R) between the p_T -spectra of

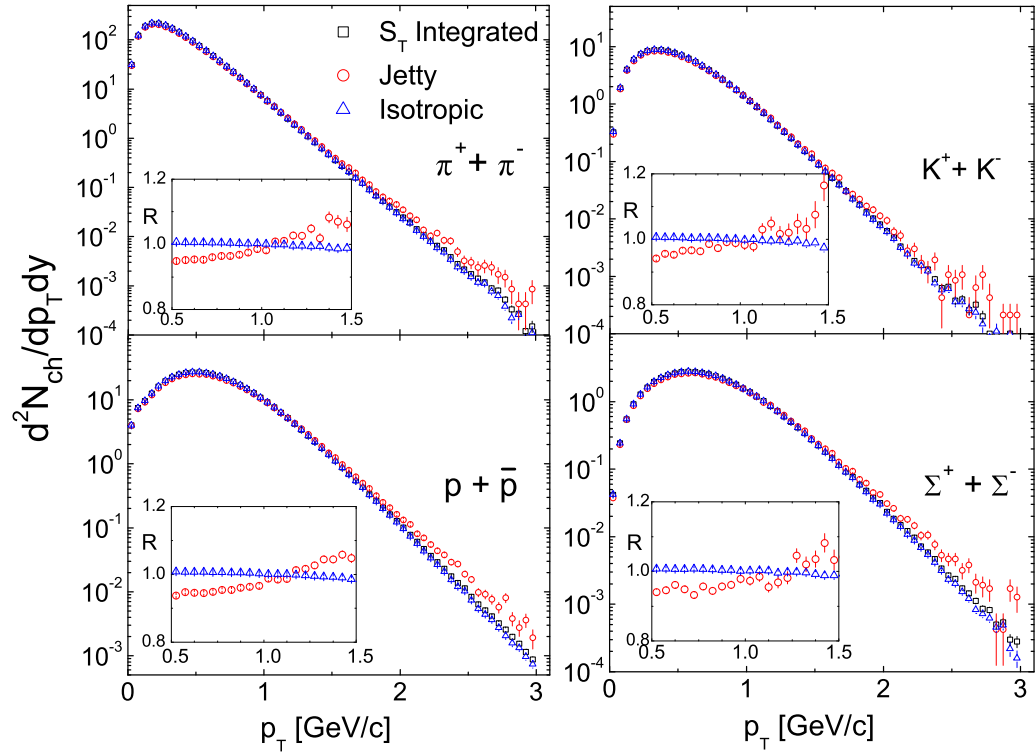


Figure 7.2: p_T -spectra of different charged hadrons in the midrapidity region for isotropic, jetty and S_T -integrated events in 20 – 30% central Au+Au collisions at $E_{\text{lab}} = 30A$ GeV. Inset: Ratio of p_T -spectra for the isotropic and jetty events to S_T -integrated events.

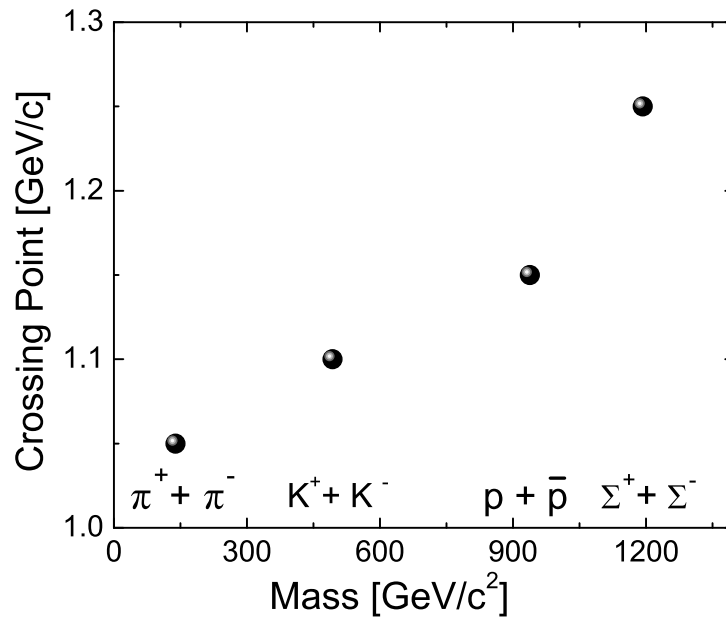


Figure 7.3: Crossing point of the ratio of the p_T spectra of isotropic and jetty events to S_T -integrated events as a function of particle mass in Au+Au collisions at $E_{\text{lab}} = 30A$ GeV.

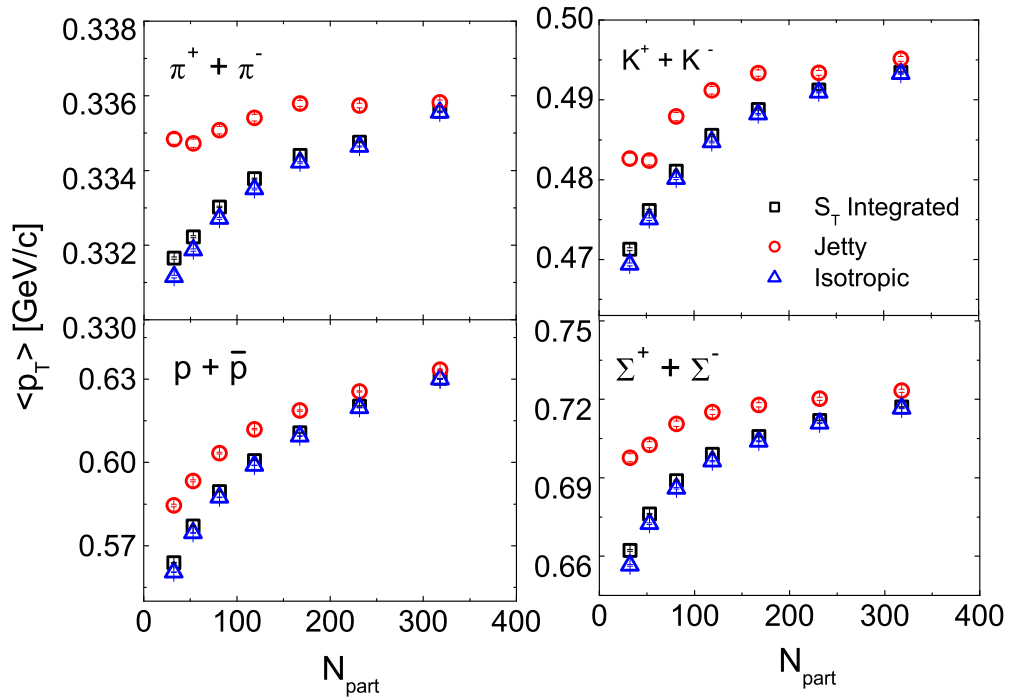


Figure 7.4: N_{part} dependence of average p_T of different charged hadrons at midrapidity in isotropic, jetty and S_T -integrated events in Au+Au collisions at $E_{\text{lab}} = 30.4$ GeV.

the isotropic (jetty) events and that of the S_T -integrated events are zoomed in for a limited p_T -range. In Figure 7.3 we notice that with an increasing rest mass of the hadron species concerned, the crossing point consistently shifts towards higher p_T . The N_{part} dependence of $\langle p_T \rangle$ corresponding to the isotropic, jetty and S_T -integrated events for different particle species is presented in Figure 7.4. It is to be noted that $\langle p_T \rangle$ increases from peripheral to central collisions, and it also increases with increasing hadron mass. This mass dependence of $\langle p_T \rangle$ may be a consequence of collective expansion in the radial flow [18]. One should also notice that the increase in $\langle p_T \rangle$ with increasing N_{part} is more prominent for the heavier masses. In central collisions more energy is deposited within the intermediate fireball. As a result higher pressure develops, and the final state particles experience comparatively higher radial push than those evolved from peripheral collisions. One can see that events belonging to different sphericity classes contribute differently to $\langle p_T \rangle$. The jetty events carry more p_T than the isotropic events. As we shall see later, being associated with a large number of soft-hadron production, the isotropic events in general have a higher integrated yield of particles. Therefore in order to conserve momentum, on an average they carry less $\langle p_T \rangle$ per particle. The $\langle p_T \rangle$ -difference between the jetty and isotropic events is higher for higher hadron mass, while it diminishes with increasing centrality. Our analysis on event separation using S_T indicates that it is possible to extract significant information on the collective flow of hadrons.

7.2.2 Integrated yields

Figure 7.5 shows the N_{part} dependence of the integrated yields (dN/dy) of pions, kaons, protons and sigma particles over the mid-rapidity ($\Delta\eta = 0.1$) region for different sphericity classes considered in this analysis. The yields of pions and protons as expected are greater than that of the strange hadrons like kaons and sigma particles. We observe that for the jetty, isotropic and S_T -integrated event samples, dN/dy at $E_{\text{lab}} = 30A$ GeV increases almost linearly with N_{part} for all the particle species considered in this analysis. Besides, it is also observed that the yield is weakly dependent on the sphericity class. The isotropic events consistently produce a little more particles than the jetty events. This observation is consistent with our results on the p_T -spectra and $\langle p_T \rangle$ distribution presented above. Soft hadron production, which is a characteristic feature of the isotropic events, is more abundant at the present beam energy. The observations of Figure 7.4 and Figure 7.5 actually manifest a momentum sharing, i.e. higher number of particles are produced in the isotropic events, and therefore each particle on an average should carry less $\langle p_T \rangle$. Our observation in this regard is consistent with that obtained from an AMPT (string melting) based analysis performed at the LHC energies [17]. In Figure 7.6 we plot the N_{part} -dependence of the particle yield normalized by the number of participant nucleon pairs. The variation in

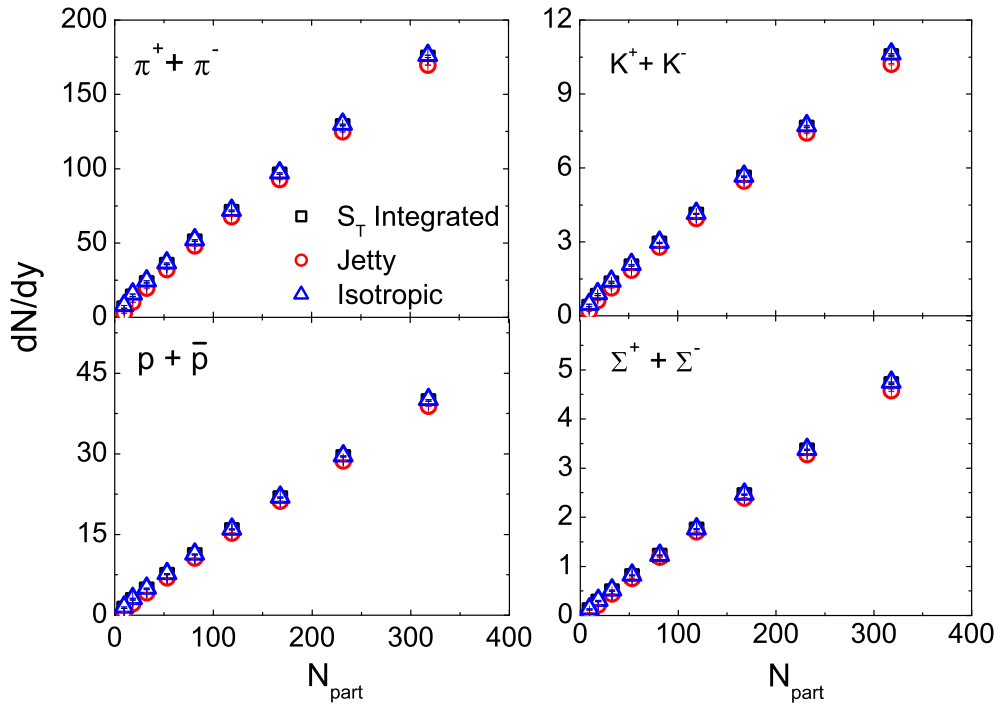


Figure 7.5: Integrated yields in the midrapidity region of different charged hadrons as a function of N_{part} for the isotropic, jetty and S_T -integrated events in Au+Au collisions at $E_{\text{lab}} = 30A$ GeV.

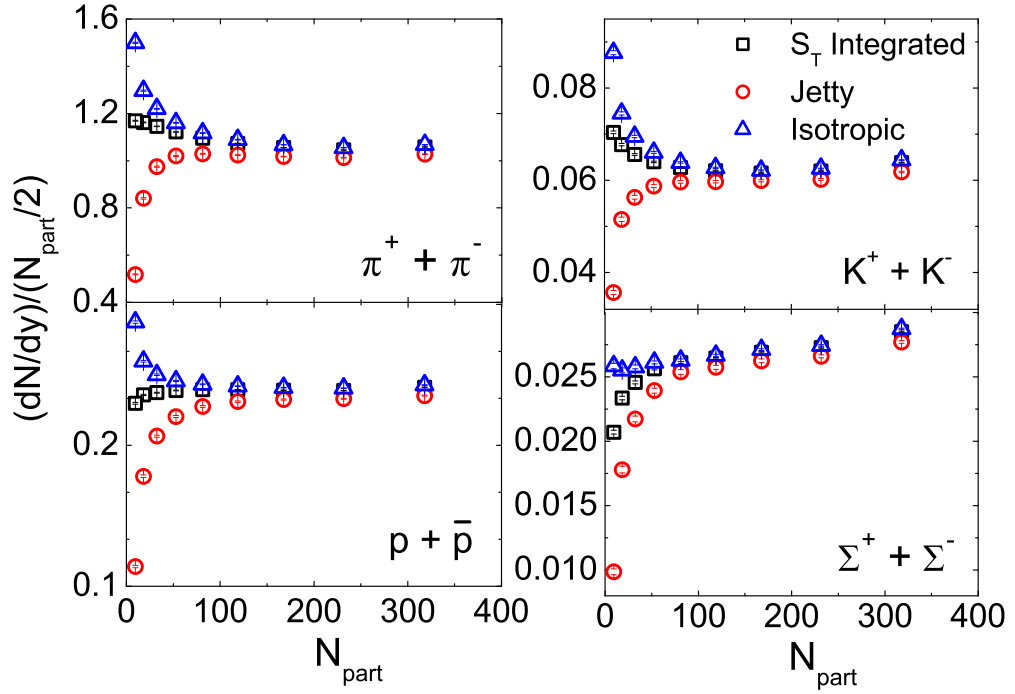


Figure 7.6: Integrated yields in the midrapidity region of different charged hadrons per participant nucleon pair as a function of N_{part} for the isotropic, jetty and S_T -integrated events in Au+Au collision at $E_{\text{lab}} = 30A$ GeV.

this normalized yield behaves differently for the jetty, isotropic and S_T -integrated events in peripheral collisions, a feature that is not so obvious in the dN/dy versus N_{part} plot, shown in Figure 7.5. In the mid-central to central collisions, the normalized yield remains almost uniform for all three S_T -categories of events. Compared to the jetty events, the contribution to the normalized yield coming from isotropic events, is significantly higher in the peripheral and marginally higher in the central collisions. Such an observation can be understood from the fact that the yield is dominated by soft production of charged hadrons, which again is dominated by the particles coming out of isotropic events. For the isotropic as well as peripheral class of events, the normalized yields of pions, kaons and protons diminish by some amount with increasing N_{part} , and then they remain almost uniform. It is quite possible that in these events soft-hadrons are to some extent absorbed within the collision region, a feature that initially increases with increasing size of the overlapping part of the colliding nuclei, and compensated thereafter by a growing number of binary NN collisions, and an increasing number of particles produced thereof. For the sigma particle the normalized yield shows a very small linear growth with increasing N_{part} . On the other hand, for the jetty events the normalized yields for all four types of hadrons considered, increase with increasing N_{part} by some amount for the peripheral class of events, and then they saturate to a uniformity for the more central classes. For S_T -integrated events, except for the Σ -particle, the normalized yield remains almost always uniform with N_{part} for all

three other hadron species considered. For the Σ -particle the normalized yield initially increases by a small amount and then becomes uniform.

7.2.3 Collective flow

Centrality dependence

We compute v_2 and v_3 for all charged hadrons in the midrapidity region ($|\eta - \eta_0| < 1.0$) as functions of N_{part} , and present our results respectively in Figure 7.7 and Figure 7.8 for different S_T -categories. In general we observe that for both S_T -categories, the v_2 -values are smaller for the extreme central and peripheral events. As mentioned before, in a central collision the overlapping part of the colliding nuclei is nearly symmetric, and therefore the pressure gradient that develops after initial compression, is not too large to generate a strong elliptical flow. On the other hand, in a peripheral collision the overlapping part is highly asymmetric in geometry. However, due to the small number of particles contained within the overlap region, the effect of v_2 cannot be carried through to the final state. The v_2 -values peak around mid-central collisions, which is a consequence of both finite initial state asymmetry and a sufficient number of produced particles that carries the information. It is also observed from Figure 7.7 and Figure 7.8 that at all centralities v_2 is greater in magnitude than v_3 . This may be attributed to the fact that v_2 develops from the geometric asymmetry of the overlapping region as well as from the initial state fluctuations of the participating nucleons. On the other hand v_3 arises only from the initial state fluctuations.

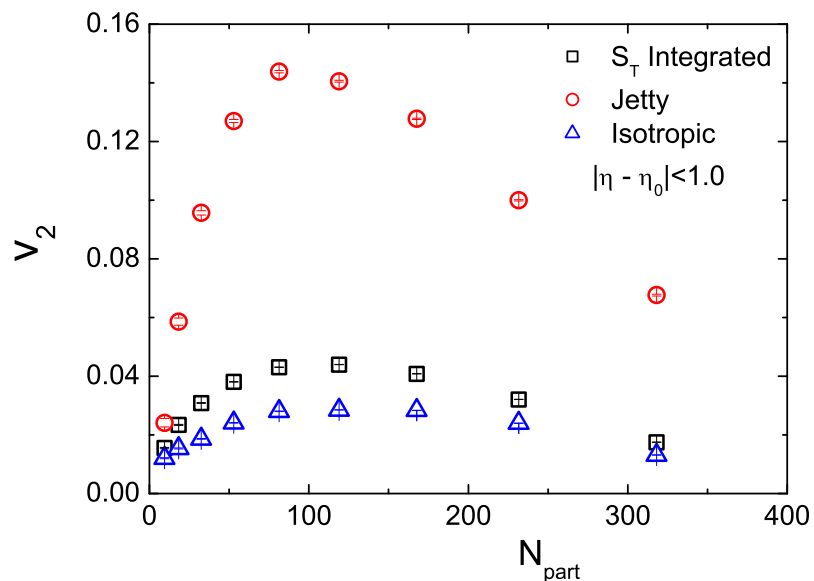


Figure 7.7: Elliptic flow coefficient (v_2) as a function of N_{part} at midrapidity for isotropic, jetty and S_T -integrated events in Au+Au collisions at $E_{\text{lab}} = 30A$ GeV.

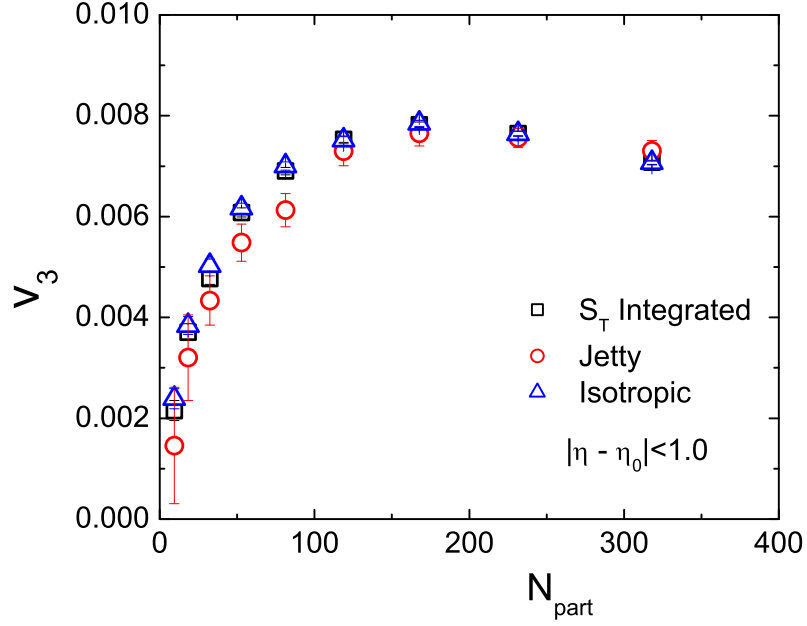


Figure 7.8: Triangular flow coefficient (v_3) as a function of N_{part} at midrapidity for isotropic, jetty and S_T integrated events in Au+Au collisions at $E_{\text{lab}} = 30A$ GeV.

It is evident that in comparison to the initial geometric asymmetry and subsequent pressure gradient developed thereof, the initial state fluctuation is a weaker phenomenon. There is no reason that these fluctuations should depend on the collision centrality. The same is reflected in Figure 7.8, where we find that except for some peripheral classes v_3 is not very sensitive to the collision centrality. With increasing N the v_3 -values increase from extreme peripheral to mid-central collisions, and within the mid-central to central region they remain almost uniformly distributed. Our observations on the centrality dependence of v_2 and v_3 are consistent even with the results obtained from RHIC [19] and LHC [20] experiments, and also with some model calculations at FAIR energies [21, 22]. The effect of centrality on v_2 and v_3 is going to be further scrutinized when we study them as functions of p_T .

In Figure 7.7 we also find that the v_2 -values obtained for the jetty events are consistently larger than those obtained for the isotropic events over the entire centrality range considered. All three v_2 -distributions peak around $N_{\text{part}} = 100$, and for the jetty events the peak value is not only several times larger than that of the isotropic events, but it is also comparable to typical v_2 -values obtained at much higher collision energies [20]. The fact that the isotropic events have very low v_2 -values, indicate that there is less asymmetry in their azimuthal distribution. As expected, the S_T -integrated v_2 -distribution lies in between the jetty and isotropic, although it is much closer to the isotropic distribution, which once again confirms the predominance of the latter in our minimum bias Au+Au event sample. On the other hand, in Figure 7.8 we do not notice statistically significant differences in the v_3 -values obtained for the jetty and isotropic events. In order to better understand the

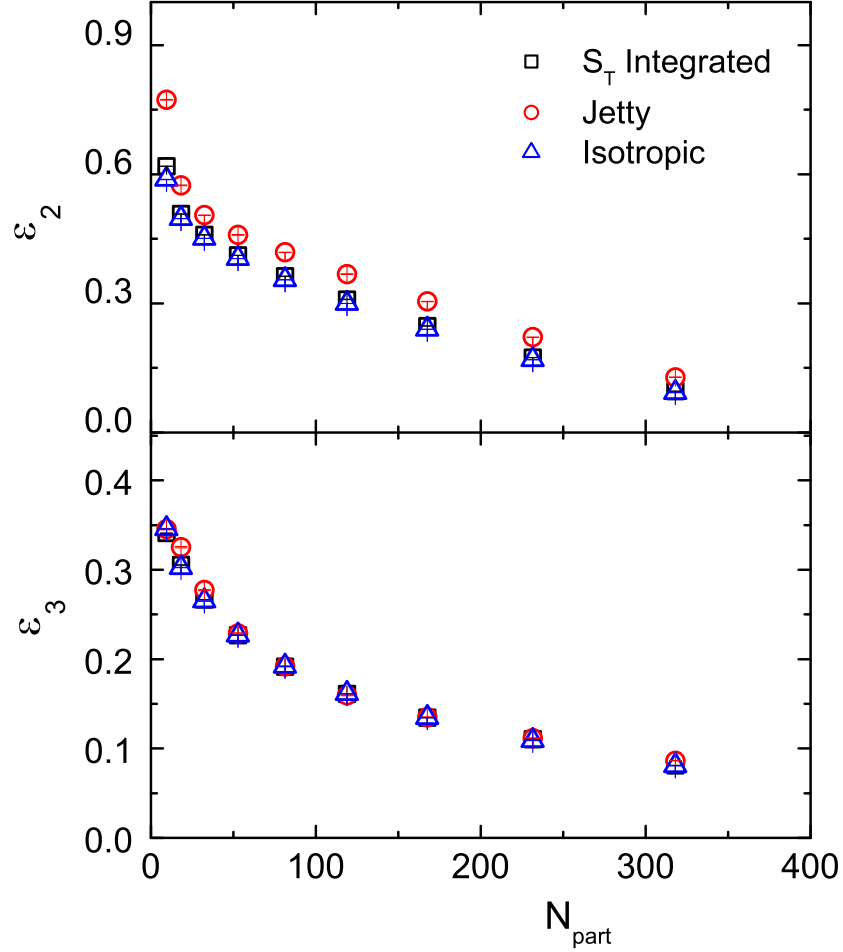


Figure 7.9: Eccentricity (upper panel) and triangularity (lower panel) against N_{part} for isotropic, jetty and S_T -integrated events in Au+Au collisions at $E_{\text{lab}} = 30A$ GeV.

S_T -dependence of the flow parameters, we examine the spatial asymmetries present in the initial states of the Au+Au events. We compute the eccentricity (ε_2) and triangularity (ε_3) parameters, and in Figure 7.9 plot them as functions of N_{part} . We notice that both ε_2 and ε_3 monotonically decrease with increasing N_{part} . Except for a few most peripheral classes of events, ε_2 -values for jetty, isotropic and S_T -integrated events are not significantly different at all other centralities. The ε_2 -values of the jetty events only marginally exceed those of the isotropic. We have repeated similar kind of analysis for the ε_3 parameter, and found that the corresponding differences in the jetty and isotropic events are even smaller in magnitude. As ε_3 originates only from the initial state fluctuations, it should be independent of the event geometry. Scaling out of the effects of geometry from the flow parameters is a common practice that is followed in different AB collision experiments [23]. This eventually helps us to understand the physics of (re)scattering and effects of multiplicity on the flow parameters. We have scaled v_2 by the respective ε_2 , and in Figure 7.10 plotted the ratio against N_{part} . For all three categories of events the v_2/ε_2 -ratio monotonically rises from

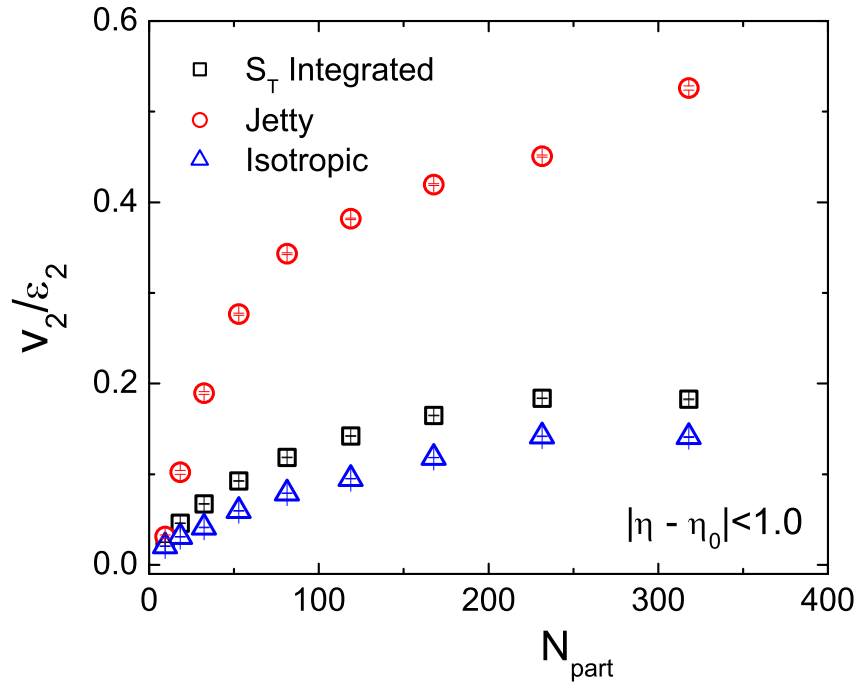


Figure 7.10: Elliptic flow coefficient (v_2) scaled by the eccentricity parameter (ε_2) plotted against N_{part} at midrapidity for isotropic, jetty and S_T -integrated events in Au+Au collisions at $E_{\text{lab}} = 30A$ GeV.

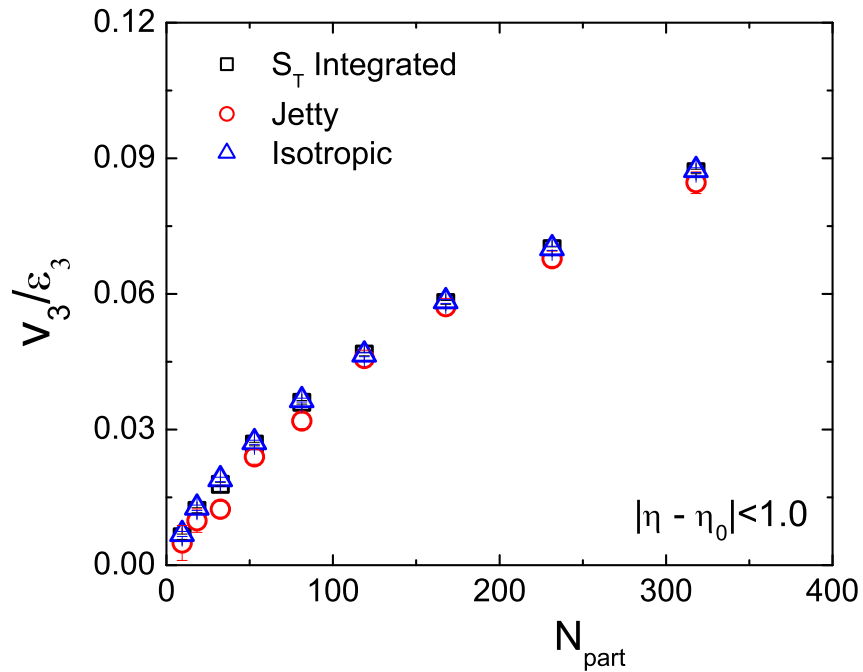


Figure 7.11: Triangular flow coefficient (v_3) scaled by the triangularity parameter (ε_3) plotted against N_{part} at midrapidity for isotropic, jetty and S_T -integrated events in Au+Au collisions at $E_{\text{lab}} = 30A$ GeV.

peripheral to central collisions. The rise is most prominent for the jetty class of events, but quite moderate for the isotropic. As expected, in this regard the S_T -integrated event sample behaves very similar to the isotropic class of events. Our observation suggests that the elliptic flow is quite strong in the jetty class of events. Even after the removal of the effects of geometry, no scaling in the centrality dependence of v_2/ε_2 -ratio can be seen for different S_T -categories of events. We may therefore argue that the observed differences in the v_2 -values in jetty and isotropic events cannot simply be attributed to the initial state asymmetries. Differences in the final state collective interactions are also responsible for our sphericity dependent elliptic flow results. The centrality dependence of the S_T -integrated v_2/ε_2 -ratio is not very much different from the corresponding trends observed in the RHIC and LHC experiments [24, 25], except that in the present case their magnitudes are lower. As expected in Figure 7.11 we see that the v_3/ε_3 ratio, being dependent only on the initial state fluctuations, grows identically with N_{part} for all three classes of events. The rise, almost linear in nature, may be considered as a consequence of multiplicity scaling [26].

p_T dependence

The p_T -dependence of collective flow parameters of charged hadrons at different centrality classes has been investigated in several experiments [19, 27–29]. We too have examined the same for v_2 and v_3 at three different centrality classes and for three event samples belonging to different S_T -categories. Our results on $v_2(p_T)$ are schematically presented in Figure 7.12. For the most central 0 – 10% collisions the v_2 -values are always quite small both for the isotropic and S_T -integrated event samples. However in the same centrality class, v_2 for the jetty events rises almost linearly with p_T . In the mid-central 30 – 40% and peripheral 60 – 70% collisions, v_2 for the isotropic and S_T -integrated event samples are a little higher in magnitude. STAR results for the S_T -integrated events obtained from the Au+Au collision at $\sqrt{s_{NN}} = 7.7$ GeV are incorporated [19] in the plot for mid-central collisions, which matches quite well with our simulated results. For the S_T -integrated class of events, with increasing p_T a systematic rise in the v_2 -values can be seen. On the other hand, for the isotropic events the initial rise in v_2 is followed by a saturation beyond $p_T = 1.5$ GeV/c in both the 30 – 40% and 60 – 70% centrality classes. In the mid-central collisions the v_2 -values for the jetty events are significantly higher than those obtained for the other two centrality classes, and they rise quite sharply with p_T . From Figure 7.7 it has already been confirmed that the contribution to v_2 from the jetty events is maximum in mid-central collisions. Similar type of observation is also noted in Figure 7.12 in the 30 – 40% centrality class. Figure 7.13 once again illustrates that v_3 is independent of centrality. The reason, as discussed, is that the phenomenon stems out only from initial state fluctuations, and therefore, is not sensitive to the event shape which is based on the distribution of final state particles.

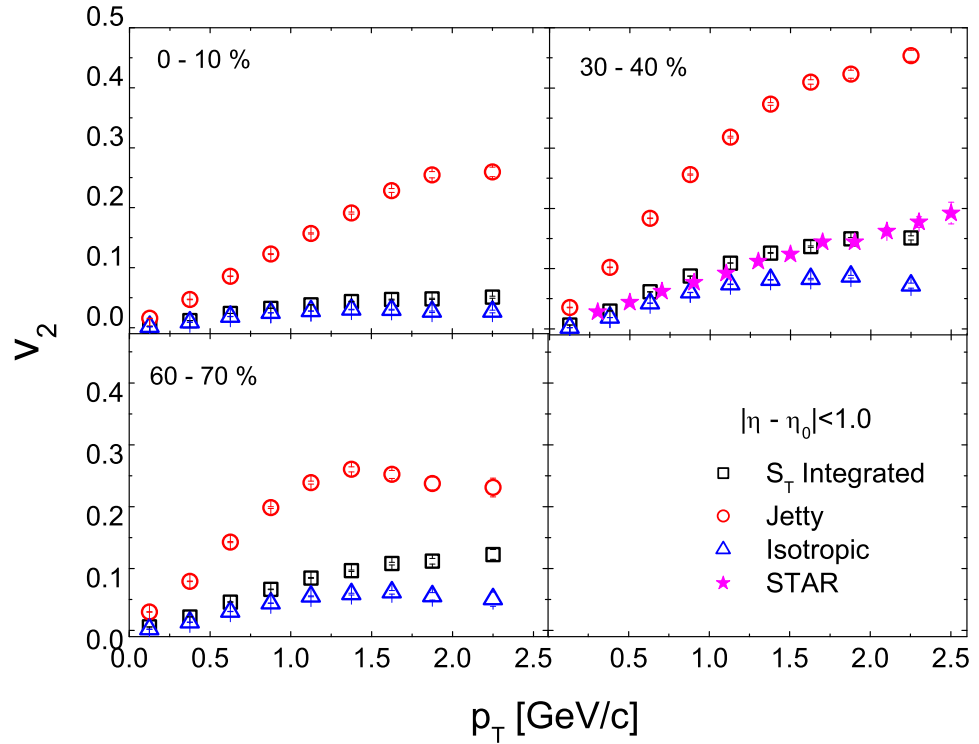


Figure 7.12: p_T -dependence of v_2 of charged hadrons at different centrality classes for isotropic, jetty and S_T -integrated events in Au+Au collisions at $E_{\text{lab}} = 30A$ GeV.

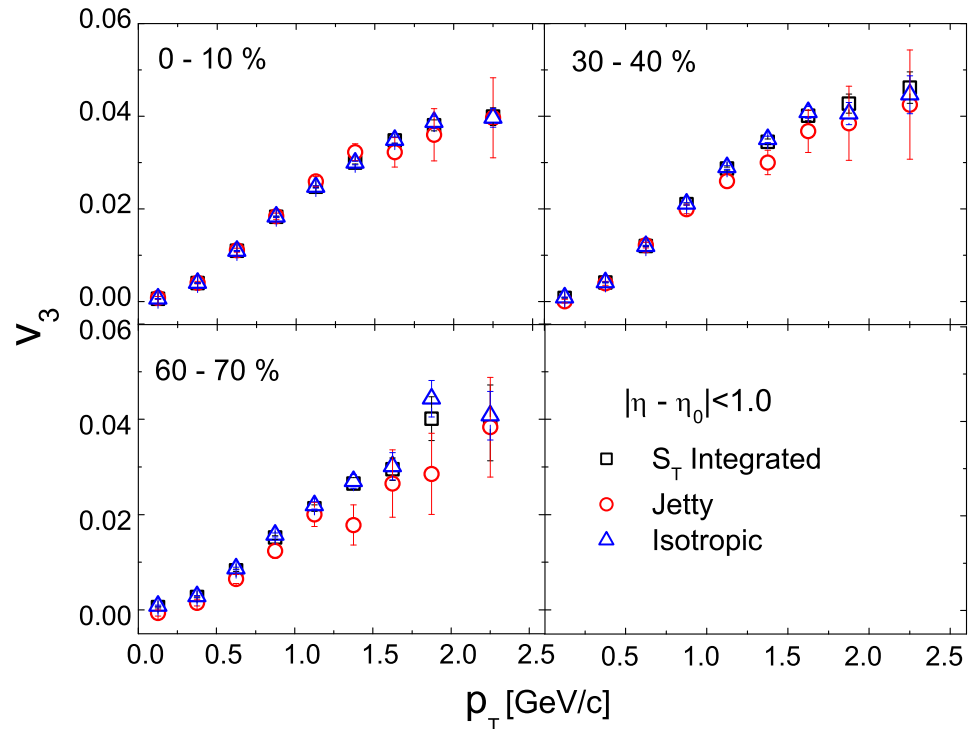


Figure 7.13: p_T -dependence of v_3 of charged hadrons at different centrality classes for isotropic, jetty and S_T -integrated events in Au+Au collisions at $E_{\text{lab}} = 30A$ GeV.

7.3 Conclusion

We have performed an event shape engineering on Au+Au collision events at $E_{\text{lab}} = 30A$ GeV generated by the AMPT (SM) model. The transverse sphericity parameter is used to classify events into jetty and isotropic categories. For both classes of events we have examined the transverse momentum spectra and centrality dependence of the yield of different charged hadrons. The centrality dependence of average transverse momentum has also been studied. The centrality and transverse momentum dependence of the elliptic and triangular flow parameters for all charged hadrons are investigated. Results obtained for the S_T -integrated events are used for comparison. Distinct features in the characteristics of jetty and isotropic events are observed, which cannot be attributed simply to geometrical and/or multiplicity effects. The jetty events may not be quite abundant in our simulated event sample, but in several aspects they behave quite differently from the isotropic and min-bias events. In particular, the hadron mass dependence of the crossing point obtained from the transverse momentum spectra, and significant differences in the elliptical flow parameter values are worth mentioning. We believe that the event topology based results of this analysis will act as a good reference baseline for future experimental investigations.

Bibliography

- [1] J. R. Ellis, M. K. Gaillard, and G. G. Ross, Nucl. Phys. B **111**, 253 (1976).
- [2] E. Farhi, Phys. Rev. Lett. **39**, 1587 (1977).
- [3] H. Georgi and M. Machacek, Phys. Rev. Lett. **39**, 1237 (1977).
- [4] G. Abbiendi *et al.* (OPAL Collaboration), Eur. Phys. J. C **40**, 287 (2005).
- [5] S. Chekanov *et al.* (ZEUS Collaboration), Nucl. Phys. B **767**, 1 (2007).
- [6] A. Banfi, G. P. Salam, and G. Zanderighi, JHEP **408**, 062 (2004).
- [7] A. Banfi, G. P. Salam, and G. Zanderighi, JHEP **1006**, 038 (2010).
- [8] R. Rath, A. Khuntia, S. Tripathy, and R. Sahoo, MDPI Physics **2**, 679 (2020).
- [9] A. Khuntia, S. Tripathy, A. Bisht, and R. Sahoo, J. Phys. G **48**, 035102 (2021).
- [10] B. Abelev *et al.* (ALICE Collaboration), Eur. Phys. J. C **72**, 2124 (2012).
- [11] G. Benci (ALICE Collaboration), Nucl. Phys. A **982**, 507 (2019).
- [12] G. Aad *et al.* (ATLAS Collaboration), Eur. Phys. J. C **72**, 2211 (2012).

- [13] G. Aad *et al.* (ATLAS Collaboration), Phys. Rev. D **88**, 032004 (2013).
- [14] V. Khachatryan *et al.* (CMS Collaboration), Phys. Lett. B **699**, 48 (2011).
- [15] N. Mallick, S. Tripathy, R. Sahoo, and A. Ortiz, J. Phys. G **48**, 045104 (2021).
- [16] A. Banfi, G. P. Salam, and G. Zanderighi, Eur. Phys. J. C **47**, 113 (2006).
- [17] N. Mallick, S. Tripathy, and R. Sahoo, arXiv:2001.06849 (2020).
- [18] L. Adamczyk *et al.* (STAR Collaboration), Phys. Rev. C **96**, 044904 (2017).
- [19] L. Adamczyk *et al.* (STAR Collaboration), Phys. Rev. C **86**, 054908 (2012).
- [20] K. Aamodt *et al.* (ALICE Collaboration), Phys. Rev. Lett. **105**, 252302 (2010).
- [21] S. Sarkar, P. Mali, and A. Mukhopadhyay, Phys. Rev. C **95**, 014908 (2017).
- [22] S. Sarkar, P. Mali, and A. Mukhopadhyay, Phys. Rev. C **96**, 024913 (2017).
- [23] B. Alver *et al.* (PHOBOS Collaboration), Phys. Rev. Lett. **98**, 242302 (2007).
- [24] C. Adler *et al.* (STAR Collaboration), Phys. Rev. C **66**, 034904 (2002).
- [25] S. Chatrchyan *et al.* (CMS Collaboration), Phys. Rev. C **87**, 014902 (2013).
- [26] H. Caines, Eur. Phys. J. C **49**, 297 (2007).
- [27] C. Alt *et al.* (NA49 Collaboration) Phys. Rev. C **68**, 034903 (2003).
- [28] S. S. Adler *et al.* (PHENIX Collaboration), Phys. Rev. Lett. **91**, 182301 (2003).
- [29] K. Aamodt *et al.* (ALICE Collaboration), Phys. Lett. B **719**, 18 (2013).

Concluding remarks

This thesis is based on a simulation study of some bulk properties and collective flow of charged hadrons coming out of AB collisions. Event generators like the UrQMD and AMPT (default and string melting) are used to build up AB event samples at incident beam energies that are typically expected from the SIS-100/300 accelerator(s) at the Facility for Anti-proton and Ion Research (FAIR). Though we have examined the incident beam energy dependence and system size dependence of some features of collective flow by using different collision systems, our study mainly focuses on the Au+Au interaction at $E_{\text{lab}} = 30A$ GeV. Near this energy value we expect significant baryon stopping, comparable values of baryon and meson density in the final hadronic states, and an enhanced production of strangeness. Monte-Carlo Glauber model has been used to determine the initial geometry and centrality of the collisions. In this concluding section, we have summarized the major observations of our study, and have tried to identify the future scope of this kind of simulation based analysis. We believe that our investigation is going to set a good reference baseline for the experimental results on collective flow expected from the CBM-FAIR project.

We have observed a longitudinal scaling in the η -distributions of charged hadrons, and when their average transverse momentum is studied as functions of η . While the integrated yield per participant pair obtained from the UrQMD generated events follows a power law dependence on N_{part} , that from the AMPT remains almost uniformly distributed. The UrQMD results in this regard are consistent with the prediction of a wounded nucleon model. A mass dependent flattening of the p_T -spectra confirms the presence of collectivity (radial flow) in the medium produced in AB collisions.

Collective fluid-like behaviour of hadronic matter produced under extreme thermodynamic conditions is explored from the Fourier decomposition of anisotropic azimuthal distributions of the final state particles. Particularly, the elliptic flow coefficient v_2 is of utmost importance, which allows us to examine the evolution of early stages of a high-energy AB collision. Elliptical anisotropy is found to be maximum in the mid-central and central events

generated by the AMPT in its string melting configuration. The triangular flow parameter v_3 on the other hand, is very little dependent on the collision centrality, and the UrQMD model does not produce any triangular flow at all. It should be remembered that v_3 is generated only from the initial geometric fluctuations. Through out our investigation we have taken care of the initial state fluctuations, and noticed that the proper quantification of geometrical anisotropy present in the overlapping part of the colliding nuclei, is made by a participant eccentricity $\varepsilon_{\text{part}}$ and not by the nuclear eccentricity ε_{std} . We do not notice any unusual (exotic) behaviour of the flow parameters with regard to their dependences on N_{part} , p_T or η . Rather multiplicity scaling effects are found when flow parameters are measured against particle density. In conformity with the hydrodynamic prediction, transport model simulations also preserve the mass ordering of hadrons, however a constituent quark number scaling is observed only in the string melting mode of AMPT. AMPT (string melting) also turns out to be most suitable candidate to reproduce the experimental flow results in Au+Au collisions at $\sqrt{s_{NN}} = 7.7$ GeV available from the STAR experiment, which naively manifests the role of partonic interactions/dof even at lower beam energies. High precision CBM data are expected to shed further light on these issues.

The matter formed in an AB collision at RHIC and LHC, is thermalized within a very short time and expands collectively thereafter almost like a perfect fluid with very small value of shear viscosity over entropy (η/s). Higher partonic cross section, a parameter that can be tuned in the AMPT (string melting) model, corresponds to a lower specific viscosity (η/s). A combined analysis of v_2 and v_3 and their relative strength is believed to be capable of providing useful information related to the specific viscosity of the fireball medium. A higher partonic cross section turns out to be more efficient in transforming the initial anisotropy, either geometric or fluctuating in nature, to the final state momentum anisotropy. Triangular flow appears to be more sensitive to the partonic cross section or the specific viscosity of the medium. In contrast to the LHC results we find a strong pseudorapidity dependence of v_2 and v_3 , which in our case can be attributed to the highest particle densities in the central pseudorapidity region. Moreover these observations reveals the effect of higher amount of baryon stopping expected at the FAIR energies.

We have explored the effects of hadron multiplicities, multiple rescattering and collision geometry on the collective behaviour of final state hadrons produced in small (Si+Si and Ni+Ni), medium (In+In) and large (Au+Au) sized systems at $E_{\text{lab}} = 30A$ GeV. We do not notice any significant change in the properties (except differences in magnitude) of the fireball medium although the system size varies considerably. When geometric effects are scaled out, v_2 appears to be independent of the system size, an observation that manifests that within the framework of the models used, the rescattering mechanism is similar in different colliding systems. An entropy driven soft hadron production appears to be the

main reason behind most of these observations. Moreover, $\varepsilon_{\text{part}}$ once again turns out to be the more appropriate choice to measure geometric anisotropy.

Besides the azimuthal distribution of particle numbers and the Fourier (flow) coefficients estimated thereof, we have also investigated the azimuthal distribution of transverse or radial velocity (v_T). For a non-ideal viscous fluid, as the case may be at FAIR conditions, the shear tension is expected to be proportional to the gradient of the radial velocity along the azimuthal direction, which again is related to the anisotropy in the radial velocity distribution. We have presented the azimuthal distribution of total transverse velocity, and after removing the influence of multiplicity that of the mean transverse velocity. We observe that the dominant contribution to the final state asymmetry is coming from the multiplicity distribution and only a small fraction of it is due to the kinematic reason. Gross features of the anisotropy parameter v_2 corresponding to the transverse velocity, are similar to that measured from usual azimuthal distributions of charged hadrons, i.e., highest in mid-central collisions and linearly dependent on p_T . The azimuthally integrated value of the radial flow is maximum for the most central collisions. This observation can be explained in terms of more energy being deposited by the colliding nuclei in central AB collisions which subsequently gives rise to more radial pressure. Our simulated results are consistent with those obtained from the RHIC and LHC experiments, and do not require any new dynamics for their interpretation.

We have employed an event shape variable, called the transverse sphericity, particularly to understand the dynamics of particle production mechanism and collective flow of hadronic matter in AB collisions at $E_{\text{lab}} = 30A$ GeV. The AMPT (string melting) generated events are classified into isotropic and jetty categories. The jetty events are rare (less than one in ten min. bias events) at the energy considered, but on several occasions they behave quite differently from the isotropic or minimum bias events, and the differences can not be attributed either to geometric or multiplicity reasons. We observe a crossing in the p_T -spectra of charged hadrons in the jetty and isotropic events, and the crossing point depends on the hadron mass involved. Considerable differences in the average p_T and v_2 values are observed for these two event categories. The jetty events produce significantly higher amount of elliptic flow.

In spite of the fact that a thorough simulation based analysis has been performed using microscopic transport models, we believe that until the experimental data from CBM-FAIR become available there is enough scope to further extend this kind of investigation. Firstly, one can perform a parameter scan of the models that are already used, and/or use other event generators based on transport and statistical models to compare with the present set of results. It would be quite worthwhile to see the results of a more detailed analysis, as the minimum bias event samples are segregated with respect to different hadron species and

for event subsamples belonging to different event shape categories. Significant differences observed in the average transverse momentum and elliptic flow parameter values, and a hadron mass dependence of the crossing point in the p_T -spectra of hadrons, are indeed quite prospective issues in this regard. Further analysis can also be made to extract the freeze-out parameters like the chemical potential, to examine the cluster properties and to study the correlations and event-by-event fluctuations of conserved quantities. Effects of non-flow correlations is another area that has not been fully explored in this investigation.

Appendix A

Two-body kinematics

Let us now discuss the kinematics of two-body interaction and some variables that are commonly used to characterize the particle production process in high-energy interactions. A detailed account of the topic can be found in Refs.¹. If otherwise not mentioned we shall stick to the natural unit system ($\hbar = c = k_B = 1$). A two body \rightarrow many-particle inclusive reaction is customarily written as,

$$A + B \Rightarrow p_1 + p_2 + \cdots + p_n + X$$

where X stands for anything, i.e. all possible particles that in a given experiment are not subjected to any observation (measurement). In contrast, a reaction like

$$A + B \Rightarrow p_1 + p_2 + \cdots + p_n$$

where all the final-state particles are detected, is an exclusive one. A high-energy AB collision can be represented as,

$$\text{Projectile (A) + Target (B) } \Rightarrow \text{Nuclear fragments + Produced particles}$$

In this type of collisions different types of new particles are produced, most of which ($\sim 90\%$) are π -mesons. The number of particles belonging to a particular species in an event is called the multiplicity of that particular species. By measuring the multiplicity one gets an idea about the degrees of freedom released in the collision process. The distributions of final state particles are important observables. The differential distributions are often measured in terms of the longitudinal variable rapidity (y) and the transverse variable (p_T) of the

¹C. Y. Wong, Introduction to High-Energy Heavy-Ion Collisions, World Scientific (1994); M. Klemant, R. Sahoo, T. Schuster and R. Stock, Lect. Notes Phys. 785, 23 (2010); The Physics of the Quark-Gluon Plasma: Introductory Lectures, (Eds.) S. Sarkar, S. Satz and B. Sinha, Springer-Verlag, Berlin, Germany (2010).

particles concerned. Let us now discuss the significance of these variables in the context of two body kinematics.

Depending on whether it is a fixed target or a collider type experiment, in high-energy collisions either or both of the colliding objects move at relativistic speed ($\beta \lesssim 1$), and the produced particles also travel with a speed comparable to that of the light. As one moves from one Lorentz frame to another it is therefore convenient to work with such kinematic variables that have definite transformation properties. In high-energy collisions the beam line is conventionally taken along the z -axis, which may be called the longitudinal direction. The $(x - y)$ plane is considered as the transverse plane. A Lorentz transformation (LT) involving only translation (no rotation) is called Lorentz Boost. If we consider a Lorentz Boost along the \hat{z} -direction by a velocity $v = c\beta$ then the space-time transformation can be written as,

$$\begin{pmatrix} t' \\ z' \end{pmatrix} = \begin{pmatrix} \gamma & -\beta\gamma \\ -\beta\gamma & \gamma \end{pmatrix} \begin{pmatrix} t \\ z \end{pmatrix} \quad (\text{A-1})$$

where $\gamma = 1/\sqrt{1 - \beta^2}$ is called the Lorentz factor. The x and y -coordinates being normal to the direction of the boost, do not change under LT. Similarly, the energy-momentum components of a particle of rest mass m are given by $p = (E, \bar{p})$, where $\bar{p} = (p_x, p_y, p_z)$ is the 3-momentum of the particle, and $p^2 = E^2 - \bar{p}^2 = m^2$ is again a Lorentz invariant quantity. Under a Lorentz boost along the \hat{z} -direction these components transform as,

$$\begin{pmatrix} E' \\ p'_z \end{pmatrix} = \begin{pmatrix} \gamma & -\beta\gamma \\ -\beta\gamma & \gamma \end{pmatrix} \begin{pmatrix} E \\ p_z \end{pmatrix} \quad (\text{A-2})$$

In a two body collision where the target is fixed in laboratory, suppose $p_1 = (E_1, \bar{p}_1)$ and $p_2 = (E_2 = m_2, \bar{p}_2 = 0)$ are respectively the 4-momenta of the projectile and the target. The total 4-momentum of the system in the LS is given by,

$$(p_1 + p_2)^2 = m_1^2 + m_2^2 + 2E_1 m_2 \quad (\text{A-3})$$

The 4-momentum square of such a system should be Lorentz invariant. Therefore, the total energy available in the center of mass (momentum) is

$$E_{cm} = \sqrt{s} = \sqrt{m_1^2 + m_2^2 + 2m_2 E_1} \quad (\text{A-4})$$

It is evident that for a nucleon-nucleon (NN)-system at high incident energy $\sqrt{s} \sim E_1^{1/2}$. The center of mass moves in the LS in the direction of the projectile with a velocity β_{cm}

given by the Lorentz factor

$$\gamma_{cm} = \frac{1}{\sqrt{1 - \beta_{cm}^2}} = \frac{E_1 + m_2}{\sqrt{s}} \quad (\text{A-5})$$

On the other hand, in a collider experiment if the incident energies are very high, i.e. ($E_1, E_2 \gg m_1, m_2$) then,

$$E_{cm}^2 = (p_1 + p_2)^2 = (E_1 + E_2)^2 - (\bar{p}_1 + \bar{p}_2)^2 \simeq 4E_1 E_2 \quad (\text{A-6})$$

If $E_1 = E_2 = E$ then $E_{cm} \simeq 2E$, and the CM energy increases linearly with E . If an AB collision is viewed as an independent superposition many elementary NN collisions then the AB collision is called incoherent. In such a case for a symmetric central collision between two identical nuclei, i.e. for an AA collision, the total CM energy is related to the CM energy of an NN system ($\sqrt{s_{NN}}$) as $\sqrt{s} = A\sqrt{s_{NN}}$, and corresponding Lorentz factor is given by,

$$\gamma_{cm} = \frac{E}{M} = \frac{\sqrt{s}}{2Am_N} = \frac{\sqrt{s_{NN}}}{2m_N} \quad (\text{A-7})$$

If on the other hand, each colliding nucleus behaves like a single massive object then the collision is fully coherent. In non-central, asymmetric and coherent collisions between two nuclei, it is difficult to fix the effective CM frame, which depends on the impact parameter as well as on the degree of coherence of the collision. Therefore, the number of participating and spectator nucleons need to be determined first, posing extra problems particularly in soft processes. In hard processes that more likely are to be found in central collisions, the NN frame still works.

The rapidity

The dimensionless boost parameter rapidity, is the relativistic measure of the velocity of a particle. It is a suitable choice to describe the longitudinal dynamics of a system of relativistic particles. The space-time rapidity of a particle is defined as,

$$y = \frac{1}{2} \ln \left(\frac{t + z}{t - z} \right) \quad (\text{A-8})$$

where t is the time and z is the space co-ordinate of the particle along the beam direction. For particles created exactly at the center of mass of the interacting system, $y = 0$. The space-time rapidity is however experimentally not measurable, it is used mainly for theoretical calculations. Therefore, the energy-momentum rapidity is introduced,

$$y = \frac{1}{2} \ln \left(\frac{E + p_z}{E - p_z} \right) = \frac{1}{2} \ln \left(\frac{E + p_z}{m_T} \right) \quad (\text{A-9})$$

Here $E = \sqrt{|\vec{p}|^2 + m^2}$ and $m_T = \sqrt{m^2 + p_T^2}$ is the transverse mass of the particle. The most interesting property of the rapidity variable is that, it is additive under Lorentz boost. As a result, the overall shape of the rapidity distribution of particles remains unchanged under a longitudinal boost. In the nonrelativistic limit, the rapidity of a particle traveling along the longitudinal direction is equal to the velocity of the particle measured in the unit of velocity of light in vacuum. The energy E and the longitudinal momentum p_z of a particle are related to the rapidity by the relations,

$$E = m_T \cosh y \quad \text{and} \quad p_z = m_T \sinh y \quad (\text{A-10})$$

The energy and momentum of the CMS in the LS are respectively, $\gamma_{cm}\sqrt{s}$ and $\beta_{cm}\gamma_{cm}\sqrt{s}$. The rapidity of the CM in the LS is therefore,

$$y_{cm} = \frac{1}{2} \ln \left(\frac{\gamma_{cm}\sqrt{s} + \beta_{cm}\gamma_{cm}\sqrt{s}}{\gamma_{cm}\sqrt{s} - \beta_{cm}\gamma_{cm}\sqrt{s}} \right) = \frac{1}{2} \ln \left(\frac{1 + \beta_{cm}}{1 - \beta_{cm}} \right) \quad (\text{A-11})$$

The rapidity values of a particle in the CMS (primed) and LS (unprimed) are given respectively by,

$$y' = \frac{1}{2} \ln \left(\frac{E' + p'_z}{E' - p'_z} \right) \quad \text{and} \quad y = \frac{1}{2} \ln \left(\frac{E + p_z}{E - p_z} \right) \quad (\text{A-12})$$

Using Equation (A-2) in Equation (A-9) one gets,

$$y = \frac{1}{2} \ln \left(\frac{E' + p'_z}{E' - p'_z} \right) + \frac{1}{2} \ln \left(\frac{1 + \beta}{1 - \beta} \right) = y' + y_{cm} \quad (\text{A-13})$$

Therefore in a CMS \rightarrow LS transformation the rapidity distribution remains unaltered, with the y -scale shifted for every particle by a fixed amount y_{cm} . For a fixed target experiment, the beam rapidity can be obtained by using the relation (A-10). For the beam particle p_t is zero. The rapidity of beam particle (y_1) is given by,

$$y_1 = \cosh^{-1} \left(\frac{E}{m_1} \right) = \cosh^{-1} \left(\frac{\sqrt{s_{NN}}}{2m_N} \right) = \sinh^{-1} \left(\frac{p_z}{m_1} \right) \quad (\text{A-14})$$

where m_1 is the rest mass of the beam particle.

The pseudorapidity

Both the energy and the longitudinal momentum of a particle are necessary to determine the rapidity of that particle. But in many experiments it is not possible to measure both. In such cases it is instead convenient to use the pseudorapidity variable (η). Suppose a particle is emitted at an angle θ with respect to the beam axis. From Equation (A-9) we get the

rapidity as,

$$y = \frac{1}{2} \ln \left(\frac{(m^2 + |\bar{p}|^2)^{1/2} + |\bar{p}| \cos \theta}{(m^2 + |\bar{p}|^2)^{1/2} - |\bar{p}| \cos \theta} \right) \quad (\text{A-15})$$

If the kinetic energy of the particle is very high ($|\bar{p}| \gg m$) then Equation (A-15) reduces to

$$y = \frac{1}{2} \ln \left(\frac{|\bar{p}| + |\bar{p}| \cos \theta}{|\bar{p}| - |\bar{p}| \cos \theta} \right) = -\ln \tan \left(\frac{\theta}{2} \right) = \eta \quad (\text{A-16})$$

In terms of the linear momentum components η is expressed as

$$\eta = \frac{1}{2} \ln \left(\frac{|\bar{p}| + p_z}{|\bar{p}| - p_z} \right) \Rightarrow e^\eta = \sqrt{\left(\frac{|\bar{p}| + p_z}{|\bar{p}| - p_z} \right)} \quad (\text{A-17})$$

From the above equations the following relations are obtained,

$$|\bar{p}| = p_T \cosh \eta \quad \text{and} \quad p_l = p_T \sinh \eta \quad (\text{A-18})$$

Rapidity and pseudorapidity are interchangeable and are related to each other by,

$$y = \frac{1}{2} \ln \left(\frac{\sqrt{p_T^2 \cosh^2 \eta + m^2} + p_T \sinh \eta}{\sqrt{p_T^2 \cosh^2 \eta + m^2} - p_T \sinh \eta} \right) \quad (\text{A-19})$$

and

$$\eta = \frac{1}{2} \ln \left(\frac{\sqrt{m_T^2 \cosh^2 y - m^2} + m_T \sinh y}{\sqrt{m_T^2 \cosh^2 y - m^2} - m_T \sinh y} \right) \quad (\text{A-20})$$

η is used as an approximation of y when the angular distribution of the produced particles is measured, and only when the relation $E \cong |\bar{p}| \gg m$ holds good. In high-energy interactions the approximation $\eta \cong y$ is good for the pions and other light weight particles. However, if such an approximation is not valid then the respective distributions are related in the following way,

$$\frac{d^2 N}{d\eta dp_T} = \sqrt{1 - \frac{m^2}{m_T^2 \cosh^2 y}} \frac{d^2 N}{dy dp_T} \quad (\text{A-21})$$

The azimuthal angle variable ϕ , defined over the transverse plane is expressed as $\phi = \tan^{-1}(p_y/p_x)$. This is another Lorentz invariant quantity, often used to measure the distribution of final state particles.

Invariant yield

We notice that $y = y(p_z, E)$. Therefore,

$$\begin{aligned}
 dy &= \frac{\partial y}{\partial p_z} dp_z + \frac{\partial y}{\partial E} dE \\
 &= dp_z \left[\frac{\partial y}{\partial p_z} + \frac{\partial y}{\partial E} \frac{\partial E}{\partial p_z} \right] \\
 &= dp_z \left[\frac{E}{E^2 - p_z^2} - \frac{p_z}{E^2 - p_z^2} \cdot \frac{p_z}{E} \right] \\
 &= \frac{dp_z}{E}
 \end{aligned} \tag{A-22}$$

We also notice the Lorentz invariance of dp_z/E and that of dy . As a result,

$$\begin{aligned}
 \frac{d^3 p}{E} &= \frac{d\mathbf{p}_T dp_z}{E} \\
 &= p_T dp_T d\varphi dy
 \end{aligned} \tag{A-23}$$

becomes Lorentz invariant. Often the Lorentz invariant differential yield is expressed as,

$$\begin{aligned}
 E \frac{d^3 N}{dp^3} &= \frac{1}{p_T} \frac{d^3 N}{dp_T d\varphi dy} \\
 &= \frac{1}{2\pi p_T} \frac{d^2 N}{dp_T dy}
 \end{aligned} \tag{A-24}$$

where p_T is the transverse mass and y is the rapidity (to be discussed later) of the particle concerned.

List of publications

Peer reviewed journal publications

9. Soumya Sarkar, Provash Mali, and Amitabha Mukhopadhyay, *Transverse sphericity based event classification in Au+Au collision at $E_{\text{lab}} = 30A$ GeV in A Multi Phase Transport model*, Communicated to Phys. Rev. C (2021).
8. Soumya Sarkar, Provash Mali, and Amitabha Mukhopadhyay, *System size dependence of harmonic flow parameters in a multiphase transport model at $E_{\text{lab}} = 30A$ GeV*, Communicated to Eur. Phys. J. A (2021).
7. Soumya Sarkar, Provash Mali, Somnath Ghosh, and Amitabha Mukhopadhyay, *Radial Flow in a Multiphase Transport Model at FAIR Energies*, Adv. High Ener. Phys. **2018**, 7453752 (2018).
6. Soumya Sarkar, Provash Mali, and Amitabha Mukhopadhyay, *Azimuthal anisotropy in particle distribution in a multiphase transport model*, Phys. Rev. C **96**, 024913 (2017).
5. S. Sarkar, P. Mali, and A. Mukhopadhyay, *Simulation study of elliptic flow of charged hadrons produced in Au + Au collisions at energies available at the Facility for Antiproton and Ion Research*, Phys. Rev. C **95**, 014908 (2017).
4. P. Mali, S. Sarkar, S. Ghosh, A. Mukhopadhyay, and G. Singh, *Multifractal detrended fluctuation analysis of particle density fluctuations in high-energy nuclear collisions*, Physica A **424**, 25 (2015).
3. P. Mali, A. Mukhopadhyay, S Sarkar, and G. Singh, *Azimuthal correlation and collective behaviour in nucleus-nucleus collisions*, Phys. Atom. Nucl. **78**, 258 (2015).

2. Provash Mali, Amitabha Mukhopadhyay, Soumya Sarkar and Gurmukh Singh, *Azimuthal structure of charged particle emission in $^{28}\text{Si-Ag}(\text{Br})$ interaction at 14.5A GeV and $^{32}\text{S-Ag}(\text{Br})$ interaction at 200A GeV*, Int. J. Mod. Phys. E **23**, 1450027 (2014).
1. Provash Mali, Soumya Sarkar, Amitabha Mukhopadhyay, and Gurmukh Singh, *Wavelet analysis of shower track distribution in high-energy nucleus-nucleus collisions*, Adv. High Ener. Phys. **2013**, 759176 (2013).

Contribution to CBM Progress Report

6. Soumya Sarkar and Amitabha Mukhopadhyay, *Fluctuation of elliptic flow parameter at an expected FAIR energy*, CBM Progress Report **2019**, 183 (2020).
5. Soumya Sarkar, Provash Mali and Amitabha Mukhopadhyay, *Initial state longitudinal asymmetry in the AMPT model under FAIR CBM condition*, CBM Progress Report **2018**, 184 (2019).
4. Soumya Sarkar, Provash Mali and Amitabha Mukhopadhyay, *System size dependence of elliptic flow at FAIR energies*, CBM Progress Report **2017**, 165 (2018).
3. Soumya Sarkar, Provash Mali, Somnath Ghosh, and Amitabha Mukhopadhyay, *Azimuthal anisotropy of hadrons in AMPT model at FAIR energy*, CBM Progress Report **2016**, 190 (2017).
2. Soumya Sarkar, Somnath Ghosh, Provash Mali, and Amitabha Mukhopadhyay, *Simulation results on elliptic flow at FAIR energies*, CBM Progress Report **2014**, 141 (2015).
1. Soumya Sarkar, Amitabha Mukhopadhyay, and Subhasis Chattopadhyay, *Sensitivity of the CBM-MUCH to mass modifications of ρ mesons*, CBM Progress Report **2013**, 116 (2014).

Conference Proceedings

11. Soumya Sarkar, Provash Mali, and Amitabha Mukhopadhyay, *Collective flow in jetty and isotropic events in Au+Au collision at 30A GeV*, DAE Symposium on Nuclear Physics **65**, 734 (2021).
10. Soumya Sarkar, Provash Mali, and Amitabha Mukhopadhyay, *Initial state longitudinal asymmetry at FAIR-CBM energy*, DAE Symposium on Nuclear Physics **64**, 748 (2019).

9. Soumya Sarkar and Amitabha Mukhopadhyay, *Azimuthal correlation in nuclear collisions at FAIR energy*, DAE Symposium on Nuclear Physics **63**, 938 (2018).
8. Soumya Sarkar, Provash Mali, and Amitabha Mukhopadhyay, *System size dependence of collective flow at FAIR energy*, DAE Symposium on Nuclear Physics **62**, 854 (2017).
7. Soumya Sarkar and Amitabha Mukhopadhyay, *Initial fluctuations and triangular flow in AMPT Model at FAIR Energy*, DAE Symposium on Nuclear Physics **61**, 776 (2016).
6. Soumya Sarkar and Amitabha Mukhopadhyay, *Azimuthal anisotropy of transverse rapidity at CBM energy in the AMPT model*, DAE Symposium on Nuclear Physics **60**, 752 (2015).
5. Soumya Sarkar, Somnath Ghosh, Provash Mali, and Amitabha Mukhopadhyay, *Elliptic flow in Au-Au collision at 20A GeV*, DAE Symposium on Nuclear Physics **59**, 764 (2014).
4. Provash Mali, Amitabha Mukhopadhyay, Soumya Sarkar, and Somnath Ghosh, *Charge balance function in pp collision at 200 GeV*, DAE Symposium on Nuclear Physics **59**, 750 (2014).
3. Soumya Sarkar, Amitabha Mukhopadhyay, and Subhasis Chattopadhyay, *Mass modification of rho meson at SIS 300 energy*, DAE Symposium on Nuclear Physics **58**, 734 (2013).
2. Provash Mali, Soumya Sarkar, Somnath Ghosh, Amitabha Mukhopadhyay, and Gurmukh Singh, *Collective flow in nucleus- nucleus collisions*, DAE Symposium on Nuclear Physics **58**, 694 (2013).
1. Provash Mali, Soumya Sarkar, Somnath Ghosh, Amitabha Mukhopadhyay, and Gurmukh Singh, *Detrended fluctuation analysis in multiparticle production*, DAE Symposium on Nuclear Physics **58**, 702 (2013).

Azimuthal anisotropy in particle distribution in a multiphase transport modelSoumya Sarkar,^{1,2} Provash Mali,¹ and Amitabha Mukhopadhyay^{1,*}¹*Department of Physics, University of North Bengal, Siliguri 734013, West Bengal, India*²*Department of Physics, Siliguri College, Siliguri 734001, West Bengal, India*

(Received 22 February 2017; revised manuscript received 8 June 2017; published 31 August 2017)

Anisotropic flow of hadronic matter is considered a sensitive tool to detect the early-stage dynamics of high-energy heavy-ion collisions. Taking the event-by-event fluctuations of the collision geometry into account, the elliptic flow parameter and the triangular flow parameter derived from the azimuthal distribution of produced hadrons are investigated within the framework of a multiphase transport (AMPT) model, at a collision energy that in near future will typically be available at the Facility for Antiproton and Ion Research. The dependence of elliptic and triangular flow parameters on initial fluctuations, on parton scattering cross sections and their mass ordering on different hadron species, and on the constituent quark number scaling are examined. The AMPT simulation cannot exactly match the elliptic flow results on Pb+Pb collision at 40A GeV of the NA49 experiment. The simulation results presented in this work are expected to provide us with an insight to study flow properties at high baryonic density and at moderate temperature, and with an opportunity to compare similar results available from Relativistic Heavy Ion Collider and Large Hadron Collider experiments.

DOI: [10.1103/PhysRevC.96.024913](https://doi.org/10.1103/PhysRevC.96.024913)**I. INTRODUCTION**

The study of azimuthal anisotropy of final-state hadrons is believed to be one of the most important tools that can extract significant information regarding particle interactions in a hot and dense nuclear and/or partonic medium produced in high-energy heavy-ion collisions. Properties of this kind of matter are widely believed to be guided by the rules of quantum chromodynamics (QCD). Several important results on the collective behavior of final-state particles have already been obtained by using the Fourier decomposition of their azimuthal distributions. Among all, the second-harmonic coefficient, also known as the elliptic flow parameter (v_2), is of special interest [1]. Large v_2 values observed in the Relativistic Heavy Ion Collider (RHIC) [2–5] and Large Hadron Collider (LHC) [6–9] experiments, are understood to be due to a strongly interacting nature of the extended QCD state composed of loosely coupled quarks and gluons. The v_2 parameter is sensitive to the equation of state, transport properties of the medium, degree of thermalization achieved by the system, and also to the initial conditions of a collision [10–14]. At low transverse momentum (p_T) a mass ordering of v_2 with respect to different hadron species, and a scaling with respect to the number of constituent quarks (NCQ), of which the hadron under consideration is made, have been observed both in RHIC [15–17] and in LHC experiments [18]. The NCQ scaling enables us to understand how significant the partonic degrees of freedom are, in the intermediate “fireball” created in any high-energy nucleus-nucleus (AB) collision [19,20].

In recent years the third-harmonic coefficient v_3 of the Fourier decomposition of the azimuthal distribution, also called the triangular flow parameter, has gained attention and has also been studied extensively [21–23]. Originally, it was perceived, though, that due to a left-right symmetry prevailing

in the transverse plane of a collision, the contribution from odd harmonics to the particle azimuthal distribution would vanish. However, now it is widely accepted that the event-by-event fluctuating position of the nucleons participating in an AB collision often assumes a triangular shape (preferably called the triangularity), which with the evolution of the interacting system is converted into a momentum space anisotropy. Triangular flow is sensitive to the correlations present in the early stage of the AB collision, and it has been proposed that the triangular anisotropy can explain the near side “ridge” and the away-side “shoulder” structures present in two-particle (dihadron) azimuthal correlations [21]. Furthermore, triangular flow is also believed to be sensitive to the viscous effects of the “fireball” medium as suggested by some simulation studies on relativistic viscous hydrodynamics [24,25]. At high temperature and low baryon density, triangular flow of produced hadrons has been studied as a function of p_T , pseudorapidity (η), centrality (often measured in terms of the number of participating nucleons N_{part}), and triangularity (ϵ_3) [26–31]. But the effect of the aforementioned initial fluctuations on final-state azimuthal anisotropy is not yet fully explored at low and moderate collision energies. The upcoming Compressed Baryonic Matter (CBM) experiment [32] to be undertaken at the Facility for Anti-proton and Ion Research (FAIR), is dedicated to study the color-deconfined QCD matter at low to moderate temperature and at high baryon density. The CBM will be a fixed target experiment on AB interactions where the proposed incident beam energy will be in the range $E_{\text{lab}} \sim 10\text{--}40$ GeV per nucleon. At such interaction energies it is expected that a baryon density $\rho_b \sim 6\text{--}12$ times the normal nuclear matter density will be created in the central rapidity region [33]. As far as high-energy AB interactions are concerned, the CBM experiment will be complementary to the ongoing RHIC and LHC programs.

As mentioned above, the harmonic flow coefficients (v_n) of different order (n), or each type of anisotropy can be obtained from the Fourier expansion of the azimuthal distribution

*amitabha_62@rediffmail.com

of produced particles, the azimuthal angle being measured with respect to that of a participant plane angle (ψ_n) [34]. The azimuthal angle distribution of particles can be Fourier decomposed as [31]

$$\frac{dN}{d\phi} \propto \left[1 + 2 \sum_{n=1}^{\infty} v_n \cos \{n(\phi - \psi_n)\} \right], \quad (1)$$

where ϕ is the momentum azimuthal angle of each particle, and ψ_n is the azimuthal angle of the participant plane associated with the n th harmonic that maximizes the eccentricity of the participating nucleons. In the center-of-mass system of the participating nucleons ψ_n is given by

$$\psi_n = \frac{1}{n} \left[\arctan \frac{\langle r^2 \sin(n\phi) \rangle}{\langle r^2 \cos(n\phi) \rangle} + \pi \right], \quad (2)$$

where (r, ϕ) denote the position coordinates of participating nucleons in a plane polar system, and $\langle \rangle$ denotes a density weighted average over the initial states. As the number and position coordinates of participating nucleons fluctuate from one Au+Au collision event to the other, they are going to affect ψ_n and, therefore, the v_n values. On the other hand, the initial geometric deformation of the overlapping region of two colliding nuclei is quantified by

$$\varepsilon_n = \frac{\sqrt{\langle r^2 \cos(n\phi) \rangle^2 + \langle r^2 \sin(n\phi) \rangle^2}}{\langle r^2 \rangle}. \quad (3)$$

Taking the effects of initial fluctuations into account the anisotropic flow parameter v_n is defined as

$$v_n = \langle \cos[n(\phi - \psi_n)] \rangle. \quad (4)$$

Our present understanding of the dynamics of partonic and/or hadronic matter produced in AB collisions around FAIR energy lacks experimental evidence. Under such circumstances we have to rely on model calculations and Monte Carlo simulations built thereof. For all practical purposes, simulation codes that can describe the nature of global variables associated with multiparticle production in high-energy interactions with reasonable success should be chosen for a more in-depth study. Very recently we have reported some such simulated results on the centrality dependence of elliptic flow parameter, and on some aspects of kinetic radial flow of charged hadrons at FAIR energies [35]. However, due importance to issues like initial fluctuations and parton degrees of freedom are not given in that analysis. The main objective of this article is, therefore, to use a set of simulated multiparticle emission data on Au+Au collision at $E_{\text{lab}} = 30A$ GeV, and study the azimuthal anisotropy of charged hadrons in the final state, where the effects of event-to-event initial fluctuations and binary (partonic) scattering are taken into account. From statistical considerations [36] it has been shown that in fixed target AB experiments, at and around $E_{\text{lab}} = 30A$ GeV the expected net baryon density in the intermediate ‘‘fireball’’ should be the highest. Therefore, it is worthwhile to examine the behavior of flow parameters in a baryon-rich environment and compare them with those obtained at a high-energy-density and low-baryon-density condition prevalent in the RHIC and LHC experiments. For the sake of completeness, we have studied a few general features of multiparticle emission

data, examined the flow parameters for different hadron species, and verified the NCQ scaling.

The paper is organized as follows. In Sec. II we summarize a multiphase transport (AMPT) model, in Sec. III we sequentially describe the results obtained from this analysis followed by some discussions, and, finally, in Sec. IV, we conclude with a brief summary of our observations.

II. THE AMPT MODEL

As we intend to investigate the dependence of several observables on a parton-parton scattering cross section, it is necessary to choose an event generator that has an built-in provision for partonic degrees of freedom. AMPT is a hybrid transport model consisting of four major components, namely the initial conditions, the partonic interactions, the conversion from partonic to hadronic matter, and finally, the hadronic interactions [37]. In AMPT the initial conditions are obtained through two-body nucleon-nucleon (NN) interactions. It uses a Glauber formalism to determine the positions of participating nucleons and generates hard minijets (partons) and soft excited strings (hadrons) by using the heavy-ion jet interaction generator (HIJING) [38]. The AMPT model can be used in two configurations, the default version and the string melting version. The basic difference between these two versions lies in modeling the excited strings. In the string melting mechanism beyond a certain critical energy density, excited strings (hadrons) and minijets (partons) cannot coexist. Therefore, it is necessary to melt or convert the strings into partons, i.e., a meson is converted into a quark-antiquark pair, a baryon into three quarks, etc. The scattering among quarks and the original hard partons are then described by Zhang’s parton cascade (ZPC) model [39], which includes two-body elastic scattering with an in-medium cross section obtained from perturbative QCD (pQCD), where the effective gluon screening mass is used as a parameter. After the binary collisions cease to progress, the partons from minijets and partons from melted strings hadronize through a quark coalescence mechanism. However, in the AMPT default mode the energy of the excited strings is not used in the partonic stage. The scattering occurs only among the minijet partons based on the ZPC model and their hadronization is described by the Lund string fragmentation mechanism. After hadronization, either in the string melting version or in the default version, the hadron dynamics is modeled by a relativistic transport (ART) model [40], which includes both elastic and inelastic scatterings of baryonic, mesonic, and baryomesonic nature. Previous calculations have shown that flow parameters consistent with experiment can be developed through AMPT, and the model can successfully describe different aspects of collective behavior of AB interactions [41–43]. The string melting version of AMPT should be even more appropriate to model particle emission data where a transition from nuclear matter to deconfined QCD state is expected. We have used the AMPT model (string melting version) to generate 10^6 minimum bias fixed target Au+Au interactions at $E_{\text{lab}} = 30A$ GeV.

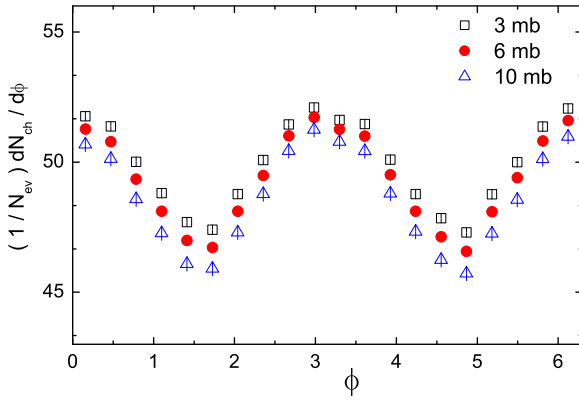


FIG. 1. Azimuthal angle (measured in radian) distribution of charged hadrons produced in Au+Au collision at $E_{\text{lab}} = 30A$ GeV.

III. RESULTS

In this section, we describe the results obtained by analyzing Au+Au minimum bias event sample at $E_{\text{lab}} = 30A$ GeV simulated by the AMPT (string melting) model. Unless otherwise specified, our results pertain to all charged hadrons produced in the Au+Au collisions. To begin, the azimuthal angle distributions are schematically plotted in Fig. 1 for three different two-body (partonic) scattering cross sections (σ). The σ values are chosen to match the relevant and previously studied high-energy AB interactions [31,43]. For $\sigma = 3$ (10) mb the number density of charged hadrons is found to be highest (lowest). Prominent anisotropies are observed in all three distributions that need to be investigated further. In Fig. 2 we have plotted the p_T distributions of some identified hadrons that come out of the AMPT generated Au+Au events at $E_{\text{lab}} = 30A$ GeV. We observe the expected exponential decay in the distribution with increasing p_T . The thermal region, i.e., the straight portion in the semilog plot of p_T distribution for each hadron species, which in the present case roughly is $1.5 \leq p_T \leq 2.5$ GeV/c, is fitted with an $dN_{\text{ch}}/dp_T \sim \exp(-\beta p_T)$ type of function. The values of

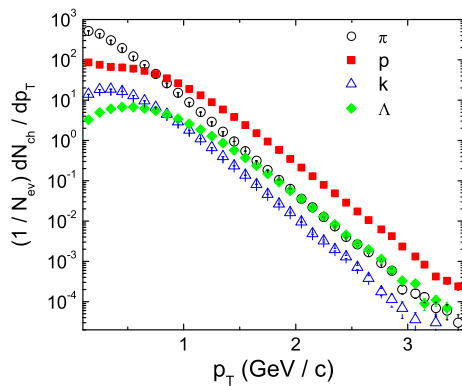


FIG. 2. p_T distribution of identified charged hadrons produced in Au+Au collision at $E_{\text{lab}} = 30A$ GeV.

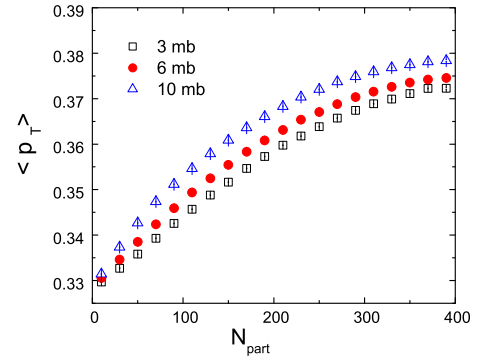


FIG. 3. Average p_T of inclusive charged hadrons produced in the Au+Au collision at $E_{\text{lab}} = 30A$ GeV plotted against centrality.

fit parameter β are 2.344 ± 0.007 , 2.339 ± 0.014 , 2.113 ± 0.003 , and 2.063 ± 0.007 , respectively, for pions, kaons, protons, and lambda particles, indicating the flatness or steepness of the corresponding distribution. Hydrodynamics predicts that due to a collective radial motion, heavier particles gain more in p_T , leading thereby to a flattening in the corresponding p_T spectrum. As a consequence, for heavier particles at low p_T , reduced v_2 values are expected and the rise of v_2 with p_T should shift towards larger p_T . In Fig. 3 the average transverse momentum $\langle p_T \rangle$ is plotted against the centrality measure N_{part} of the collision. We see that after an initial linear rise, the $\langle p_T \rangle$ value saturates with increasing centrality beyond $N_{\text{part}} \approx 300$. In conformity with our expectation, $\langle p_T \rangle$ values lie within a narrow range between 0.33 and 0.38 GeV/c, with a mean lying somewhere around 0.35 GeV/c. At all centrality we observe that a higher σ consistently results in a higher $\langle p_T \rangle$, indicating thereby that the chance of binary interaction positively influences the extent to which transverse degrees of freedom are excited in the intermediate “fireball.” In Ref. [35] we have attributed a higher saturation value of $\langle p_T \rangle$ to a higher isotropic radial flow of charged hadrons in the transverse plane.

A. Dependence on initial geometry

In Fig. 4 we present the centrality dependence of the initial geometric eccentricity (ε_2) and triangularity (ε_3) in the midrapidity region ($0 \leq y \leq 4$) obtained through Eq. (3). As expected, ε_n decreases with N_{part} . It should be noted that ε_2 is always greater than ε_3 except for the highest centrality region where they merge with each other. Taking the initial fluctuations into account [Eq. (4)], we have calculated the elliptic (v_2) and triangular (v_3) flow parameters, and in Fig. 5 and Fig. 6 plotted their average values, respectively, as functions of eccentricity and triangularity in four different intervals of centrality. Extreme central and peripheral collisions are kept out of the purview of this part of the analysis. It is observed that both v_2 and v_3 increase with the corresponding geometric measure of anisotropy of the overlapping part of the colliding nuclei. However, with increasing ε_2 the rise in v_2 is steeper than that of v_3 with increasing ε_3 . As expected, this is an indication that the efficiency with which the initial

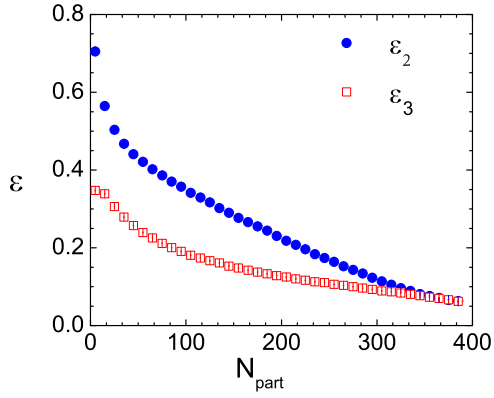


FIG. 4. Centrality dependence of ε_n of the overlapping region of Au+Au collision at $E_{\text{lab}} = 30A$ GeV.

spatial anisotropy gets converted into final-state momentum space anisotropy is more in elliptic flow than in the triangular flow. One should, however, keep it in mind that the latter is not a consequence of any dynamics, but merely is an outcome of initial fluctuations present in the distribution of participating nucleons in coordinate space. It is also interesting to note that for the four centrality intervals considered, the $v_n - \varepsilon_n$ ($n = 2, 3$) dependence becomes steeper with increasing centrality, an observation which is almost similar to that of RHIC [21].

B. Dependence on parton scattering cross section

Figure 7 shows the p_T dependence of differential elliptic flow and triangular flow parameters at midrapidity for different partonic scattering cross sections. One should note that the p_T dependence of v_2 at a particular σ has been presented both with (w) and without (w/o) considering the initial fluctuations

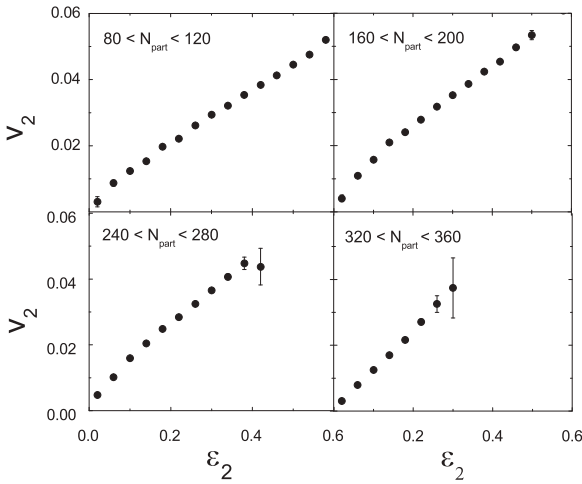


FIG. 5. v_2 as a function of ε_2 in different N_{part} intervals for Au+Au collision at $E_{\text{lab}} = 30A$ GeV with $\sigma = 3$ mb.

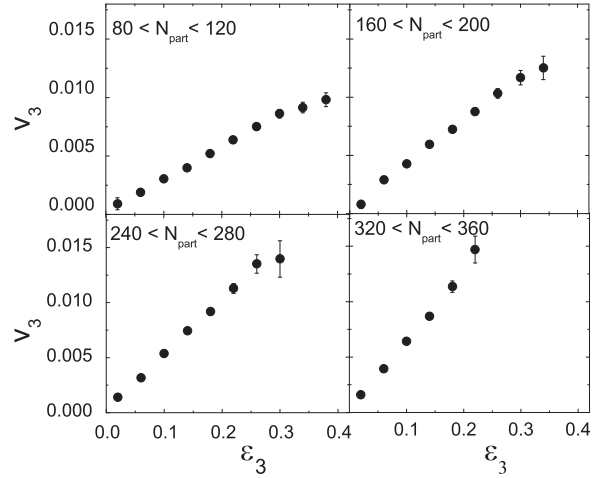


FIG. 6. v_3 as a function of ε_3 in different N_{part} intervals for Au+Au collision at $E_{\text{lab}} = 30A$ GeV with $\sigma = 3$ mb.

in the position coordinates of the participating nucleons. For all σ the v_2 values increase with increasing p_T and saturate at high p_T . It should be noted that there is a small but definite positive impact of initial fluctuations on v_2 at all σ , which grows with increasing p_T as well as with increasing σ . It is also obvious that v_3 arises from the event-by-event fluctuations present in the initial collision geometry of the system, and the pattern (not the value) of its dependence on p_T is nearly the same as that of v_2 . Once again a higher σ results in a higher triangular flow. A consistently higher magnitude of v_2 over v_3 may be attributed to the fact that, while the former arises from the geometrical asymmetry of the overlapping region as well as from initial fluctuations, the latter results only from initial fluctuations. Obviously, in comparison with the azimuthal asymmetry and the pressure gradient built thereof, the initial-state fluctuation

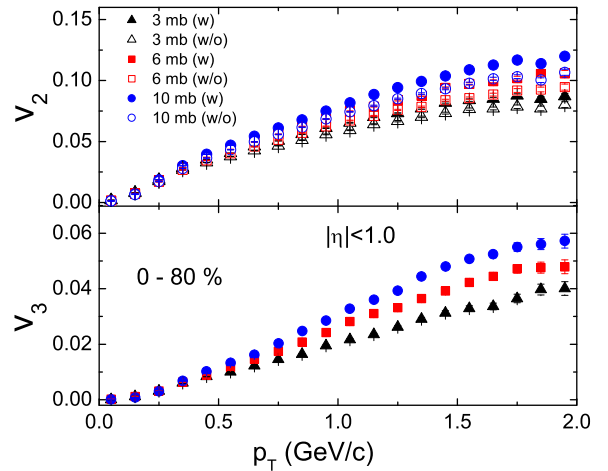


FIG. 7. v_2 and v_3 as functions of p_T at midrapidity for Au+Au collision at $E_{\text{lab}} = 30A$ GeV.

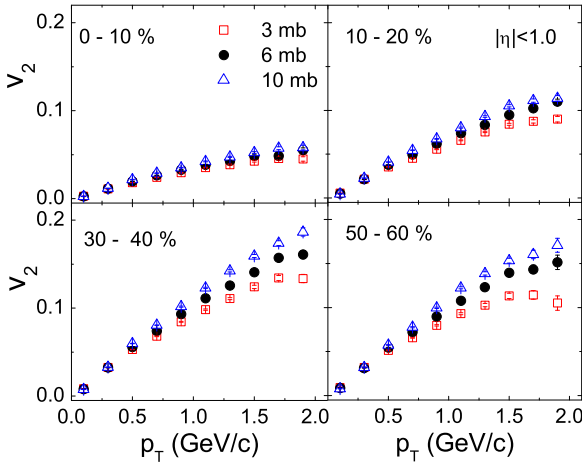


FIG. 8. p_T dependence of v_2 for different centrality windows at midrapidity for Au+Au collision at $E_{\text{lab}} = 30A$ GeV.

is a much weaker phenomenon. Further, Fig. 7 helps us understand that the conversion efficiency from coordinate space anisotropy to momentum space anisotropy grows with increasing σ , which in turn raises the magnitude of both v_2 and v_3 . It is also to be understood from Fig. 7 that with increasing p_T the relative increase in v_3 values are more than those of v_2 . Now we intend to study the centrality dependence of v_2 and v_3 at central rapidity region. In Fig. 8 we see that at low p_T for most central collisions, v_2 is almost independent of σ . However, the σ dependence becomes prominent as we approach peripheral collisions. It is to be noted that v_2 values are maximum in the midcentral region, where the dependence on the partonic cross section at high p_T is also maximum. For midcentral collisions we see a saturation, and for $\sigma = 3$ mb even a decreasing trend in v_2 at high p_T . The observations supplement our result shown in Fig. 7. In Fig. 9 we have studied a similar centrality dependence of v_3 . It is noticed that at each

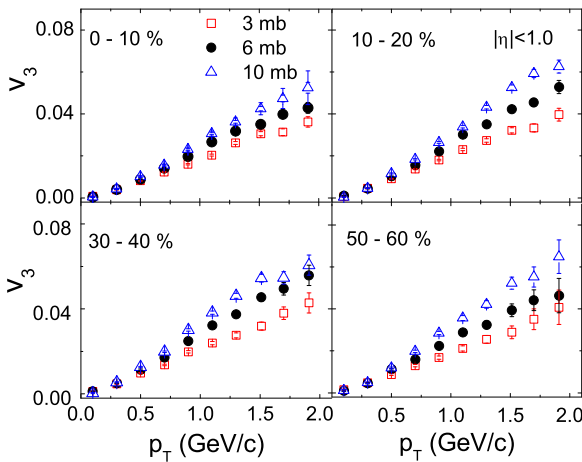


FIG. 9. p_T dependence of v_3 for different centrality windows at midrapidity for Au+Au collision at $E_{\text{lab}} = 30A$ GeV.

centrality bin considered, the variation of v_3 with p_T is more or less identical to that of v_2 . In other words, the triangular flow is less sensitive to centrality. This is an expected result as the elliptic flow is caused by the pressure gradient created over the almond shape of the overlapping part of a collision, but triangular flow is caused from the fluctuations present in this shape. A smaller eccentricity of the overlapping part results in a higher pressure gradient and hence a larger value of elliptic flow. However, it is not necessary for the initial fluctuations to increase or decrease with centrality percentage.

Before proceeding further it would perhaps be prudent to compare our AMPT simulation with existing experimental result(s) on elliptic flow at comparable energy. For this purpose, we have chosen the NA49 experiment on Pb+Pb collisions at $E_{\text{lab}} = 40A$ GeV [44]. It has to be mentioned that in Ref. [44] the standard n th coefficient of anisotropy has been evaluated by using a formula,

$$v_n = \frac{\langle \cos[n(\phi - \Phi_n)] \rangle}{\langle \cos[n(\Phi_n - \Phi_R)] \rangle}, \quad (5)$$

that is different from Eq. (4), which we used. In Eq. (5) Φ_n represents the azimuthal angle of the event plane as explained in Ref. [44], and Φ_R represents that of the reaction plane, i.e., the azimuthal angle of the impact parameter b . In this work, we are interested only in investigating the effects arising from a fluctuating number of participating nucleons from one event to the other. While simulating the data we have not, therefore, taken the changes in the orientation of the impact parameter into account. While determining v_n , we do not have to, therefore, consider the event plane or its fluctuation. Moreover, in Ref. [34] it has been shown that $\Phi_n \approx \Phi_R$. For our simulated data, Eq. (5) therefore reduces simply to

$$v_n = \langle \cos(n\phi) \rangle. \quad (6)$$

In Fig. 10 we have plotted v_2 against p_T for charged pions and protons separately as obtained from the NA49 experiment [44]. Corresponding AMPT-simulated values are also shown in the graph within the same p_T and same rapidity ranges as that of the experiment, as well as using the same centrality criteria as those used in Ref. [44]. In spite of using a reasonably wide range of σ values ($\sigma = 0.1, 1.5, 3.0, 6.0$ mb), we observe that neither the default version of AMPT nor the AMPT (string melting) version can match the entire set of experimental results for any single partonic cross section. For soft hadrons ($p_T < 1.0$ GeV/c), the experimental points behave in a fairly regular manner, at least in the peripheral (more than 33.5% centrality) and in midcentral (12.5–33.5% centrality) collisions. The AMPT, however, exceeds the experiment in this region for all partonic cross sections used either in its SM version, or in the default version. It is to be noted that each 40A GeV Pb+Pb simulated event sample used in this context has the same statistics (i.e., 10^6 Pb+Pb minimum bias events) as that for the 30A GeV Au+Au simulated samples used in this paper. The disagreement at low p_T between experiment and simulation is more prominent in midcentral collisions for pions, and in peripheral as well as in midcentral collisions for protons. The percentage errors (statistical only) associated with the simulated v_2 values for pions in the $p_T < 1.0$ GeV/c range are <4% in peripheral and <3% in midcentral collisions.

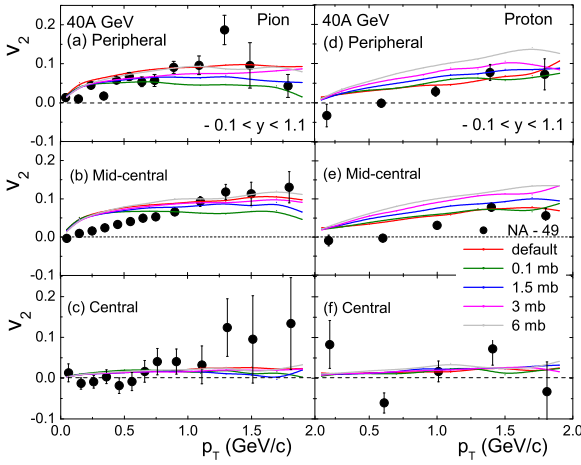


FIG. 10. NA49 data on p_T dependence of v_2 obtained from Pb+Pb interactions at 40A GeV compared with AMPT simulation (both default and string melting) for pions and protons at different partonic cross sections and at different centralities. The experimental values are shown as points, while corresponding simulations are shown by continuous curves.

Corresponding errors for protons are $<9\%$ in peripheral and $<5\%$ in midcentral collisions. On the other hand, in most central collisions the experimental values at high p_T are associated with large errors, and more than one simulation lines pass through them. In order to match the experiment with simulation, either the model perhaps requires a fine tuning, or, to reduce errors, there must be experiments with higher statistics. The CBM experiment is expected to generate much larger statistics than the NA49 experiment, and it would therefore be interesting to see to what extent the flow results of AMPT simulation can come into agreement with the CBM experiment.

The probability distributions of asymmetry parameters obtained eventwise are now schematically represented in Fig. 11 and in Fig. 12 for the same four centralities that are chosen before in this analysis, but only for one σ (3 mb) [45]. The event-to-event fluctuations in the number of participating nucleons are taken into consideration. To compare these distributions with the corresponding eccentricity distributions, both v_n and ε_n are first scaled by their respective mean values, and then these scaled variables are converted to the respective standard normal variables. A strict proportionality like $v_n \propto \varepsilon_n$ should result in a complete overlapping of the $P(v_n/\langle v_n \rangle)$ and $P(\varepsilon_n/\langle \varepsilon_n \rangle)$ distributions. However, for $n = 2$ and 3 such overlapping can be seen only in limited regions. Significant differences between distributions of asymmetry and eccentricity parameters are seen in the most peripheral event sample ($80 \leq N_{\text{part}} \leq 120$). We, however, see less mismatch between v_3 and ε_3 distributions than that between v_2 and ε_2 . The v_3 distributions are consistently wider than the v_2 distributions. While both the flow parameters are almost symmetrically (normally) distributed, the eccentricity distributions are visibly skewed.

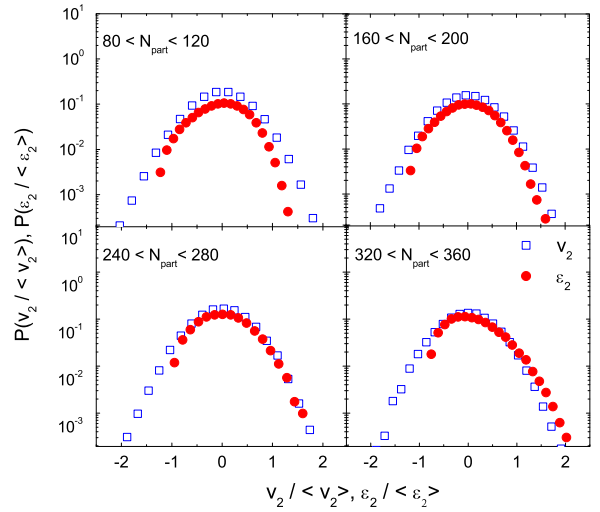


FIG. 11. Distributions of $v_2/\langle v_2 \rangle$ and $\varepsilon_2/\langle \varepsilon_2 \rangle$ for charged hadrons in Au+Au collisions at $E_{\text{lab}} = 30A$ GeV.

In Fig. 13 and Fig. 14 we schematically represent the centrality dependence of v_n/ε_n , a ratio known to be related to the freeze-out temperature [22]. Though in Fig. 5 we found that in limited centrality intervals v_2 is proportional to ε_2 , the v_2/ε_2 ratio shows a lot of variation with varying centrality. We see that in the low-centrality region the v_2/ε_2 ratio increases almost linearly with increasing centrality, becomes nonlinear in the midcentral region, reaches a maximum at $N_{\text{part}} \approx 250$, and, finally, drops down from its maximum point within a very small interval of very high centrality, where the spatial asymmetry of the almond-shaped overlapping region of the colliding Au nuclei is vanishingly small. It has been argued that in the low-density limit of the intermediate “fireball” created in AB

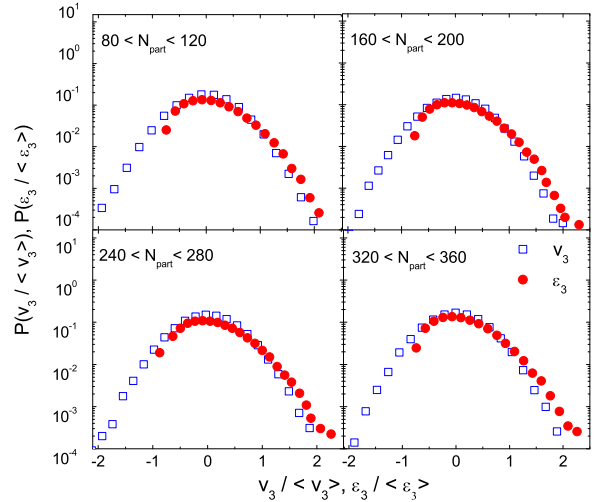


FIG. 12. Distributions of $v_3/\langle v_3 \rangle$ and $\varepsilon_3/\langle \varepsilon_3 \rangle$ for charged hadrons in Au+Au collisions at $E_{\text{lab}} = 30A$ GeV.

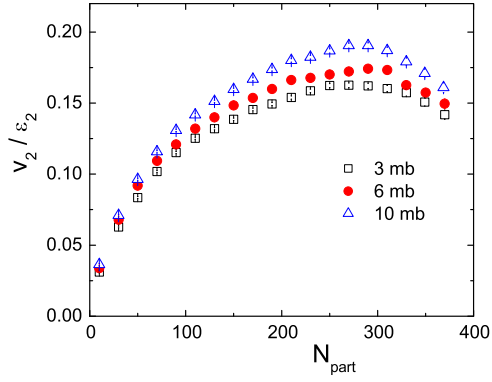


FIG. 13. Elliptical flow scaled by eccentricity against centrality for Au+Au collision at $E_{\text{lab}} = 30A$ GeV.

collisions, the elliptic flow should be proportional to the elliptic anisotropy and the initial particle density [46], which certainly is not the case for our analysis. The eccentricity-scaled elliptic flow is highest at the highest σ considered in this analysis. On the contrary, the triangular flow parameter when scaled by the corresponding triangularity increases monotonically (almost linear) with increasing centrality. Once again a higher σ consistently results in a higher scaled triangular flow. It appears that an experimentally obtained v_n/ϵ_n ratio can perhaps be modeled by suitably adjusting σ as a parameter. To further verify the behavior of scaled elliptical flow under the low-density limit, in Fig. 15 we have plotted the v_2/ϵ_2 ratio against the particle density in the transverse plane. Once again it is found that, except for a few very high centrality intervals, the proportionality

$$\frac{v_2}{\epsilon_2} \propto \frac{1}{S} \frac{dN_{\text{ch}}}{dy} \quad (7)$$

holds. The proportionality constant may depend on the hydro limit of v_2/ϵ_2 , the binary scattering cross section, and the velocity of the elastic wave in the medium concerned [47]. Here S is the transverse area of the overlapping zone of

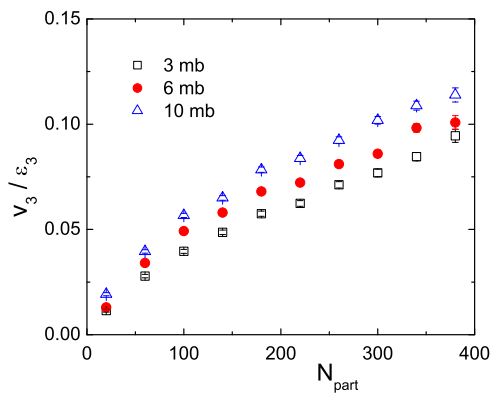


FIG. 14. Triangular flow scaled by triangularity plotted against centrality for Au+Au collision at $E_{\text{lab}} = 30A$ GeV.

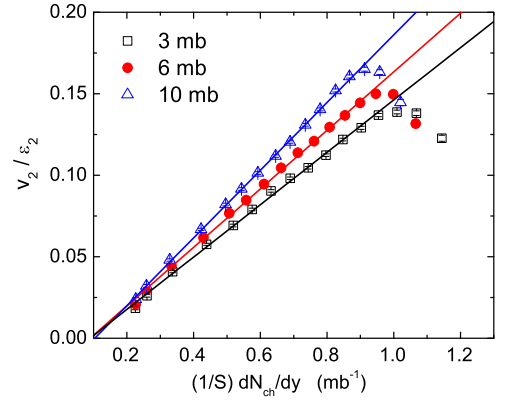


FIG. 15. Elliptical flow scaled by eccentricity plotted against particle density in the transverse plane for Au+Au collision at $E_{\text{lab}} = 30A$ GeV. Solid lines represent best fits to the linear portion of the data.

the colliding nuclei, and dN_{ch}/dy is the rapidity density (a measure of rescattering within the “fireball”) of charged hadrons. A higher σ corresponds to a higher slope of the linear relationship as prescribed in Eq. (7). At a few extreme high centralities the observed sudden deviation from the linear rising trend of the rest, may be attributed to a different physics associated with the corresponding “fireball” medium, which is potentially an interesting issue that needs further scrutiny.

C. Relative strength of v_2 and v_3

We also compute the relative magnitude of the triangular flow with respect to the elliptic flow as a function of N_{part} in different p_T intervals and within $\Delta\eta = \pm 1.0$ about the central η value of the distribution. In Fig. 16 the relative strength of v_3 is observed to increase with centrality, and the rate of increase

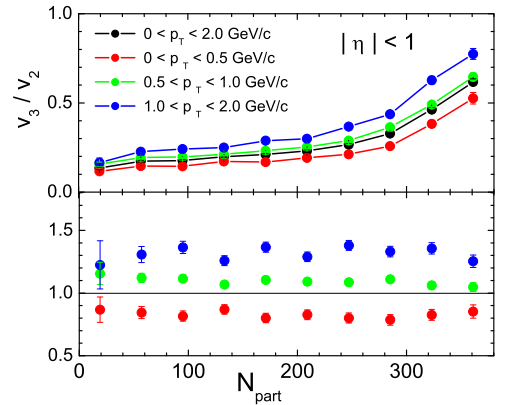


FIG. 16. v_3/v_2 ratio plotted as a function of N_{part} in different p_T intervals for Au+Au collision at $E_{\text{lab}} = 30A$ GeV (upper panel). The same plot, but now the values of v_3/v_2 for a given p_T interval is scaled by the corresponding ratio for the entire p_T interval ($0 \leq p_T \leq 2.0$ GeV/c (lower panel).

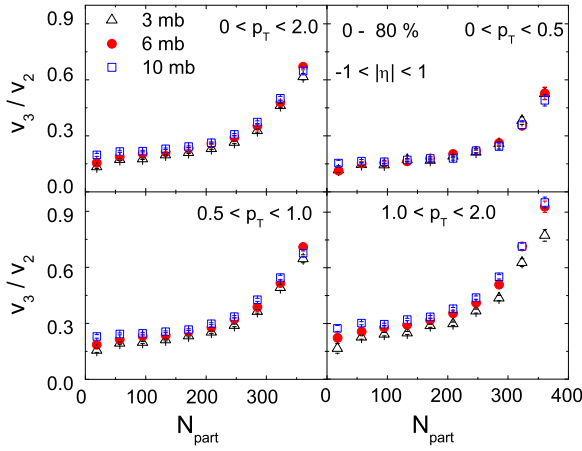


FIG. 17. Dependence of v_3/v_2 on N_{part} in different p_T bins for Au+Au collision at $E_{\text{lab}} = 30A$ GeV.

is higher at the highest centrality region. The results shown in Fig. 16 pertain to $\sigma = 3$ mb. Similar analysis, however, is also performed at $\sigma = 6$ and 10 mb. The gross features of the v_3/v_2 ratio as a function of N_{part} are found to be more or less similar at all σ values considered. The v_3/v_2 ratio is consistently higher at higher p_T . However, when we divide the v_3/v_2 ratio corresponding to a particular p_T interval with that of the entire p_T interval, which in our case is $0 \leq p_T \leq 2.0$ GeV/c, we find that the v_3/v_2 ratio so normalized becomes almost independent of the centrality within statistical uncertainties. This result is schematically presented in the lower panel of Fig. 16, and our observation in this regard is similar to that of an AMPT simulation of RHIC experiment [21]. When we plot the same ratio against N_{part} in different p_T intervals but for different σ [Fig. 17], we see that the relative magnitude of v_3/v_2 initially remains almost constant and then increases nonlinearly with increasing centrality following almost a power law. At low p_T (≤ 0.5 GeV/c) as well as for the entire p_T range, however, it is more or less independent of σ . As shown in the lower panels of Fig. 17, the σ dependence of v_3/v_2 increases marginally at the high p_T range.

D. Species dependence and NCQ scaling

An important aspect of azimuthal anisotropy is the mass ordering of flow parameters of identified hadron species produced in high-energy AB interactions. In Fig. 18 we present the v_2 and v_3 values plotted against p_T at midrapidity for the 0–80% centrality range for different species of produced hadrons, tuning our simulated data to $\sigma = 3$ mb. Below $p_T \approx 1.1$ GeV/c both the elliptic and the triangular flow parameters show an obvious mass ordering, i.e., higher v_n for lower mass hadrons, which is consistent with the hydrodynamic prediction. It is interesting to note that beyond $p_T \approx 1.2$ GeV/c this mass ordering is no longer preserved. It actually gets inverted between mesons and baryons, and at $p_T > 1.4$ GeV/c the mass ordering trends for baryons and mesons split into two separate bands. This feature can be ascribed to the

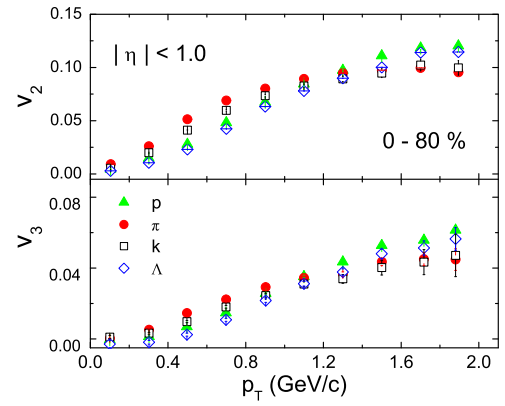


FIG. 18. Species dependence of v_2 (upper panel) and v_3 (lower panel) as a function of p_T for Au+Au collision at $E_{\text{lab}} = 30A$ GeV.

fact that, provided an extended QCD state is formed, both v_2 and v_3 are expected to depend on the constituent partonic degrees of freedom of respective baryon and meson species. As mentioned above, a redistribution of the momentum anisotropy will then build up due to a mass-dependent flattening of the p_T spectra caused by a radial flow generated during the hadronization process, thus resulting in the mass splitting. Similar mass ordering has been reported in RHIC [3,16,48] and LHC experiments [18], and in AMPT simulation of AB collisions at RHIC and FAIR energies [31,43]. It is perhaps due to the quark coalescence mechanism that there is a tendency of the differential flow parameters pertaining to a particular hadron species (meson or baryon) to group together. The recombination of constituent quarks neighboring each other in phase space is also expected to lead to a uniform behavior in the way the flow parameters should depend on the transverse degrees of freedom. In particular, when appropriately scaled by the number of constituent quarks, hadrons belonging to different species are supposed to depend identically on p_T . The phenomenon known as NCQ scaling [19] has been verified in RHIC experiments [49], is considered to be an important evidence of partonic degrees of freedom present in the “fireball,” and is an integrated consequence of both partonic and hadronic interactions [50]. In Fig. 19 we have shown the dependence of v_2 and v_3 on the transverse kinetic energy $K_T = \sqrt{p_T^2 + m_0^2} - m_0$. Following the proposal made in Ref. [19], the K_T and v_2 values are scaled by n_q , while v_3 is scaled by $n_q^{3/2}$. In general, v_n has to be scaled by $n_q^{n/2}$, which specifies how partonic interactions differently influence the flow parameters pertaining to different harmonics. Within statistical uncertainties, our result agrees reasonably well with NCQ. One may speculate that the collective behavior has developed quite early in the partonic stage of the fireball, and it also corroborates a quark coalescence picture of hadronization. A phenomenologically motivated fit function of the form

$$\frac{v_n}{n_q^{n/2}} = \frac{a + bx + cx^2}{d - x} - \frac{a}{2}, \quad (8)$$

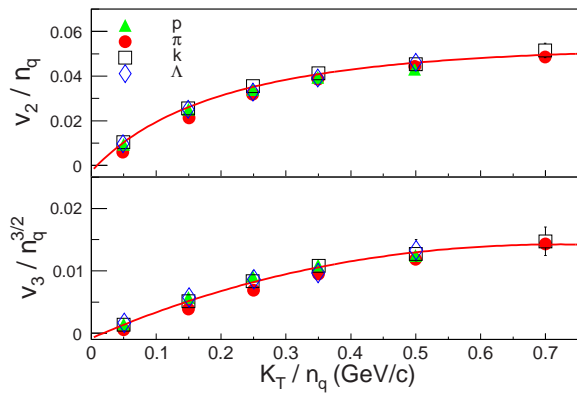


FIG. 19. v_2 (upper panel) and v_3 (lower panel) scaled by the constituent quark numbers of hadrons as a function of K_T/n_q for Au+Au collision at $E_{\text{lab}} = 30A$ GeV.

where $x = K_T/n_q$, describes the scaling satisfactorily [51]. However, at this stage, we do not intend to assign any physical significance to the fit.

IV. SUMMARY

In the framework of the AMPT (string melting) model, in this paper we have presented some results on elliptic and triangular flow of charged hadrons produced in Au+Au interactions at $E_{\text{lab}} = 30A$ GeV. Dependence of flow parameters on initial conditions and binary (partonic) scattering cross section

are investigated. The major observations of this analysis are summarized below. The AMPT (string melting) version is capable of generating momentum space anisotropy even at FAIR energies. The dependence of both elliptic and triangular flow parameters on the corresponding geometrical asymmetry, transverse momentum of charged hadrons, and centrality of collision are as expected. Event-to-event initial fluctuations not only result in a nonzero triangular flow but also have a small but definite positive impact on the elliptic flow. The dependence of flow parameters on partonic scattering cross section is almost always qualitatively similar but quantitatively different by a small amount. However, the NA49 experimental results, particularly at low p_T and in midcentral to peripheral collisions, could not be satisfactorily reproduced by the AMPT simulation either in its default mode or in the string melting version, even though several different partonic cross sections are used. In future while putting the CBM results to a similar comparative test, one will have to be, therefore, careful about the experimental conditions, the statistics, and the technique(s) of data analysis. Except for some low and very high values of anisotropy, to a good approximation the respective initial eccentricities are capable of representing the distributions of asymmetry parameters considered in this analysis. Both the mass ordering of flow parameters of charged hadrons belonging to different species and the scaling with respect to their constituent quark numbers are observed. These simulated results will help us understand several issues related to the collective behavior of hadronic and/or partonic matter in a baryon-rich and moderate-temperature environment until real experiments are held.

-
- [1] S. A. Voloshin, A. M. Poskanzer, and R. Snellings, *Collective Phenomena in Non-Central Nuclear Collisions*, in Landolt-Börnstein series, Relativistic Heavy Ion Physics, Vol. 1/23 (Springer-Verlag, 2010), pp. 293–333.
- [2] K. H. Ackermann *et al.* (STAR Collaboration), *Phys. Rev. Lett.* **86**, 402 (2001).
- [3] C. Adler *et al.* (STAR Collaboration), *Phys. Rev. Lett.* **87**, 182301 (2001).
- [4] S. S. Adler *et al.* (PHENIX Collaboration), *Phys. Rev. Lett.* **98**, 172301 (2007).
- [5] A. Adare *et al.* (PHENIX Collaboration), *Phys. Rev. Lett.* **91**, 182301 (2003).
- [6] K. Aamodt *et al.* (ALICE Collaboration), *Phys. Rev. Lett.* **105**, 252302 (2010).
- [7] K. Aamodt *et al.* (ALICE Collaboration), *Phys. Rev. Lett.* **107**, 032301 (2011).
- [8] G. Aad *et al.* (ATLAS Collaboration), *Phys. Lett. B* **707**, 330 (2012).
- [9] S. Chatrchyan *et al.* (CMS Collaboration), *Phys. Rev. Lett.* **109**, 022301 (2012).
- [10] H. Sorge, *Phys. Rev. Lett.* **78**, 2309 (1997).
- [11] J.-Y. Ollitrault, *Phys. Rev. D* **46**, 229 (1992).
- [12] P. Romatschke and U. Romatschke, *Phys. Rev. Lett.* **99**, 172301 (2007).
- [13] M. Luzum and P. Romatschke, *Phys. Rev. C* **78**, 034915 (2008).
- [14] P. Huovinen *et al.*, *Phys. Lett. B* **503**, 53 (2001).
- [15] J. Adams *et al.* (STAR Collaboration), *Phys. Rev. Lett.* **95**, 122301 (2005).
- [16] B. Abelev *et al.* (STAR Collaboration), *Phys. Rev. C* **75**, 054906 (2007).
- [17] B. Abelev *et al.* (STAR Collaboration), *Phys. Rev. C* **81**, 044902 (2010).
- [18] B. Abelev *et al.* (ALICE Collaboration), *J. High Energy Phys.* **06** (2015) 190.
- [19] D. Molnar and S. A. Voloshin, *Phys. Rev. Lett.* **91**, 092301 (2003).
- [20] X. Dong *et al.*, *Phys. Lett. B* **597**, 328 (2004).
- [21] B. Alver and G. Roland, *Phys. Rev. C* **81**, 054905 (2010).
- [22] D. Teaney and L. Yan, *Phys. Rev. C* **83**, 064904 (2011).
- [23] S. Gavin and G. Moschelli, *Phys. Rev. C* **86**, 034902 (2012).
- [24] B. H. Alver, C. Gombeaud, M. Luzum, and J.-Y. Ollitrault, *Phys. Rev. C* **82**, 034913 (2010).
- [25] B. Schenke, S. Jeon, and C. Gale, *Phys. Rev. C* **82**, 014903 (2010); **85**, 024901 (2012).
- [26] L. Adamczyk *et al.* (STAR Collaboration), *Phys. Rev. C* **88**, 014904 (2013).
- [27] K. Aamodt *et al.* (ALICE Collaboration), *Phys. Lett. B* **719**, 18 (2013).
- [28] D. Solanki, P. Sorensen, S. Basu, R. Raniwala, and T. Nayak, *Phys. Lett. B* **720**, 352 (2013).
- [29] X. Sun (for the STAR Collaboration), *Nucl. Phys. A* **931**, 1194 (2014).

- [30] X. Sun *et al.*, *J. Phys. G* **42**, 115101 (2015).
- [31] L. X. Han, G. L. Ma, Y. G. Ma, X. Z. Cai, J. H. Chen, S. Zhang, and C. Zhong, *Phys. Rev. C* **84**, 064907 (2011).
- [32] J. Aichelin *et al.*, *The CBM Physics Book*, edited by B. Friman, C. Hohne, J. Knoll, S. Leupold, J. Randrup, R. Rapp, and P. Senger (Springer, Berlin, 2010).
- [33] H. Stoecker and W. Greiner, *Phys. Rept.* **137**, 277 (1986).
- [34] A. M. Poskanzer and S. A. Voloshin, *Phys. Rev. C* **58**, 1671 (1998).
- [35] S. Sarkar, P. Mali, and A. Mukhopadhyay, *Phys. Rev. C* **95**, 014908 (2017).
- [36] J. Randrup and J. Cleymans, *Phys. Rev. C* **74**, 047901 (2006).
- [37] B. Zhang, C. M. Ko, B.-A. Li, and Z.-W. Lin, *Phys. Rev. C* **61**, 067901 (2000); Z.-W. Lin, C. M. Ko, B.-A. Li, B. Zhang, and S. Pal, *ibid.* **72**, 064901 (2005).
- [38] X. N. Wang and M. Gyulassy, *Phys. Rev. D* **44**, 3501 (1991).
- [39] B. Zhang, *Comput. Phys. Commun.* **109**, 193 (1998).
- [40] B. A. Li and C. M. Ko, *Phys. Rev. C* **52**, 2037 (1995).
- [41] Z.-W. Lin and C. M. Ko, *Phys. Rev. C* **65**, 034904 (2002); L.-W. Chen *et al.*, *Phys. Lett. B* **605**, 95 (2005).
- [42] B. Zhang, L.-W. Chen, and C. M. Ko, *Nucl. Phys. A* **774**, 665 (2006); L.-W. Chen and C. M. Ko, *Phys. Lett. B* **634**, 205 (2006); J. Xu and C. M. Ko, *Phys. Rev. C* **83**, 034904 (2011).
- [43] P. P. Bhaduri and S. Chattopadhyay, *Phys. Rev. C* **81**, 034906 (2010); M. Nasim, L. Kumar, P. K. Netrakanti, and B. Mohanty, *ibid.* **82**, 054908 (2010).
- [44] C. Alt *et al.* (NA49 Collaboration), *Phys. Rev. C* **68**, 034903 (2003).
- [45] C. Gale, S. Jeon, B. Schenke, P. Tribedy, and R. Venugopalan, *Phys. Rev. Lett.* **110**, 012302 (2013).
- [46] S. A. Voloshin and A. M. Poskanzer, *Phys. Lett. B* **474**, 27 (2000).
- [47] H.-J. Drescher, A. Dumitru, C. Gombeaud, and J.-Y. Ollitrault, *Phys. Rev. C* **76**, 024905 (2007).
- [48] C. Adler *et al.* (STAR Collaboration), *Phys. Rev. Lett.* **89**, 132301 (2002).
- [49] S. Afanasiev *et al.* (PHENIX), *Phys. Rev. Lett.* **99**, 052301 (2007); J. Adams *et al.* (STAR), *ibid.* **92**, 052302 (2004); A. Adare *et al.* (PHENIX), *ibid.* **98**, 162301 (2007); L. Adamczyk *et al.* (STAR), *Phys. Rev. C* **93**, 014907 (2016); B. I. Abelev *et al.* (STAR), *ibid.* **77**, 054901 (2008).
- [50] L. Zheng, H. Li, H. Qin, Q.-Y. Shou, and Z.-B. Yin, *Eur. Phys. J. A* **53**, 124 (2017).
- [51] P. Sorensen, *Quark-Gluon Plasma 4*, edited by R. C. Hwa and X.-N. Wang (World Scientific, Singapore, 2010), pp. 323–374.